

# **High Gain Broadband mm-Wave Antenna Arrays for Short-range Wireless Communication Systems**

Issa Mohamed

A Thesis  
In the Department  
of  
Electrical and Computer Engineering

Presented in Partial Fulfilment of the Requirements  
For the Degree of  
Doctor of Philosophy (Electrical and Computer Engineering) at  
Concordia University  
Montréal, Québec, Canada

December 2019

© Issa Mohamed, 2019

**CONCORDIA UNIVERSITY**  
**SCHOOL OF GRADUATE STUDIES**

This is to certify that the thesis prepared

By: Issa Mohamed

Entitled: High Gain Broadband mm-Wave Antenna Arrays for Short-range Wireless  
Communication Systems

and submitted in partial fulfillment of the requirements for the degree of

Doctor Of Philosophy (Electrical and Computer Engineering)

complies with the regulations of the University and meets the accepted standards with respect to  
originality and quality.

Signed by the final examining committee:

\_\_\_\_\_  
Dr. Mehdi Hojjati Chair

\_\_\_\_\_  
Dr. Yahia Antar External Examiner

\_\_\_\_\_  
Dr. Alexei Kokotov External to Program

\_\_\_\_\_  
Dr. Robert Paknys Examiner

\_\_\_\_\_  
Dr. Ahmed A. Kishk Examiner

\_\_\_\_\_  
Dr. Abdel Sebak Thesis Supervisor

Approved by \_\_\_\_\_  
Dr. Rastko Selmic, Graduate Program Director

December 5, 2019

\_\_\_\_\_  
Dr. Amir Asif, Dean  
Gina Cody School of Engineering & Computer Science

## **Abstract**

### **High Gain Broadband mm-Wave Antenna Arrays for Short-range Wireless Communication Systems**

**Issa Mohamed, Ph.D.**  
**Concordia University, 2019**

Recently, the ever-increasing demand for fifth-generation (5G) wireless applications has turned millimeter-wave (mm-wave) multi-beam array antenna into quite a promising research direction. Besides offering a remarkable bandwidth for high-speed wireless connectivity, the short wavelengths (1 to 10 mm) of mm-wave signals makes the size of the antenna array with beamforming network (BFN) compatible with a transceiver front-end. The high losses associated with mm-wave wireless links and systems considered the foremost challenge and may restrict the wireless communication range. Therefore, a wideband substrate integrated waveguide (SIW)-based antenna with high gain and beam scanning capabilities would be a solution for these challenges, as it can increase the coverage area of mm-wave wireless systems and mitigate the multipath interference to achieve a high signal to noise (S/N) ratio, and thereby fulfill the link budget requirements.

This thesis focuses on the analysis and design of single- and multi-beam mm-wave antenna arrays based on SIW technology to fulfill the growing demand for wideband high-gain planar antenna arrays with beam steering capability at V-band. A tapered slot antenna (TSA) and cavity-backed patch antenna are used as the main radiators in these systems to achieve high-gain and high efficiency over a wide range of operating frequencies. Accordingly, numerous design challenges and BFN-related issues have been addressed in this work.

Firstly, an antipodal Fermi tapered slot antenna (AFTSA) with sine-shaped corrugations is proposed at V-band. The antenna provides a flat measured gain of 20 dB with a return loss better than 22 dB. In addition, A broadband double-layer SIW-to-slotline transition is proposed to feed a planar linearly tapered slot antenna (PLTSA) covering the band 46-72 GHz. This new feeding technique, which addresses the bandwidth limits of regular microstrip-to-slotline transitions and avoids the bond wires and air bridges, is utilized to feed a 1x4 SIW-based PLTSA array.

Secondly, a new cavity-backed aperture-coupled patch antenna with overlapped 1-dB gain and impedance bandwidth of 43.4 % (56-87 GHz) for  $|S_{11}| < -10$  dB and an average gain of 8.2 dBi is

designed. A detailed operating principle is presented. Based on the proposed element, an SIW based 1x8 array is constructed, whose beam-shape is synthesized by amplitude tapering according to Taylor distribution to reduce the sidelobe level. Moreover, a four-layered 4x4 cavity-backed antenna array with a low-loss full-corporate SIW feed network is implemented for gain and aperture efficiency enhancement. The measured results exhibited a bandwidth of 38.4 % (55.2-81.4 GHz) for  $|S_{11}| < -10$  dB and a gain of 20.5 dBi. A single-layer right-angle transition between SIW and air-filled WR15 waveguide along with an equivalent circuit model is introduced and used to measure the performance of both proposed linear and planar arrays.

Thirdly, two 1-D scanning multi-beam array designs based on SIW technology, at 60 GHz, have been presented. The first design is a compact multi-beam scanning 4x4 slot antenna array with broadside radiation. The BFN is implemented using a dual-layer 4x4 Butler matrix, where the  $45^\circ$  and  $0^\circ$  phase shifters are designed on a separate layer with different permittivity, resulting in a significant size reduction compared to a conventional single layer. A detailed theoretical analysis, principle of operation and the circuit-model of the proposed phase shifter have been discussed, showing less dispersion characteristics compared to ordinary phase shifters. The measured results show an azimuthal coverage of  $121^\circ$ . The second design is a wideband high gain multi-beam tapered slot antenna array with end-fire radiation. An SIW Butler matrix with a modified hybrid crossover is used as a BFN. The fabricated prototype exhibits a field of view of  $97^\circ$  in the azimuthal plane, with measured gain ranges from 12.7 to 15.6 dBi.

Lastly, a novel three-layered SIW-fed cavity-backed linearly polarized (LP) patch antenna element is presented, covering a bandwidth of 36.2 % (53-76.4 GHz) with a flat gain ranging from 7.6 to 8.2 dBi. A compact two-layered beam forming network is designed with a size reduction of 28 % compared to a standard one-layered BFN without affecting its s-parameters. The results show that the impedance bandwidth is 31.1 % (51.5-70.5 GHz) for  $|S_{11}| < -16$  dB with an average insertion loss of 1.3 dB. The proposed antenna element and BFN are employed to form a compact 2x2 multibeam array at 60 GHz for 2-D scanning applications. The array shows a bandwidth better than 27 % with a radiation gain of up to 12.4 dBi and radiation efficiency of 80%. The multi-beam array features four tilted beams at  $33^\circ$  from a boresight direction with  $45^\circ$ ,  $135^\circ$ ,  $225^\circ$  and  $315^\circ$  in azimuth directions, i.e., one beam in each quadrant.



## **Acknowledgements**

I would to express my deepest gratitude and thanks to my supervisor, Prof. Abdel Razik Sebak for his patience, for being generous with his time and for countless great ideas and advices that assisted me to overcome the difficulties of research. The completion of this thesis would not have been possible without his significant support. I am truly indebted to him for his insightful comments and uncompromising attention to details.

Also, I would like to thank the committee members, Prof. A. Kishk, Prof. R. Paknys, Prof. Y. Antar and Prof. A. Kokotov for their review of my thesis and their numerous constructive comments and feedback.

I would like to express sincere appreciation to all of my PhD colleagues for their help and friendship.

I would like to express a deep sense of gratitude to my family.

# Table of Contents

<b>List of Figures .....</b>	<b>ix</b>
<b>List of Tables .....</b>	<b>xv</b>
<b>List of Abbreviations .....</b>	<b>xvi</b>
<b>Chapter 1 Introduction.....</b>	<b>1</b>
1.1 Background and Motivation.....	1
1.2 Problem Statement .....	3
1.3 MMW Propagation Challenges.....	4
1.3.1 Free Space Loss .....	5
1.3.2 Atmospheric Attenuation.....	5
1.3.3 Rain Losses .....	5
1.3.4 Path Blockage Attenuation .....	7
1.4 60 GHz Channel Characteristics .....	7
1.4.1 Antenna Characteristics .....	8
1.4.2 Link Budget .....	8
1.5 Objectives.....	9
1.6 Thesis Outline .....	10
1.7 Contributions.....	11
<b>Chapter 2 Literature Review .....</b>	<b>13</b>
2.1 Theoretical Background and Methodology.....	13
2.1.1 Substrate Integrated Waveguide (SIW) .....	13
2.1.2 Tapered Slot Antenna .....	15
2.1.3 Multibeam Scanning Array Antenna.....	17
2.1.4 Simulation Software Packages.....	18
2.2 Tapered Slot Antennas .....	19
2.3 Cavity Backed Antennas .....	21
2.4 Multibeam Scanning Array Antenna.....	24
<b>Chapter 3 Design and Realization of Broadband High-gain MMW Antennas.....</b>	<b>27</b>
3.1 Introduction .....	27

3.2	High-Gain Dielectric-Loaded Antipodal Fermi Tapered Slot Antenna .....	28
3.2.1	Antenna Design and Configuration .....	28
3.2.2	Experiments and Discussions .....	30
3.3	A Broadband Double-Layered Planar LTS Antenna with Low Cross-Polarization .....	36
3.3.1	Antenna Element Design and Configuration .....	36
3.3.2	Simulated and Measured Results .....	38
3.3.3	1x4 Array Design and Experimental Validation.....	41
3.4	Antipodal Fermi Tapered Slot Antenna Array.....	44
3.4.1	Array Design.....	44
3.4.2	Simulated Results.....	45
3.5	Broadband Transition of SIW to Air-filled Rectangular Waveguide .....	46
3.5.1	Transition Design and Working Principal .....	46
3.5.2	Measurement Results and Discussion.....	50
3.6	A Compact Wideband SIW-Fed Cavity-Backed Patch Antenna Arrays .....	52
3.6.1	Antenna Element.....	52
3.6.2	Linear Antenna Array .....	57
3.6.3	Planar Antenna Arrays.....	66
<b>Chapter 4</b>	<b>One-dimensional Scanning Array Antennas .....</b>	<b>75</b>
4.1	Introduction .....	75
4.2	Multi-Beam Slot Antenna Array Fed by Dual-Layered 4x4 Butler Matrix .....	75
4.2.1	Single Element Design and Characterization .....	76
4.2.2	Beamforming Network Design .....	78
4.2.3	Multibeam Array and Measurements.....	90
4.3	Multibeam End-Fire Fermi Tapered Slot Antenna Array .....	95
4.3.1	Single Element Design and Characterization .....	95
4.3.2	Beamforming Network Design .....	95
4.3.3	Fabrication and Measurements .....	107
<b>Chapter 5</b>	<b>Two-dimensional Scanning Multibeam Cavity-Backed Patch Antenna Array .....</b>	<b>113</b>
5.1	Introduction .....	113
5.2	Single Element Design and Realization .....	113
5.2.1	Geometry and Working Principle .....	114
5.2.2	Antenna Performance.....	117

5.2.3	Measurement of Single Element .....	121
5.3	2-D Multibeam Array .....	123
5.3.1	Antenna Array Structure .....	124
5.3.2	Beamforming Network .....	125
5.4	Measurement Results and Discussion .....	130
<b>Chapter 6</b>	<b>Conclusion and Future Work .....</b>	<b>136</b>
6.1	Conclusion.....	136
6.2	Future Work .....	138
<b>Bibliography</b>	.....	<b>139</b>
<b>List of Publication</b>	.....	<b>149</b>

## List of Figures

Figure 1.1: Average atmospheric absorption versus frequency [20] .....	6
Figure 1.2: Rain attenuation at microwave and MMW frequencies [3] .....	6
Figure 1.3: Multipath of short-range wireless communications .....	7
Figure 1.4: MMW transmitter, receiver, and wireless link .....	9
Figure 2.1: Topology of an SIW structure synthesized using metallic vias.....	14
Figure 2.2: The measured complex permittivity of RT/Duroid 6002 substrate .....	15
Figure 2.3: Different taper profiles of ATSA, microstrip-to-slot transition and electric field distribution at various cross-sections.....	16
Figure 2.4: Phased array antenna .....	18
Figure 2.5: An SIW-based cavity-backed antennas.(a) Patch [J1].(b) Slot [74].(c) ME dipole [79]..	23
Figure 2.6: Switched-beam array with Butler matrix network .....	25
Figure 3.1: AFTSA geometry .....	29
Figure 3.2: Modified antenna configurations: (a) AFTSA with delta-shaped slot and (b) Dielectric- loaded AFTSA with a diamond-shaped slot.....	29
Figure 3.3: Impact of varying loaded AFTSA amplitude corrugation on $ S_{11} $ and the realized gain	30
Figure 3.4: Top (T) and bottom (B) views of fabricated prototypes of AFTSA, AFTSA with delta- shaped slot and loaded AFTSA with a diamond-shaped slot (from right to left) . .....	31
Figure 3.5: Simulated and measured realized gain and $ S_{11} $ of the three antennas .....	31
Figure 3.6: Simulated results of the impact of delta-shaped slot and dielectric-loaded with a diamond- shaped slot on the F/B ratio of AFTSA. ....	32
Figure 3.7: Gain measurement setup, (a) two standard gain horns (SGH), (b) standard gain horn and antenna under test (AUT) .....	33
Figure 3.8: Measured and simulated total efficiency (%).(a) AFTSA. (b) AFTSA with a delta-shaped slot. (c) LAFTSA with a diamond-shaped slot.....	34
Figure 3.9: Simulated and measured radiation patterns of AFTSA at 60 GHz.....	35
Figure 3.10: Simulated and measured radiation patterns of AFTSA with a delta-shaped slot at 60 GHz .....	35
Figure 3.11: Simulated and measured radiation patterns of LAFTSA with a diamond-shaped slot at 60 GHz .....	35
Figure 3.12: Geometry and design parameters of the proposed SIW-based planar linearly tapered slot antenna (PLTSA) (a) Top view and (b) Perspective view.....	37
Figure 3.13: Top and bottom view of planar linearly tapered slot antenna prototype .....	39

Figure 3.14: Measured and simulated $ S_{11} $ and realized gain of the proposed PLTS antenna.....	39
Figure 3.15: Simulated and measured radiation of an element PLTS antenna at 54, 60 and 66 GHz ..	40
Figure 3.16: Top and bottom view of the PLTS antenna array prototype .....	41
Figure 3.17: Measured and simulated $ S_{11} $ and realized gain of the proposed PLTS antenna array..	42
Figure 3.18: Simulated and measured radiation of the PLTS antenna array at 54, 60 and 66 GHz ..	43
Figure 3.19: The proposed 4-element AFTSA array: (a) 3-D , (b) top, (c) bottom and (d) side view	44
Figure 3.20: $ S_{11} $ of the antipodal Fermi tapered slot antenna (AFTSA) array.....	45
Figure 3.21: Comparison between realized gain of single element and 1x4 AFTSA array.....	45
Figure 3.22: E- and H-plane radiation patterns of the AFTSA array at 60 GHz .....	46
Figure 3.23: Perspective view of the proposed SIW to waveguide transition .....	47
Figure 3.24: Top view of the SIW-to-WG transition .....	47
Figure 3.25: Electric field vector distribution at 63 GHz. (a) At the cross-section plane $A-A'$ . (b) At the reference plane (see Figure 3.23) .....	48
Figure 3.26: (a) Equivalent-circuit model of the transition. (b) Simplified version .....	49
Figure 3.27: Simulated s-parameters of single transition .....	49
Figure 3.28: Fabricated back-to-back transitions. (a) Top view. (b) The back-to-back with two identical WR15 WG to coaxial adapters .....	50
Figure 3.29: Measured and simulated S-parameters of back-to-back transition.....	51
Figure 3.30: Geometry of cavity-backed patch antenna element. (a) 3-D view. (b) Substrate 1. (c) Substrate 2. (d) Substrate 3 .....	53
Figure 3.31: Electric field distribution of the proposed element. (a) At the cavity. (b) At the patch ..	53
Figure 3.32: The effect of two modified antennas on $ S_{11} $ and gain referenced to the proposed antenna (cavity+ patch) .....	54
Figure 3.33: Simulated $ S_{11} $ and gain of the cavity-backed antenna element .....	54
Figure 3.34: Simulated radiation patterns of the proposed antenna element at 56, 62, 68, 74, 80 and 86 GHz .....	56
Figure 3.35: Layout of the unequal 8-way SIW power divider with Taylor distribution .....	58
Figure 3.36: Simulated S-parameters. (a) Equal T-junction divider (stage 1). (b) Unequal Y-junction divider (stage3) .....	59
Figure 3.37: Simulated S-parameters of the proposed 8-way SIW feeding network with Taylor distribution .....	59
Figure 3.38: Simulated phase response of the 8-way SIW power divider with Taylor distribution...	60

Figure 3.39: (a) Geometry of the SIW-to-WR15 transition (top view).(b) Simulated S-parameters	.61
Figure 3.40: Geometry of the proposed 1x8 cavity-backed patch array	62
Figure 3.41: Photo of the fabricated prototype for the proposed 1x8 cavity-backed patch array. (a) Disassembled. (b) Assembled. (c) Radiation test	62
Figure 3.42: Simulated and measured $ S_{11} $ and gain of the 1x8 cavity-backed patch array	64
Figure 3.43: Simulated and measured radiation patterns of the 1x8 cavity-backed patch array at 56, 62, 74 and 79 GHz	65
Figure 3.44: Top view of each layer of the 2x2-element cavity-backed patch subarray with detailed design parameters. (a) Substrate 1. (b) Substrate 2. (c) Substrate 3. (d) Substrate 4	66
Figure 3.45: Field distributions of the 4-way divider close to the cavity-divider interface. (a) Magnetic field. (b) Electric field	67
Figure 3.46: Simulated $ S_{11} $ and gain of the 2x2-element cavity-backed patch subarray	67
Figure 3.47: Simulated radiation patterns of the 2x2-element cavity-backed patch subarray	68
Figure 3.48: 3-D view of the proposed 4x4 cavity-backed patch array with full-corporate feeding network	69
Figure 3.49: Photo of the fabricated prototype for the proposed 4x4 cavity-backed patch array. (a) Disassembled (b) Assembled. (c) Radiation test	70
Figure 3.50: Simulated and measured $ S_{11} $ and gain of the 4x4 cavity-backed patch array	71
Figure 3.51: Simulated and measured radiation patterns of the 4x4 cavity-backed patch array at 56, 62, 68, 74 and 79 GHz	72
Figure 4.1: Schematic of branch SIW slot antenna with details of one slot parameters. ( $W_{siw} = 2.25mm$ , $L_a = 8.8mm$ )	76
Figure 4.2: Simulated $ S_{11} $ of a single branch slot array	77
Figure 4.3: Simulated E- and H-plane radiation patterns of a single branch slot array at 60 GHz	77
Figure 4.4: Block diagram of a 4x4 Butler matrix	78
Figure 4.5: Geometry and detailed dimensions of the $90^\circ$ hybrid coupler	79
Figure 4.6: Simulated S-parameters of the 3 dB coupler. (a) Magnitude. (b) Phase	80
Figure 4.7: Phase shifts introduced by various phase shifters	81
Figure 4.8: Phase versus width response of 6002- and 3035-filled waveguides with equal length ( $L = 7mm$ ) at 60 GHz	83
Figure 4.9: Double-layered offset longitudinal slot-coupled transition. (a) Longitudinal cross section. (b) Equivalent circuit model	83

Figure 4.10: Geometry of the crossover and proposed SIW phase shifter: (a) Top view of crossover (substrate 2 not shown), and (b) Pictorial view of phase shifter with crossover as a reference .....	85
Figure 4.11: Simulated S-parameters of the crossover .....	86
Figure 4.12: Electric field distribution of the $45^0$ phase shifter and crossover. (a) Top view. (b) Longitudinal section view.....	86
Figure 4.13: Simulated S-parameters of $45^0$ phase shifter. (a) Magnitude. (b) Phase response .....	87
Figure 4.14: Simulated S-parameters of $0^0$ phase shifter. (a) Magnitude. (b) Phase response .....	87
Figure 4.15: Topology of the proposed SIW Butler matrix .....	87
Figure 4.16: Simulated S-parameters of the SIW matrix with port 1 excitation.....	88
Figure 4.17: Simulated S-parameters of the SIW matrix with port 2 excitation.....	89
Figure 4.18: Phase differences between output ports ( $P_i$ , port $i$ excited, where $i = 1, 2, \dots, 4$ ). ....	89
Figure 4.19: Photograph of the fabricated SIW multi-beam slot array.....	90
Figure 4.20: Measured and simulated S-parameters of the multi-beam slot array. (a) Port 1 excitation. (b) Port 2 excitation. ....	91
Figure 4.21: Photograph of the prototype in anechoic chamber for radiation patterns test .....	92
Figure 4.22: Simulated radiation pattern for all 4 input ports of the multibeam slot array. (a) 58.5 GHz. (b) 60 GHz. (c) 61.5 GHz .....	93
Figure 4.23: Measured radiation pattern of all 4 input ports for the multibeam slot array at 60 GHz .....	94
Figure 4.24: Measured gain for different input port excitation of the proposed multibeam slot array	94
Figure 4.25: Top and ground view of TSA as seen from top ( $A_c=0.5 \text{ mm}$ , $k =$ , $W_{ap}=2.8 \text{ mm}$ , $c=4$ , $b = 0.3$ , $a= 2.3$ ).....	96
Figure 4.26: Simulated $ S_{11} $ and gain of the proposed TSA .....	96
Figure 4.27: Simulated E- and H-plane radiation patterns of the single TSA at 60 GHz .....	97
Figure 4.28: Layout of the SIW 3-dB coupler .....	98
Figure 4.29: Performance of the SIW 3dB coupler. (a) S-parameters. (b) Differential phase and magnitude of port 2 and 3 .....	98
Figure 4.30: Topology of the modified SIW hybrid crossover with geometric dimensions .....	99
Figure 4.31: The impact of parameters $L$ and $\theta$ on the S-parameters of hybrid crossover .....	100
Figure 4.32: Simulated S-parameters of the proposed SIW hybrid crossover .....	101
Figure 4.33 Simulated S-parameters of the SIW phase shifters .....	102
Figure 4.34: Simulated differential phases of the proposed SIW phase shifters .....	103



Figure 4.35: Electric field distribution of the SIW phase shifters referenced with modified crossover,(a) $0^0$ and (b) $45^0$ phase shifter .....	103
Figure 4.36: Geometry of the SIW Butler matrix .....	104
Figure 4.37: Simulated S-parameters of the SIW Butler matrix. (a) Port 1 excitation. (b) Port 2 excitation .....	105
Figure 4.38: Electric field distribution of the proposed SIW Butler matrix. (a) Port 1 excitation. (b) Port 2 excitation .....	106
Figure 4.39: Output phase difference of Butler matrix. ( $P_i$ , port i excited, where $i=1,2,3$ and 4) ..	106
Figure 4.40: Photograph of the assembled prototype of the proposed multibeam end-fire FTSA array .....	107
Figure 4.41: Measured and simulated reflection coefficients of the multibeam end-fire FTSA array for port 1 and 2 excitations .....	108
Figure 4.42: Measured and simulated isolation between input ports of the multibeam end-fire FTSA array for port 1 and 2 excitations .....	109
Figure 4.43: Measured and simulated radiation patterns of the proposed multibeam FTSA array ..	111
Figure 4.44: Measured and simulated gain of the FTSA array with port 1 and 2 excitation .....	112
Figure 5.1: Geometry of the proposed cavity-backed patch antenna. (a) Exploded view. (b) Feed layer (substrate #1). (c) Cavity layer (substrate #2).(d) Antenna layer (substrate #3).....	114
Figure 5.2: Electric field distribution at different layers of the proposed cavity-backed patch antenna: (a) E-field magnitude of the $TE_{10}$ mode in SIW feed (b) radiating E-field above the patch at height of 1 mm .....	115
Figure 5.3: Simulated reflection coefficient and gain of the single cavity-backed patch antenna....	115
Figure 5.4: Comparison of the proposed antenna with cavity-only and patch-only antennas in terms of $ S_{11} $ and radiation gain.....	117
Figure 5.5: The effect of number of vias on the reflection coefficient .....	118
Figure 5.6: Simulated E- and H-plane radiation patterns of the proposed cavity-backed patch antenna at 53, 57, 60, 65, 70, and 76 GHz .....	119
Figure 5.7: Simulated radiation efficiency of the proposed cavity-backed patch antenna .....	120
Figure 5.8: Fabricated prototype of the proposed cavity-backed patch antenna element. (a) Disassembled. (b) Assembled.....	122
Figure 5.9: Simulated and measured $ S_{11} $ and radiation gain of cavity-backed patch antenna element .....	122
Figure 5.10: Photograph of TRL calibration kit used to de-embed the WR15 to coaxial and transition from measurements.....	122

Figure 5.11: Comparison between measured and simulated radiation patterns for E- and H-plane of the cavity backed patch antenna element at 55, 60, 65 GHz .....	123
Figure 5.12: Exploded view of the proposed multibeam 2x2 cavity-backed patch antenna array. (Substrates #1 to #3 are 0.508-mm thick Rogers 6002 and substrate #4 is 0.254-mm thick Rogers 588 coupling slots .....	124
Figure 5.13: SIW 90° hybrid coupler. (a) Geometry ( $L_1 = 3.75 \text{ mm}$ , $L_2 = 3.06 \text{ mm}$ and $W_c = 3.9 \text{ mm}$ ). (b) Simulated s-parameters. (c) Differential magnitude and phase of output ports .....	125
Figure 5.14: Geometry of the proposed SIW beam-forming network .....	126
Figure 5.15: BFN performance with port 1 excitation. (a) S-parameters performance. (c) Phase differences between output ports .....	127
Figure 5.16: The proposed SIW E-plane 180° bend. (a) Perspective view. (b) Top view (where $W_{slot} = 0.4 \text{ mm}$ , $L_{slot} = 2.5 \text{ mm}$ , $X_1 = 1.66 \text{ mm}$ and $X_2 = 0.4 \text{ mm}$ ) (c) Reflection and transmission coefficient .....	128
Figure 5.17: Fabricated prototype of the proposed multibeam cavity-backed patch array. (a) Top view (b) Bottom view. (c) Prototype connected to WR15 waveguides for s-parameters test. (d) Prototype inside anechoic chamber for radiation pattern test.....	129
Figure 5.18: Measured and simulation s-parameters of the multibeam array with port 1 excitation	131
Figure 5.19: Measured S-parameters of fabricated antenna array with ports 2, 3, and 4 excitations	131
Figure 5.20: Measured and simulated radiation patterns of the proposed multibeam cavity-backed patch array at 55, 60 and 66 GHz .....	133
Figure 5.21: Measured radiation patterns of $xoz$ - and $yo$ z-plane for different port excitations at 60 GHz. (a) port 2 (b) port 3 and (c) port 4 .....	134
Figure 5.22: Simulated radiation pattern of the multibeam cavity-backed patch array at 45°, 135° cut planes and principal planes ( $xoz$ - and $yo$ z-plane) with port 1 excitation for 55, 60 and 66 GHz .....	134
Figure 5.23: Simulated radiation patterns for all input ports of the proposed multibeam cavity-backed patch array .....	135
Figure 5.24: Gain and directivity of the proposed multibeam cavity-backed patch array .....	135

## List of Tables

Table 3.1: Optimized dimensions of AFTSAs .....	29
Table 3.2: Optimized dimensions of the proposed antenna .....	38
Table 3.3: Optimized dimensions of the SIW-to-WR15 transition .....	48
Table 3.4: Comparison between proposed SIW-to-WR15 and reported transitions.....	50
Table 3.5: Dimensions of cavity-backed patch antenna element.....	52
Table 3.6: Comparison between proposed cavity-backed and reported MMW antenna elements .....	57
Table 3.7: Dimensions of power dividers of each stage [Units: mm].....	58
Table 3.8: Taylor weights distribution and S-parameters .....	61
Table 3.9: Measured radiation characteristics of the 1x8 cavity-backed patch array .....	64
Table 3.10: Dimensions of the 2x2 cavity-backed subarray .....	67
Table 3.11: Comparison between proposed and previously published MMW antenna arrays.....	74
Table 4.1: Ideal output phase difference of BM with different input port excitation .....	78
Table 4.2: Calculated dimensions of the coupling region of the $90^\circ$ hybrid.....	80
Table 4.3: Calculated dimensions of the coupling region of the crossover .....	86
Table 4.4: Optimized dimensions of the $45^\circ$ and $0^\circ$ phase shifters [Units: mm] .....	86
Table 5.1: Dimensions of the proposed antenna .....	115
Table 5.2: Comparison among proposed and reported 60-GHz LP antenna .....	121
Table 5.3: Theoretical phase of the output ports of the proposed BFN .....	126
Table 5.4: Comparison between proposed BFN and other work.....	129
Table 5.5: Theoretical phase difference along x- and y-axis and main directions of multibeam array .....	132

## List of Abbreviations

2-D	Two-Dimensional
3-D	Three-Dimensional
AFTSA	Antipodal Fermi Tapered Slot Antenna
ATSA	Antipodal Tapered Slot Antenna
BFN	Beamforming Network
BER	Bit Error Rate
CPW	Coplanar Waveguide
CWSA	Constant Width Slot Antenna
CST MWS	Computer Simulation Technology Microwave Studio
DOA	Direction-of-Arrival
EIRP	Effective Isotropic Radiated Power
EM	Electromagnetic
F/B	Front-to-Back Ratio
FCC	Federal Communication Commission
FDTD	Finite Difference Time Domain
FE	Finite Element
FIT	Finite Integration Technique
Gbps	Gega bits per seconds
HDMI	High Definition Multimedia Interface
HFSS	High Frequency Structure Simulator
ISI	Inter-Symbol Interference
ISM	Industrial, Scientific, and Medical
ITU	International Telecommunication Union
LAFTSA	Loaded Antipodal Fermi Tapered Slot Antenna
LTSA	Linear Tapered Slot Antenna
LTCC	Low Temperature Co-fired Ceramic
LMS	Lease Mean Square
LOS	Line of Sight
MMW	Millimeter Wave

5G	Fifth Generation
MIMO	Multiple-Input Multiple-Output
MoM	Method of Moments
NLOS	Non-Line of Sight
PCB	Printed Circuit Board
RFID	Radio Frequency Identification
SMI	Sample Matrix Inversion
SLL	Side Lobe Level
SNR	Signal-to-Noise Ratio
SIW	Substrate Integrated Waveguide
TSA	Tapered Slot Antenna
VSWR	Voltage Standing Wave Ratio
WLAN	Wireless Local Area Networks
RWG	Rectangular Waveguide

# Chapter 1 Introduction

## 1.1 Background and Motivation

The era of millimetre-wave (MMW) technology goes back several decades, where they have mainly been used in military operations. MMW is a key technology for realizing the future fifth-generation (5G) wireless communication networks and contributes to fulfilling the requirements of like-fibre and low-latency wireless connectivity. The MMW region occupied the range of electromagnetic spectrum between 30 and 300 GHz, which corresponds to wavelengths from 10 to 1 mm [1]. Recently, the large unlicensed band (57-71 GHz), allocated by the US Federal Communication Commission (FCC) [2], has attracted much attention from industrial and academic researchers to satisfy the explosive growth of 5G services. The 14 GHz of the license-free band around 60 GHz is dedicated to industrial, scientific, and medical (ISM) applications. These services include uncompressed high-definition video streaming, automotive radars, point-to-point communications, wireless local area networks (WLAN) and indoor wireless systems, Internet-of-Things (IoT), WiGig and Machine-to-Machine (M2M) communications. 60 GHz technology has also become among the best candidate for security-related imaging applications due to their advantages over infrared and x-ray imaging mainly because of their characteristics of non-ionizing radiation and vision ability through poor weather. In addition, with up to 10 Gbps, MMW technology is a promising candidate for cable replacement for the 5G applications.

However, most efforts focused on the realization and development of short- and mid-range wireless communication because of the challenge of high losses (16 dB/Km) at a 60-GHz band caused by atmospheric absorption [3]. The FCC has authorized the use of an equivalent isotropic radiated power (EIRP) up to 40 dBm at a distance of 3 m to compensate for these losses [4]. Although this high attenuation supports frequency reuse and reduces interference, it is considered to be the main challenge faced by researchers. Designing a compact 60 GHz antenna with excellent characteristics in terms of high gain, wide bandwidth, high efficiency, and radiation patterns has, therefore, become an essential first step to compensate for the high attenuation and thus increase the communication distance between the source and destination. Therefore, MMW antenna with this characterization becomes a fundamental part of existing MMW wireless systems. Recently,

different types of MMW antennas have been used to overcome the above-mentioned issues. For instance, the antipodal tapered slot antenna (ATSA) [5]-[7] not only provides high gain to overcome the high attenuation problem, but it can also provide large bandwidth and be built onto an array to enhance the gain. Printed antenna arrays are another promising approach to increase the gain, and thus improve the communication range. Furthermore, printed antenna arrays can easily incorporate with a beamforming network for constructing a switched beam antenna array.

Other substantive issues at 60 GHz are none-line of sight (NLOS) propagation and human shadowing, which limit the maximum achievable data rate due to inter-symbol interference ISI [8]. One approach to increase the gain and attain a steerable beam is by using a phased array antenna. When MMW systems utilize phased array antennas to achieve a high-data-rate wireless link, precise alignment between transmitter and receiver is necessary to avoid multipath issues. Adaptive beamforming (BF) array can be used to build such a reliable link and fulfil the requirements of a link budget. In other words, adaptive beamforming algorithms can be used to calculate the amplitude and/or phase of all array elements as a means to track the best channel quality. However, these antenna array systems have a sophisticated structure, and hence, they are expensive to implement. Moreover, massive multiple-input multiple-output (MIMO) technology, which supports multiple independent channels, can be used to enhance the capacity and link robustness (diversity). However, fixed multibeam antenna arrays fed by passive beamforming networks (BFNs) have the advantages of simple structure, low-cost and low power dissipation, making them more suitable over adaptive beamforming. A BFN has  $N$  input ports, and  $M$  output ports connected to  $M$ -element array will produce  $N$  beam directions corresponding to input port excitation. Various passive BFN designs based on substrate integrated waveguide (SIW) technology have been proposed, for switched beam antenna array, such as Blass matrix [9], Nolen matrix [10], Rotman lens [11] and Butler matrix [12]. As compared to Nolen and Blass matrix, Butler matrix requires less number of hybrid couplers so that it has a lower loss and low-cost, which makes it suitable for switched beam networks.

One-dimensional (1-D) scan systems usually steer the beam in the azimuth or elevation plane using a phase control technique where a linear phase gradient is changed along the array input contour. A beamforming network (BFN) feed linear array features more flexibility, as it can be fed the array elements from the edge side. In two-dimensional (2-D) scan systems that feed planar arrays, phase-

controlled beams can be steered in the azimuth and elevation directions. However, the implementation of beamforming networks of 2-D scan systems is critical as the phase difference varies along with the two directions. However, to implement BFN and feed network for a large array, different components such as power dividers, 3- dB couplers, phase shifters and cross overs are required. At low frequency, these components, usually configured by using the microstrip technique as it has the benefits of planar layout, easy integration with other planar circuits and cost-effective. As frequency increases to the MMW spectrum, microstrip lines suffer from high radiation loss and interference, which makes it unsuitable for BFNs and feed networks of large scale array. Due to the high power handling capability and low loss, metallic waveguide technology is widely used to implement MMW components. Unfortunately, their bulky size prevents them from being integrated with active components, microstrip lines, and coplanar waveguides (CPWs). Moreover, they are expensive and not suitable for mass production. Substrate integrated circuit (SIC) is a technology by which the 3-D structures converts to their corresponding planar forms and thus can be fabricated using a low-cost PCB process. Substrate integrated waveguide, which is part of SICs, can be effectively used to solve the mentioned issues and play a key role in realizing high efficient MMW components. SIW is an integrated waveguide-like structure in a planar form which preserves most advantages of non-planar conventional rectangular waveguides (RWG), including high-Q (low loss) and high power capability [13]. Moreover, SIWs can be easily connected to or integrated with conventional transmission lines such as microstrip and CPW to operate over a wide frequency range.

## **1.2 Problem Statement**

Millimeter wave (MMW), unlicensed bands of 57-71 GHz, 76-81 GHz and 81-86 GHz, are characterized by high directivity, massive bandwidth and very low latency, where the wide bandwidth is the most important parameter for high-speed wireless connectivity. Therefore, they have attracted much attention from a wide variety of academic researchers and industrial partners to fulfill the increasing demand of the fifth-generation (5G) applications, such as WiGig, HDMI, FWA, D2D, smart networks, automotive radar systems and security imaging.

The main problem associated with MMW bands is that the high atmospheric absorption loss, which is approximately 16 dB/Km at 60 GHz, limits their wireless communication range. In addition,



MMW wireless communication systems suffer from multipath fading channel issue that increases the inter-symbol interference, which degrades the signal to noise ratio (S/N). Therefore, a wideband antenna with high gain and beam scanning capability would be an effective solution for these challenges, as it can increase the coverage area of MMW wireless systems and mitigate the multipath interference to achieve a high S/N ratio.

In recent years, numerous efforts, which use various techniques and structure modifications, have been reported to solve the problems mentioned above by improving the bandwidth and gain [14, 65, 73, 79, 82, 85, 87, 89] as well as by implementing multi-beam antenna array [15-18, 124-125, 128, 152].

In this thesis, a wideband high-gain 1x8 and 4x4 cavity-backed aperture-coupled patch antenna arrays with SIW full-corporate feed network, working within a frequency range of 55-81 GHz, are designed, prototyped and measured, showing a maximum gain of 20.8 dBi. In addition, a compact double-layered switched-beam slot antenna array based on SIW technology is implemented and prototyped at MMW bands. Moreover, the work in this thesis realizing a compact 2-D scanning multibeam 2x2 cavity-baked patch array with wide bandwidth and high radiation gain for high-speed short-range applications at MMW bands. The proposed antenna and beam scanning arrays would be a practical solution to address the above-stated challenges and establish a robust MMW wireless link.

### **1.3 MMW Propagation Challenges**

MMW signals around specific frequency bands suffer from high free space losses, oxygen absorption, and their low ability to penetrate solid materials. Accordingly, MMW signals only propagate short distances, even under good weather conditions. These characteristics could be considered as advantages in some applications, such as highly secure operations. However, at other MMW bands, where atmospheric losses are relatively low, long-distance communications can be achieved. The most critical MMW attenuation factors are explained in the following subsections.

### 1.3.1 Free Space Loss

For a practical wireless link, the received power ( $P_R$ ) can be described by the Friis transmission formula [19].

$$P_R(dB_m) = P_T(dB_m) + G_R(dB) + G_T(dB) - 20 \log_{10} \left( \frac{4\pi R}{\lambda} \right) \quad (1.1)$$

where  $G_R$  and  $G_T$  are the receiver and transmitter gains, respectively, and  $P_T$  is the transmitted power. The last term represents the free-space loss ( $L_{fs}$ ) in decibels, which is dependent only upon the frequency and link distance ( $R$ ). It is obvious that at the MMW frequency bands, the free space loss can be considerable, even at short distances. For this reason, MMW systems are preferred for short- and mid-range wireless communications.

### 1.3.2 Atmospheric Attenuation

The atmosphere contains various gas molecules, such as water vapour ( $H_2O$ ) and oxygen ( $O_2$ ). These molecules have different mechanical resonant frequencies and, therefore, the atmospheric absorption of MMW varies with frequency, as shown in Figure 1.1. The high attenuation at particular frequencies results in a short propagation distance. For example, at 60 GHz the oxygen absorption is high, leading to an attenuation value of 16 dB/Km [3]. However, low atmospheric attenuation occurs at other spectrum windows, such as a window from 70 to 100 GHz, which has an attenuation value of 0.5 dB/Km. Accordingly, long-distance applications are suitable around this window. Due to the relatively low attenuation, windows at 140 and 240 GHz can be used for ultrahigh data rate wireless applications. Moreover, attenuation varies with pressure, temperature, and humidity; where these physical factors should be taken into account.

### 1.3.3 Rain Losses

MMW signals are nearly the same size as raindrops, resulting in scattering of radio signals, which in turn leads to multipath interference. This scattering has a significant impact on the propagation of MMW signals. For instance, attenuation caused by a medium rain of 12.5 mm/hour, as shown in Figure 1.2, at 60 GHz is roughly 6 dB/Km [3]. Another source for attenuation is the foliage blockage, which in some cases has as much impact as attenuation caused by atmospheric layers.

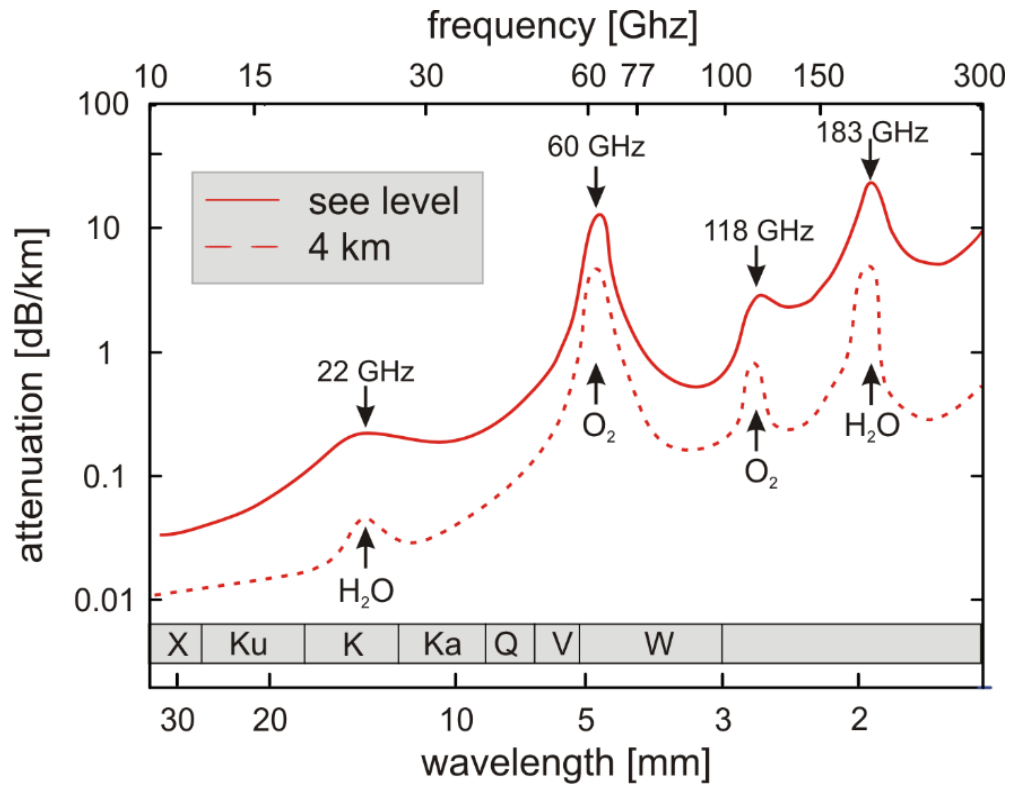


Figure 1.1: Average atmospheric absorption versus frequency [20].

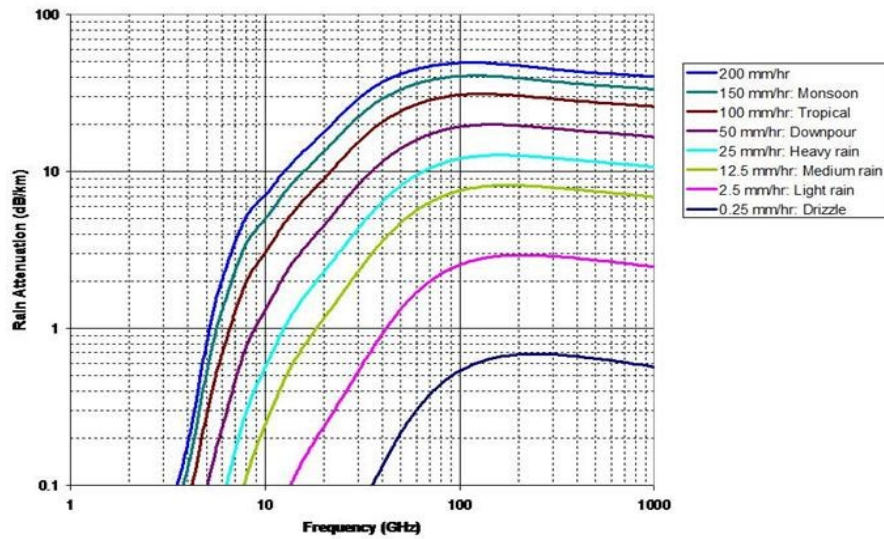


Figure 1.2: Rain attenuation at microwave and MMW frequencies [3].

### 1.3.4 Path Blockage Attenuation

MMW wireless links usually are a line of sight, where any obstacle in the transmission path deteriorates the signal. In addition, MMW signals often diffracted due to the presence of close solid objects [19,21].

## 1.4 60 GHz Channel Characteristics

The high attenuation of propagating signals at some MMW bands enable frequency re-use for short-range applications, which increases the capacity of a communication system. For a given distance, the capacity can be improved by increasing the bandwidth or the SNR. On the other hand, the EIRP of a 60 GHz channel is restricted to 40 dBm by the FCC, which limits the data transfer speed. Therefore, a high directive antenna can be used to increase the power gain. In an indoor short-range wireless link, multipath usually present (as shown in Figure 1.3). The signals travel from the source to the destination in different paths and thus arrive at different times, causing a phase difference or channel fading. These out of phase signals tend to cancel each other out when they arrive the receiving antenna.

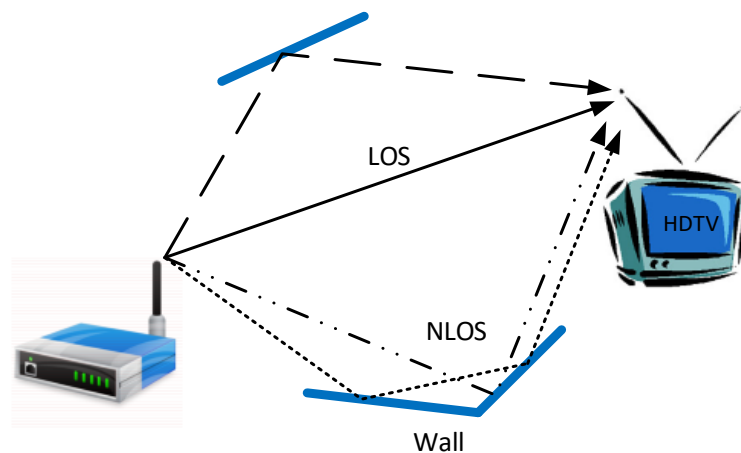


Figure 1.3: Multipath of short-range wireless communications.

### 1.4.1 Antenna Characteristics

For high-directive single element antennas operating at 60 GHz, robust wireless links are not easy to achieve, even in the case of LOS. This is mainly due to the obstacle movement, which can easily block the channel path. A switched beam or phased array antenna can be used to avoid this blockage, and thus create a reliable wireless link. An array antenna is essential to accomplish this task. With the implementation of a large phased array, the phase shift varies continuously between elements, where the complex phase control network is required. In addition, there are other challenges, such as feed network loss and strong coupling between antenna elements. These issues make the fabrication of (good quality) phased array antennas an expensive operation. There are more practical solutions, such as using equalization techniques and accepting the multipath option or using a LOS link with simple unequalised modulation. The second solution focuses on the beam steering technique to increase the data rate of the wireless link.

### 1.4.2 Link Budget

A wireless link, as shown in Figure 1.4, depends on many parameters, such as range, data rate, and bit error rate (BER) for robust communication. For specified parameters, the link budget can be used to evaluate system performance [22]. The overall link margin depends on many factors, where the most important is defined by the following expressions:

Average thermal noise power per bit (dB) =  $N = -174 + \log_{10}(R_b)$ , where the  $R_b$  (Gb/s) is the bit rate.

Average noise power per bit (dBm) =  $P_N = N + N_f$ , where  $N_f$  is the noise figure of the receiver.

Total path loss (dB) =  $PL = P_T + G_T + G_R - P_N - S - M_{\text{shad}} - I - L_{fs}$

where  $P_T$ ,  $G_T$ ,  $G_R$ , and  $L_{fs}$  are as defined in section 1.3.1,  $S$  is minimum  $E_b/N_0$  for the Additive.

White Gaussian Noise (AWGN) channel, in dB,  $M_{\text{shad}}$  is the shadowing link margin (dB), and  $I$  is the implementation loss (dB) (filter distortion, phase noise and frequency error).

Input noise level (dBm) =  $10 \log(KTB)$ , where  $K = 1.381 \times 10^{-23}$  J/K,  $T = 290$  K, and  $B$  is the bandwidth; and maximum operating range  $R = 10^{PL/10n}$  (m), where  $n$  is the path loss exponent.

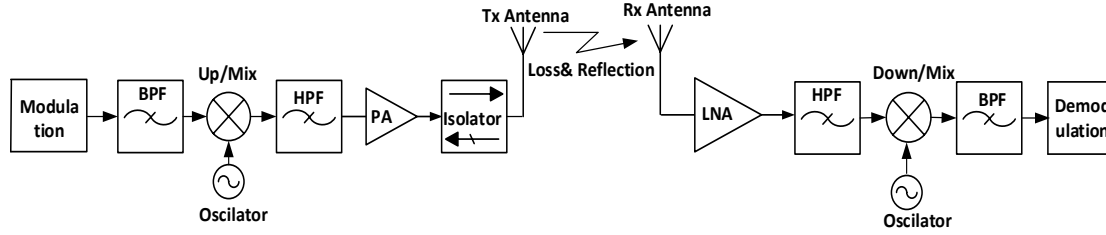


Figure 1.4: MMW transmitter, receiver, and wireless link.

## 1.5 Objectives

The main objective of this work is to investigate different methods and approaches to design a high gain antenna element and array with a focus on compact planar structures for 60-GHz short- and mid-range applications. The structures are mainly functioning to address the atmospheric attenuation associated with 60 GHz signals. Another aim of this work is to design and realize 1-D beamforming array with end-fire and broadside radiation and 2-D scanning phased array antenna, based on the SIW beamforming network, for 60 GHz wireless connectivity. The three structures are designed to work in a multipath fading channel environment and to reduce the inter-simple interference. These goals have been accomplished by carrying out the following:

1. Design, dielectric-loaded antipodal Fermi tapered slot antenna (AFTSA) with a delta-shaped slot for performance improvement, in terms of gain, efficiency, front to back ratio and radiation symmetry over a wide bandwidth. Moreover, design, a wideband substrate integrated waveguide (SIW)-based planar linearly tapered slot antenna array with low cross-polarization by utilizing double-layer substrates for gain enhancement.
2. Design a wideband 1x8 array at 60 GHz, with a low side lobe level and low cross-polarization, whose beam-shape is synthesized by amplitude tapering according to Taylor distribution. In addition, a broadband 4x4 cavity-backed antenna array with a full-corporate SIW feed network for aperture efficiency enhancement. A single-layer right-angle broadband transition between SIW and air-filled WR15 waveguide with low insertion loss is implemented to feed the proposed Arrays.
3. Design, and measure a wideband high-gain multibeam end-fire antenna array based on a 4x4 SIW Butler matrix by utilizing an AFTSA as radiated elements.

4. Analysis and design a compact Butler matrix by using two-layered wideband SIW phase-shifter for 1-D switched-beam slot antenna array.
5. Design a compact two-layered BFN for realizing a 2-D scanning multibeam  $2 \times 2$  cavity-backed patch array with a wide operating frequency range and stable radiation gain.

## 1.6 Thesis Outline

This thesis is organized into six chapters, as follows:

Chapter 2 gives a literature review and background introduction to SIW, tapered slot antenna, cavity-backed antenna and beamforming technology.

Chapter 3 focuses on the development of two types of MMW antennas. The first type is the tapered slot antenna (TSA), where different configurations are designed, prototyped and tested. Moreover, a  $1 \times 4$  linearly TSA array is introduced in order to enhance the gain. The second antenna type is the cavity-backed antenna, where a novel wideband cavity-backed aperture-coupled patch antenna is presented. Based on the proposed element, a wideband  $1 \times 8$  array is introduced at 60 GHz, whose beam-shape is synthesized by amplitude tapering according to Taylor distribution. Moreover, a  $4 \times 4$  antenna array with a full-corporate feeding network is designed. In addition, a novel wideband transition from SIW to air-filled WR15 has been proposed and demonstrated at V-band.

In chapter 4, two different designs of one-dimensional (1-D) switched multi-beam antenna arrays, which employ an SIW Butler matrix as a beamforming network, are investigated and prototyped for validation. The first design is a multibeam broadside SIW slotted antenna system fed by a compact dual-layered  $4 \times 4$  Butler matrix. The second design is a wideband multibeam end-fire array, which in a Fermi tapered slot antenna is used as a radiating element and a single-layered  $4 \times 4$  Butler matrix for BFN.

In chapter 5, we present a  $2 \times 2$  multi-beam phased array employing a novel wideband linearly polarized (LP) cavity-backed patch antenna. A compact two-layered SIW-based BFN is utilized to feed the proposed two-dimensional (2-D) scanning Array. The principle of operation is discussed, and the prototyped results are compared to simulated HFSS results.

Chapter 6 presents the conclusion, followed by suggestions for future work.

## 1.7 Contributions

In this thesis, the main contributions are summarized as follows (Journal papers [J] and conference papers [C] are listed at the end of the thesis document):

A high-gain antipodal Fermi tapered slot antenna (AFTSA) with sine-shaped corrugations is introduced, where an elliptical-shaped dielectric slab is used as a guiding structure to improve the radiation characteristics in terms of F/B and SLLs [J3, C7].

Design a new broadband double-layer SIW-to-slotline transition to feeding a planar linearly tapered slot antenna (PLTSA) at 60 GHz. This feeding mechanism, which overcomes the bandwidth limits of the planar antenna and maintains the low cross-polarization, is used to implement a 1x4 PLTSA array [J5, C1, C3].

A novel wideband cavity-backed patch antenna at 60 GHz with overlapped 1-dB gain and impedance bandwidth of 44.2% (55.5 to 87 GHz) is developed for 5G applications, where the gain flatness is an essential factor for high-speed wireless communications with high order modulation. Based on single element, a wideband 1x8 array is presented at 60 GHz, with a low side lobe level, whose beam-shape is synthesized by amplitude tapering according to Taylor distribution. The proposed array shows a wider bandwidth (37.6% from 54.7-80 GHz) with lower sidelobe levels over the existing published work at MMW bands. In addition, A compact 4x4 array with a bandwidth of 37.9% (54.9- 80.6 GHz) and an aperture efficiency of 91.3 % is introduced [J8].

A multi-beam broadside SIW slotted antenna system fed by a compact dual-layered 4x4 Butler matrix [J6], is developed to provides an azimuthal coverage of  $121^\circ$ . In this design, by taking the phase delay introduced by crossover as a reference, a novel wideband phase shifter is designed by stacking two substrates with different dielectric constant, on top of each other to reduce the size. Therefore, it is separated from the other components, which provide more space and high flexibility to the BFN, leading to the wide bandwidth and compact size.

A compact SIW-based 2-D multi-beam scanning array with a wide operating frequency range and high radiation gain is proposed at 60 GHz to addresses the high loss and the multipath fading channels issue [J1]. A novel wideband cavity-backed patch antenna, with overlapped 1-dB gain and impedance bandwidth of 36.2 % (53-76.4 GHz), is employed as a radiating element. In this



design, a compact two-layered beamforming network is designed with a size reduction of 28 % compared to a standard one-layered BFN without affecting its scattering parameters. In addition, a new single-layer right-angle broadband transition between SIW and air-filled WR15 WG is proposed and demonstrated at V-band, with fractional BW of 48.6 % (47.2-77.5 GHz), in order to feed the proposed multi-beam array [J2].

## Chapter 2 Literature Review

This chapter provides a literature review on different types of tapered slot antennas (TSAs), a brief history and its basic working principle. Also, a literature review on different antenna structures backing by a cavity is presented, followed by one and two-dimensional beam scanning array with passive beamforming networks (BFNs).

### 2.1 Theoretical Background and Methodology

This section introduces the methodology and briefly theoretical background required for designing substrate integrated waveguide (SIW), tapered slot antenna (TSA), and multibeam scanning antenna array.

#### 2.1.1 Substrate Integrated Waveguide (SIW)

Conventional rectangular waveguides (RWG) are usually made of hollow rectangular metallic tubes, and thus they are suitable for high power MMW systems. On the other hand, they are relatively high cost and their bulky size prevents them from being integrated with active components, such as microstrip lines, and coplanar waveguides (CPWs). Therefore, they are not suitable for compact planar circuits and low-cost mass productions. Substrate integrated waveguide (SIW) technology can be effectively used to solve the above-mentioned issues. An SIW is an integrated waveguide-like structure in a planar form which preserves most of the properties of non-planar conventional RWG [7]. Moreover, SIWs have other benefits, including low cost and low loss. They are also easy to fabricate using printed circuit boards (PCBs) and can be used in high power MMW applications. The synthesized RWG in planar form is configured by embedding two parallel rows of metallized plated vias in a dielectric substrate; in fact, it is an artificial periodic waveguide, as shown in Figure 2.1. The top and bottom metallic layers are connected by two rows of metal vias to construct the SIW. The substrate gaps on the side walls prevent the horizontal surface currents from flowing in the SIW, and so the dominant mode excited in the proposed structure is the  $TE_{10}$  mode.

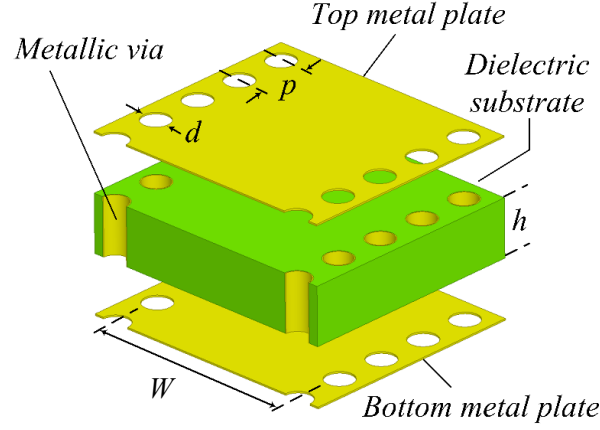


Figure 2.1: Topology of an SIW structure synthesized using metallic vias.

To prevent lateral electromagnetic leakage and reduce the losses, the main design parameters of SIW, i. e., the via-hole diameter ( $d$ ) and the longitudinal spacing ( $p$ ) between vias must satisfy the conditions given in [13],  $d \leq \lambda_g/5$  and  $p \leq 2d$ , where  $\lambda_g$  is the guided wavelength. An empirical formula to calculate the effective width of the SIW is given in [23]-[24].

$$W_{eff} = W - \frac{d^2}{0.95 p} \quad (2.1)$$

Equation (2.1) is valid for  $p < \lambda_0 \times \sqrt{\epsilon_r}/2$  and  $p < 4d$ . Another efficient approach to calculate the via diameter to longitudinal spacing ratio is analyzed in [25]. The ratio of via aspect and  $d/p$  that tolerated by the fabrication process is another a critical factor that significantly impacts on the SIW performance and should be accounted for. For instance, with simple calculations, 1 mil (25  $\mu m$ ) tolerance can change the cut-off frequency of the  $TE_{10}$  mode, as given in Equation (2.2), by about  $\pm 1$  GHz at 60 GHz for SIW designed on RT/Duroid 6002 substrate with a dielectric constant of 2.94.

$$f_{c10} = \frac{1}{2W_{eff}\sqrt{\epsilon\mu}} \quad (2.2)$$

Moreover, changing the permittivity from 2.94 to 2.84 can shift the cut-off frequency of the SIW to about 0.7 GHz at 60 GHz. Therefore, the substrate characteristics, i. e., the permittivity and loss tangent, as well as the thickness, should be appropriately chosen to mitigate the signal attenuation within the frequency band of interest. In SIW, the dielectric losses are higher than the metallic

losses. Moreover, as the thickness decreases, the Ohmic losses increase. On the other hand, changing the SIW height does not impact on the dielectric loss, as it remains constant for different thicknesses.

The uncertainty of the relative permittivity and the loss tangent given by the manufacturer is a primary source of discrepancy between the measured and simulated results at 60 GHz. The reason is that the values in the datasheet, usually, given at a lower frequency. Therefore, extracting these parameters experimentally at 60 GHz can alleviate this discrepancy. An efficient method to extract the complex permittivity is described in [26]-[27]. As a byproduct result of using an SIW TRL calibration kit, the measured permittivity of RT/Duroid 6002, as shown in Figure 2.2, is 2.82 at 60 GHz, which is lower than the datasheet value of 2.94. Moreover, the loss tangent ( $\epsilon''/\epsilon'$ ) is extracted from the measured complex permittivity, which increased by a factor of three compared to the datasheet value of 0.0012 given by the manufacturer.

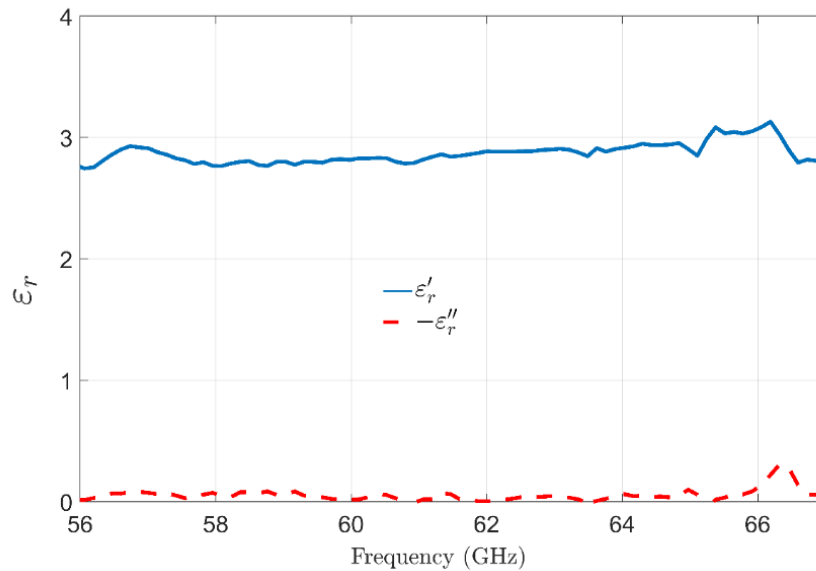


Figure 2.2: The measured complex permittivity of RT/Duroid 6002 substrate.

### 2.1.2 Tapered Slot Antenna

Tapered slot antennas (TSAs) belong to the class of surface wave antennas, a class that can achieve end-fire radiation, high gain and wide bandwidth. Moreover, they have a planar structure and can achieve symmetric radiation patterns of both principal planes. TSAs have gained attention since

early work reported by Lewis *et al.* [28] in 1974. In 1979, an exponentially tapered slot (Vivaldi) antenna was introduced by Gibson [29] to cover the frequency range 8-40 GHz. In the same year, a linearly tapered slot antenna (LTSA) operating at 9 GHz was reported by Parasad *et al.* in [30]. Usually, TSAs are fabricated using the printed circuit board (PCB) technique so that they can be easily integrated with other active components and feed systems on the same dielectric substrate. TSAs with the narrow beam width feature can be effectively used as feeding systems for reflector antennas and lenses with low spillover losses. In order to achieve travelling wave characteristics, the phase velocity ( $v_p$ ) of the surface waves along the antenna structure should be less than or equal to the speed of light in a vacuum ( $c$ ) [31]. Figure 2.3 shows antipodal TSA (ATSA) with different taper profiles: linear, exponential (Vivaldi) and Fermi tapers. The tapered slot has a narrow width at the feed side and gradually increases according to taper function, in such a way that the aperture width ( $W_a$ ) is greater than or equal to a half-wavelength at the lowest operating frequency. The electromagnetic energy is tightly coupled to the conductor on the narrow side, whereas it is more coupled to the electrical field at the aperture [29]. It has been found that the optimum value of the antenna length ( $L_{an}$ ) in the range of  $3\lambda_o$  to  $8\lambda_o$  with directivity  $D \approx 10$  ( $L_{an}/\lambda_o$ ) [32]. However, the low reflection coefficient and broadband transition between the radiating tapered slot and the feed source are the main challenges of TSA. However, numerous methods have been used to feed tapered slot antennas. One well-known method is by using a 50  $\Omega$  microstrip to slot line transition, as shown in Figure 2.3, to feed an antipodal (non-planar) TSA.

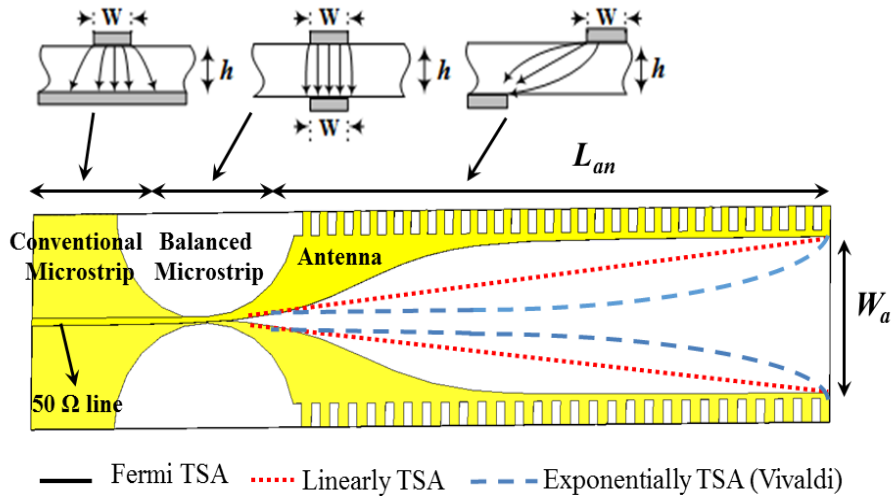


Figure 2.3: Different taper profiles of ATSA, microstrip-to-slot transition and electric field distribution at various cross-sections.

Mainly, this transition or balun (balance-unbalance) pad is used to match an unbalanced  $50\ \Omega$  microstrip to a balanced strip line that can then be matched to a radiating part by adjusting the flare angle of the tapered slot. For a conventional microstrip, as shown in Figure 2.3, the field lines are somewhat spread out, whereas, for a balanced microstrip, the field lines are concentrated in the middle. In addition, the field lines of the tapered slot trend to rotate along the antenna axis, which introduces higher cross-polarization in this type of antenna.

### 2.1.3 Multibeam Scanning Array Antenna.

For MMW wireless communications, a fixed-beam antenna cannot solve multipath problems, even with a sharp beam. Moreover, the obstacle can interrupt the channel path completely, where the loss caused by a human body or some object exceeds 30 dB [95]. In an MMW wireless link in the presence of a dynamic clutter, the beam steering/forming technique can be used to increase the signal-to-interference (SIR) ratio, and thereby fulfill the link budget requirements. In the adaptive beam steering technique, an algorithm is used to exchange the control signalling between the transmitter and the receiver, a robust LOS or NLOS wireless link can thus be aligned. During the exchange of control signalling, the position of each antenna beam with a sufficient channel quality is saved in a candidate's path table, updated periodically, and used as alternative links when the current signal is deteriorated. Phased array antenna, shown in Figure 2.4, is used to improve the gain and to steer the beam into the direction of arrival (DOA) of maximum signal. The phase and amplitude of each element in the array are controlled to form the beam shape. The beamforming algorithm is used to find the optimum weights  $W_i$  ( $i=1, \dots, M$ ) at the  $T_x$  and  $C_i$  ( $i=1, \dots, N$ ) at the  $R_x$  of the quantized phase shifters. Based on channel quality information, SNR, BER, and received signal strength indicator (RSSI), the alternative reliable wireless link is chosen in case of the currently used channel is degraded or blocked by moving obstacle [95, 22]. However, the beamforming technique can be classified into two main categories: adaptive and fixed beamforming techniques. In the adaptive technique, an antenna array with a beamformer network is used to steer the beam electronically in a desired direction without physical movement of the antenna array to track the channel variations. The desired direction was selected based on various

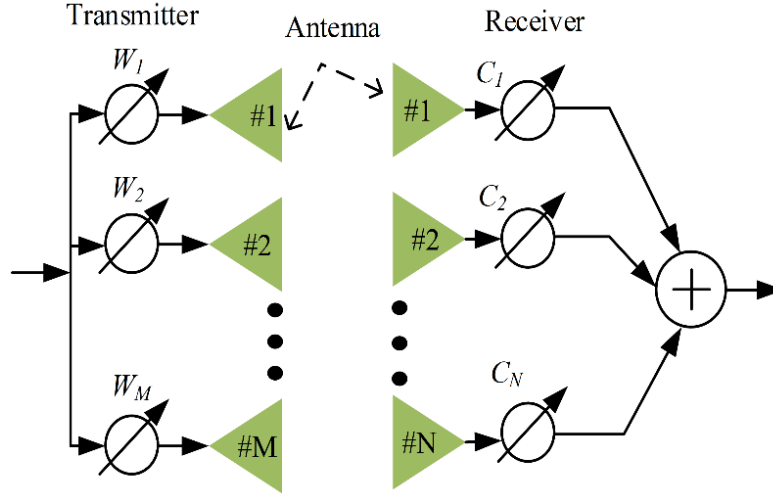


Figure 2.4: Phased array antenna.

criteria, such as channel quality information, the Signal-to-Interference-and-Noise Ratio (SINR), or a reference signal [96], [97]. In other words, the weight of each array element can be optimized using different algorithms such as the Minimum Mean Square Error (MMSE), Minimum Variance (MV), Least Mean Square (LMS) algorithm, and the Sample Matrix Inversion (SMI) algorithm. However, these adaptive antenna array systems have a complex structure, and thereby, they are expensive to implement. For fixed beamforming, many techniques can be used to achieve fixed beams, such as a switched-beam antenna array, delay-and-sum beamforming, and tapered beamforming. Usually, fixed multi-beam antenna arrays fed by passive beamforming networks (BFNs), which have the advantages of simple structure, low-cost and low power dissipation, making them more suitable over adaptive beamforming.

#### 2.1.4 Simulation Software Packages

For many antenna designs, when the electromagnetic (EM) field distribution of the antenna geometry is complex, there are no exact solutions and the numerical EM modelling techniques are needed to solve the problems. A number of different numerical techniques can be used to solve 3D-EM radiation problems. Some are performed in the time domain, such as Finite Difference Time Domain (FDTD), which is a direct solution of Maxwell's equation. Others, like Finite Elements (FE), and the Method of Moments (MoM) are performed in the frequency domain. Full-

wave analysis of antenna structures introduced in this thesis is carried out using two different commercial software packages. The first simulator is the ANSYS High Frequency Structure Simulator (HFSS) software, which is a powerful 3D-EM field simulation tool. It uses a numerical technique based on the Finite Element Method (FEM) in the frequency domain. The second simulator is Computer Simulation Technology Microwave Studio (CSTMWS), which uses the Finite Integration Technique (FIT) in the time domain. Not all techniques are suitable for a particular electromagnetic problem, hence unsuitable choice of the solver may run into issues of large computational requirement. However, one can achieve the desired accuracy and save calculation time by choosing the numerical technique that is most appropriate for the problem under consideration.

## 2.2 Tapered Slot Antennas

TSA, in general, is excited using microstrip-to-slotline transition [30, 33] where the slotline incorporated with the radiating tapered slot on one side of the substrate and the microstrip (MS) line feed on the opposite side. In [34], a coplanar waveguide (CPW) with double Y balun was used as a uniplanar transmission line feed of TSAs with different taper profiles at 60 GHz, where the stubs and air-bridges were used to improve the matching and to support the CPW odd mode operation. However, such transitions utilize frequency-dependent matching elements, thus limiting the operating bandwidth of planar TSAs. Feeding systems based on SIW technology is another approach to excite TSAs [35], where a tapered microstrip-to-SIW transition and an SIW are integrated on the same substrate. Design equations for these transitions are given in [36]. In [37], a multimode SIW is used to feed a dual V-type linear tapered slot antenna. SIW-based antipodal linearly tapered slot antenna (ALTSA) with coplanar waveguide (CPW) feed presented in [38]. One drawback of this design is that its feeding CPW impedance line does not support the 50  $\Omega$  feeding system. However, ATSA configurations [38-39, 7] suffer from high cross-polarization levels due to the bilateral structure of the antenna. An approach to overcome this limitation is proposed by Langley *et al.* in [40], where a double-layer balanced antipodal Vivaldi antenna with stripline feed is utilized to orient the electric field in the slot region parallel to the strip. A major drawback of this design is that the beam is tilted away from the end fire direction, causing a reduction of axial gain. An end-fire tapered slot antenna with different profiles has been presented in [31] where the effect of various types of substrates on the side lobe levels (SLLs) and 3 dB



beamwidth is extensively studied. Moreover, TSAs with different inner taper profiles: exponentially tapered slot antenna (ETSA) (Vivaldi), constant width slot antenna (CWSA), broken linearly tapered slot antenna (BLTSA), and defined by Fermi-Dirac function, were proposed by Sugawara et al. [34] and mainly used to improve the antenna radiation pattern at millimeter-wave frequencies. Moreover, Sugawara et al. studied the characteristics of MM-Wave tapered slot antenna with corrugated edges. In addition, the impact of rectangular and sine-shaped corrugation on Fermi TSA parameters is presented in [41]. A modified antipodal Vivaldi antenna for bandwidth enhancement is presented [42], which covers the frequency range from 4 to 50 GHz with a maximum gain of 12 dBi. In [7], zero-index metamaterials have been used to improve the gain of antipodal Vivaldi antenna (AVA). A lens-loaded antipodal Vivaldi antenna with rectangular corrugated edges is proposed in [43] to miniaturize the size with improved radiation pattern. Moreover, various modified Vivaldi antennas have been investigated for miniaturized and improved radiation characteristics [44-45]. Recently, a wideband antipodal Vivaldi antenna which loaded with notched tapered slots to improve the gain and reduce the sidelobe level is presented [46]. A corrugated edge tapered slot antenna with low SLL and improved cross-polarization has been presented in [47].

The wide bandwidth and high directivity of TSA arrays make them highly attractive for remote sensing research and radar applications. Recently, TSA with comb-shaped slits is introduced in [48], where a miniaturized SIW T-shaped 8-way power divider is used to form 1x8 TSA Array for Q-band applications. In addition, the sliced notch approach of TSA is applied by Logan et al. [49-50] to implement Vivaldi array with low cross-polarization. LTSA array with a feeding system based on SIW technology is demonstrated in [35]. A three-dimensional (3-D) array relies on SIW technology is presented in [51], where a Fermi tapered slot antenna is used as a radiating element to enhance the gain and to minimize the coupling between adjacent elements. Another configuration of a 3-D array using cavity-backed Vivaldi antenna is reported in [52]. However, the spacing between radiating elements in a TSA array is a critical parameter; it will increase the grating lobes and mutual coupling between elements. The high mutual coupling may also cause a significant reflection coefficient and scanning blindness. Mutual coupling between two linearly tapered slot antennas formed in the coplanar and stacked arrangement has been measured [53], where the results show that the mutual coupling is decreased with antenna separations. Recently, an efficient method to mitigate the mutual coupling between two Fermi TSA using metamaterial-

based corrugation is investigated [54]. Another example where the metamaterial is used to mitigate the mutual coupling of the MMW MIMO antenna is discussed in [55].

### 2.3 Cavity Backed Antennas

In many applications, the combination of SIW and the conventional waveguide is required to measure the s-parameters of SIW-based components or to test the radiation performance of an antenna designed based on SIW technology. There is thus a pressing need for an effective transition between SIW and air-filled rectangular waveguide (RWG). Different approaches and designs have been investigated to improve the parameters of SIW-to-RWG transitions. One approach for realizing a wideband SIW-to-RWG transition is by using an antipodal fin line probe inserted into the metal waveguide to work as impedance or waveform transformers [56]. A broadband transition between air-filled standard waveguide and SIW is presented in [57], where the transition is realized by using a radial probe inserted into the height-tapered metal waveguide. A broadband SIW-to-WG transition which is achieved by using an SIW-fed linearly flared antipodal slot line inserted into a waveguide is presented in [58] for W-band applications. A multi-layer transition between the SIW and WR-15 waveguide working at V-band proposed in [59]. The drawbacks of such a transition are the high insertion loss and the difficulty of alignment between different layers. A transition between laminate waveguide (LWG) in a multi-layer LTCC substrate and an RWG has been demonstrated in [60]. An E-plane right-angle transition from SIW to air-filled WG has been reported in [61], in which a stepped waveguide and two inductive posts are applied to improve the matching. Other transitions are configured using longitudinal slot etched on the broad wall of the SIW [62-63]. All SIW-to-RWG transitions [56-58] are in-line coupling form and usually feature a wide bandwidth; however, in these transitions, the RWG needs to be machined in a metal block to connect with SIW, which increase both the complexity and size. Transitions reported in [59-63] are in right-angle configuration, wherein a coupling aperture is etched on the top wall of SIW to convert the fundamental  $TE_{10}$  mode of SIW to  $TE_{10}$  mode in RWG. Although these type of transitions have advantages of compact size and less complexity, they have a relatively narrow bandwidth compared to the in-line transitions.

Due to the low profile, lightweight and ease of fabrication using low-cost printed circuit board (PCB) technology, microstrip patch antennas have drawn much attention from both industry and

academia. The major drawbacks of the single patch antenna are its inherent narrow bandwidth and low gain, which makes it unsuitable in many cases for 5G wireless applications, whether it is used as a stand-alone element or in an array. Different excitation approaches to address these drawbacks are reported in the literature, such as L-probe feed patch antenna using LTCC technology [65], aperture coupled feeding technique [66], and series-fed E-shaped patch [67]. A simple, straightforward, solution to enhance the bandwidth is to use a thicker substrate, but the high separation between the patch and ground plane increases the surface wave, leading to degradation in the radiation pattern characteristics. One efficient solution is to place a cavity enclosure underneath the patch, which not only enhance the gain and reduced the backward radiation, but also suppress the surface waves, leading to a high-efficiency antenna. Therefore, for the last two decades, a cavity backing different type of planar antenna gained much interest from antennas designer. Usually, cavity housing in a metallic block [68] is utilized to reduce the surface waves, suppress back lobes, improve the gain and increase the bandwidth of microstrip patch antennas, but at the expense of increased cost, size and complexity. Alternatively, SIW cavities have been widely used for backing various types of antennas, as shown in Figure 2.5, such as patch antennas [69]-[73], slot antennas [74]-[78] and magneto-electric dipole antenna [79,80]. Moreover, besides the compact planar profile and low-cost, cavity-backed antennas based on SIW technology have an excellent integration capability with other components. Except for reference [70], all reported work [69]-[80] is designed on low-cost SIW PCB technology. Moreover, a cavity backing slot antenna based on different technology, including ridge gap waveguide (RGW) [81-82] and LTCC [70, 83], is investigated for gain and bandwidth enhancement. Recently, an SIW cavity-backed E-shaped patch antenna for Q-LINKPAN applications is presented in [84], in which a coplanar waveguide (CPW) with a metalized via is employed to generate one more resonant mode for bandwidth enhancement.

However, the cavity-backed antenna has a moderate gain (7-9 dBi) and cannot use as a stand-alone element for most 5G systems and high data rate wireless applications. Therefore, antenna arrays became vitally important to fulfilling the requirements of 5G applications. In recent years, numerous feeding techniques have been used to implement wideband antenna arrays for gain enhancement and improved efficiency. However, achieving the features of high gain with wide bandwidth, in SIW slotted arrays, is challenging. Therefore, a trade-off is required in many cases, such as in designs in [85]-[86], where a single-layered SIW slotted array is proposed for 60 GHz

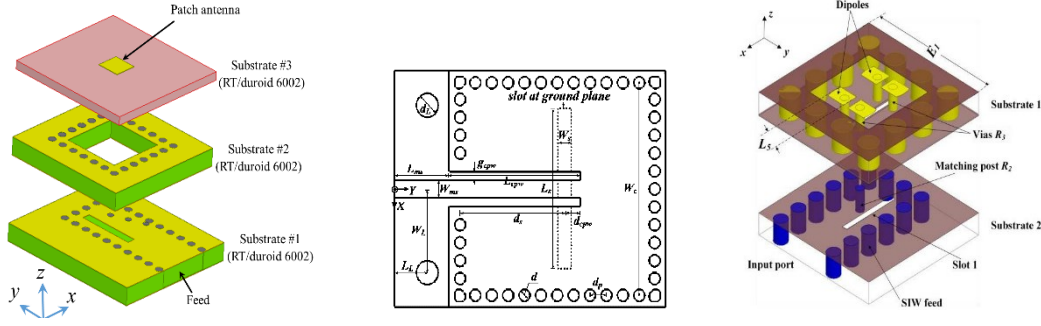


Figure 2.5: An SIW-based cavity-backed antennas. (a) Patch [J1]. (b) Slot [74]. (c) ME dipole [79].

applications. Various structures of magneto-electric (ME) dipole antenna arrays, backed by a metallic [87] and an SIW cavity [79]-[80], have been investigated in order to achieve high gain, high efficiency and wide bandwidth. Two side-by-side dipoles with an SIW cavity in between are used to implement a 1x8 array [88]. An aperture coupled feeding based on substrate integrated waveguide (SIW) is employed for a large-scale patch array [89]. A four-element series-fed array [67] and a 2x2 array [84], which use an E-shaped patch antenna, are proposed to achieve an impedance bandwidth of 21.7 % and 34.4 %, respectively. L-shaped and modified L-shaped probe patch antennas are used to configure a 4x4 array designed on LTCC [65] and PCB [90], respectively, to enhance the operating bandwidth. A double-layered 2x2 SIW cavity-backed microstrip antenna array is proposed in [71], where the array is excited by a coaxial probe which is soldered to a microstrip line printed on the top layer. In [72], an SIW cavity-backed rectangular patch antenna is used to implement a 4x4 array, where the patch short-circuited with the ground using metallic via placed at the center of the patch to enhance the bandwidth and radiation efficiency. However, in the structures that use a coaxial probe feed or short-circuited vias, the cavity height should be small, as the inductance generated by the probe or via becomes significantly large. Recently, an SIW-fed cavity-backed patch antenna at V-band has been proposed by Y. Li et al. in [91], which introduced an additional coupling aperture between the SIW-feed and the aluminum cavity to enhance the impedance bandwidth further. The same authors also proposed a cavity-backed aperture-coupled patch antenna in [92], where a rectangular patch is placed between an SIW circular cavity, and the air-filled cavity etched on an aluminum plate to reduce the surface wave and coupling effects. A 32x64 cavity-backed slot [93] and 1x8 cavity-

baked patch [94] antenna array is implemented with a low side lobe level, whose beam-shape is synthesized by amplitude tapering according to Taylor distribution.

## 2.4 Multibeam Scanning Array Antenna

Since the 1960s, Butler matrix (BM) has been widely used as a passive BFN to produce progressive phase shifts between radiating elements for phased array antenna and radar applications [98]–[99]. A switched-beam array with a Butler matrix network is shown in Figure 2.6, which provides pre-defined multiple fixed beams to cover an angular sector area. Butler matrix usually composed of 90° hybrid couplers, phase shifters, and crossover, which is cost-effective compared with other beamforming networks. The beam direction is selected based on which Butler matrix input port is used, and are usually 4, 8, or 16 ports. In addition, it is a reciprocal network that used to transmit or receive the signal with well-isolated ports from each other. Usually, BM is designed and implemented using microstrip lines [100]–[102], CPW [130] or stripline [103], because of their low cost, simple fabrication process and ease of integration with other circuits. A cost-effective approach based on microstrip lines is employed to configure a Butler matrix network operating at 60 GHz for one- and two-dimensional scanning presented in [104] and [105], respectively. An electronically steerable parasitic array radiator of DRA with beam scanning from -22 to +22 for X-band applications have been investigated [106]. Moreover, a BFN without phase shifters and crossovers designed based on microstrip lines at C-band for one-dimensional scanning is reported in [107]. Switching-beam capability using electro-magnetic periodic structures for 5G applications is introduced in [108].

However, BFN designed based on microstrip lines technique suffers from high Ohmic and radiation losses at MMW frequencies, which leads to reduced efficiency of the overall beamforming system. One approach to tackle this issue is by utilizing substrate integrated waveguide (SIW). Since the SIW combines the excellent features of planar transmission lines and conventional metallic rectangular waveguides, various components based on SIW technology have been developed, such as hybrid couplers [109], phase shifters [110]–[111], and crossovers [112]. An SIW phase shifter is proposed in [113], where a delay line and an equal length unequal-width phase shifter are combined to achieve a flat relative phase shift over a wideband. Moreover, a wide variety of passive BFNs has been proposed to feed phased array systems, such as the Rotman lens

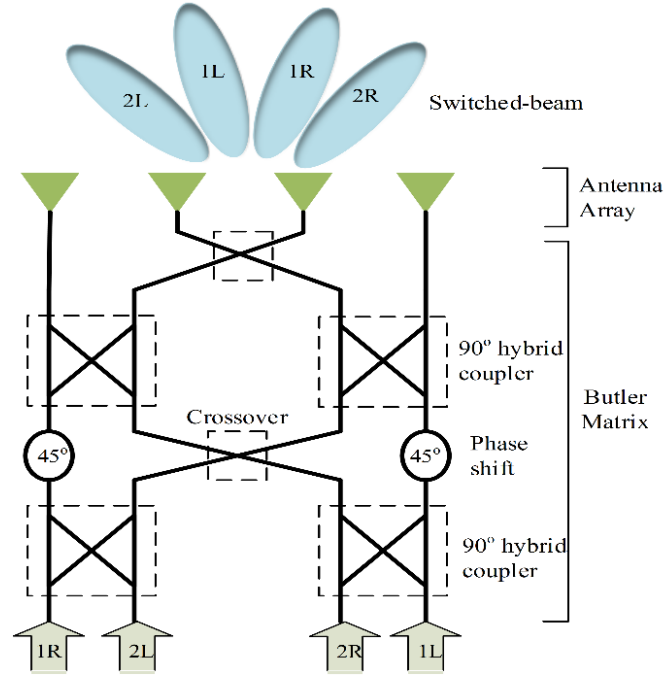


Figure 2.6: Switched-beam array with Butler matrix network.

[114] - [115], the Blass matrix [9] and the Nolen matrix [116]. ]. In addition, SIW-based Butler matrix is widely used as a BFN in multi-beam array [117], as it required less number of hybrid couplers compared to Nolen and Blass matrix. Therefore, the Butler matrix has a lower loss and low-cost, that make it attractive for beamforming array applications. Recently, an SIW Butler matrix fed end-fire magneto-electric dipole antenna array for 1-D and 2-D multibeam end-fire radiation has been proposed in [118] and [119], respectively. Moreover, various examples of the one- and two-dimensional scan array based on the Butler matrix have been investigated in [120-122], and [123-125], respectively.

At low frequencies, where the electrical length is large, the main concern is the miniaturization of the Butler matrix. In [126] a planar artificial transmission line is proposed to design a miniaturized 4x4 Butler matrix with a simple fabrication process for RFID applications. Furthermore, a novel design is implemented by using suspended stripline to minimize the size and to reduce the losses of the Butler matrix [127]. At high frequencies, the large size of the beamforming network with the extended transmission lines for measurement purposes deteriorates the radiation performance and increases the losses, leading to reduced radiation efficiency. Various designs have been reported in the literature to address these challenges by shrinking the size of multibeam antenna

arrays. In [128], a compact size SIW based eight-port BFN is designed to feed a 2x2 antenna array to obtain 2-D scanned beam patterns. Another approach to miniaturizing the size is achieved using a multi-folded SIW Butler matrix [129]. A low-cost configuration of the Butler matrix without crossover and using a CPW multilayer technology is reported in [130]. A compact size Butler matrix based on two-layer SIW technology has been investigated in [131] for KU-band application. As the operating frequency of Butler matrices shifts to MMW frequency bands, the implementation of phase shifters with straight SIWs becomes a difficult task. To address this issue and facilitate the design of the SIW based phase shifter, a smooth curved delay line is proposed [12], where the phase introduced by the crossover is regarded as a reference. A 24-beams slot array using a power splitter to minimize the Butler matrix is introduced in [132] that covers  $360^\circ$  over azimuth angle for MIMO applications. Another simple solution is to implement the crossover by using two cascaded  $90^\circ$  hybrid couplers [133]- [134]. However, these topologies will increase the area occupied by the BFNs, where the size reduction is a major concern for beamforming applications.

## Chapter 3 Design and Realization of Broadband High-gain MMW Antennas

### 3.1 Introduction

The interest in broadband high-gain MMW Antennas has continued to grow with the high demand for 5G wireless applications. Recently, many research activities have been focused on the unlicensed ISM bands around 60 GHz, which offer an opportunity for broadband and high-data-rate short-range wireless connectivity. On the other hand, the high propagation losses associated with these frequencies are considered one of the critical issues that need to be addressed. According to Shannon theorem [135], the channel capacity is directly related to the bandwidth and signal to noise ratio (S/N) as given by equation (3.1). Thus, narrow bandwidth at low-frequency bands cannot completely satisfy the requirements of high-speed applications.

$$C = BW \log_2(1 + S/N) \quad (3.1)$$

A reasonable solution is to shift the operating frequency to higher bands. Therefore, a broadband high gain antenna is needed to compensate for these losses and thereby realize a high-speed MMW robust channel link.

This chapter focus on the development of two types of MMW antennas. The first type is the tapered slot antenna (TSA), where different configurations of single elements are designed, prototyped and tested to verify the simulated results. Moreover, a 1x4 linearly TSA array is introduced in order to enhance the gain. The second antenna type is the cavity-backed antenna, where a novel wideband cavity-backed aperture-coupled patch antenna is presented. Based on the proposed element, a wideband 1x8 array is introduced at 60 GHz, with a low side lobe level, whose beam-shape is synthesized by amplitude tapering according to Taylor distribution. Moreover, a 4x4 antenna array with a full-corporate feeding network is designed. In addition, a novel wideband transition from SIW to air-filled rectangular waveguide has been proposed and demonstrated at V-band to facilitate the measurements of the antenna arrays. All antenna arrays in this chapter are developed based on substrate integrated waveguide (SIW) technology to increase the gain and to reduce the losses at MMW bands.



## 3.2 High-Gain Dielectric-Loaded Antipodal Fermi Tapered Slot Antenna

In this work, an antipodal Fermi tapered slot antenna (AFTSA) with sine-shaped corrugations is presented. To improve the antenna characteristics, in terms of impedance matching, radiation symmetry and gain, two modified antennas are constructed and evaluated. The first modified antenna is formed by cutting out a delta-shaped slot from the AFTSA, the second by loading an elliptical-shaped dielectric slab (LAFTSA) and cutting out a diamond-shaped slot from the antenna substrate.

### 3.2.1 Antenna Design and Configuration

Figure 3.1 shows the geometry and the main design parameters of the AFTSA with sine corrugations. The antenna is fabricated on an 8.7-mil thick RO4003 substrate having a relative permittivity of 3.55, covered on both sides by 17.5 $\mu$ m-thick copper. It is flared on either side of the substrate in opposite directions to configure the Fermi-Dirac taper profile according to the following equation:

$$f(z) = -a/1 + e^{-b(z-c)} \quad (3.2)$$

where ( $a=4.8$ ) is an asymptotic value of the taper width, and the parameter ( $b=0.35$ ) is related to the gradient at the inflection point ( $c=4$ ) of the Fermi-Dirac function. A balun pad (microstrip-to-slot transition) must be used to achieve the required impedance matching. The antenna length was selected as  $3\lambda_o \leq L_s \leq 8\lambda_o$  and the aperture width as  $W_{ap} \geq \lambda_o/2$ , where  $\lambda_o$  is the free space wavelength at 60 GHz. These values produced the best performance. The corrugation profile is represented by  $A_c * \sin((2\pi/k)z)$ , where ( $k=1.05$ ) is the period, and  $A_c$  is the amplitude. The distance between the edge of aperture and substrate is  $d$ . A delta-shaped slot with length  $L_t$  was cut-out of the substrate to lower the dielectric permittivity at the aperture of the AFTSA, as shown in Figure 3.2 (a). In Figure 3.2 (b), an elliptical-shaped dielectric is loaded in front of the AFTSA (LAFTSA), with a diamond-shaped slot cut-out of the substrate. Dimensions of the proposed antennas are listed in Table 3.1.

Table 3.1: Optimized dimensions of AFTSAs.

Parameter	$L_s$	$L_f$	$L_d$	$W_f$	$W_g$	$W_{ap}$	$W$	$L_t$	$L_e$	$a_e$	$b_e$	$d$
Value(mm)	35	18	21	0.58	12	9.2	13	18	10	4	8.5	3.8

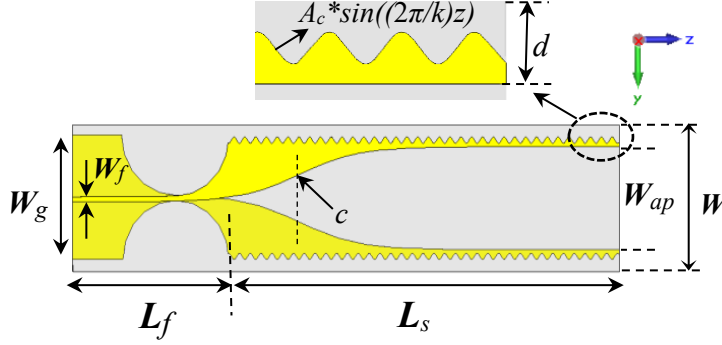


Figure 3.1: AFTSA geometry.

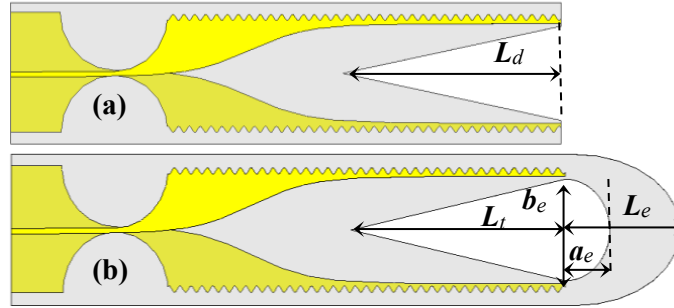


Figure 3.2: Modified antenna configurations: (a) AFTSA with delta-shaped slot and (b) Dielectric-loaded AFTSA with a diamond-shaped slot.

The impact of varying the corrugation amplitude ( $A_c$ ) on the gain and  $|S_{11}|$  is simulated using CST MWS, as shown in Figure 3.3. As  $A_c$  increases to the value of 0.3 mm, the gain increases to a maximum value of 19.1 dB, then starts to decrease with a further increase of  $A_c$ . It can be observed that improvement in return loss is achieved with the appropriate choice of corrugation amplitude ( $A_c = 0.3$  mm). On the other hand, relatively small or high values of  $A_c$  lead to deterioration in  $|S_{11}|$ .

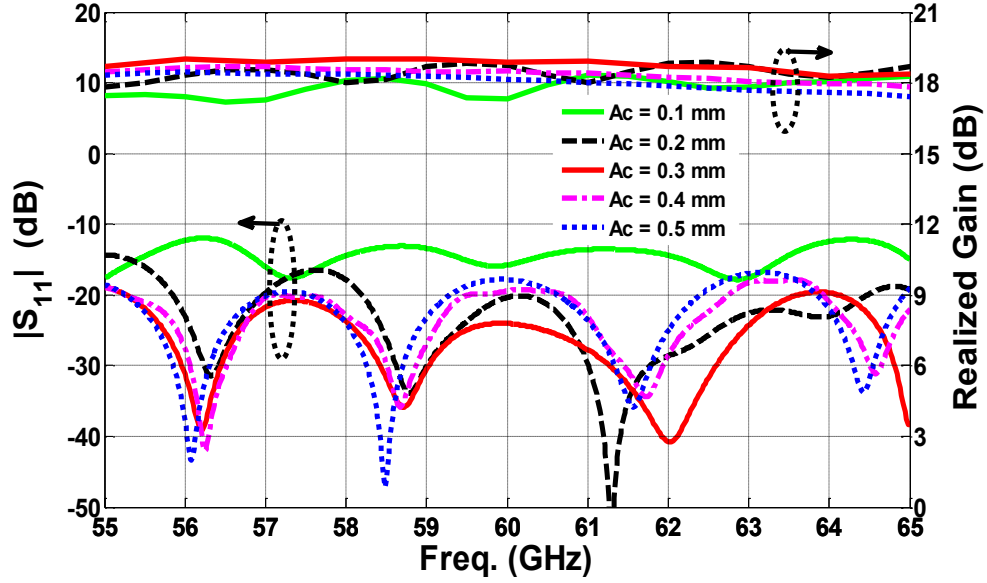


Figure 3.3: Impact of varying loaded AFTSA amplitude corrugation on  $|S_{11}|$  and the realized gain.

### 3.2.2 Experiments and Discussions

Figure 3.4 shows top and bottom views of the fabricated prototypes. Figure 3.5 shows both simulated and measured gain and  $|S_{11}|$  of the three antennas. For the standard AFTSA, the simulated  $|S_{11}|$  is less than -17 dB over the entire band, whereas the measured value is less than -20 dB in the range of 56-64 GHz and slightly higher at both ends of the band. The simulated and measured gain is  $18.5 \pm 0.4$  and  $18.8 \pm 0.8$  dB, respectively, over the operating bandwidth. The simulated  $|S_{11}|$  of the AFTSA with a delta-shaped slot is less than -20 dB over the entire band, compared to measured values of less than -25 dB up to 60 GHz and increases to -21 dB above this frequency. The overall average gain is 19 dB for both simulated and measured results. The simulated  $|S_{11}|$  of the LAFTSA with a diamond-shaped slot, shown in figure 2 (b), is less than -20 dB, with measured values of less than -22 dB over the entire band. The simulated and measured overall gain is 20 dB over the entire band.

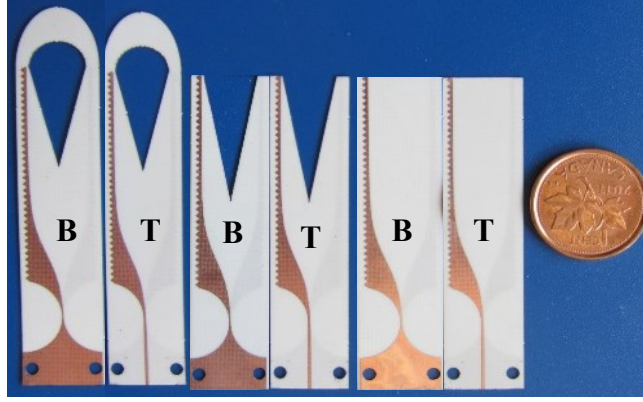


Figure 3.4: Top (T) and bottom (B) views of prototypes of AFTSA, AFTSA with delta-shaped slot and loaded AFTSA with a diamond-shaped slot (from right to left) .

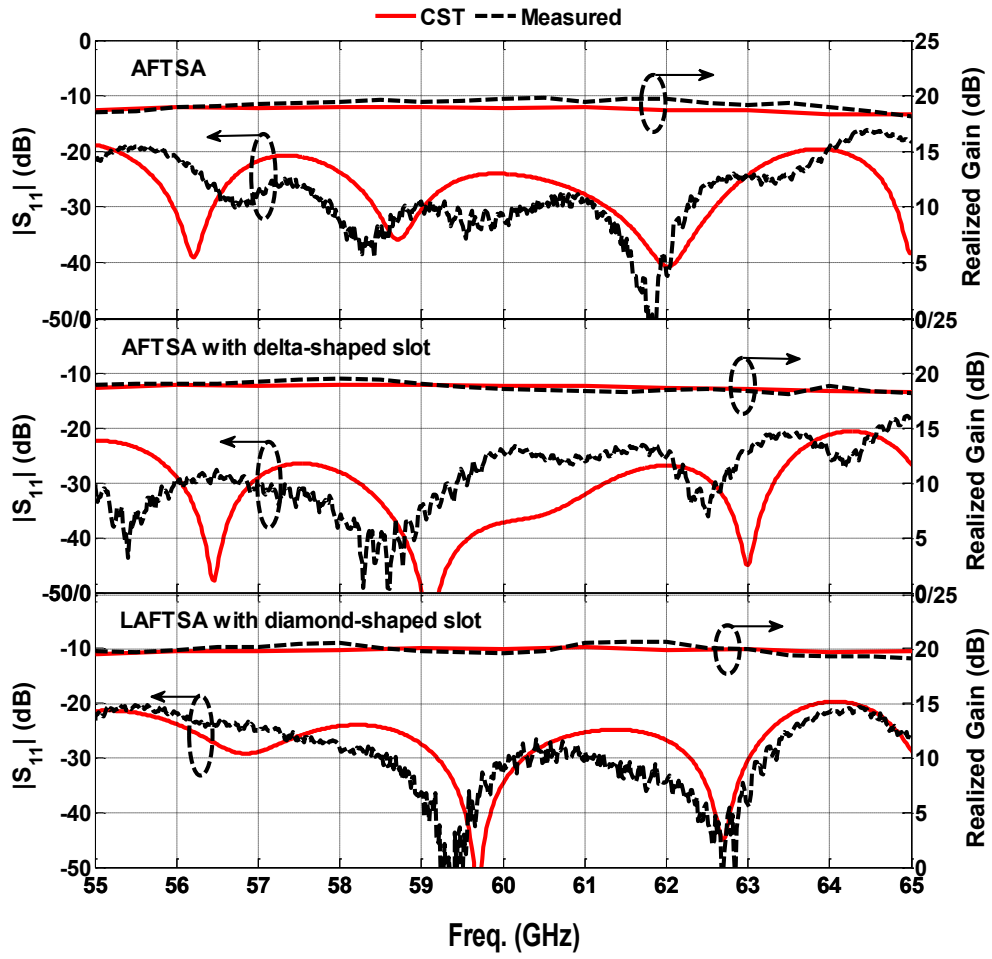


Figure 3.5: Simulated and measured realized gain and  $|S_{11}|$  of the three antennas.

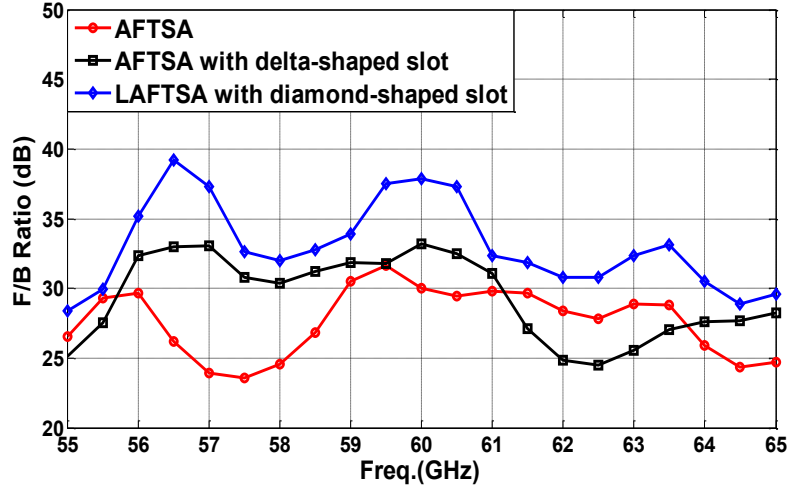


Figure 3.6: Simulated results of the impact of delta-shaped slot and dielectric-loaded with a diamond-shaped slot on the F/B ratio of AFTSA.

Figure 3.6 shows the simulated front-to-back (F/B) ratio of the three proposed antennas. The simulated F/B ratio of AFTSA decreases to around 25 dB in the range of 56.5-58.5 GHz and at the upper end of the band, whereas an overall value of 28 dB is obtained at other frequencies. For the AFTSA with a delta-shaped slot, the overall value of the simulated F/B ratio is around 31 dB in the range from 56 to 61 GHz and decreases to 27.5 dB at other frequencies. The LAFTSA with a diamond-shaped slot achieves an overall simulated F/B ratio of around 32 dB over the entire band. The directivity/gain method [136] is used to measure the efficiencies of the three prototype antennas, mainly due to its simplicity and easy adaptation to lab setups. This method is dependent upon the measured gain ( $G_{\text{Measured}}$ ) and calculated directivity ( $D_{\text{Simulated}}$ ), which can be used to determine the total antenna efficiency as:

$$\eta = \frac{P_{\text{rad}}}{P_{\text{in}}} = \frac{G_{\text{Measured}}}{D_{\text{Simulated}}} \quad (3.3)$$

where  $P_{\text{rad}}$  and  $P_{\text{in}}$  are the power radiated by the antenna and the input power to the antenna, respectively. The directivity was calculated by CST MWS, whereas the measured gain was estimated using two standard gain horn antennas, as shown in Figure 3.7, with applying the Friis transmission formula [137]:

$$G_{\text{AUT}} = \frac{1}{G_{\text{SGH}}} \left( \frac{p_r}{p_t} \right) \left( \frac{4\pi R}{\lambda_0} \right)^2 = |S_{21}|^2 \left( \frac{4\pi R}{\lambda_0} \right)^2 \quad (3.4)$$

where  $G_{AUT}$  and  $G_{SGH}$  are the gains of the antenna under test (receiving antenna) and of the standard horn (transmitting antenna), respectively. The received to transmitted power ratio ( $p_r/p_t$ ) is the measured direct transmission coefficient  $|S_{21}|^2$  by Agilent N5227A vector network analyzer. In addition, the distance between the transmitting and receiving antennas ( $R$ ) satisfied the far-field condition  $R \geq 2D^2/\lambda_0$ , where  $D$  is the largest dimension of either antenna, and  $\lambda_0$  is the free-space wavelength.

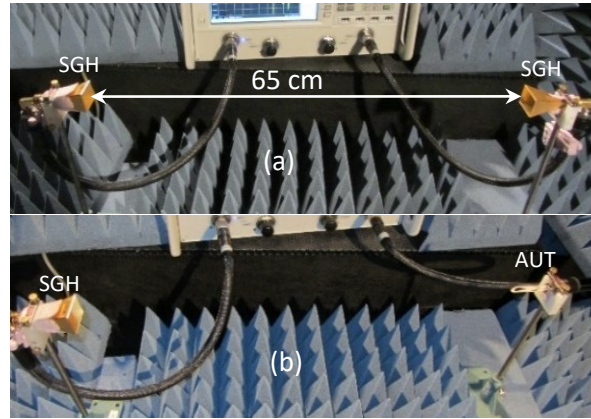


Figure 3.7: Gain measurement setup, (a) two standard gain horns (SGH), (b) standard gain horn and antenna under test (AUT).

Figure 3.8 (a) shows the simulated and measured total AFTSA efficiency. The simulated and the measured overall total efficiency is about 91% and 93%, respectively, over the entire band. Figure 3.8 (b) represents both the simulated and the measured total efficiency of AFTSA with a delta-shaped slot. In the frequency range of 55-58.5 GHz, the total simulated efficiency is  $\approx 90\%$ , whereas it is  $\approx 94\%$  for the average measured value. Beyond this range, the total simulated efficiency increases to about 93%, while the average measured value decreases to about 90%. Figure 3.8 (c) depicts the simulated and measured total efficiency of a LAFTSA with a diamond-shaped slot. The measured overall total efficiency is about 93%, which fluctuates around the simulated results. There are slight discrepancies of about 3 to 5.5% in the efficiency between the measured and the simulated values. This discrepancy may be due to the fabrication tolerance, waveguide-to-coax adapter mismatch, and/or to measurement errors, such as inaccurate alignment between the standard horn and the antenna under test. Figure 3.9 presents the simulated and measured E-plane ( $yz$ -plane) and H-plane ( $xz$ -plane) radiation patterns of AFTSA at 60 GHz. The

measured and simulated results show excellent agreement. As can be seen in figure 3.10, cutting a delta-shaped slot of AFTSA reduces the side lobe levels in both the E- and H-planes. Figure 3.11 shows the simulated and measured radiation patterns of a LAFTSA with a diamond-shaped slot at 60 GHz, revealing that the SLLs were reduced to the values of -12 and -19.5 dB in the E- and H-planes, respectively. In addition, a directive main beam is achieved in the two principal planes. As compared to the standard AFTSA, the LAFTSA with a diamond-shaped slot has a higher gain, lower SLLs, narrower beamwidth, and a higher F/B ratio.

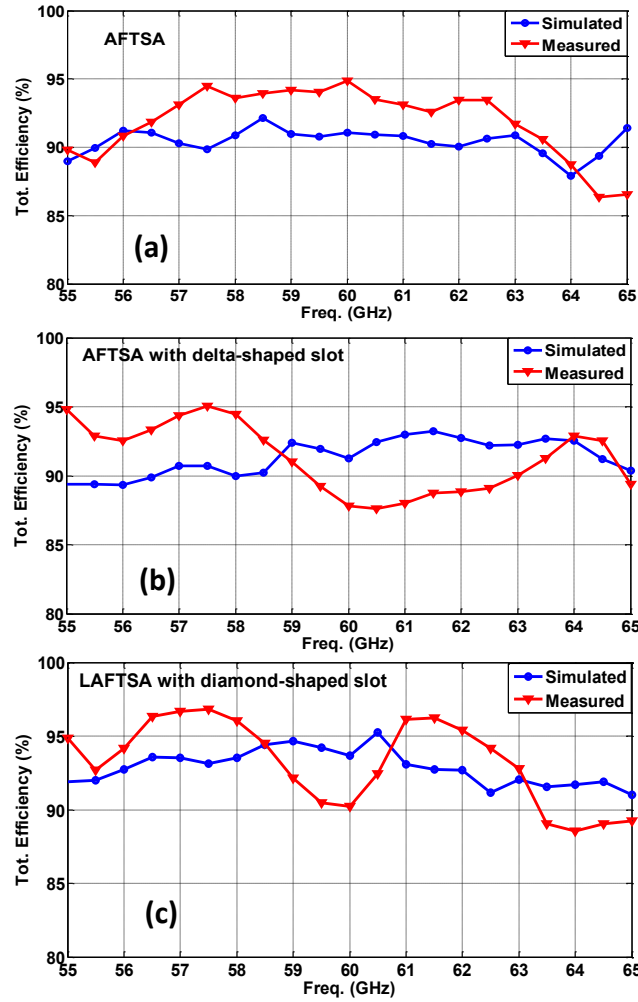


Figure 3.8: Measured and simulated total efficiency (%). (a) AFTSA. (b) AFTSA with a delta-shaped slot. (c) LAFTSA with a diamond-shaped slot.

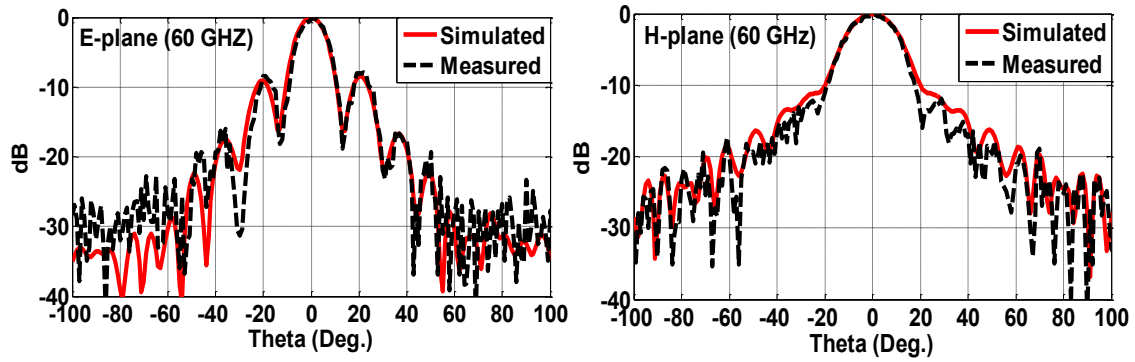


Figure 3.9: Simulated and measured radiation patterns of AFTSA at 60 GHz.

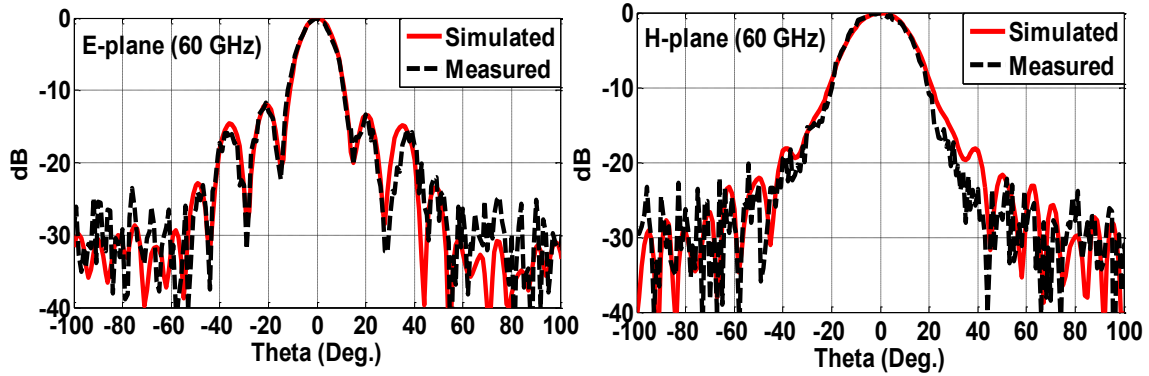


Figure 3.10: Simulated and measured radiation patterns of AFTSA with a delta-shaped slot at 60 GHz.

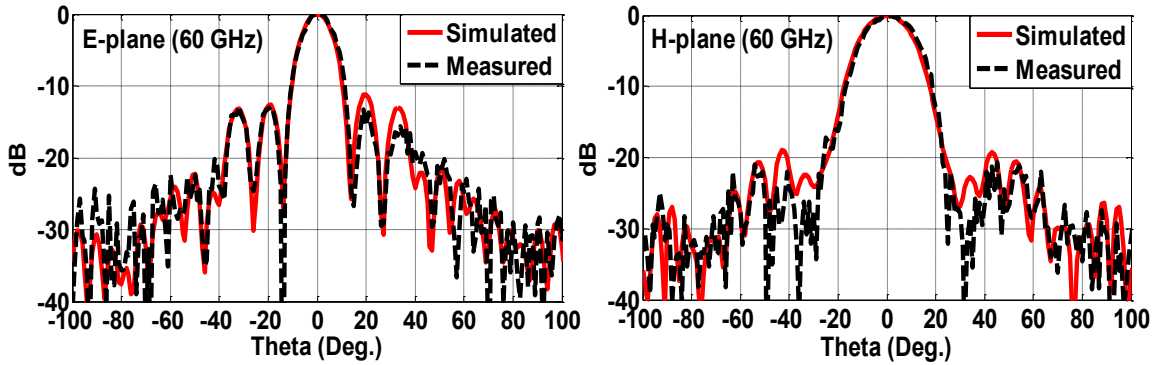


Figure 3.11: Simulated and measured radiation patterns of LAFTSA with a diamond-shaped slot at 60 GHz.



### 3.3 A Broadband Double-Layered Planar LTS Antenna with Low Cross-Polarization

The low reflection coefficient and broadband transition between the radiating tapered slot and the feed source are the main challenges of planar tapered slot antennas (PTSA). In general, these antennas excited using microstrip-to-slotline transition, where the slotline incorporated with the radiating tapered slot on one side of the substrate and the microstrip (MS) line feed on the opposite side. Such transitions utilize frequency-dependent matching elements, thus limiting the operating bandwidth of planar TSAs. Although the antipodal tapered slot antenna (ATSA) configurations achieve broadband performance, they all suffer from high cross-polarization levels, which limit their use as radiating elements in phased array applications. Novel design to overcome this limitation is proposed in this work, where a double-layered TSA is utilized to achieve wide bandwidth and low cross-polarization.

#### 3.3.1 Antenna Element Design and Configuration

The antenna structure with the main design parameters is illustrated in Figure 3.12 (a). Two identical layers of Rogers RT/Duroid 6002 substrate both of thickness  $h = 0.127$  mm, dielectric constant  $\epsilon_r = 2.94$  and  $\tan \delta = 0.0012$  are used to design the proposed antenna. As can be seen in Figure 3.12 (b), the top and bottom metallic layers are connected by two rows of plated-through hole vias to construct the SIW, whereas the middle metallic layer (tapered slot antenna) is placed between the two substrates. Since the phase velocity ( $V_p$ ) is inversely proportional to the dielectric constant, coating both sides of the tapered slot antenna with dielectric will enhance the surface to be an effective slow wave structure ( $V_p \leq c$ ), where  $c$  is the speed of light. Moreover, covering the tapered slot with dielectric will minimize the mutual coupling between elements in case of an array. For TSAs with a thin supporting substrate, the beam width will be wider, and with a relatively thick substrate, the beam width will deteriorate. On the other hand, the fabrication of SIW on a thin substrate will increase the metallic losses, which cause a reduction of antenna efficiency, especially at high frequencies. Therefore, for high efficiency and symmetrical radiation patterns of the proposed antenna, the dielectric constant ( $\epsilon_r$ ) and thickness ( $h$ ) of the substrate are chosen to satisfy the conditions published in [31].

$$0.005 < \frac{t_{eff}}{\lambda_0} < 0.03, \quad t_{eff} = (\sqrt{\epsilon_r} - 1) h \quad (3.5)$$

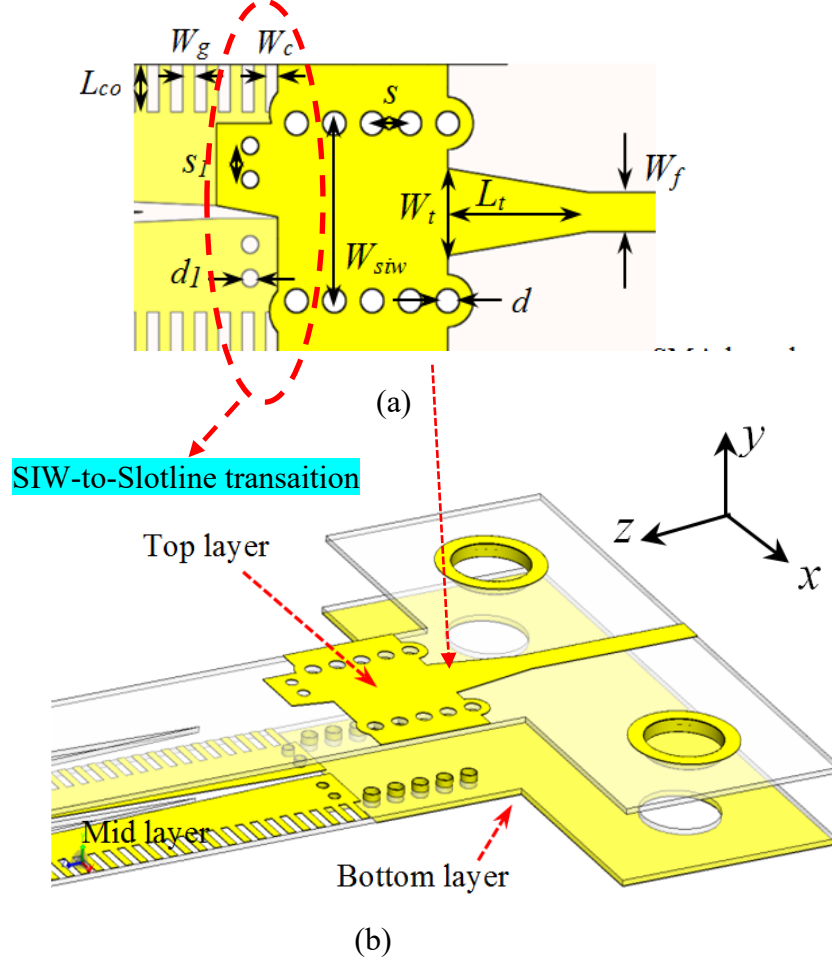


Figure 3.12: Geometry and design parameters of the proposed SIW-based planar linearly tapered slot antenna (PLTSA) (a) Top view and (b) Perspective view.

where  $t_{eff}$  is the effective thickness of the substrate and  $\lambda_0$  is the free space wavelength at the band center. To satisfy equation (3.5), a delta-shaped slot with a length of about  $5\lambda_0$  is cut in the two substrate layers to lower the  $\epsilon_r$  of the supporting substrates. Moreover, in order to fulfill the broadband end fire radiation characteristics of a TSA antenna, the antenna length ( $La$ ) should be in the range of  $3\lambda_0 \leq La \leq 8\lambda_0$  and the terminating slot width  $Wa \geq 0.5\lambda_0$  [31]. The optimized flare angle  $\alpha = 5.2^\circ$  is used to satisfy these two conditions and at the same time to achieve symmetrical radiation patterns in both principal planes. Since the gain is proportional to the length, a trade-off between the gain and antenna length ( $La$ ) is necessary for mechanical strengthening. A rectangular corrugation is added to the outer edges of both strip conductors to reduce the antenna width ( $Wa$ )

and to improve the input return loss. In order to feed the PLTSA (polarized in the x-direction) using SIW (polarized in the y-direction) , an SIW-to-slotline transition is required. This transition is formed using two metallic plates of a rectangular trapezoid shape with two pairs of blind vias to connect the upper and lower metal walls of the SIW to the right and left strip conductor, respectively. Moreover, standard MS-to-SIW transition is designed to enable the end launch connector to excite the antenna. To support only the  $TE_{10}$  mode and to prevent electromagnetic leakage in the SIW structure within the frequency range of interest, the SIW width ( $W_{siw}$ ) and via diameter to spacing d/s ratio is calculated based on empirical equations and conditions, reported in [23, 138]. The optimized dimensions of the proposed antenna are summarized in Table 3.2.

Table 3.2:  
dimensions of the

Parameter	Value (mm)	Parameter	Value (mm)
$L_a$	34	$d$	0.4
$W_a$	3.0	$S$	0.65
$L_c$	31.5	$W_f$	0.64
$L_{co}$	0.78	$L_t$	2.2
$W_c$	0.2	$W_t$	1.35
$W_{siw}$	2.58	$S_l$	0.5

Optimized  
proposed antenna.

### 3.3.2 Simulated and Measured Results

A prototype of the proposed antenna has been fabricated, as shown in Figure 3.13 and tested to verify the simulated results obtained by the frequency-domain solver of Ansys HFSS. Each layer of the prototype is fabricated using a low-cost single-layer PCB technology. After that, the two layers are joined using adhesive and pressure process. The fabricated antenna is fed by a 1.85 mm V-band end-launch connector (manufactured by Southwest Microwave). Figure 3.14 shows the simulated and measured frequency response of  $|S_{11}|$  and realized gain. The simulated and measured return loss is less than -10 dB over the frequency range 46-72 GHz. Note that the  $|S_{11}|$  is measured up to 67 GHz due to the measurement limit of the Agilent N5227A vector network analyzer (VNA). In addition, the antenna shows a maximum gain of 16.2 dB, as shown in Figure 3.14. The measured gain is estimated from calibrated data of two standard gain V-ban horn antennas [137].

The measured gain is marginally lower than the simulated result, perhaps due to fabrication error and inaccurate alignment between the standard horn and the antenna under test.

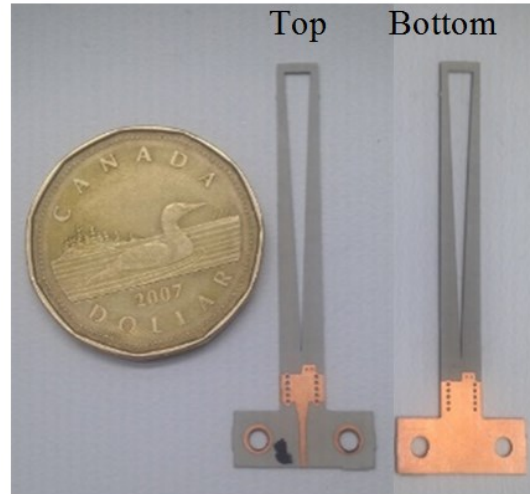


Figure 3.13: Top and bottom view of planar linearly tapered slot antenna (PLTSA) prototype.

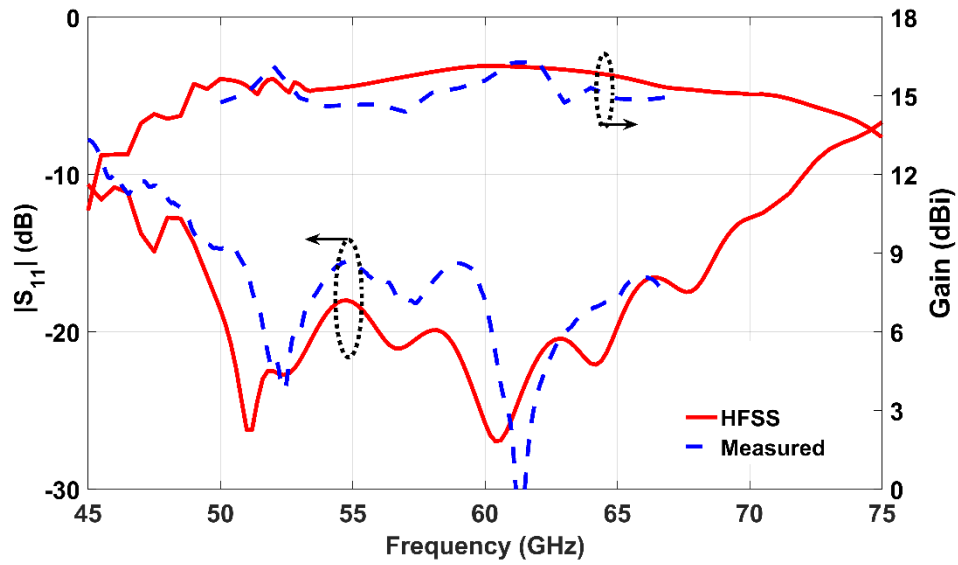


Figure 3.14: Measured and simulated  $|S_{11}|$  and realized gain of the proposed PLTS antenna.

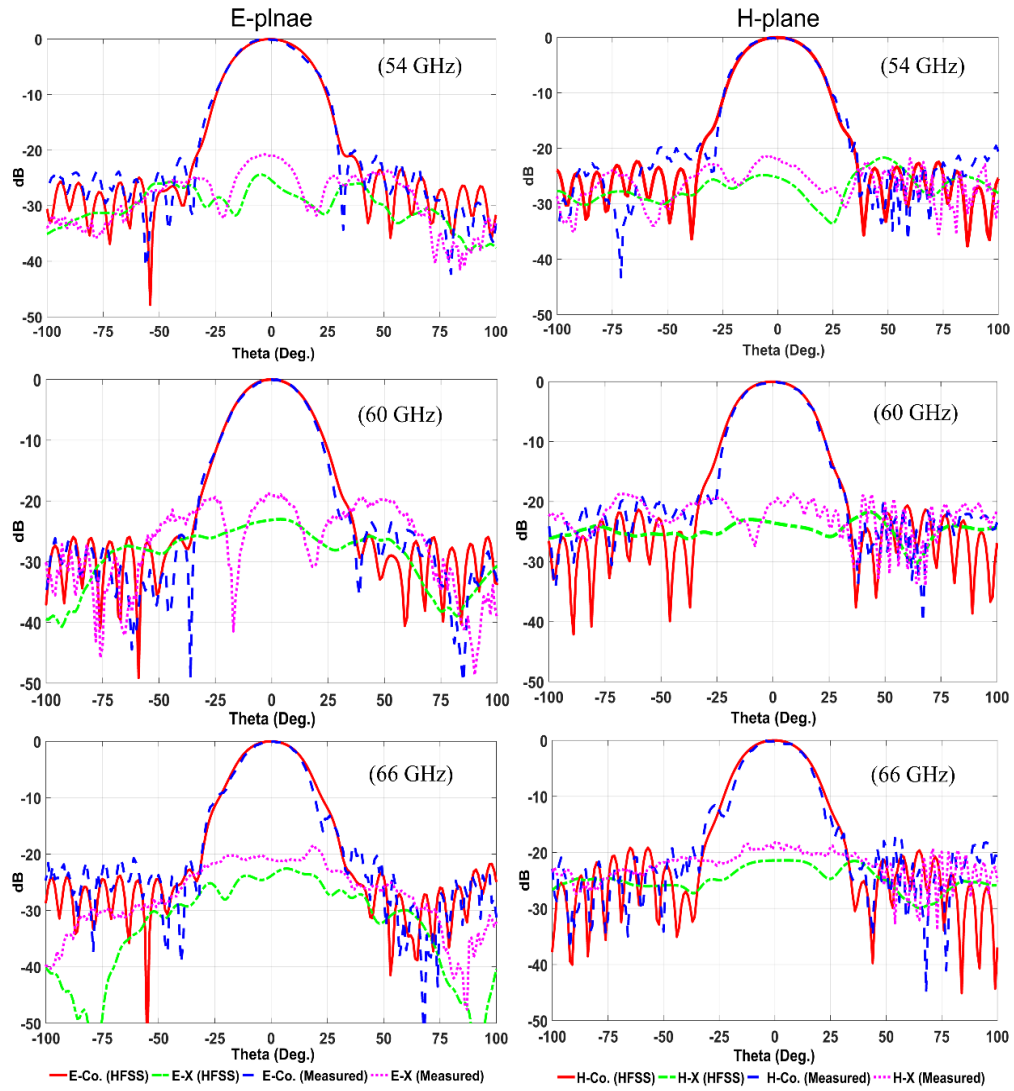


Figure 3.15: Simulated and measured radiation of an element PLTS antenna at 54, 60 and 66 GHz.

Figure 3.15 represents a comparison between simulated and measured E-plane ( $xz$ -plane) and H-plane ( $yz$ -plane) radiation patterns at 54, 60 and 66 GHz. For E- and H- planes, the simulated and measured -3dB beamwidths are  $33^\circ$ ,  $31^\circ$  and  $29^\circ$  at 54, 60 and 66 GHz, respectively. In addition to the benefits of the planar structure and compact profile of the proposed antenna, the results demonstrate an excellent symmetric radiation pattern of the principal planes over the entire band of interest, making the antenna highly suitable as a feeding source of parabolic antennas with very low spillover and low blockage losses. The simulated SLL of E- and H-plane is - 25 dB at 54 GHz

and increases to -21 dB at 66 GHz. The measured SLL is almost better than 19 dB overall the band of interest. The simulated cross-polarization level of principal planes is better than 24 dB at 54 and 60 GHz, whereas it increases to -21 dB at 66 GHz. For measured results of E- and H-plane, the cross-polarization level is -21 dB, -19 dB and -18 dB at 54, 60 and 66 GHz, respectively. A bridge of the same substrate material with width ( $W_b = \lambda_0/4$ ) is utilized at the antenna termination end to correctly align the two conducting strips of the tapered slot in the  $xz$ -plane. Since the antenna has a directive beam and low SLL, the measured efficiency was estimated ( 86.4% @ 60 GHz ) from the measured gain and the approximate directivity  $D \approx (41253)/(\theta_E \theta_H)$  [139], where  $\theta_E$  and  $\theta_H$  are the HPBW in degrees of the E- and H-planes, respectively. The antenna exhibits a simulated efficiency of 94 %.

### 3.3.3 1x4 Array Design and Experimental Validation

The single element designed in the previous subsection is utilized as a radiating element to construct a 1x4 planar LTSA Array. A photograph of the fabricated prototype is presented in Figure 3.16. The fabricated antenna is fed by a 1.85 mm V-band end-launch connector (manufactured by Southwest Microwave). A wideband SIW power divider is designed to feed the LTSA array over the frequency range from 54 to 66 GHz. For maximum gain, the 4-way power divider is designed with uniform amplitude and zero phase delay between output ports.



Figure 3.16: Top and bottom view of the PLTS antenna array prototype.

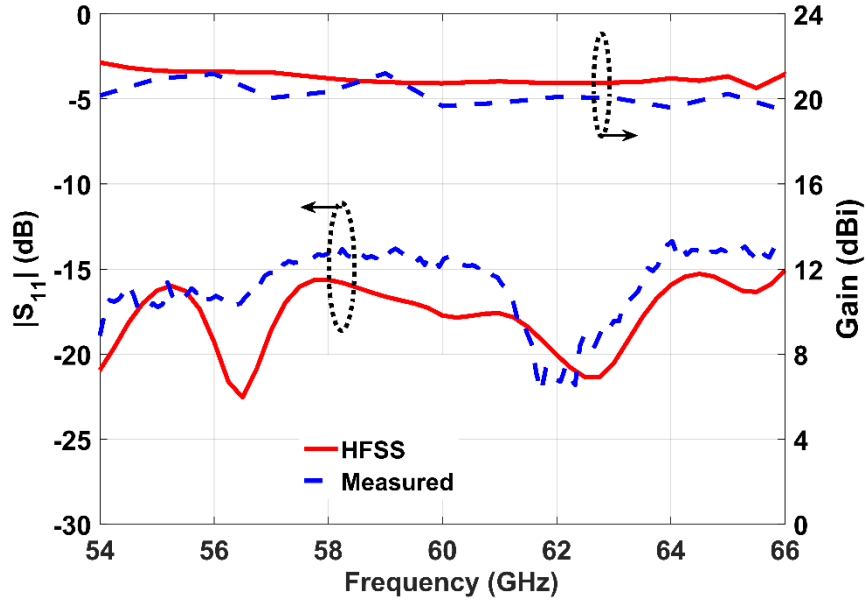


Figure 3.17: Measured and simulated  $|S_{11}|$  and realized gain of the proposed PLTS antenna array.

Generally, a trade-off between wide bandwidth and low insertion loss is required. In this work, three inductive posts are embedded in the power divider at each stage in such a way that the reflection is minimized with further improvement in the operating bandwidth. Moreover, avoiding the  $90^\circ$  bends in the proposed power divider ensures that the electric field energy has a smooth transition between the input port and output ports. Figure 3.17 depicts a comparison between measured and HFSS simulated results of  $|S_{11}|$  and realized gain. As can be seen, the measured and simulated return loss is better than 14 dB and 16 dB, respectively. Over the band of interest, the simulated and measured gain is  $21 \pm 0.5$  dB and  $20.2 \pm 0.8$  dB, respectively. Figure 3.18 illustrates the measured and simulated radiation patterns of the proposed array at 54, 60 and 66 GHz. For E-plane, the measured and simulated  $-3$  dB beamwidth is  $10.5^\circ$  over whole the band. Due to the size of the single element and power divider, the array is designed with an inter-element spacing of  $1.1 \lambda_0$ . The simulated and measured E-plane SLL is less than -13 dB at 54 GHz and decreases to -15 dB at 66 GHz. For H-plane, the HPBW's are  $30^\circ$ ,  $27^\circ$  and  $25^\circ$  at 54, 60 and 66 GHz, respectively. The array shows simulated and measured H-plane SLL better than 21 dB and 19 dB, respectively. For both principal planes, the simulated and measured cross-polarization levels are less than -21 and -18 dB, respectively. The measured efficiency was estimated (79.2 % @ 60 GHz) by the

measured gain and the approximate directivity  $D \approx (32400)/(\theta_E \theta_H)$  , where  $\theta_E$  and  $\theta_H$  are the HPBW's in degrees of the E- and H-planes, respectively. The simulated efficiency is 87.3 %.

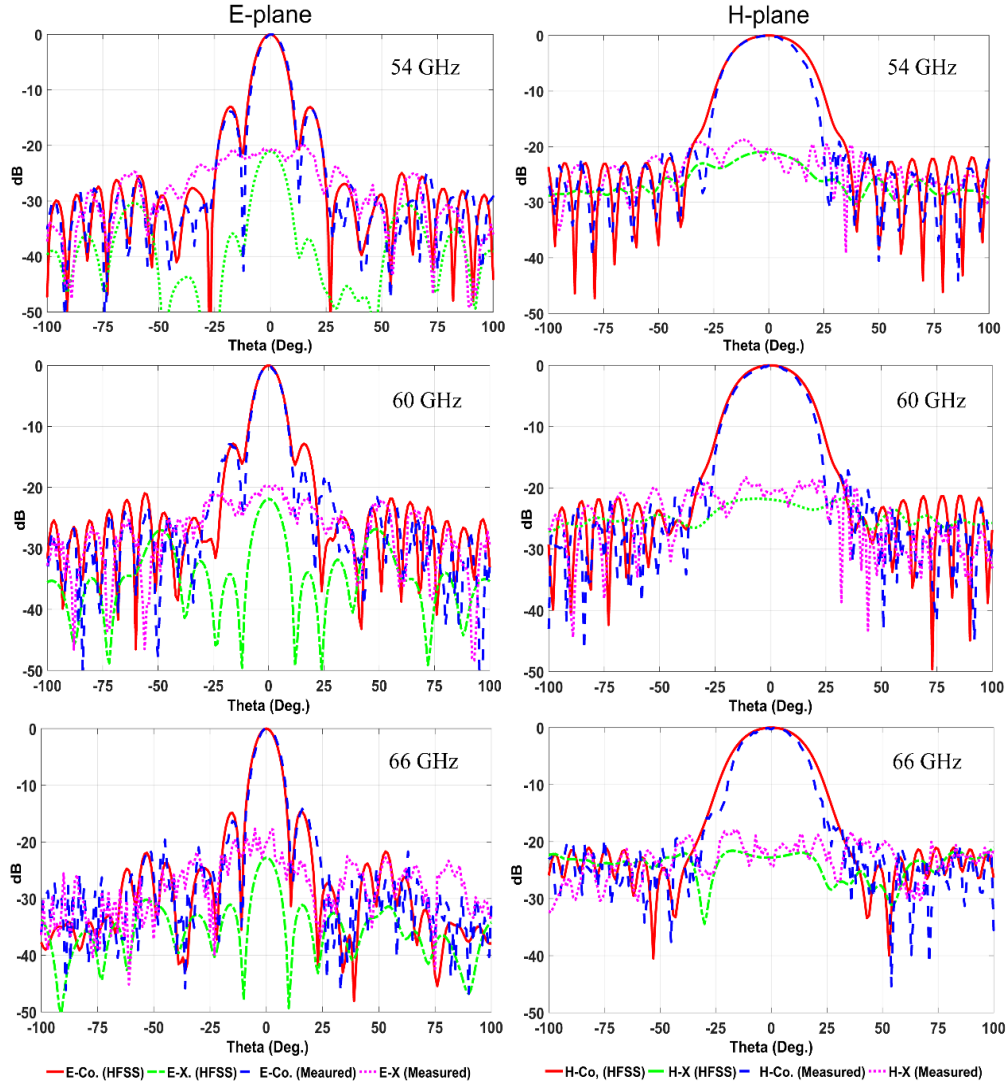


Figure 3.18: Simulated and measured radiation of the PLTS antenna array at 54, 60 and 66 GHz.



### 3.4 Antipodal Fermi Tapered Slot Antenna Array

In this section, a wideband 4-element antipodal Fermi tapered slot antenna (AFTSA) array with SIW-based feeding network is presented. A four-way H-plane SIW-based power divider with low loss is used to feed the proposed array. The stacked configuration with mirrored elements in H-plane is utilized to minimize the inter-element spacing of the array and to lower the cross-polarization levels. For verification, the simulated results are carried out using CST and HFSS simulators.

#### 3.4.1 Array Design

Figure 3.19 depicts the stacked array configuration in combination with the feeding network. The distance between radiating elements is  $0.75 \lambda_0$  at 60 GHz. A wideband four-way SIW power divider is used to feed the proposed array. An MS-to-SIW transition and horizontal to vertical orientation microstrip transition are utilized to connected the radiating elements to the output ports of the power divider. Since the beamwidth of a single element antenna in H-plane is wider than those of E-plane, the stacked structure is more efficient to improve the radiation symmetry compared to a coplanar structure. Moreover, with stacked configuration, the inter-element spacing can be changed easily by adjusting the distance between the output ports of the power divider, thus minimize the mutual coupling between elements. The SIW width  $W_{siw}=2.5\text{mm}$  and via diameter to spacing ratio  $d/s = 0.57$  ( $d=0.32\text{mm}$  and  $s=0.56\text{mm}$ ). The length of the tapered microstrip is  $L_t=2.2\text{ mm}$  with a width  $W_t=1.55\text{ mm}$ , are optimized to match the input impedance of the SIW.

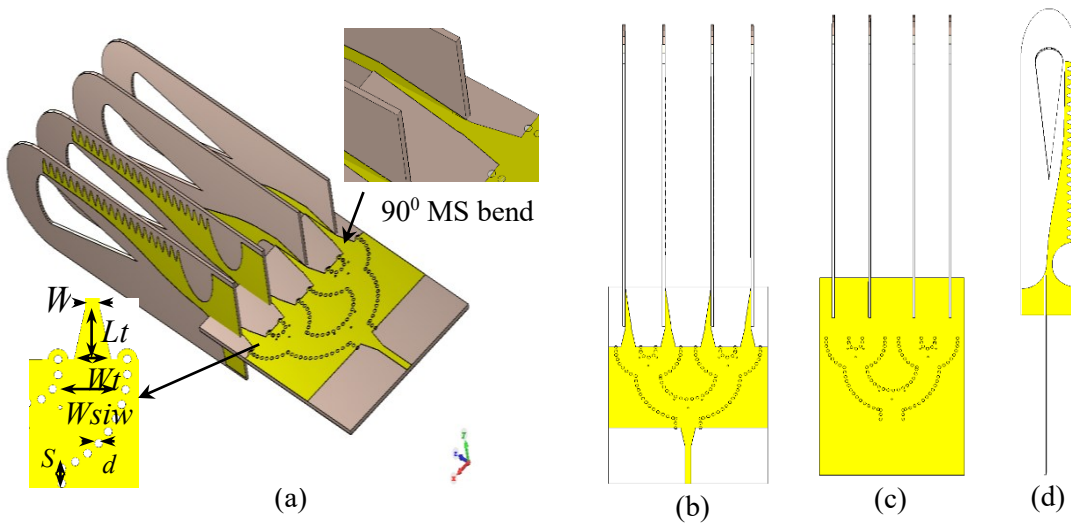


Figure 3.19: The proposed 4-element AFTSA array: (a) 3-D , (b) top, (c) bottom and (d) side view.

The feed network and antenna element is designed on Rogers RT/Duroid 6002 substrate with thickness  $h=0.254\text{ mm}$ ,  $17.5\text{ }\mu\text{m}$  copper thickness and dielectric constant  $\epsilon_r = 2.94$ . Note that the antenna element is a modified version of the antenna presented in section 3.1.

### 3.4.2 Simulated Results

The results are carried out by using two commercial simulators, CST Microwave studio and Ansoft HFSS. Figure 3.20 shows the return loss of the array over the frequency range 55-65 GHz. It can be observed that the  $|S_{11}|$  is less than -14 dB over the entire band. Figure 3.21 illustrates the comparison between the realized gain of a single element and the antenna array. As evidenced by both simulators, the single element antenna exhibits a flat gain of  $15.5\pm 0.4\text{ dB}$  over the frequency band of interest. The realized gain of the proposed AFTSA array increases by 4.7 dB compared to the single element. The losses may be attributed to the feeding network and the mutual coupling between elements.

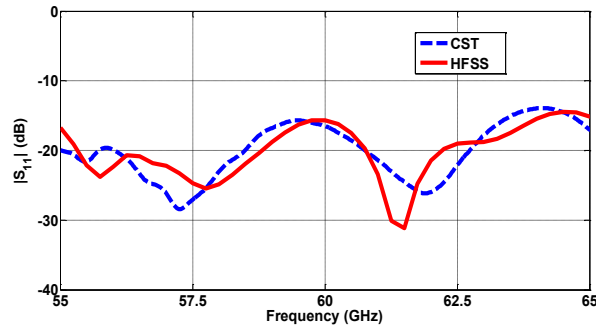


Figure 3.20:  $|S_{11}|$  of the antipodal Fermi tapered slot antenna (AFTSA) array.

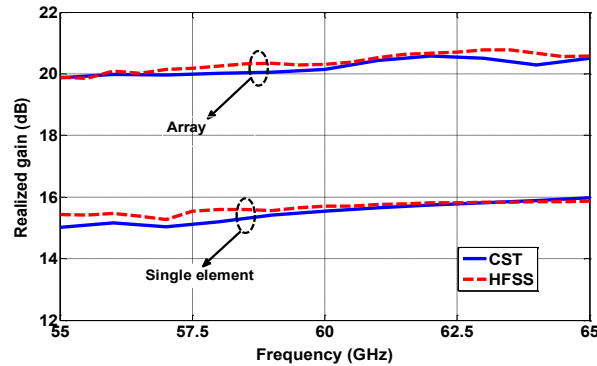


Figure 3.21: Comparison between realized gain of single element and 1x4 AFTSA array.

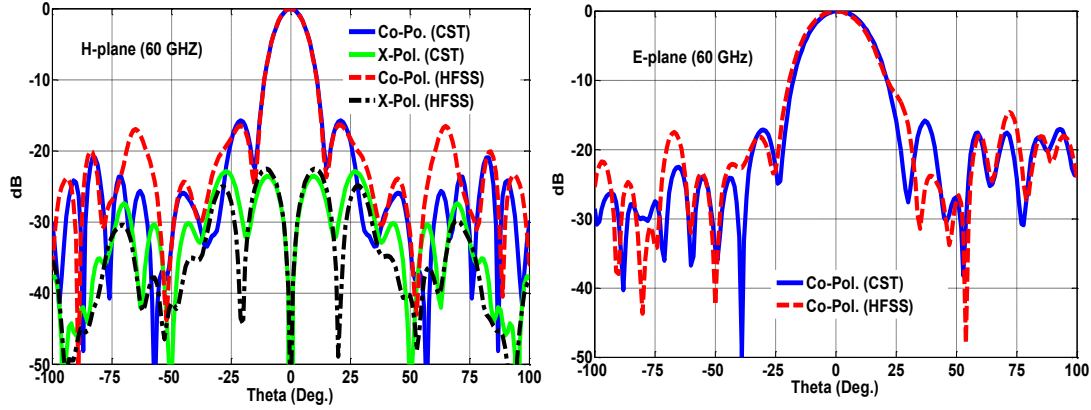


Figure 3.22: E- and H-plane radiation patterns of the AFTSA array at 60 GHz.

Figure 3.22 shows the radiation patterns of E-plane ( $yz$ -plane) and the H-plane ( $xz$ -plane) at 60 GHz. The SLL is better than 16 dB over the entire band. In E-plane, the cross-polarization is -23 dB. The stacked array with mirrored configuration is effectively suppressed the cross-polarization level in H-plane (less than -50 dB).

### 3.5 Broadband Transition of SIW to Air-filled Rectangular Waveguide

In many applications, the combination of SIW and the conventional waveguide is required to measure the s-parameters of SIW-based components or to test the radiation performance of antenna designed based on SIW technology. There is thus a pressing need for an effective and low-cost transition between SIW and air-filled rectangular waveguide (RWG). In this section, a novel wideband right-angle transition between SIW and standard WR-15 RWG is proposed at V-band.

#### 3.5.1 Transition Design and Working Principal

Figure 3.23 depicts the 3-D geometry of the proposed transition. The WR-15 RWG is directly mounted on the top surface of the SIW substrate to form E-plane right-angle transition. The aperture-coupled patch antenna is utilized to connect the SIW and RW-15 RWG. In order to obtain broader matching performance, two pairs of inductive posts are placed symmetrically into the SIW transformer and separated by a distance of  $W1$  and  $W2$ , as shown in Figure 3.24. Moreover, circular sectors with radius  $R$  concentric with the inductive posts are employed to enhance the coupling between the SIW and RW-15 waveguide and help to satisfy the fabrication tolerance as well. The

transition is designed on 0.508 mm-thick Rogers RT/ Duroid 6002 laminate with a dielectric constant of 2.94, loss tangent of 0.0012, and copper cladding of  $18 \mu\text{m}$ . The via diameter to pitch ratio ( $d/P= 1.8$ ) is set based on the conditions reported in [13]. In addition, to prevent the higher

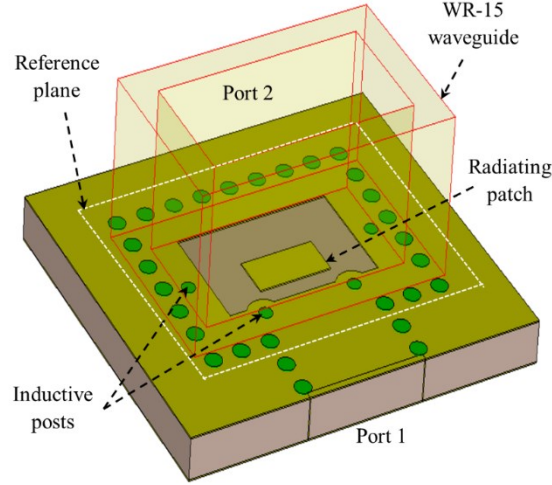


Figure 3.23: Perspective view of the proposed SIW to waveguide transition.

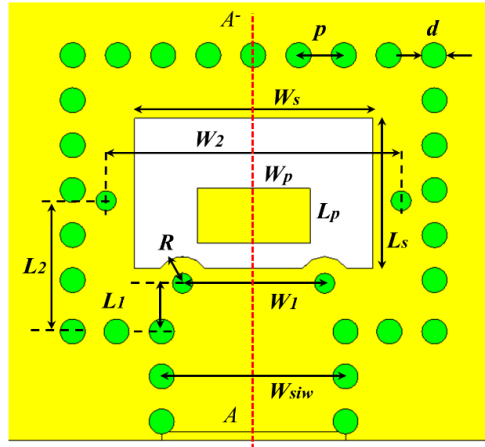


Figure 3.24: Top view of the SIW-to-WG transition.

order modes from propagation and to work far enough from the cutoff frequency, the equivalent width of SIW is set to  $2.0 \text{ mm}$ , and accordingly, the width of SIW ( $W_{\text{siw}}=2.18 \text{ mm}$ ) is calculated from approximated equation (9) published in [23]. Optimized dimensions of the transition are listed in Table 3.3. The vector of electrical field distributions at the cross-section  $AA'$  plane and at the SIW-WR15 interface are illustrated in Figure 3.25. The  $\text{TE}_{10}$  mode of SIW structure in the horizontal direction is converted into the  $\text{TE}_{10}$  mode of the standard WR-15 waveguide in the

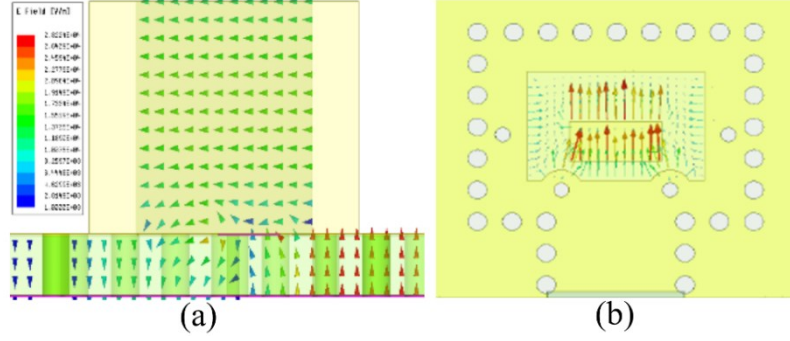


Figure 3.25: Electric field vector distribution at 63 GHz. (a) At the cross-section plane  $A-A'$ . (b) At the reference plane (see Figure 3.23).

Table 3.3: Optimized dimensions of the SIW-to-WR15 transition.

Parameter	$L_1$	$L_2$	$L_s$	$L_p$	$W_1$	$W_2$	$W_p$	$W_s$	$d$	$p$	$R$
Value (mm)	0.54	1.5	1.85	0.67	1.75	3.35	1.65	2.8	0.3	0.54	0.37

vertical direction via aperture coupled patch antenna, which works as waveform and impedance transformer. The reason for bandwidth improvement of the proposed transition is that by adding two pairs of inductive posts, we can balance the effect of capacitance between the upper metal of the SIW transformer (SIW cavity) and the ground, hence improving the impedance matching over a wide frequency range. In addition, adjusting the radius of circular sectors and the patch offset from the slot center can control the capacitive effect between the patch and the slot edges, which further improves the matching between the SIW and WR-15 waveguides. Figure 3.26 shows the equivalent circuit model of the proposed transition.  $C_c$  represents the capacitance between the upper metal surface and the ground of the cavity.  $L_v$  denotes the metalized vias inside the SIW cavity.  $C_1$  and  $C_2$  represent the capacitance between the slot edge and the lower and upper edge of the patch, respectively.  $L_s$  represents the inductance due to the effect of the short-ended stub. The equivalent capacitances  $C_1^-$ ,  $C_2^-$  and  $C_3^-$  are obtained using simple Y to  $\Delta$  transformation:

$$C_1^- = \frac{C_1 C_c}{A}, \quad C_2^- = \frac{C_2 C_c}{A}, \quad C_3^- = \frac{C_1 C_2}{A} \quad (3.6)$$

where  $A = C_1 + C_2 + C_c$

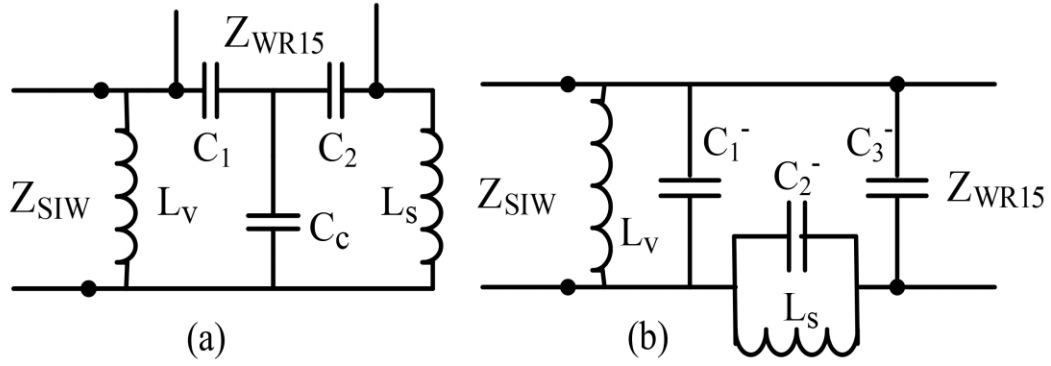


Figure 3.26: (a) Equivalent-circuit model of the transition. (b) Simplified version.

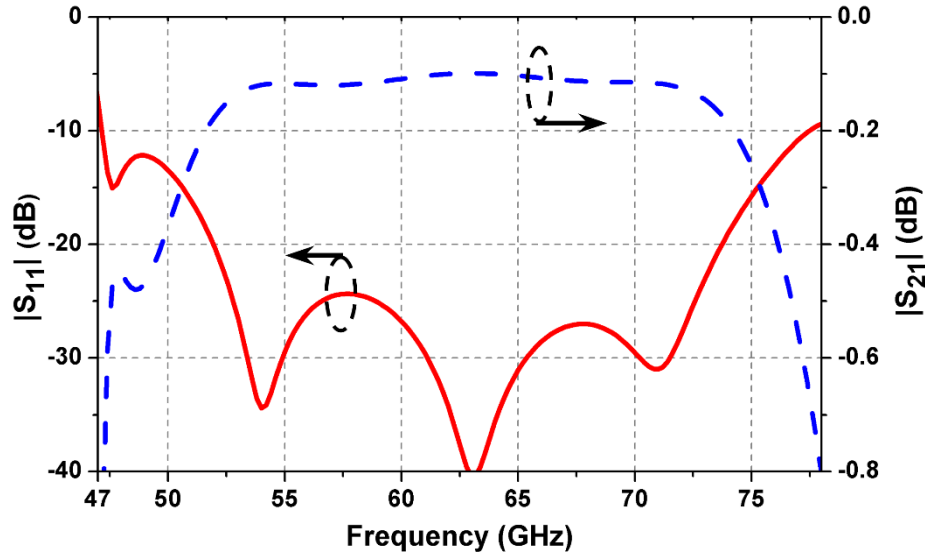


Figure 3.27: Simulated s-parameters of single transition.

The simulated reflection and transmission coefficient of a single transition is illustrated in Figure 3.27. It is clear that the single transition has a fractional bandwidth of 48.6 % from 47.2 to 77.5 GHz for return loss better than 10 dB. The insertion loss is less than 0.5 dB over the frequency range 47.6-76.7 GHz. Table 3.4 summarises the comparison between proposed and right-angle transitions in the literature. It can be seen that the proposed transition demonstrated wide bandwidth, low insertion loss and designed on one layer with a simple structure, which makes it suitable for mass production and practical applications.

Table 3.4: Comparison between proposed SIW-to-WR15 and reported transitions.

Ref.	Transition Type	No. of Layers	IL (dB)	RL (dB)	FBW%(GHz)
[59]	SIW-RWG	Three layers	0.58	$\geq 10$	36.5 % (51.3-74.2)
[60]	LWG-RWG	Eight Layers (LTCC)	0.4	$\geq 10$	10.6 % (28.5-31.7)
[61]	SIW-RWG	One layer +stepped WG	0.6	$\geq 15$	17.3 % (32.7-38.8)
[62]	SIW-RWG	One layer +stepped WG	0.55	$\geq 15$	25.7 % (30.5-39.5)
[63]	SIW-RWG	One layer	1.2	$\geq 10$	3.4% (34.2-35.4)
[64]	MS-RWG	One layer	0.5	$\geq 15$	6.9% (73.9-79.2)
<b>This work</b>	<b>SIW-RWG</b>	<b>One layer</b>	<b>0.5</b>	<b><math>\geq 12</math></b>	<b>45.5% (48.6-77.3)</b>

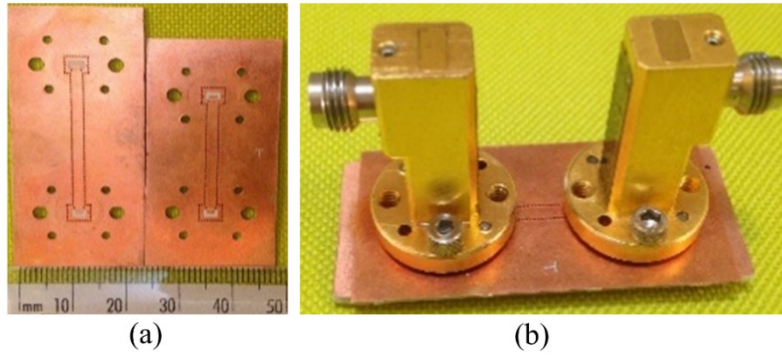


Figure 3.28: Fabricated back-to-back transitions. (a) Top view. (b) The back-to-back with two identical WR15 WG to coaxial adapters.

### 3.5.2 Measurement Results and Discussion

In order to experimentally validate the simulated results and estimate the losses of the SIW section, two back-to-back configurations are designed and fabricated as shown in Figure 3.28 (a). To measure the performance of the proposed transition, a back-to-back prototype is connected with two standard WR-15 to coaxial transitions, as shown in Figure 3.28 (b). The measured results are carried out with Agilent N5227A vector network analyzer (VNA). For accurate measurements, the loss of WR15 waveguide to the coaxial adapter is calibrated out using TRM calibration method, where the reference plane is defined at the WR15-SIW interface. The simulated and measured S-parameters of the back-to-back transition are shown in Figure 3.29. Due to the measurement limitations of the VNA, the upper limiting frequency of the measured result is 67 GHz. The

measured and simulated results are in good agreement. The simulated  $|S_{11}|$  is less than -12 dB for the frequency range from 48.6 to 77.4 GHz, whereas the measured one is less than -10 dB in the range 48.8-67 GHz. The simulated insertion loss of the back-to-back transition varies from -0.7 to -1.3 dB in the frequency range from 48.8 to 77 GHz, and the measured results vary from -0.86 to -1.7 dB over the band 49.4-67 GHz. The estimated losses of 20 mm SIW section is about 0.7 dB, wherein two prototypes of back-to-back transitions with different lengths are employed in the measurements. Therefore, the measured insertion loss of a single transition is  $< 0.5$  dB. The slight discrepancy between simulated and measured results may be due to the fabrication tolerance and surface roughness.

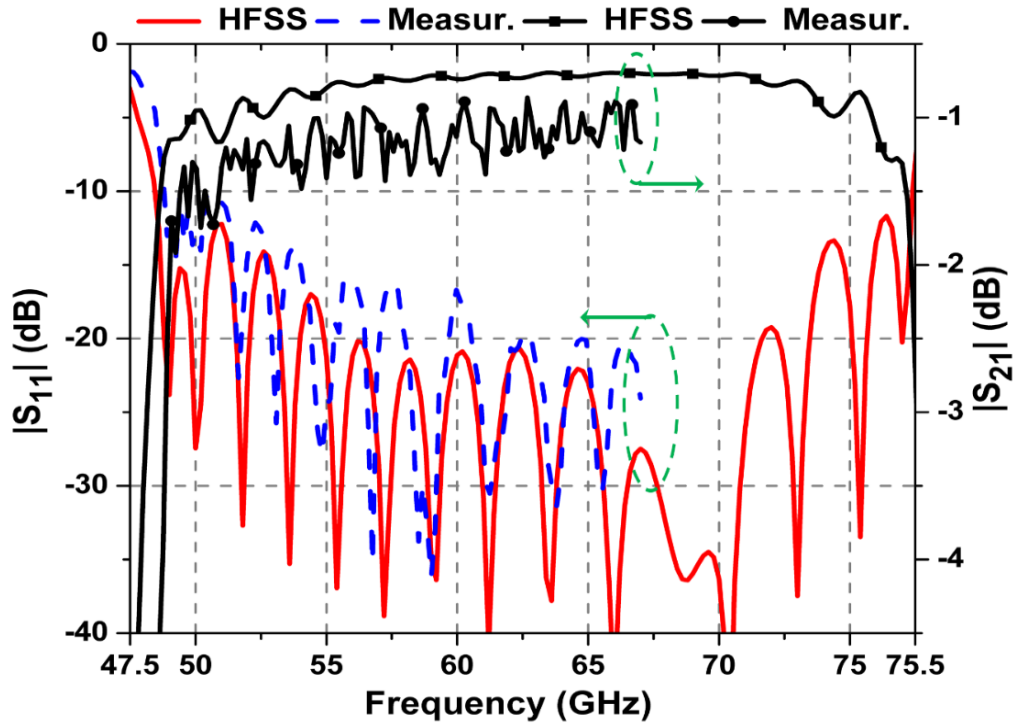


Figure 3.29: Measured and simulated S-parameters of back-to-back transition.



### 3.6 A Compact Wideband SIW-Fed Cavity-Backed Patch Antenna Arrays

In this section, the geometry and operating principle of a wideband linearly polarized (LP) cavity-backed aperture-coupled patch antenna have been discussed. In addition, the design, simulation and measurements of a 1x8 and 4x4 array, based on the proposed element, are introduced.

#### 3.6.1 Antenna Element

##### 3.6.1.1 Geometry and Working Principle

The perspective view and main geometrical parameters of the proposed antenna element are shown in Figure 3.30. The antenna is configured by stacking three substrates on top of one another. Substrates 1 and 2 are 0.508 mm-thick Rogers RT/ Duroid 6002 laminate with a dielectric constant of 2.94, a loss tangent of  $\tan \delta = 0.0012$ , and copper cladding of 18  $\mu\text{m}$ . Substrate 3 is Rogers 5880 with  $\epsilon_r = 2.2$ ,  $\tan \delta = 0.0009$ , and thickness of 0.254 mm. The patch is printed on the top of substrate 3, which is thin to suppress the surface waves. The air-filled circular plated cavity is formed in substrate 2. Unlike a CNC-machined metallic cavity, the proposed plated cavity can be easily fabricated using a standard PCB process, leading to low cost and lightweight structure. Moreover, the air-filled cavity has a low  $Q$  factor, which contributes to widening the bandwidth of the proposed antenna. The SIW feed network is embedded in substrate 1, which is composed of two rows of metallized vias, where the via diameter  $R_I$  and pitch  $P_I$  is chosen to avoid energy leakage and to be within the limits of fabrication tolerances. The patch is electromagnetically coupled to the SIW feed through a longitudinal offset slot etched on the top wall of substrate 1 with three offset vias to enhance the matching over a wide bandwidth. The optimized dimensions of the proposed antenna element are listed in Table 3.5.

Table 3.5: Dimensions of cavity-backed patch antenna element.

Parameter	$R_{C1}$	$R_{P1}$	$L_{S1}$	$W_{S1}$	$W_{SIW}$	$R_I$
Value (mm)	1.25	0.54	2.3	0.32	2.25	0.15
Parameter	$R_2$	$L_1$	$L_2$	$L_{a1}$	$W_{a1}$	$P_I$
Value (mm)	0.12	0.6	0.46	4.4	4.4	0.54

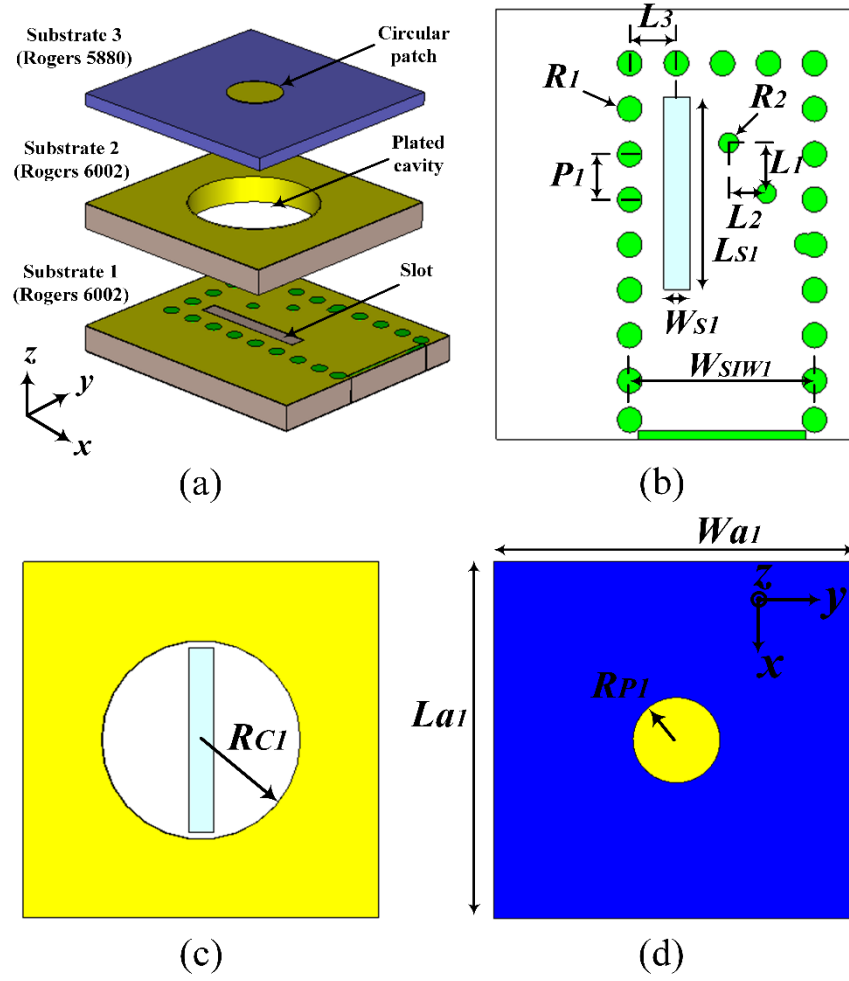


Figure 3.30: Geometry of cavity-backed patch antenna element. (a) 3-D view. (b) Substrate 1. (c) Substrate 2. (d) Substrate 3.

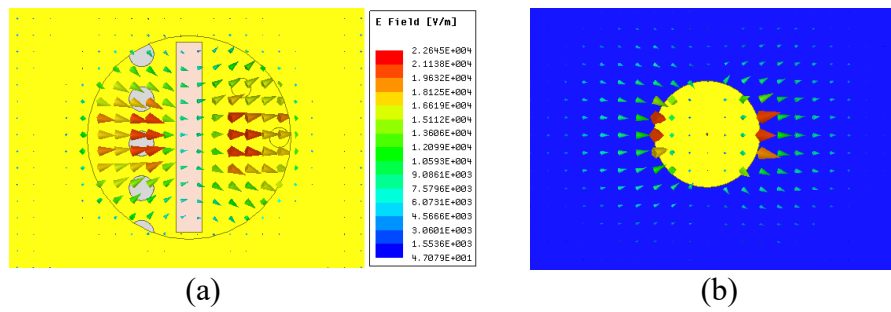


Figure 3.31: Electric field distribution of the proposed element. (a) At the cavity. (b) At the patch.

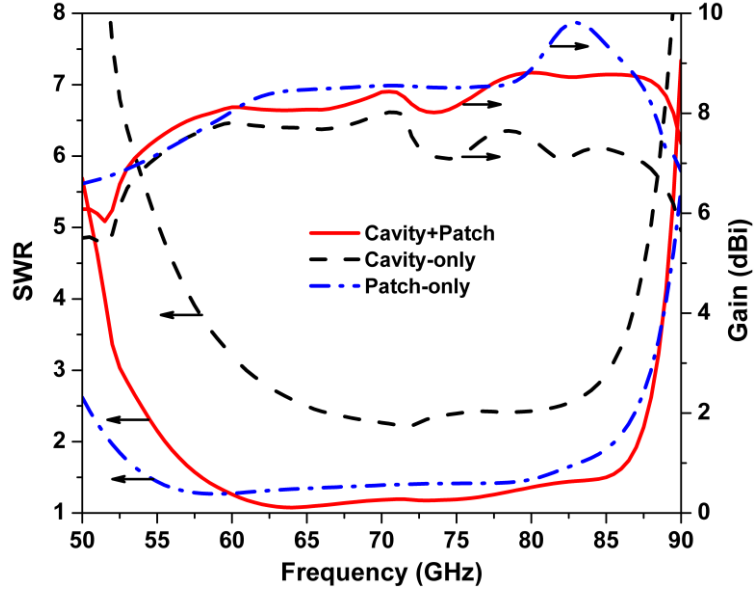


Figure 3.32: The effect of two modified antennas on SWR and gain referenced to the proposed antenna (cavity+ patch).

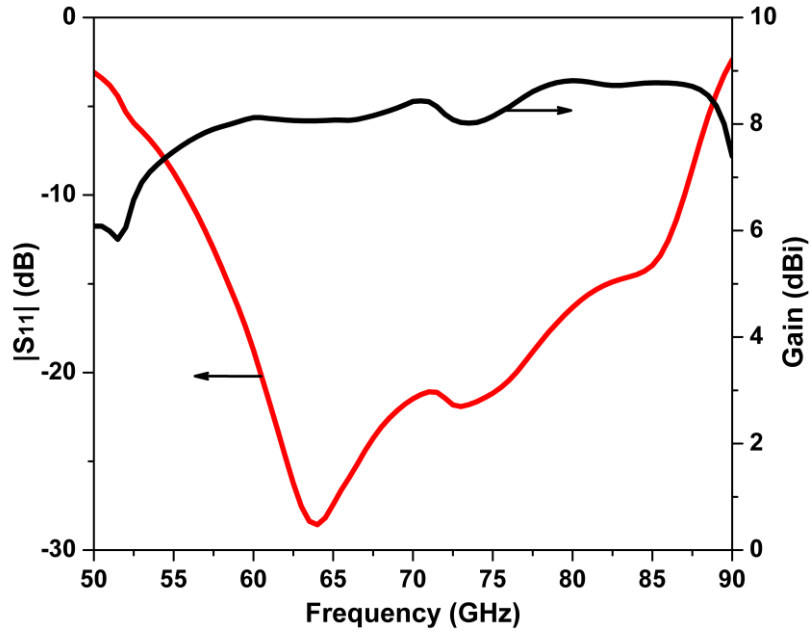


Figure 3.33: Simulated  $|S_{11}|$  and gain of the cavity-backed patch antenna element.

The SIW width ( $W_{siw} = 2.25 \text{ mm}$ ) is chosen so that the desired operating band is far enough from the cutoff frequency of  $TE_{10}$  mode. The fundamental mode  $TE_{10}$  of the SIW generates a transverse electric field across the longitudinal slot, which is coupled to the patch antenna through the circular cavity. At the cavity aperture, the E-field components in the x-axis direction are cancelled as they

are out of phase and the E-field component will only be in the y-axis direction shown in Figure 3.31 (a), which is coupled to the patch and generates the patch mode shown in Figure 3.31 (b). Moreover, two modified antennas, i.e., a cavity-only without patch and patch-only without a cavity, have been simulated to further understand the impact of each part on the antenna performance. For comparison, the gain and the standing-wave ratio (SWR) response of the proposed and the two modified antennas is shown in Figure 3.32. As can be seen, the cavity-only structure reduces the gain, which is especially noticeable at higher frequencies. In addition, the patch antenna plays a vital role for impedance matching as can be deduced from the impact of the cavity-only structure on SWR, where the structure is mismatched. On the other hand, the cavity has less effect on the SWR as indicated by the patch-only response. Moreover, the cavity has a high impact on the gain flatness, where the gain ranges from 7.1 dBi to 9.8 dBi, over the band of interest.

### 3.6.1.2 Antenna Element Performance

Figure 3.33 depicts the simulated  $|S_{11}|$  and radiation gain of the proposed antenna. As can be seen, the antenna exhibits a simulated impedance bandwidth of 44.2 % (55.5-87 GHz) for  $|S_{11}| < -10$  dB with an average gain of 8.2 dBi (7.6-8.8 dBi) over the entire band. Moreover, the proposed antenna achieves an overlapped 1-dB gain and impedance bandwidth of 43.4 % (56-87 GHz), which is much broader than what the literature reports. The radiation patterns of the E- and H-planes at different frequencies are shown in Figure 3.34. The antenna element shows an excellent symmetrical stable radiation pattern in both principal planes over the entire band. For the E- and H-planes, the cross-polarization ranges from -22 dB at 56 GHz to -33 dB at 86 GHz, whereas the front to back ratio (FBR) is -17 dB.

For comparison, the performance of the proposed and previously reported MMW antenna elements are summarized in Table 3.6. The proposed antenna shows the broader overlapped 1 dB gain and impedance bandwidth. Despite the large impedance bandwidth introduced by [65], the antenna element is implemented on LTCC with 10 layers, which increases the cost and complexity. Moreover, the considerable gain variation limits the impedance bandwidth usage. The design in [84] shows wide an impedance bandwidth with stable radiation gain, but the very high cross-polarization makes it unsuitable for most applications. The designs in [87] and [91] used metallic parts which usually need CNC machining process, leading to high cost.

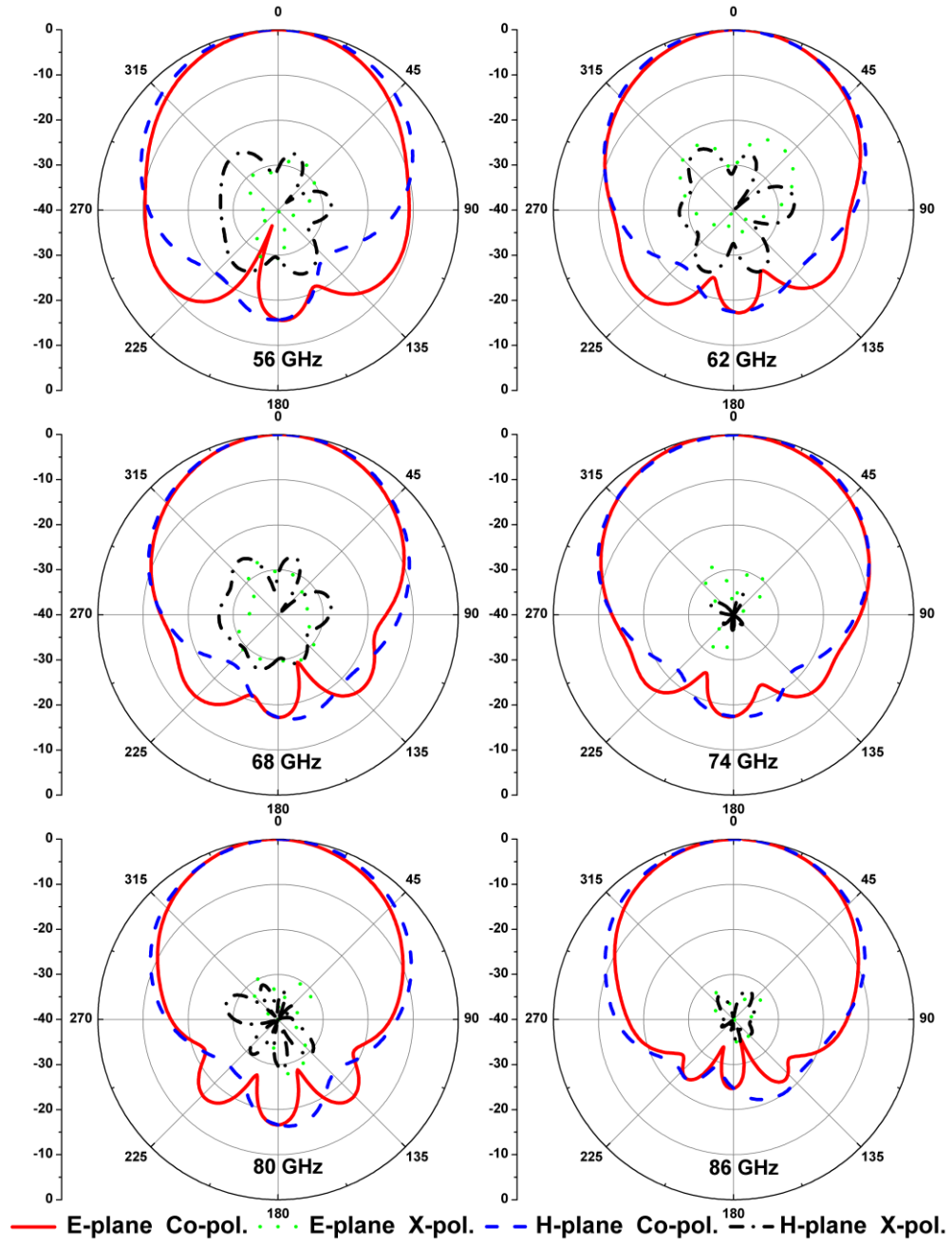


Figure 3.34: Simulated radiation patterns of the proposed antenna element at 56, 62, 68, 74, 80 and 86 GHz.

Table 3.6: Comparison between proposed cavity-backed and reported MMW antenna elements.

Ref.	Antenna Type	1-dB Gain B.W.	Gain (dBi)	X-pol. (dB)	FBW% (GHz)
[91]	Cavity-backed patch (4 layer PCB)	31.5%	7-8.5	-30	29.6 % (49.6-66.7)
[65]	L-probe patch (10 layers LTCC)	24%	0-7	NA	50.4 % (46-77 )
[90]	L-probe patch (1 layer PCB)	32%	4.4-7.6	-19	37 % (55-80)
[84]	E-shaped patch (1 layer PCB)	37%	7.4-8.2	-8	32 % (37.5-52)
[87]	Cavity-backed dipole (2 layer Hybrid)	23%	7.8-8.7	-35	19.6 % (35.3-43)
[79]	Cavity-backed dipole (2 layer PCB)	31.5 %	7.5-9.4	-19	38.7 % (50-74)
This work	Cavity-backed patch (3 layer PCB)	46 %	7.6-8.8	-22	44.2 % (55.5-87 )

### 3.6.2 Linear Antenna Array

Based on the antenna element designed in the previous subsection, a 1x8 array with a low side lobe level is introduced in this subsection. A wideband 8-way SIW power divider with amplitude tapering and an identical phase, which complies with Taylor distribution, is used to feed the proposed array. In addition, T- and Y-junction SIW power dividers with unequal power dividing ratios and identical phase are designed to implement the 8- way power divider. Finally, a wideband SIW-to-WR15 transition that facilitates the measurements is introduced in this subsection. All simulation results are carried out using an Ansoft HFSS simulator.

#### 3.6.2.1 Feed Network

In addition to the antenna element, a wideband feeding network is crucial for realizing an antenna array working over a wide frequency range. Moreover, the high losses caused by large size feeding networks reduce the gain and efficiency, especially for those designed with a microstrip line technique at MMW bands. Therefore, an SIW-based feeding network is an excellent candidate to achieve antenna array with high gain, high efficiency, wideband and compact size, at 60-GHz bands. The low side lobe level is another critical parameter for realizing robust automotive radar

systems. Usually, low SLL is achieved by amplitude tapering with equal phase, which is challenging to realize by using different path lengths in the feed network [51]. A more efficient approach for phase compensation is reported in [94]. In this work, an unequal 8-way SIW power divider with amplitude tapering is proposed, as shown in Figure 3.35.

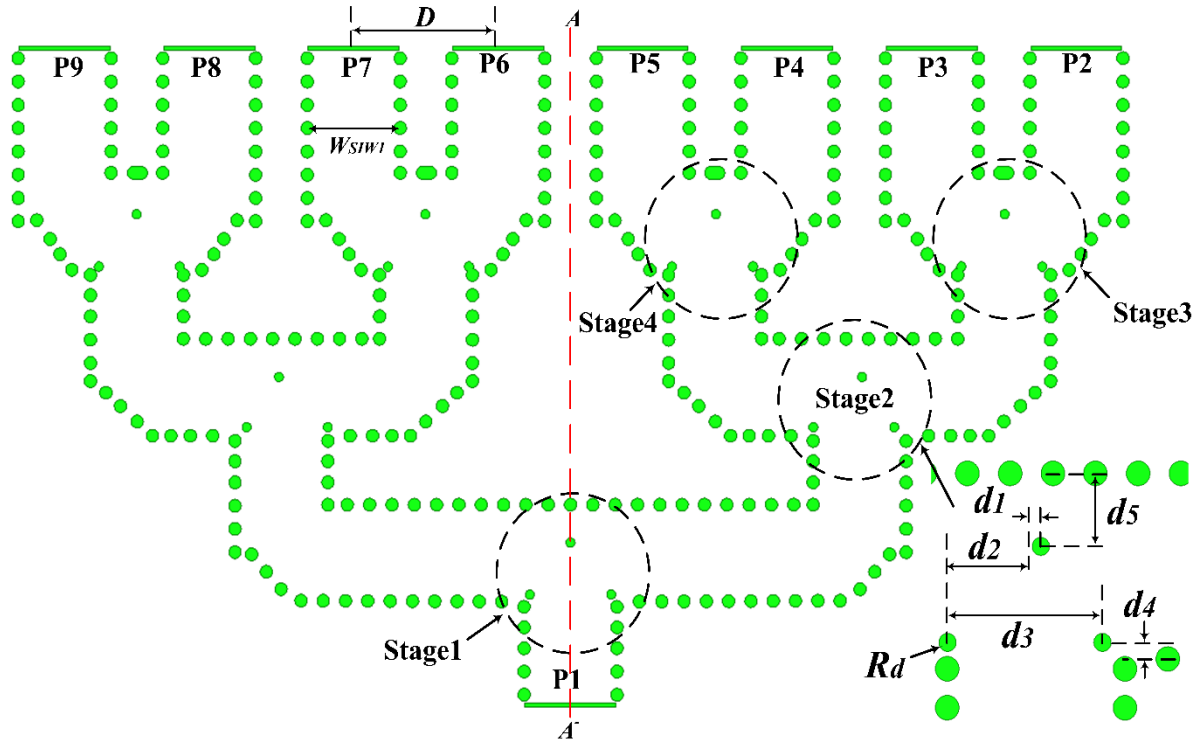


Figure 3.35: Layout of the unequal 8-way SIW power divider with Taylor distribution.

Table 3.7: Dimensions of power dividers of each stage [Units: mm].

Parameter	$d_1$	$d_2$	$d_3$	$d_4$	$d_5$	$R_d$
Stage1	0.0	0.985	1.97	0.163	0.88	0.11
Stage2	0.04	1.12	1.96	0.2	0.885	0.11
Stage3	0.009	1.037	1.96	0.075	0.69	0.11
Stage4	0.018	1.04	1.96	0.075	0.69	0.11

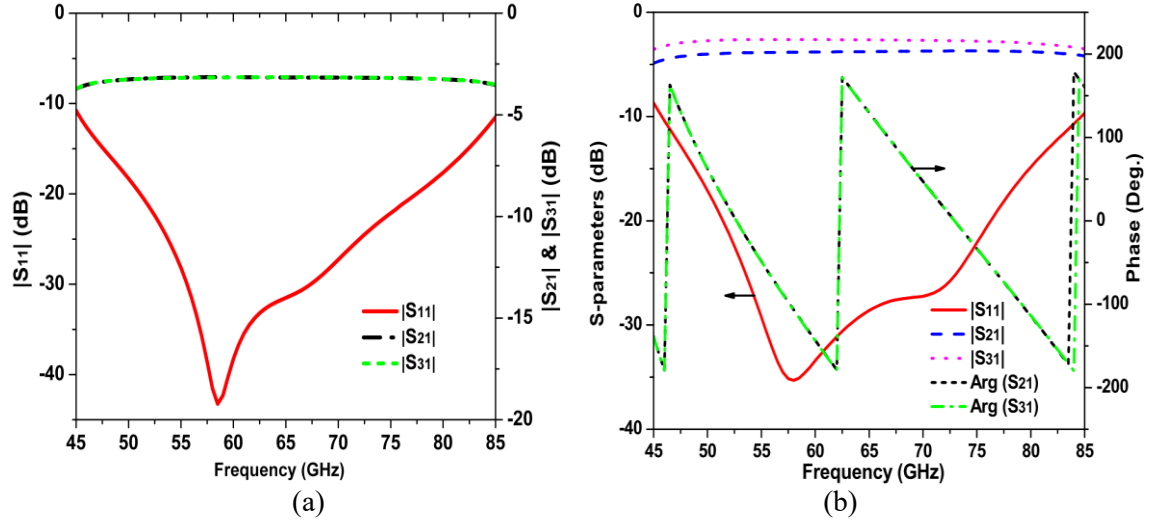


Figure 3.36: Simulated S-parameters. (a) Equal T-junction divider (stage 1). (b) Unequal Y-junction divider (stage3).

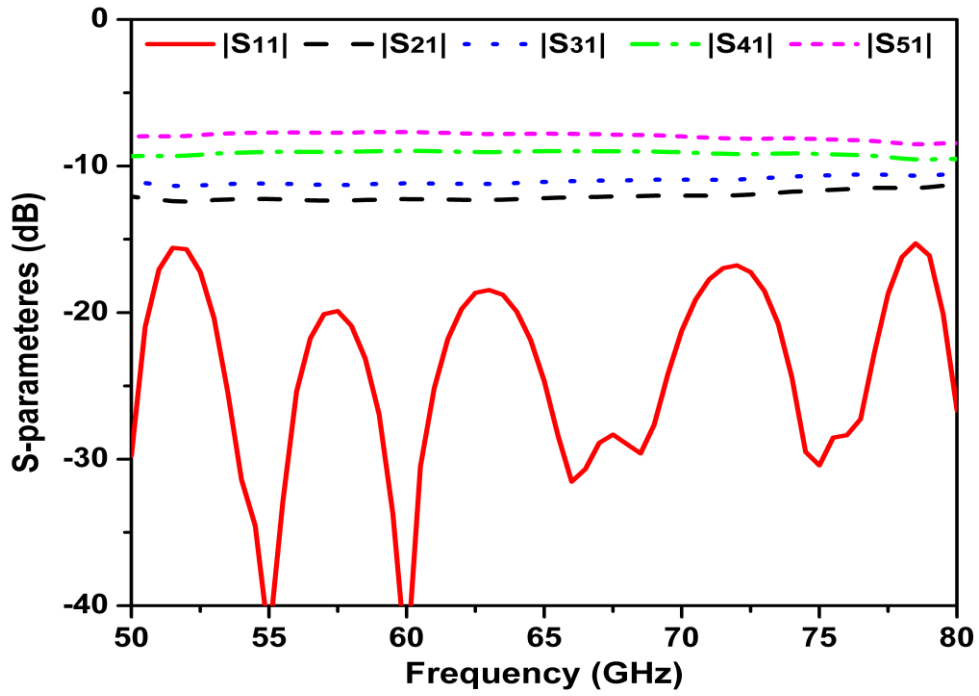


Figure 3.37: Simulated S-parameters of the proposed 8-way SIW feeding network with Taylor distribution.



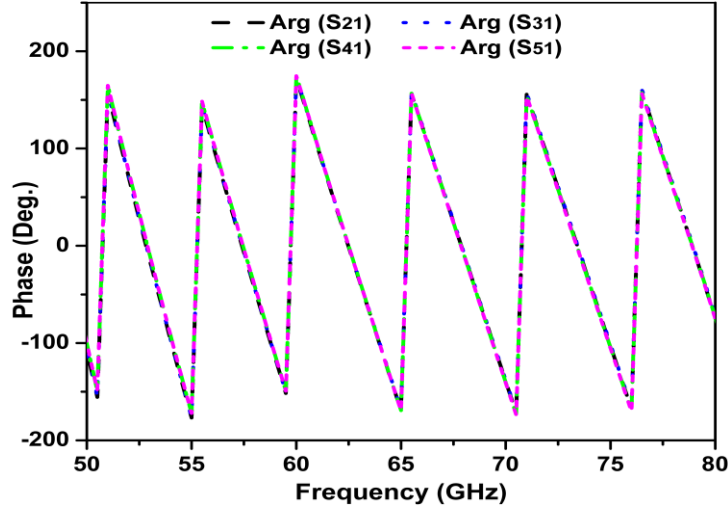


Figure 3.38: Simulated phase response of the 8-way SIW power divider with Taylor distribution.

It has a symmetrical shape around the central line AA<sup>-</sup>, and is composed of four stages: Stage 1 is an equal T-junction divider; Stage 2 is an unequal T-junction divider; Stage 3 and 4 are unequal Y-junction dividers. As shown in the zoomed-in area of Figure 3.35, for each stage, the central via is shifted to obtain the required power dividing ratio. Next, the group position of the three metallic vias is shifted for phase compensation; then each via position is slightly adjusted to improve the impedance matching. Detailed dimensions of each stage of the power divider are given in Table 3.7. Simulated S-parameters of the equal T-junction SIW power divider, which is used in stage 1, are illustrated in Figure 3.36 (a). The T-junction shows an impedance bandwidth of 53.8 % (47.5-82.5 GHz) for  $|S_{11}| < -15$  dB. Simulated S-parameters of the proposed unequal Y-junction SIW power divider, which is used in stage 3, are shown in Figure 3.36 (b). The Y-junction exhibits an impedance bandwidth of 48 % (49-80 GHz) for  $|S_{11}| < -15$  dB with zero phase shift over the entire band. The reflection coefficient of the unequal 8-way power divider is less than -15 dB within the frequency range of 50-80 GHz, as shown in Figure 3.37. Moreover, the required power-dividing ratios are successfully achieved, by applying -20 dB Taylor distribution, with zero phase shift over the band of interest. Figure 3.38 presents the phase response of the proposed unequal 8-way power divider, clearly showing that there is no phase shift between output ports within the whole band. Table 3.8 lists the 8-way Taylor weight ratio, which adopts -20 dB Taylor distribution, and the theoretical and simulated output values of each port for the power divider network. The simulated results are in good agreement with those of the Taylor distribution. Furthermore, the insertion loss

is 0.64 dB, indicating that the proposed SIW feed network is ideal for realizing a large size antenna array.

Table 3.8: Taylor weights distribution and S-parameters.

Port No.	Taylor weight (-20 dB SLLs)	Theoretical S-param. (dB)	Simulated S-param. (dB)
2,9	0.6013	-11.54	-12.19
3,8	0.6694	-10.61	-11.08
4,7	0.8765	-8.27	-8.98
5,6	1.0000	-7.12	-7.79

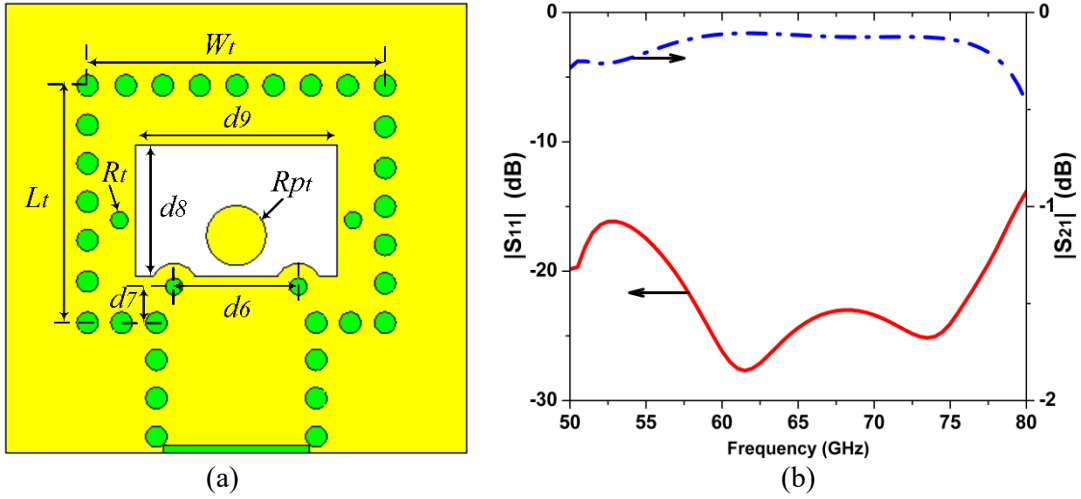


Figure 3.39: (a) Geometry of the SIW-to-WR-15 transition (top view). (b) Simulated S-parameters.

### 3.6.2.2 SIW-to-WR15 Transition

A broadband one-layered SIW-to-WR-15 transition is introduced, as shown in Figure 3.39 (a). It is a modified version of the transition in section 3.5 with dimensions in mm:  $L_t=3.3$ ,  $W_t=4.2$ ,  $R_{pt}=0.42$ ,  $R_t=0.12$ ,  $d_6=1.75$ ,  $d_7=0.5$ ,  $d_8=2.8$ ,  $d_9=2.8$ . As shown in Figure 3.39 (b), the proposed transition exhibits an impedance bandwidth of 45.4 % (50-79.4) for  $|S_{11}| < -15$  dB with an insertion loss of less than 0.2 dB over the band of interest. A wideband transition with a good matching performance is essential to implement the array, as it has a significant effect on the impedance matching bandwidth of the array.

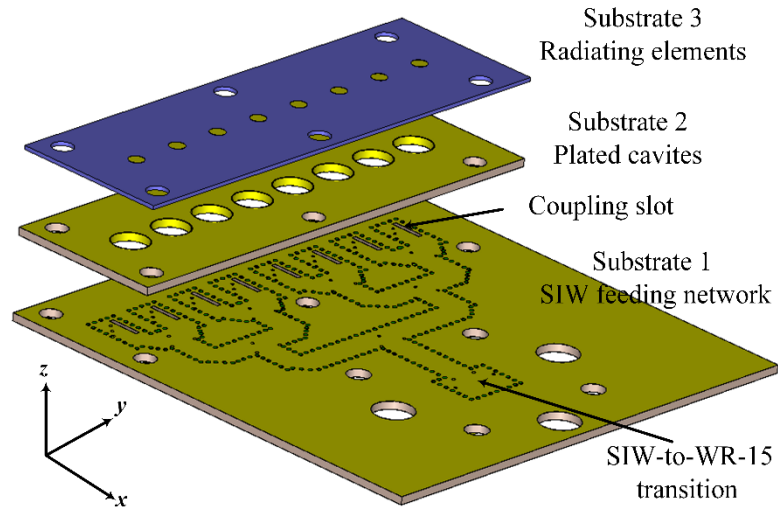
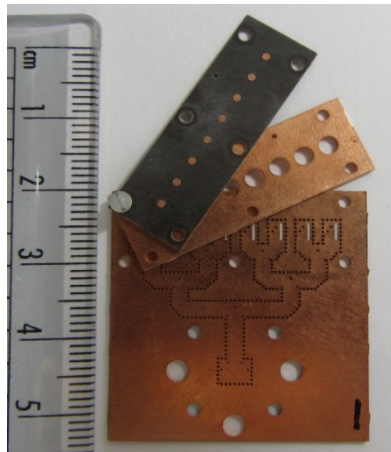
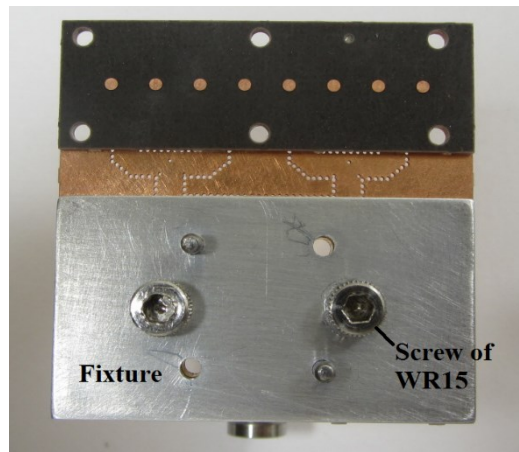


Figure 3.40: Geometry of the proposed 1x8 cavity-backed patch array.



(a)



(b)



(c)

Figure 3.41: Photo of the fabricated prototype for the proposed 1x8 cavity-backed patch array. (a) Disassembled. (b) Assembled. (c) Radiation test.

### 3.6.2.3 1x8 Array

Based on the proposed antenna element, feeding network and SIW-to-WR15 transition, a 1x8 cavity-backed patch array is designed, as depicted in Figure 3.40. The array is designed on three layers identical to those of the antenna element. The inter-element spacing is set to  $D=3.5$  mm ( $0.76 \lambda_0@65$  GHz), to avoid grating lobes.

### 3.6.2.4 Measurement and Discussion

A photograph of the fabricated prototype array is shown in Figure 3.41. Each layer is fabricated separately using a low-cost standard PCB process; the layers are then joined together using an adhesive and pressure to avoid air gaps between the different layers. The S- parameters are measured using an Agilent N5227A vector network analyzer (VNA) at lower frequencies (50-67 GHz), while they are measured using Keysight N5247B VNA at higher frequencies. The simulated and measured results of the  $|S_{11}|$  and radiation gain of the 1x8 cavity-array are shown in Figure 3.42. It can be seen that the simulated and measured impedance bandwidth for  $|S_{11}| < -10$  dB is 37.6 % (54.7 -80 GHz) and 37.7% (54.5-79.8 GHz), respectively. The array entirely covers the unlicensed band (57-71 GHz) and most of the automotive radar bands (71-76 GHz and 76-81 GHz). The gain is measured, inside an anechoic chamber, by using a standard gain horn antenna as a reference. From Figure 3.42, the simulated gain is  $16.6 \pm 0.7$  dBi over the whole band with a maximum value of 17.3 dBi at 75 GHz. Moreover, the simulated results show a 1-dB gain bandwidth of 38.9 % (56-83 GHz). The measured average gain is 16.4 dBi, which is a bit lower than the simulated one. The simulated and measured radiation pattern of the proposed 1x8 cavity-backed patch array, based on the excitation of 20-dB SLL Taylor distribution, for different frequencies, is demonstrated in Figure 3.43. The measured radiation parameters of the E-plane (yoz-plane) and H-plane (xoz-plane) are summarized in Table 3.9. The targeted -20-dB SLL is obviously achieved for frequencies below 74 GHz. At higher frequencies, the SLL is higher to some extent, which is reasonable, as tapering amplitudes differ slightly from the theoretical values of Taylor distribution. Moreover, as the frequency increases, the inter-element spacing, in terms of electrical length, increases accordingly, resulting in higher grating lobes. The cross-polarization levels of both principal planes are less than -22 dB, over the band of interest. The E-plane half-power beam width (HPBW) gradually decreases from  $10.5^\circ$  at 56 GHz to  $8^\circ$  at 79 GHz. As for the H-plane, the HPBW gradually increases from  $78^\circ$  at 56 GHz to  $82^\circ$  at 79 GHz. The simulated

radiation efficiency of the 1x8 cavity-backed patch array is about 87 %. The measured and simulated results are in good agreement.

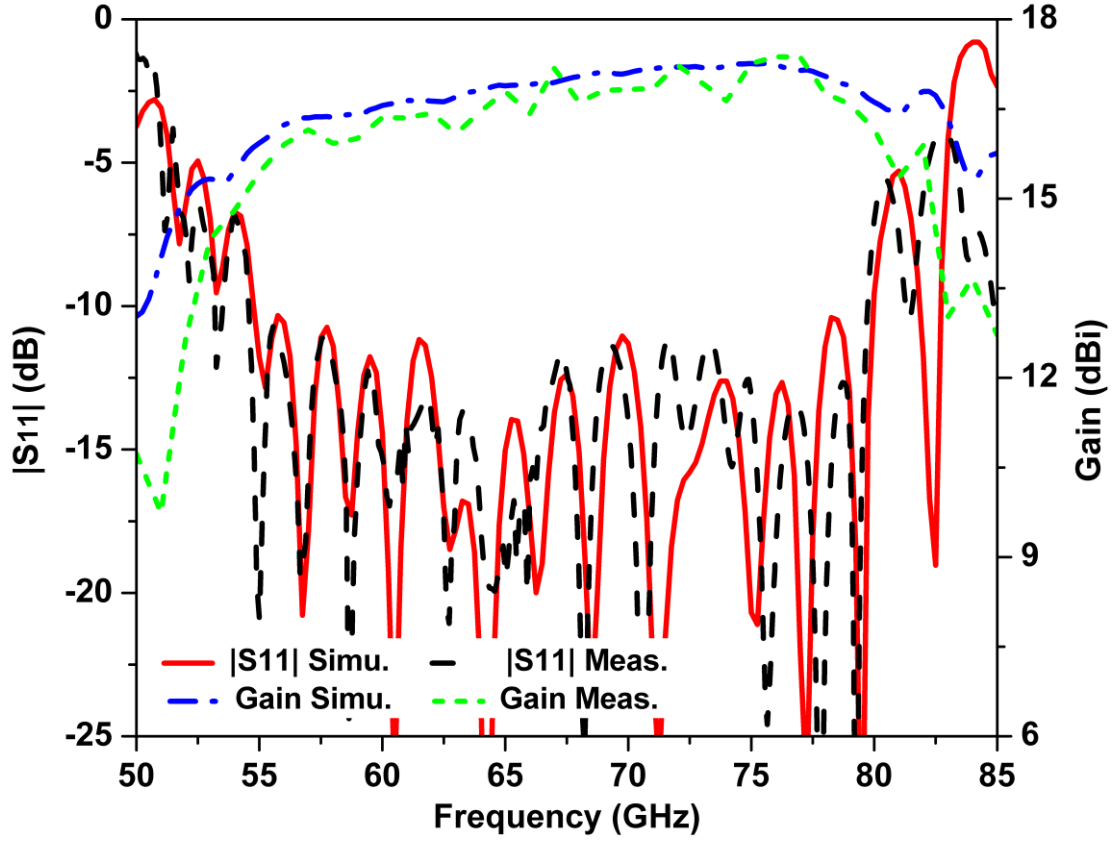


Figure 3.42: Simulated and measured  $|S_{11}|$  and gain of the 1x8 cavity-backed patch array.

Table 3.9: Measured radiation characteristics of the 1x8 cavity-backed patch array

Freq. (GHz)	E-plane ( $yoz$ -plane)			H-plane ( $xoz$ -plane)		
	HPBW	X-pol (dB)	SLL (dB)	HPBW	X-pol (dB)	SLL (dB)
56	10.6 <sup>0</sup>	-25	-21.5	77 <sup>0</sup>	-25	-
62	10 <sup>0</sup>	-25	-20	79 <sup>0</sup>	-24	-
68	9 <sup>0</sup>	-24	-19	80 <sup>0</sup>	-24	-
74	8 <sup>0</sup>	-23	-17	82 <sup>0</sup>	-23	-
79	8 <sup>0</sup>	-22	-14	82 <sup>0</sup>	-22	-

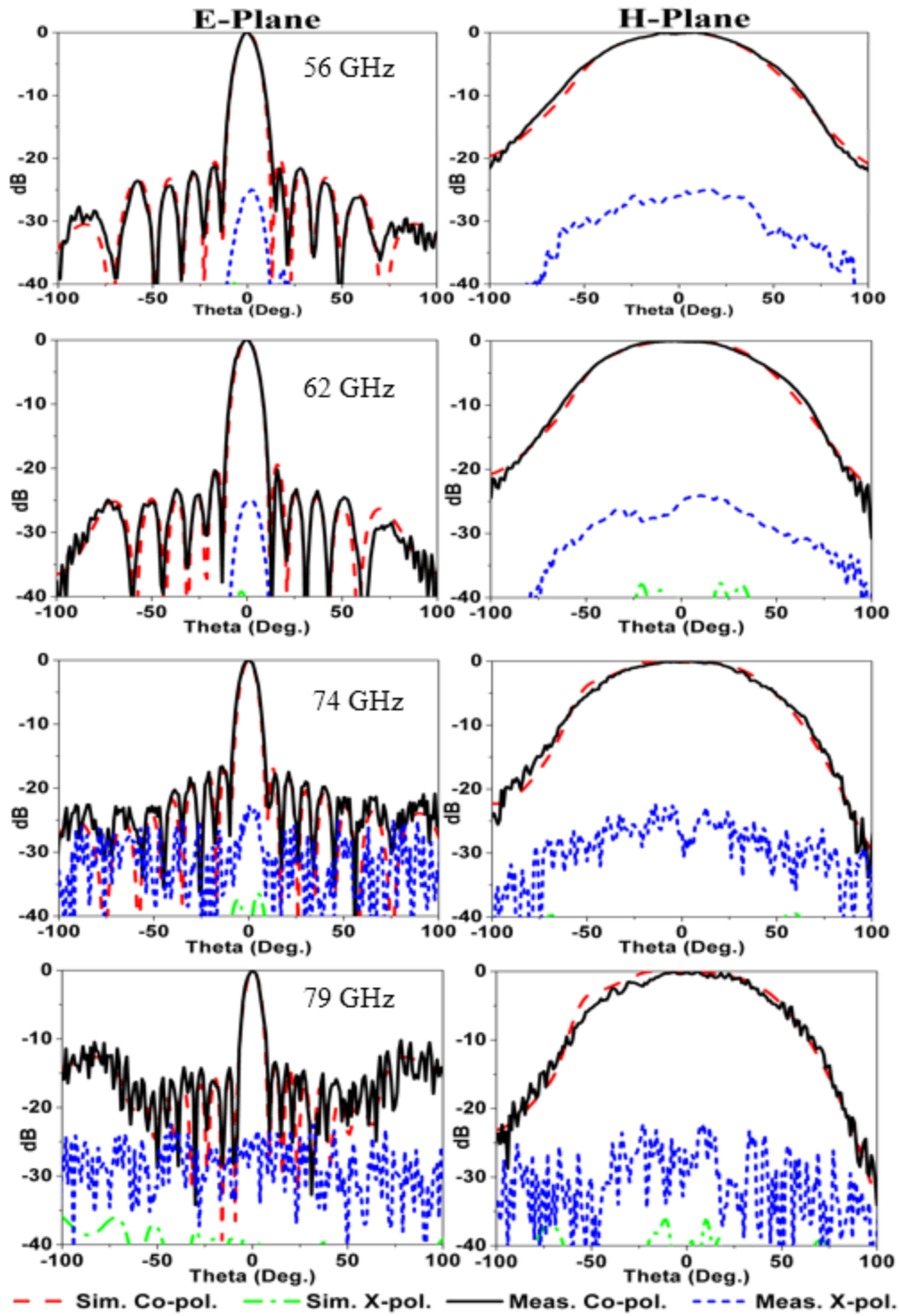


Figure 3.43: Simulated and measured radiation patterns of the 1x8 cavity-backed patch array at 56, 62, 74 and 79 GHz.

### 3.6.3 Planar Antenna Arrays

#### 3.6.3.1 2x2 Subarray

As shown in Figure 3.44, a 2x2 subarray is designed based on the proposed antenna element. It comprises four layers, which are arranged from substrate 1 at the bottom to substrate four at the top. Substrates 1 to 3 are 0.508 mm-thick Rogers 6002, and substrate 4 is Rogers 5880 with a thickness of 0.254 mm. The SIW feeding network is embedded in substrate 1. A 4-way power divider is designed in substrate 2 to couple the energy with equal amplitude and phase to four air-

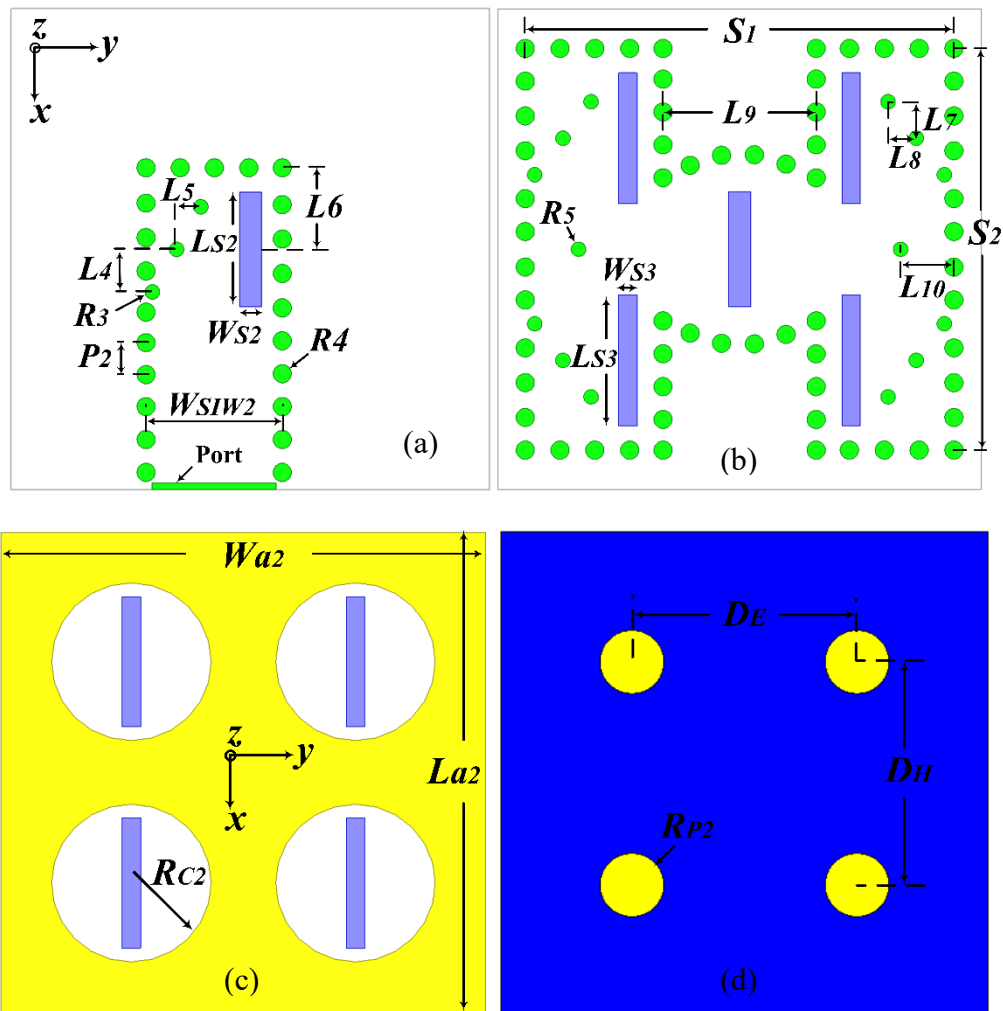


Figure 3.44: Top view of each layer of the 2x2-element cavity-backed patch subarray with detailed design parameters. (a) Substrate 1. (b) Substrate 2. (c) Substrate 3. (d) Substrate 4.

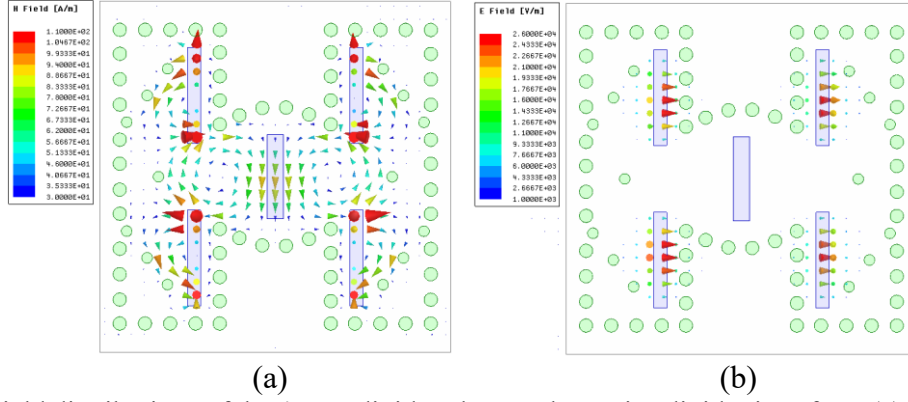


Figure 3.45: Field distributions of the 4-way divider close to the cavity-divider interface. (a) Magnetic field. (b) Electric field.

Table 3.10: Dimensions of the 2x2 cavity-backed subarray

Parameter	Value (mm)	Parameter	Value (mm)	Parameter	Value (mm)
$R_3$	0.12	$R_5$	0.12	$S_2$	6.6
$R_4$	0.15	$W_{S3}$	0.3	$R_{C2}$	2.6
$P_2$	0.54	$L_{S3}$	2.15	$W_{a2}$	7.9
$W_{S2}$	0.37	$L_7$	0.6	$L_{a2}$	7.9
$L_{S2}$	1.88	$L_8$	0.46	$R_{P2}$	0.54
$L_4$	0.7	$L_9$	2.5	$D_E$	3.65
$L_5$	0.4	$L_{10}$	0.87	$D_H$	3.65
$L_6$	1.34	$S_1$	7	$D_{SIW2}$	2.25

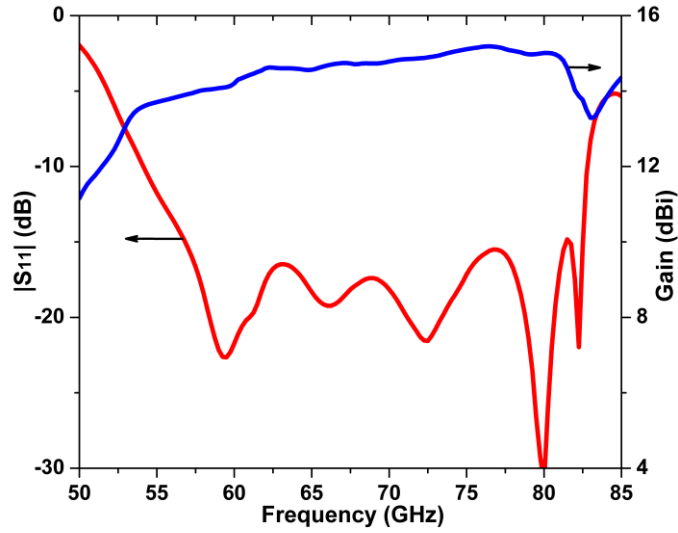


Figure 3.46: Simulated  $|S_{11}|$  and gain of the 2x2-element cavity-backed patch subarray.



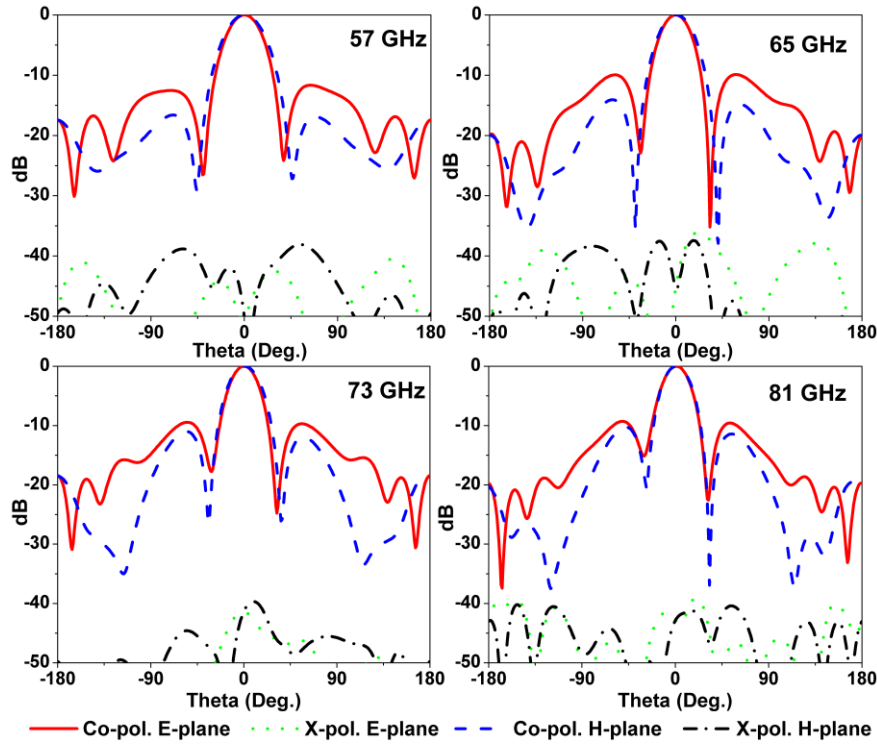


Figure 3.47: Simulated radiation patterns of the 2x2-element cavity-backed patch subarray.

filled circular cavities formed in substrate 3. The excitation of these cavities with perfectly equal amplitude and phase is of crucial importance to the subarray performance; thus, the 4-way power divider should be accurately designed and optimized. The magnetic and electric field distributions, located close to the cavity-divider interface, are shown in Figure 3.45 (a). The magnetic field components along the y -axis are arranged in opposite directions, cancelling each other so that only the magnetic field in x-axis direction exists. Moreover, the uniform distribution of the electric field shown in Figure 3.45 (b) evidence that equal amplitude and phase are coupled to the cavities. The energy is transferred between different layers by employing the aperture-coupled technique, leading to fully isolated radiating elements and the feed network. The insertion loss of the power divider is 0.3 dB. Optimized dimensions of the 2x2 subarray are given in Table 3.10. The inter-element spacing  $DE$  and  $DH$  , which are restricted by the dimensions of the 4-way power divider, are adjusted to 3.65 mm to avoid grating lobes. Simulated results of the  $|S_{11}|$  and gain of the proposed 2x2-element cavity-backed aperture-coupled patch antenna are depicted in Figure 3.46. It is seen that the 2x2-element cavity-backed patch subarray achieves an impedance bandwidth of 42.3 % (53.9-82.8 GHz) for

$|S_{11}| < -10$  dB with a maximum gain of 15.2 dBi at 76.5 GHz. The simulated E- and H-plane radiation patterns of the subarray are presented in Figure 3.47, which shows symmetrical radiation patterns in both principal planes with cross-polarization levels less than -39 dB, over the entire band of interest. The SLLs is slightly high (-11 dB), as shown in Figure 3.47, which may be attribute to amplitude imbalance of the 4-way power divider and the mutual coupling between elements.

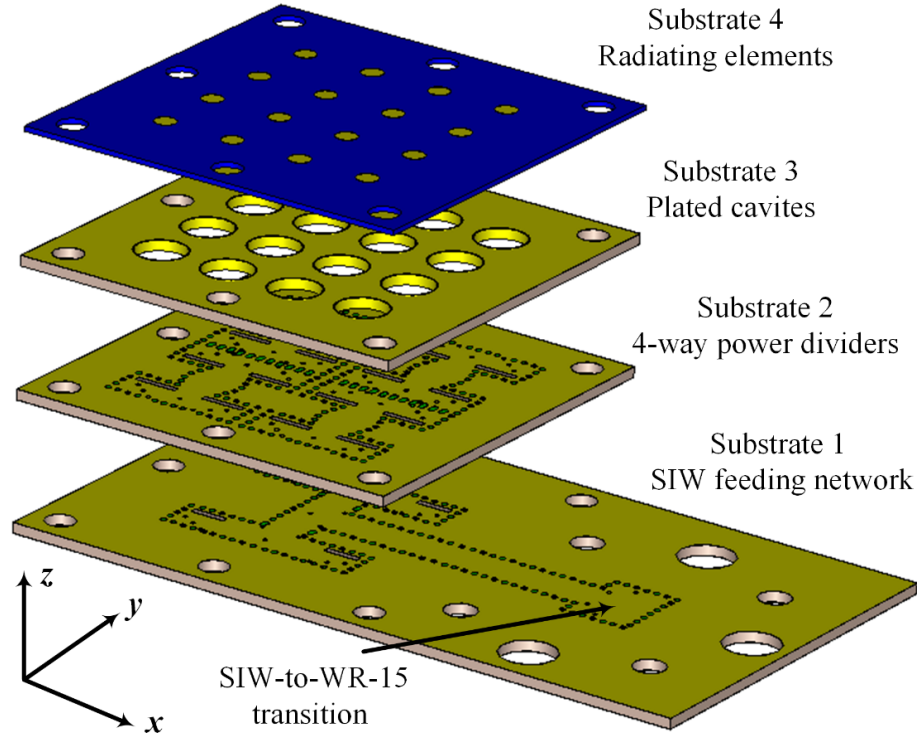


Figure 3.48: 3-D view of the proposed 4x4 cavity-backed patch array with full-corporate feeding network.

### 3.6.3.2 4x4 Antenna Array

In order to increase the antenna gain, a 4x4 antenna array with a full-corporate feeding network is designed, based on the 2x2 subarray proposed in the previous subsection, as shown in Figure 3.48. The H-junction power divider in substrate 1 is designed to operate over a wide frequency range. In addition, an SIW-to-WR15 transition is embedded in substrate 1 to facilitate the measurements.

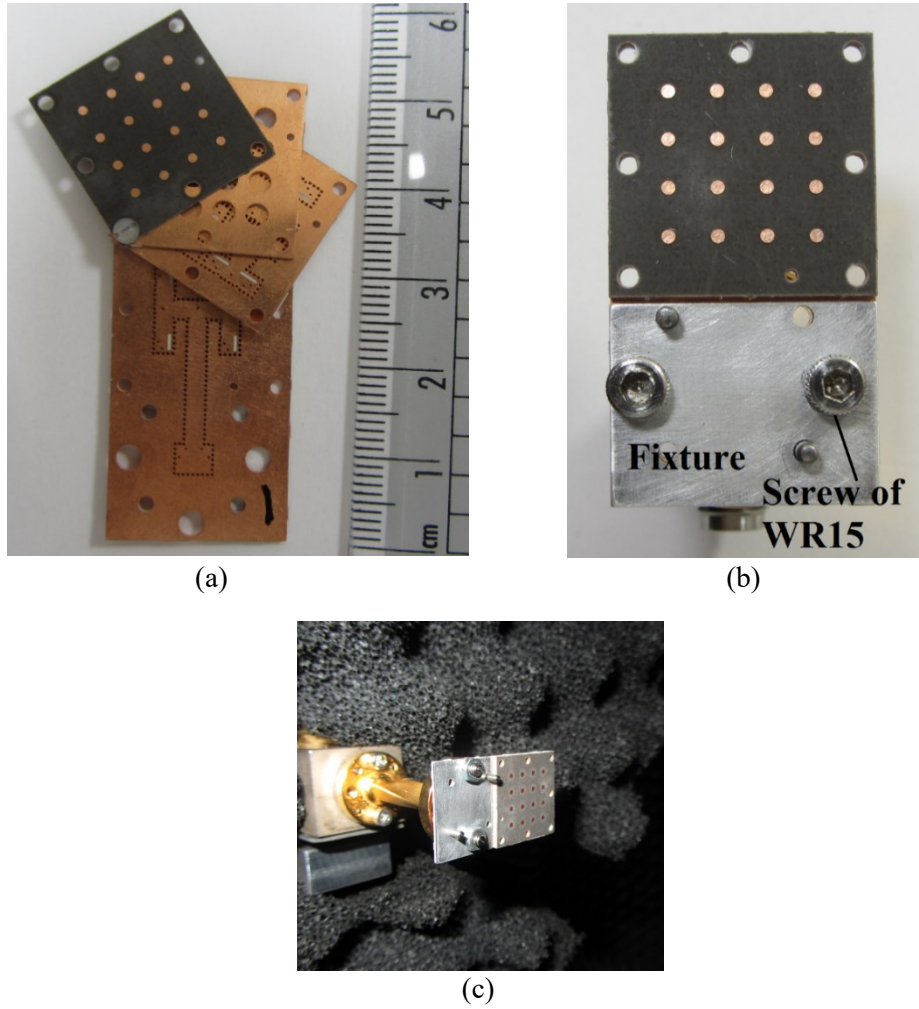


Figure 3.49: Photo of the fabricated prototype for the proposed 4x4 cavity-backed patch array. (a) Disassembled (b) Assembled. (c) Radiation test.

### 3.6.3.3 Experiments and Discussions

A prototype is fabricated and tested to validate the design, as shown in Figure 3.49. The simulated and measured prototype results of the  $|S_{11}|$  and gain are shown in Figure 3.50. The array is fabricated using a low-cost PCB process for each layer; the layers are then bonded together by a standard adhesive and pressure technique to avoid the air gaps between different layers. The proposed 4x4 array exhibits a simulated impedance bandwidth of 37.9 % (54-80.6 GHz) for  $|S_{11}| < -10$  dB, and a measured bandwidth of 38.4 % (55.2-81.4 GHz). As can be seen from Figure 3.50, the maximum simulated gain is 20.8 dBi at 79 GHz, whereas the maximum measured gain is 20.5

dBi at 64 GHz. The measured and simulated results are in good agreement. The aperture efficiency can be calculated by the following equation [140].

$$\varepsilon_{ap} = \frac{G\lambda_0^2}{4\pi A_p} \quad (3.7)$$

where  $G$  and  $A_p$  are the gain and physical aperture, respectively. With an aperture area of  $14.6 \times 14.6 \text{ mm}^2$ , the calculated aperture efficiency is 91.3 % at 65 GHz. The simulated and measured radiation patterns at different frequencies are demonstrated in Figure 3.51. Due to measuring equipment limitations inside the anechoic chamber, the radiation patterns are tested for the upper hemisphere ( $\pm 100^\circ$ ). The array shows stable broadside radiation patterns. The first SLL is less than -12 dB in both principal planes across the entire band. The measured cross-polarization is around -27 dB over the band of interest. The simulated radiation efficiency of the proposed 4x4 cavity-backed patch array is about 89 %. The measured cross-polarization is higher than the simulated one; its flat response with fluctuations at a higher frequency may be due to the limited dynamic range of the measurement setup and the high noise floor.

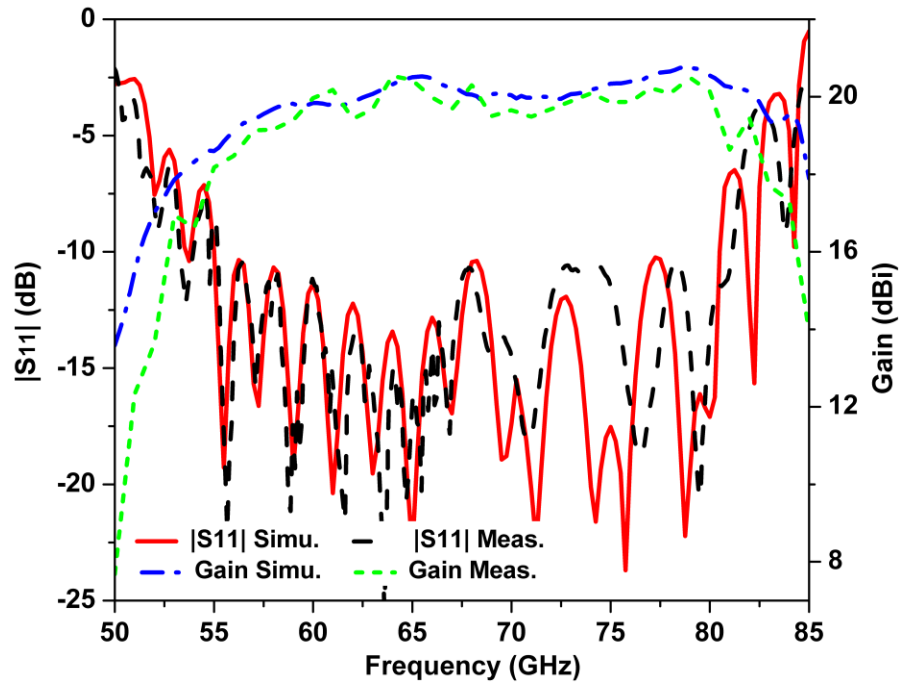


Figure 3.50: Simulated and measured  $|S_{11}|$  and gain of the 4x4 cavity-backed patch array.

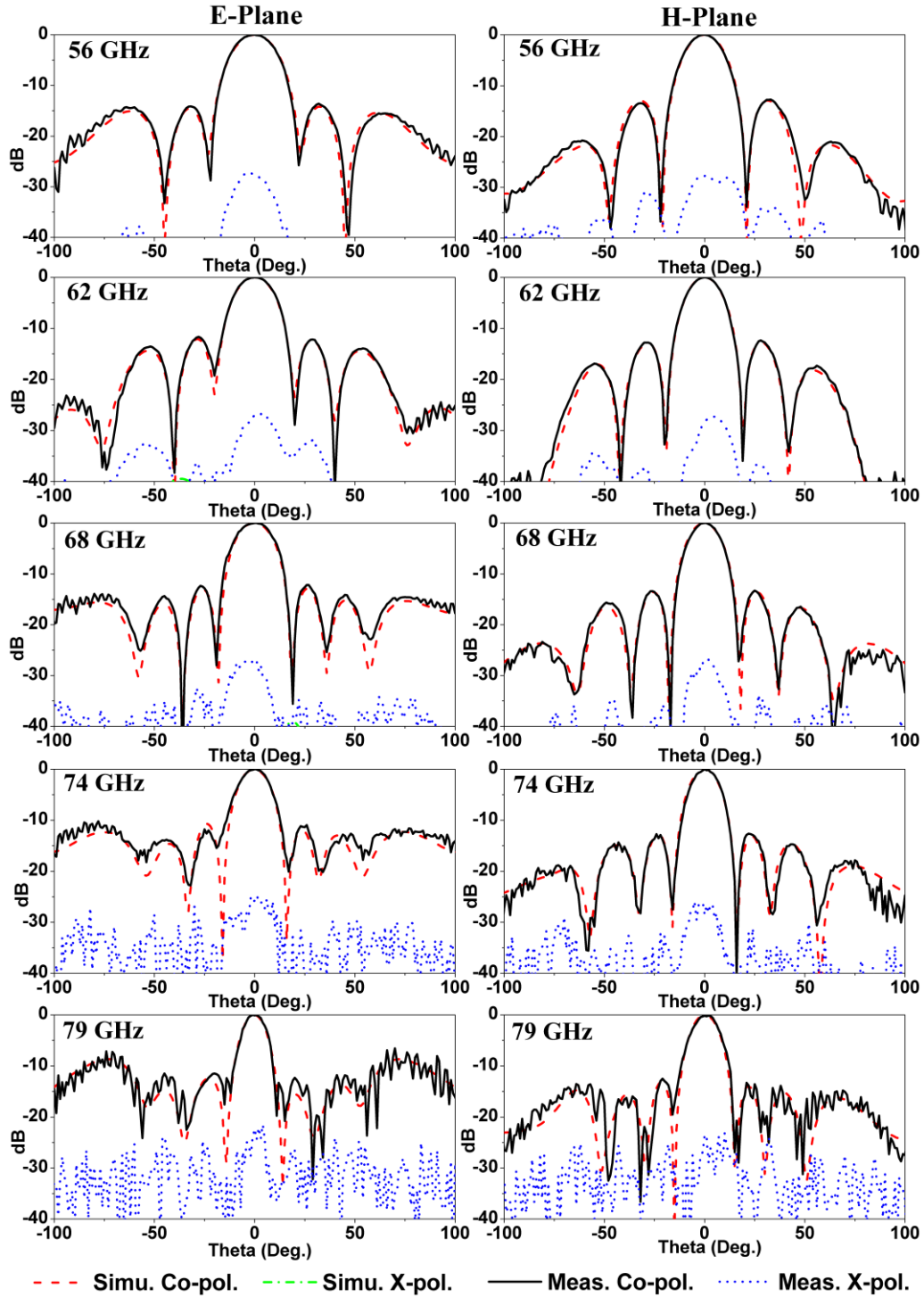


Figure 3.51: Simulated and measured radiation patterns of the 4x4 cavity-backed patch array at 56, 62, 68, 74 and 79 GHz.

The structural characteristics and performance of the proposed cavity-backed patch antenna arrays are compared with previously reported MMW arrays in Table 3.11. It is clear that both proposed arrays in this work have the broadest impedance and 3-dB gain bandwidth. Moreover, the 4x4 array has the highest aperture efficiency compared to all previously published work. Besides the compact size, the two proposed arrays also provide good radiation gain and efficiency. Although the array in [84] has a wide bandwidth and high efficiency, it suffers from limited 3-dB bandwidth and asymmetric radiation at the higher-end of the frequency band. Usually, designs with metallic parts [91], [81]-[82], [87] need a CNC machining process, which is expensive and unsuitable for mass production. Although the array design based on LTCC technology with 10 layers [65] exhibits wide bandwidth, it has a complex structure, low aperture efficiency and high cost

Table 3.11: Comparison between proposed and previously published MMW antenna arrays

Ref	Antenna Type	No. of Elem.	Size mm <sup>3</sup>	Im. BW	Gain BW (3-dB )	Peak Gain (dBi)	Aperture Efficiency
[72]	Cavity-backed patch (PCB)	4×4	NA	8.7%	41.2%	18.2	NA
[73]	Cavity-backed patch (PCB)	4×4	20×20 ×2.4	12%	12%	21.4	70.3%
[91]	Cavity-backed patch (PCB)	4×4	16.3×17.1 ×2.3	22.6%	18.8%	19.6	67.3%
[65]	L-probe patch (LTCC)	4×4	14.4×14.4 ×1	29%	18.3%	17.5	54%
[67]	E-shaped patch (PCB)	1×4	6×14.7 ×0.25	21.7%	22.2%	14.5	63.6%
[84]	E-shaped patch (PCB)	2×2	10.9×7.7 ×0.508	21.7%	22.2%	12.5	74.9%
[76]	Cavity-backed wide slot (PCB)	2×4	~ 14×5 ×0.6	11.6%	13.5%*	12.5	~50.5%
[81]	Cavity-backed slot (RGW)	16×16	70.4×64 ×12.2	11.6%	17.9% (1-dB)	>32.5	81.4%
[82]	slot (RGW)	8×8	33.6×33.6 ×9.7	17%	NA	27	88%
[83]	Cavity (LTCC)	8×8	31×31 ×1.9	17.1%	17.1%	23	41.3%
[85]	Slotted SIW (PCB)	12×12	~ 29×20 ×0.508	4.1%	4.3%*	22	~54%
[87]	Cavity-backed dipole (Hybrid)	8×8	~49.5×49.1 ×6	16.9%	23%*	27.3	86.1%
[79]	Cavity-backed dipole (PCB)	4×4	14.4×14.4 ×2.5	26.7%	26.4%	21.5	87.7%
<b>This work</b>	<b>Cavity-backed patch (PCB)</b>	<b>1×8</b>	<b>28×3.5 ×1.4</b>	<b>37.6%</b>	<b>49.5%</b>	<b>17.3</b>	<b>84.7%</b>
<b>This work</b>	<b>Cavity-backed patch (PCB)</b>	<b>4×4</b>	<b>14.6×14.6 ×1.9</b>	<b>37.9%</b>	<b>46.4%</b>	<b>20.8</b>	<b>91.3%</b>

## **Chapter 4 One-dimensional Scanning Array Antennas**

### **4.1 Introduction**

Broad bandwidth multi-beam antenna arrays fed by passive beamforming networks (BFNs) have the advantages of low-cost and low power dissipation, making them suitable for high data transfer rate over multipath fading channels. Passive BFNs based on SIW technology is more suitable than BFNs based on microstrip and coplanar waveguides at MMW bands, as they feature a low insertion loss and compact size. Butler matrix (BM) is well-known and widely being used as a beamforming network for switched-beam systems at MMW bands due to its simple structure and the ability to produce progressive phase shifts between output ports with low phase errors. In this chapter, two different designs of one-dimensional (1-D) switched multi-beam antenna arrays, which employ an SIW Butler matrix as a beamforming network, are investigated and prototyped for validation. The first design is a multibeam broadside SIW slotted antenna system fed by a compact dual-layered 4x4 Butler matrix. The second design is a wideband multibeam end-fire array, which in a Fermi tapered slot antenna is used as a radiating element and a single-layered 4x4 Butler matrix for BFN. In both designs, the simulated results were carried out using CST MWS simulator.

### **4.2 Multi-Beam Slot Antenna Array Fed by Dual-Layered 4x4 Butler Matrix**

In this section, a 60 GHz compact multi-beam slot antenna array based on a substrate integrated waveguide (SIW) is designed and fabricated. The beam forming network (BFN) is implemented using a dual-layer 4x4 Butler matrix, where the  $45^\circ$  and  $0^\circ$  phase shifters are designed on a separate layer, resulting in a significant size reduction. The proposed phase shifters are realized by taking the phase introduced by the crossover as a reference, leading to high flexibility to attain the required phase shifts using the Butler matrix.



#### 4.2.1 Single Element Design and Characterization

Due to its low profile and low cross polarization, the SIW longitude slot antenna has become widely used for multibeam array antenna applications. In this work, the SIW slot antenna has been adopted as a radiating element. The SIW slot antenna is designed based on the work reported in [138], [141] and then the CST simulator is used to optimize the design for good matching and radiation characteristics. Figure 4.1 shows the schematic view of a brunch (1x4 element subarray) SIW slot antenna with detailed dimensions of one slot. The slot length and width are  $L_s = 1.77mm$  and  $W_s = 0.19mm$ , respectively. The distance from the short-ended SIW to the slot center  $E_s = 1.17mm$ , whereas the offset from the center  $offset = 0.12mm$ . The inter-element spacing  $C_s = 2.0mm$ , which is almost equal to a half of the guided wavelength at 60 GHz.

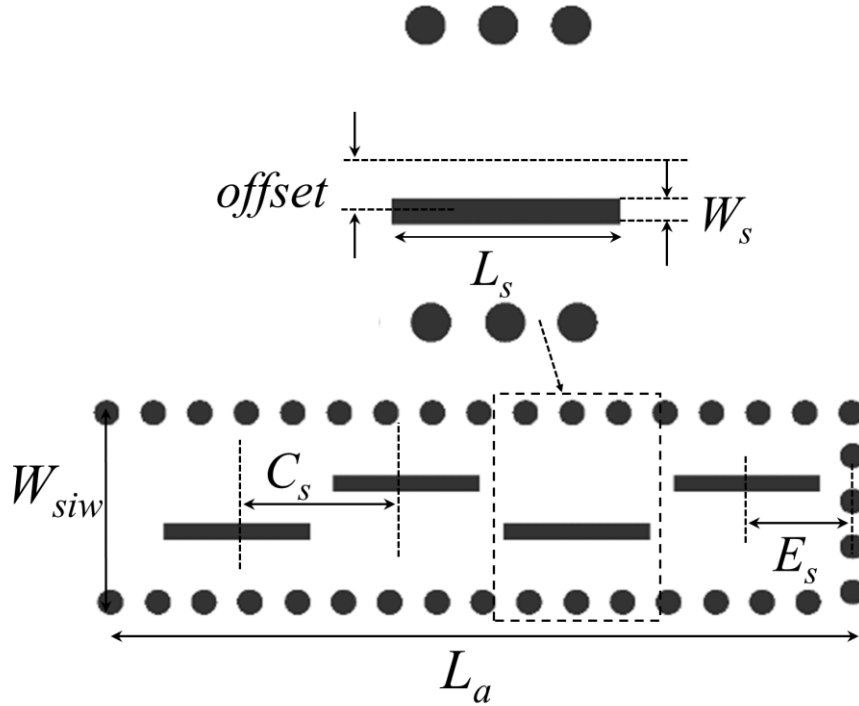


Figure 4.1: Schematic of branch SIW slot antenna with details of one slot parameters. ( $W_{siw} = 2.25mm$ ,  $L_a = 8.8mm$ ).

The simulated reflection coefficient is presented in Figure 4.2. Figure 4.3 shows the simulated E- and H-plane radiation patterns of the one branch SIW slot antenna at 60 GHz. The slot array exhibits side lobe levels of less than -22 dB for both principal planes.

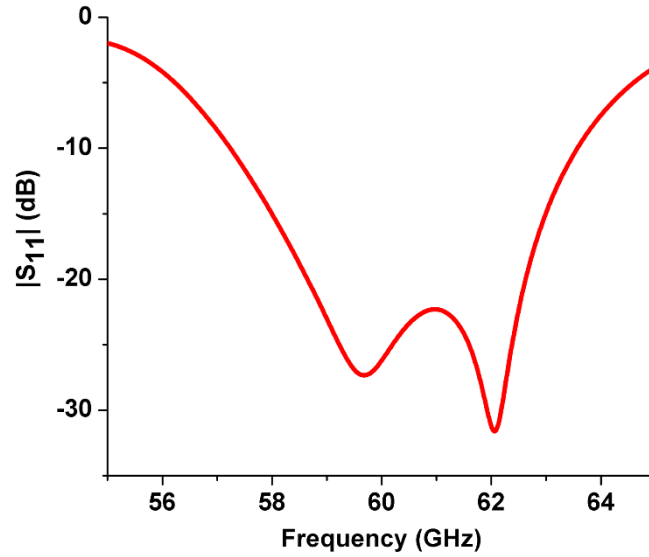


Figure 4.2: Simulated  $|S_{11}|$  of a single branch slot array.

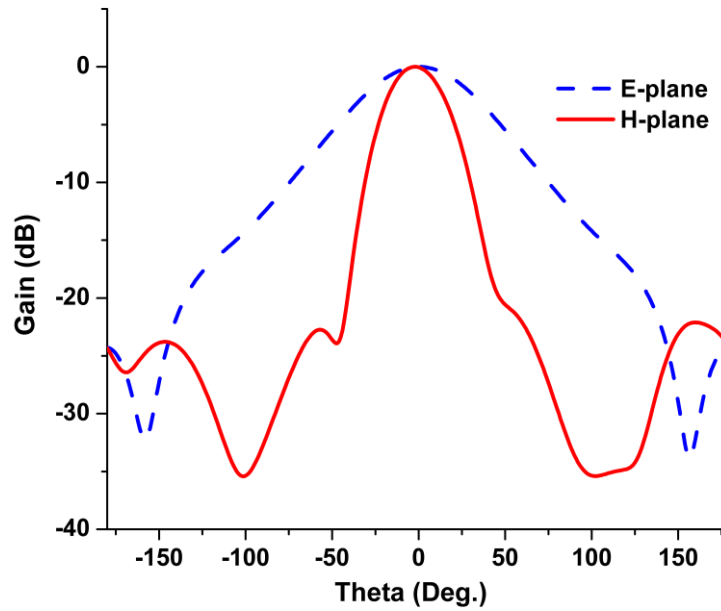


Figure 4.3: Simulated E- and H-plane radiation patterns of a single branch slot array at 60 GHz.

### 4.2.2 Beamforming Network Design

A conventional 4x4 Butler matrix is usually configured by cascading 3dB/90° directional couplers, phase shifters, and crossovers, as shown in Figure 4.4. For a Butler matrix with  $N$  input ports connected to an  $N$ -element array, the successive output phase ( $\phi$ ) can be theoretically calculated from equation (4.1), and the results for  $N = 4$  are listed in Table 4.1.

$$\phi = (2m - 1)\pi/N, \quad m \in [1 - N/2, N/2] \quad (4.1)$$

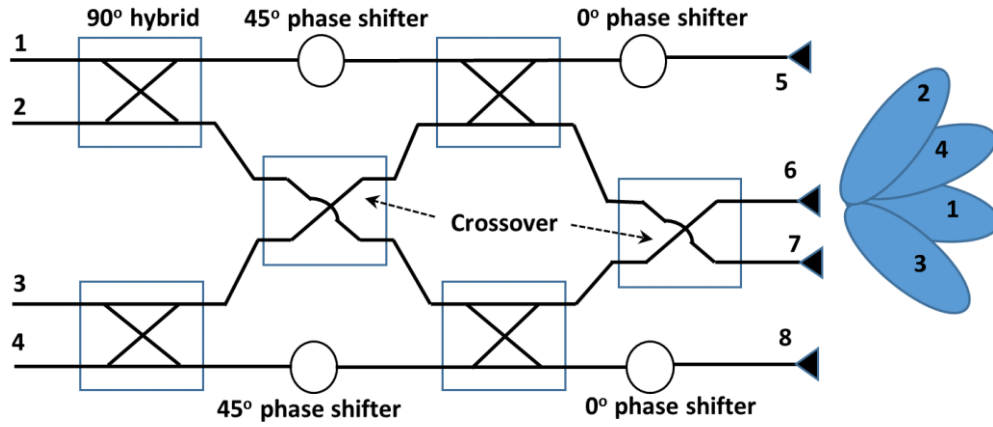


Figure 4.4: Block diagram of a 4x4 Butler matrix.

Table 4.1: Ideal output phase difference of BM with different input port excitation

Feeding port	Port1	Port1	Port1	Port1
Output phase difference ( $\phi$ )	$-45^\circ$	$+135^\circ$	$-135^\circ$	$+45^\circ$

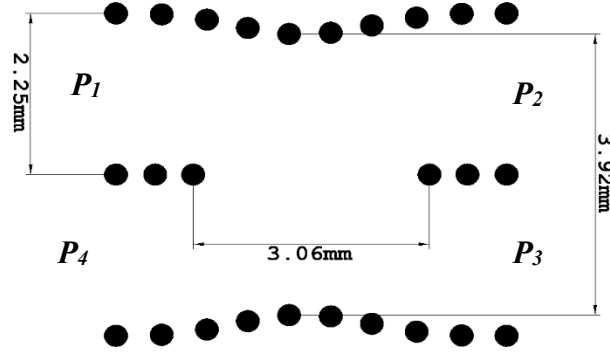


Figure 4.5: Geometry and detailed dimensions of the  $90^\circ$  hybrid coupler.

#### 4.2.2.1 3 dB / $90^\circ$ Hybrid Coupler

The layout of the SIW  $90^\circ$  hybrid coupler with the optimized dimensions by the CST simulator is illustrated in Figure 4.5. The coupler is designed on 0.254-mm-thick Rogers RT/Duroid 6002 substrate with a copper cladding of  $0.18 \mu m$ . The typical values of permittivity and loss tangent given by the manufacturer at 10 GHz are 2.94 and 0.0012, respectively. Periodic metallic vias with diameter  $S = 0.3 \text{ mm}$  and pitch  $P = 0.54 \text{ mm}$  are used to form the short-slot coupler. Based on an even- and odd-mode analysis [12] and the analysis in [142], the width ( $W_h$ ) and length ( $L_h$ ) of the coupling region is given by equation (4.2) and (4.3), respectively.

$$W_h = \frac{\pi}{k} \sqrt{\frac{4(3n+1)(n+1)}{4n+1}} \quad (4.2)$$

$$L_h = \frac{\pi}{k} \sqrt{\frac{(3n+1)(n+1)}{3}} \quad (4.3)$$

The phase difference between the  $TE_{10}$  and  $TE_{20}$  modes is represented by (4.4)

$$\Delta\phi = (\beta_e - \beta_o)l \quad (4.4)$$

where  $\beta_e$  and  $\beta_o$  are the phase constants of the  $TE_{10}$  and  $TE_{20}$  modes, respectively, and  $k$  is the wavenumber. Theoretically, the ideal magnitude of the transmission coefficients  $S_{21}$  and  $S_{31}$  is 3 dB, with a differential phase of  $90^\circ$ . The calculated results of the coupling region width ( $W_h$ ) and

length ( $L_h$ ) at 60 GHz for  $n = 1, 2$  and  $3$  are listed in Table 4.2. At 60 GHz, the SIW width of the  $TE_{10}$ ,  $TE_{20}$  and  $TE_{30}$  is approximately 1.46, 2.92 and 4.37mm, respectively. Therefore,  $n = 1$  is adopted to prevent the  $TE_{30}$  mode from propagating. By optimizing the calculated dimensions of the coupling region, one can obtain the desired power ratio (3dB) and phase difference ( $90^\circ$ ) between the output ports. The simulated magnitude and phase of  $S$ -parameters of the SIW hybrid over the frequency range from 54 to 66 GHz are shown in Figure 4.6 (a) and (b), respectively. It can be observed that the transmission coefficients are  $-3.07 \pm 0.15$  dB, while the reflection and isolation coefficients are less than  $-20$  dB. The simulated phase difference between outputs ports is  $90^\circ \pm 0.8^\circ$  over the band of interest.

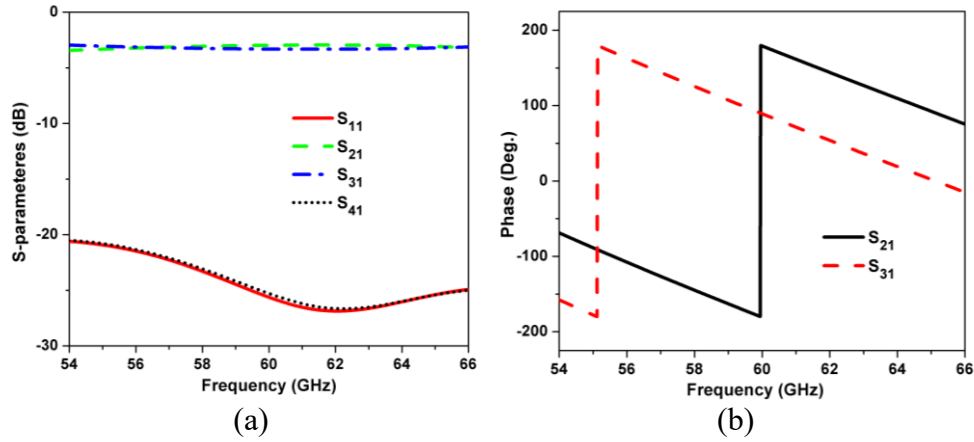


Figure 4.6: Simulated S-parameters of the 3 dB coupler. (a) Magnitude. (b) Phase.

Table 4.2: Calculated dimensions of the coupling region of the  $90^\circ$  hybrid.

$n$	1	2	3
$W_h (mm)$	3.68	4.45	5.1
$L_h (mm)$	3.38	3.85	5.3

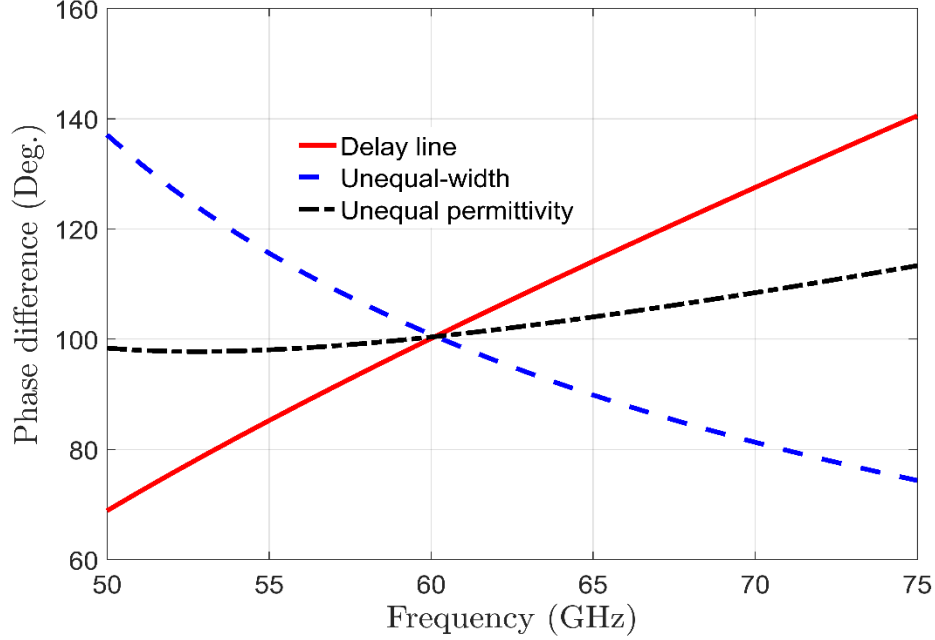


Figure 4.7: Phase shifts introduced by various phase shifters.

#### 4.2.2.2 Hybrid Crossover and Phase Shifters Design

A compact phase shifter with a flat relative phase-shift frequency response is a key component of the BFN for a multibeam antenna array. By taking the phase delay associated with the crossover as a reference, the phase shifter cannot be realized with a straight SIW phase shifter. One solution is to use a smooth curved delay line, but at the expense of increasing the size. The second approach is cascading two  $90^\circ$  hybrid couplers to implement the crossover, which increases the complexity and losses. As for the phase shifter, changing the width of the SIW will cause a change of propagation constant, and hence the required phase shift can be realized. The propagation constant can also be effectively changed by filling the SIW with different dielectric materials, as discussed in the next paragraphs. For an SIW designed on a relatively low-loss substrate, the propagation constant  $\beta(f)$  is dispersive and can be calculated from the following simplified expression ( $f$ : GHz,  $W$ : mm)

$$\beta(f) = \sqrt{\left(\frac{2\pi\sqrt{\epsilon_r}f}{300}\right)^2 - \left(\frac{\pi}{W}\right)^2} \quad (4.5)$$

where  $W$  is the equivalent width of the SIW and  $\epsilon_r$  is the relative permittivity of the substrate. Consequently, the phase shift associated with a specific length ( $L$ ) is defined by:

$$\varphi(l) = \beta(f)l \quad (4.6)$$

It is well-known that the rate of change of phase shift with respect to the frequency of a delay line almost increases linearly. On the other hand, in the case of an equal-length unequal-width phasor, the rate of change decreases as the frequency increases. Moreover, a phase shifter consists of two similar branches filled with two different substrates (unequal-permittivity phase shifter) behaves with less dispersion compared to the above-mentioned phasors, as shown in Figure 4.7. Theoretically, a very wideband phase shifter can be designed based on this technique. From Fig.4, it can be seen that increasing the length, width, or permittivity by a value of 1.07 mm, 0.8 mm or 0.56, respectively will produce the same phase shift at 60 GHz. Note that, when changing one parameter of the phase shifters, the others are fixed at reference values (i.e., length = 7 mm, width = 2.25 mm and permittivity = 2.94). Moreover, Figure 4.8 shows the calculated phase response of two identical waveguides filled with different substrates (i.e., RO6002- and RO3035- filled waveguides) for different widths at 60 GHz. As can be seen, changing the permittivity from 2.94 to 3.5 provides a 100° phase shift at a width of 2.25 mm, whereas changing the width of the 3035-filled waveguide from 2.0 to 2.5 mm achieves a 95° phase shift, showing the high flexibility of this technique to realize the required phase shift. In addition, optimizing the width provides a wider bandwidth compared to the length optimization. Through the previous discussion and taking into account the limitations of the fabrication technique, a novel compact unequal-permittivity phase shifter is proposed. Practically, to implement the proposed phase shifter, two different substrates should be stacked on top of each other. Therefore, low loss and efficient transition is required to match between two different SIW wave impedances. An SIW slot-coupled transition, consisting of an offset longitudinal slot with three matching posts embedded in each SIW, is proposed in this work. The transition has significant influence on the phase response, as an additional frequency-dependent phase delay will added to the transmission phase, thus reducing the bandwidth of the phase shifter. Therefore, understanding the principle of operation of the transition is important for a well-designed phase shifter. An extensive analysis of the slot-coupled waveguide and its equivalent-circuit is reported in [143]. The proposed transition and its equivalent circuit model are depicted in Figure 4.9 (a) and (b), respectively. The two parallel  $L_C$  circuits, i.e.,  $L_1 C_1$  and  $L_2 C_2$ ,

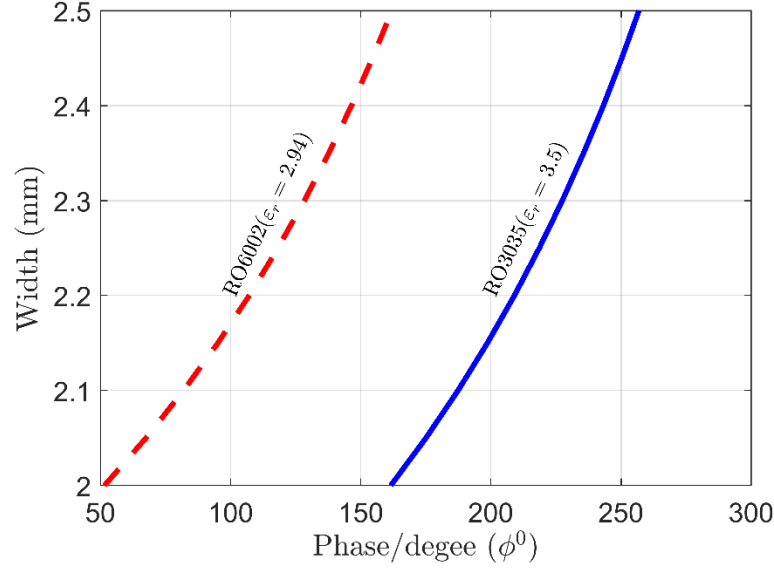


Figure 4.8: Phase versus width response of 6002- and 3035-filled waveguides with equal length ( $L = 7mm$ ) at 60 GHz.

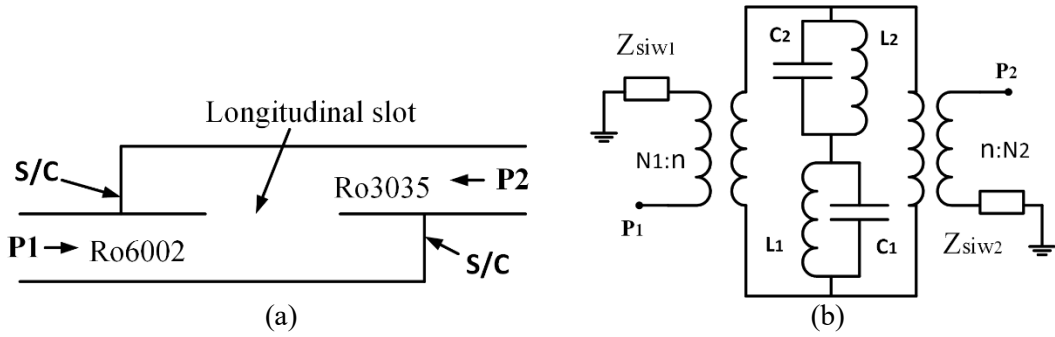


Figure 4.9: Double-layered offset longitudinal slot-coupled transition. (a) Longitudinal cross-section. (b) Equivalent circuit model.

represent the coupling behaviour between the slot and the 6002- and 3035-filled SIW, respectively. Since the wave impedance of the lower ( $Z_{siw1}$ ) and the upper SIW ( $Z_{siw2}$ ) are different, the coupling between the slot and the lower and upper SIW can be represented by the transformer ratio  $N1:n$  and  $n:N2$ , respectively. The crossover and proposed phase shifter structures with the main design parameters are illustrated in Figure 4.10 (a) and (b), respectively. The crossover is designed on a RO6002 substrate, whereas the phase shifter is designed on a RO3035 substrate with relative dielectric permittivity  $\epsilon_r = 3.5$ , loss tangent  $\tan \delta = 0.0015$ , substrate thickness  $h = 0.254mm$ , and cladding thickness of  $18 \mu m$ . The coupling between the two layers is achieved with a pair of offset longitudinal slots etched on the common wide wall. Moreover, a pair of three inductive posts offset



from the center are embedded in each layer to improve the return loss over a wideband. In addition, the width ( $Wp$ ) and length ( $Lp$ ) of the SIW phase shifter are applied to improve the match between the two layers, as well as to achieve the required phase shift. The slot with inductive posts is used as a two-layer longitude slot-coupled-waveguide transition  $n$ , where the distance from the short-ended SIW to the slot center is set approximately to a quarter of the guided wavelength at the center of the band. In a similar manner to the  $90^\circ$  hybrid, the dimensions of the coupling region parameters of the crossover can be calculated by the following equations [12]

$$W_c = \frac{\pi}{k} \sqrt{\frac{(6n+1)(2n+3)}{8n}} \quad (4.7)$$

$$L_c = \frac{\pi}{k} \sqrt{\frac{(6n+1)(2n+3)}{12}} \quad (4.8)$$

The values of  $W_c$  and  $L_c$  for  $n = 1, 2, \dots, 4$  are listed in Table 4.3, where  $n = 3$  is adopted to calculate the width and length of the coupling slot region of the crossover. Therefore, the optimized width  $W_c = 4mm$  and length  $L_c = 6.05mm$  of the coupled slot section is utilized to achieve the required coupling and isolation between the input and output ports of the crossover, as demonstrated in Figure 4.11. It can be noted that the  $|S_{22}|$ ,  $|S_{32}|$  and  $|S_{52}|$  are almost better than 20 dB over the frequency range 57-65 GHz. With the crossover as a reference, all optimized dimensions of the  $45^\circ$  and  $0^\circ$  phase shifters are listed in Table 4.4. Figure 4.12 (a) shows the electric field distribution of the  $45^\circ$  phase shifter with the crossover as a reference. Mainly, the overall phase shift arises from the straight SIW with the higher dielectric permittivity and the two slot-coupled vertical transitions as shown in Figure 4.12 (b). The simulated reflection and transmission coefficients of the  $45^\circ$  phase shifter are presented in Figure 4.13 (a). The return loss is better than 20 dB over the frequency range 55-64 GHz. The phase response of the  $45^\circ$  phasor is shown in Figure 4.13 (b), where the phase difference is  $45.5^\circ$  at the center of the band. As for the  $0^\circ$  phase shifter, the reflection coefficient is less than -20 dB over the band of interest as shown in Figure 4.14 (a), whereas the phase difference is  $0^\circ$  at the center frequency as depicted in Figure 4.14 (b).

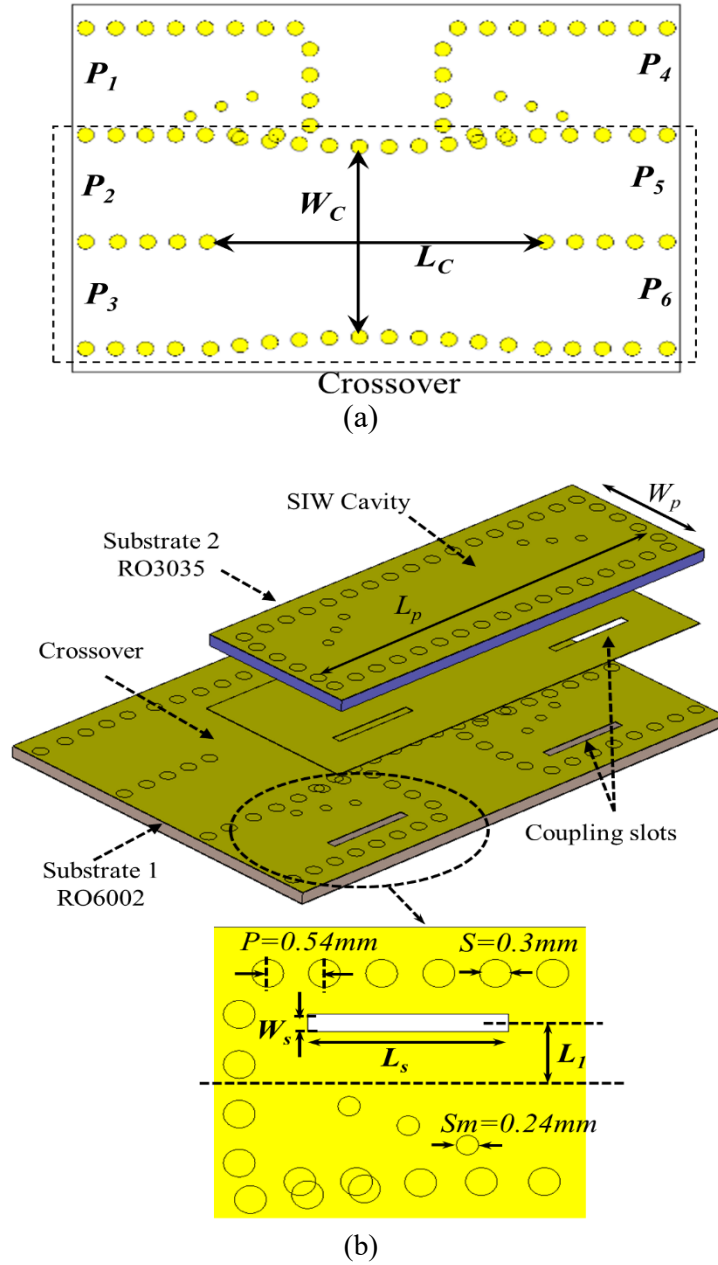


Figure 4.10: Geometry of the crossover and proposed SIW phase shifter: (a) Top view of crossover (substrate 2 not shown), and (b) Pictorial view of phase shifter with crossover as a reference.

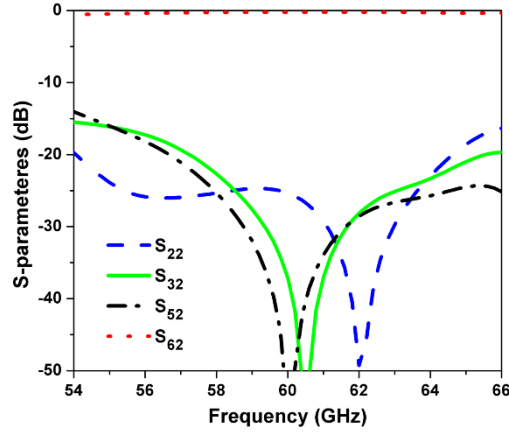


Figure 4.11: Simulated S-parameters of the crossover.

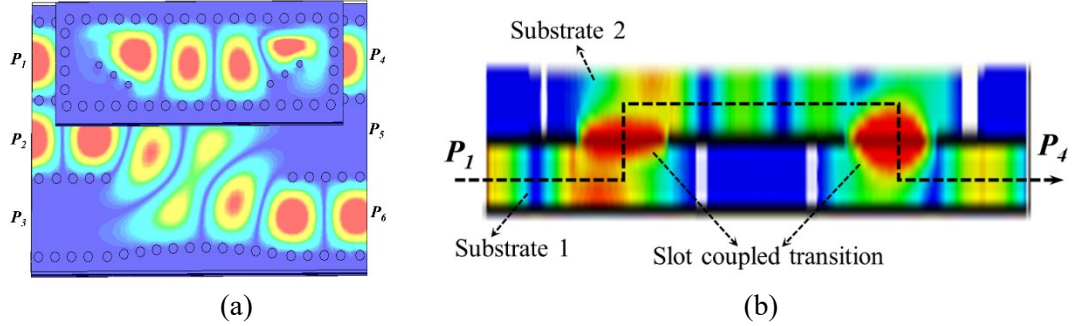


Figure 4.12: Electric field distribution of the  $45^\circ$  phase shifter and crossover. (a) Top view. (b) Longitudinal section view.

Table 4.3: Calculated dimensions of the coupling region of the crossover.

$n$	1	2	3	4
$W_c (mm)$	3.03	3.47	3.88	4.27
$L_c (mm)$	2.48	4	5.5	6.97

Table 4.4: Optimized dimensions of the  $45^\circ$  and  $0^\circ$  phase shifters [Units: mm].

Parameter (mm)	$L_s$	$W_s$	$L_l$	$W_p$	$L_p$
$45^\circ$ phase shifter	1.9	0.2	0.6	2.5	8.8
$0^\circ$ phase shifter	1.9	0.2	0.55	2.3	7.3

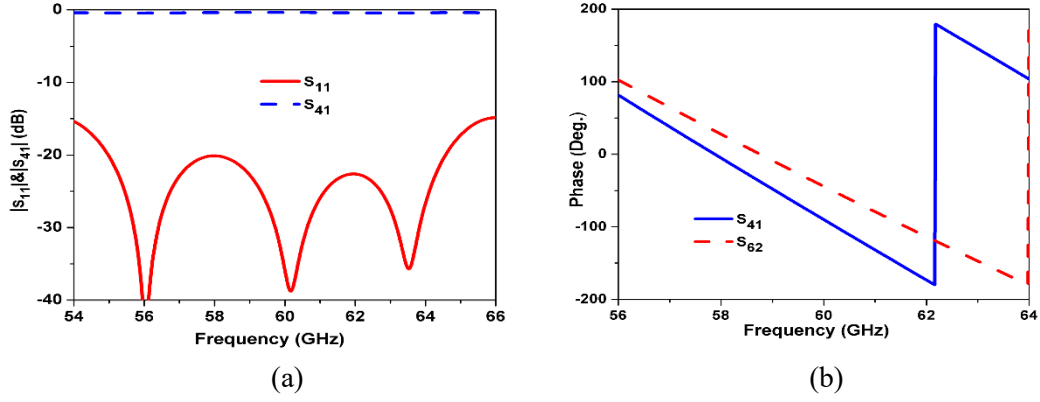


Figure 4.13: Simulated S-parameters of  $45^\circ$  phase shifter. (a) Magnitude. (b) Phase response.

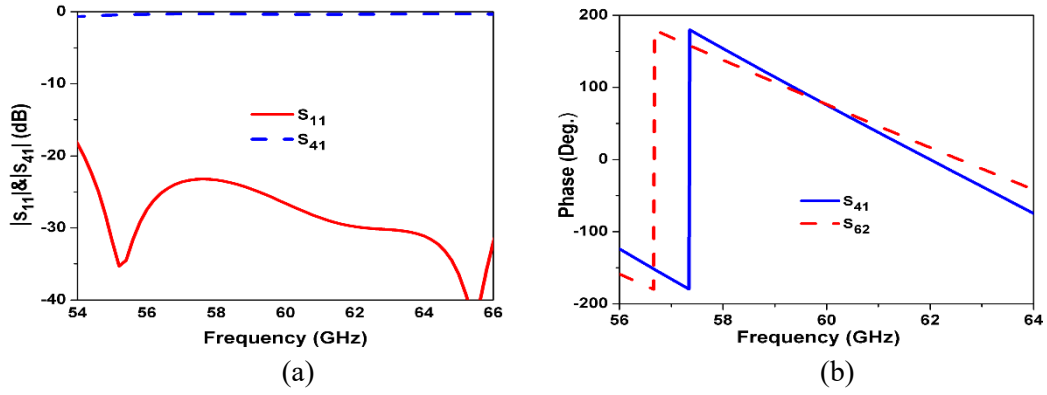


Figure 4.14: Simulated S-parameters of  $0^\circ$  phase shifter. (a) Magnitude. (b) Phase response.

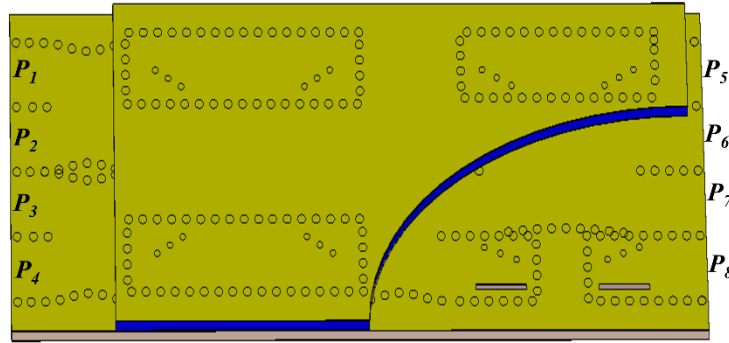


Figure 4.15: Topology of the proposed SIW Butler matrix.

### 4.2.2.3 Cascaded Butler Matrix Design

The designed components in the previous subsections, i.e., the  $90^\circ$  hybrid coupler, phase shifters, and crossover are integrated to form a compact 4x4 Butler matrix as shown in Figure 4.15, where the substrate 2 is partially removed to show the coupling slots and the crossover. Figure 4.16 shows the simulated  $S$ -parameters of the Butler matrix when port 1 is excited. Within the frequency range 57.3-63 GHz, it can be observed that the reflection and isolation coefficients are less than -18 dB, whereas the transmission coefficients from port 1 to output ports (ports 5-8) are  $6.8 \pm 0.7$  dB. Figure 4.17 depicts the simulated magnitude of  $S$ -parameters when port 2 is excited. The reflection and isolation levels are less than -18 dB over the frequency range 57.2-65 GHz, and the average value of transmission magnitudes is 6.7 dB with maximum dispersion of less than 1.1 dB within the band from 57 to 63 GHz. Due to the symmetry structure, the  $S$ -parameters with port 3 and 4 excitations are similar to those of port 2 and 1, respectively, so they are not shown. The simulated relative phase difference between adjacent output ports is presented in Figure 4.18. The theoretical (ideal) value of phase differences is  $-45^\circ$ ,  $+135^\circ$ ,  $-135^\circ$  and  $+45^\circ$ , when one of the input ports (ports 1 to 4) is excited, respectively. As can be observed from Fig.16, the peak-to-peak phase error is 140 when port 2 or 3 is excited and 160 with port 1 or 4 excitation. The Butler matrix has a compact size of  $25 \times 9.3 \times 0.508 \text{ mm}^3$ , which is very suitable as a feeding network for a 60 GHz multibeam array.

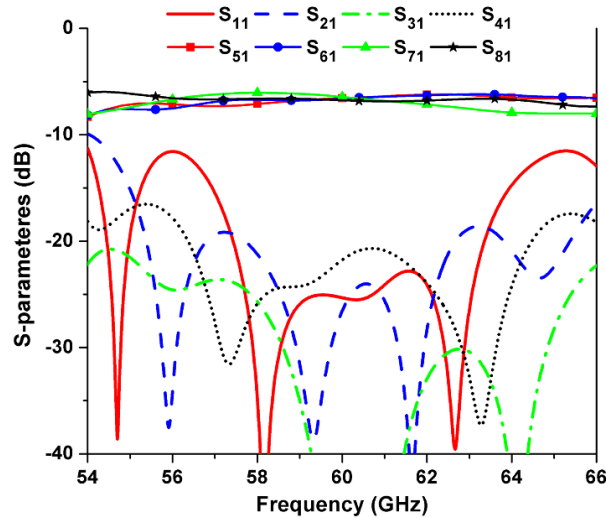


Figure 4.16: Simulated  $S$ -parameters of the SIW matrix with port 1 excitation.

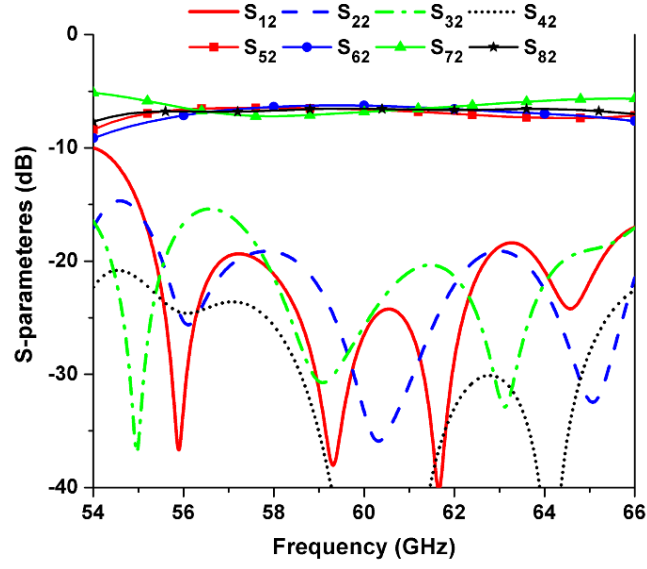


Figure 4.17: Simulated  $S$ -parameters of the SIW matrix with port 2 excitation.

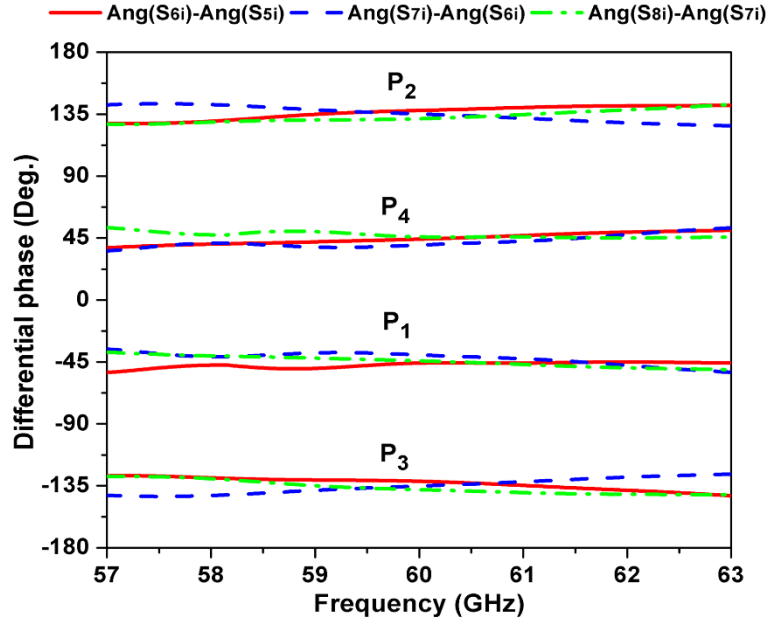


Figure 4.18: Phase differences between output ports ( $P_i$ , port  $i$  excited, where  $i = 1, 2, \dots, 4$ ).

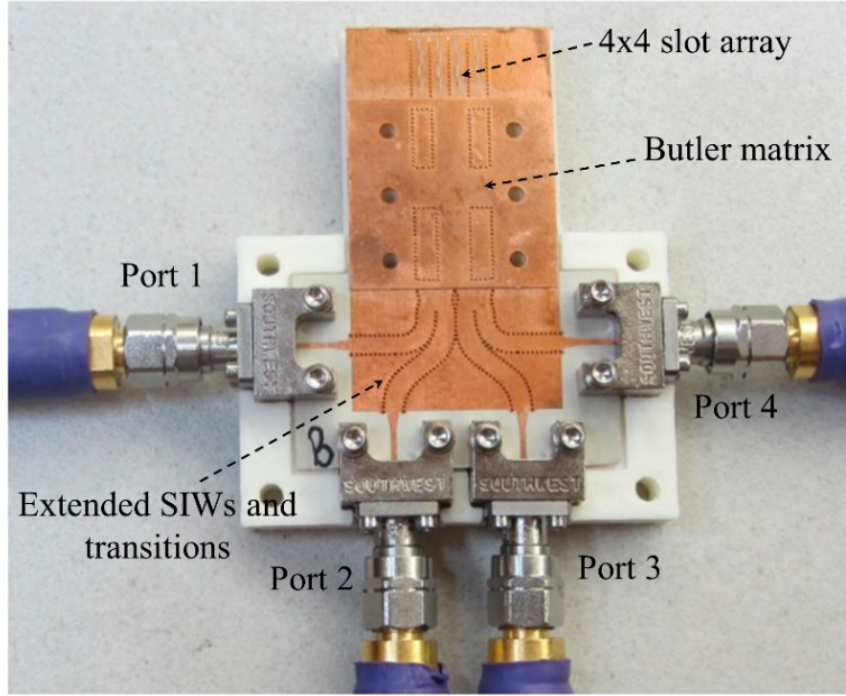


Figure 4.19: Photograph of the fabricated SIW multi-beam slot array.

### 4.2.3 Multibeam Array and Measurements

A four branches slot antennas that designed in subsection 4.2.1 are connected to the output ports of the Butler matrix to form a 4x4 slot array for steering the beam in four different directions. Theoretically, the beam directions can be calculated by (4.9) [140];

$$\theta_0 = \sin^{-1} \left( \frac{\lambda \phi}{2d\pi} \right) \quad (4.9)$$

where  $\phi$  is the relative phase difference, and  $d$  is the inter-element spacing. For a separation of a half wavelength between radiating elements with the relative phases of  $\pm\pi/4$  and  $\pm3\pi/4$ , the corresponding beam directions will be  $\pm14^\circ$  and  $\pm48^\circ$ , respectively. A photograph of the fabricated prototype is illustrated in Figure 4.19. To reduce the insertion loss, extended SIWs are designed in such a way that to avoid sharp corners, such as  $90^\circ$  bends. Moreover, MS-to-SIW transitions with the extended SIWs are utilized to facilitate the measurements of the reflection and isolation coefficients using Agilent N5227A vector network analyzer (VNA) and testing the radiation pattern in an anechoic chamber, to verify the simulated results. Figure 4.20 (a) and (b) show the

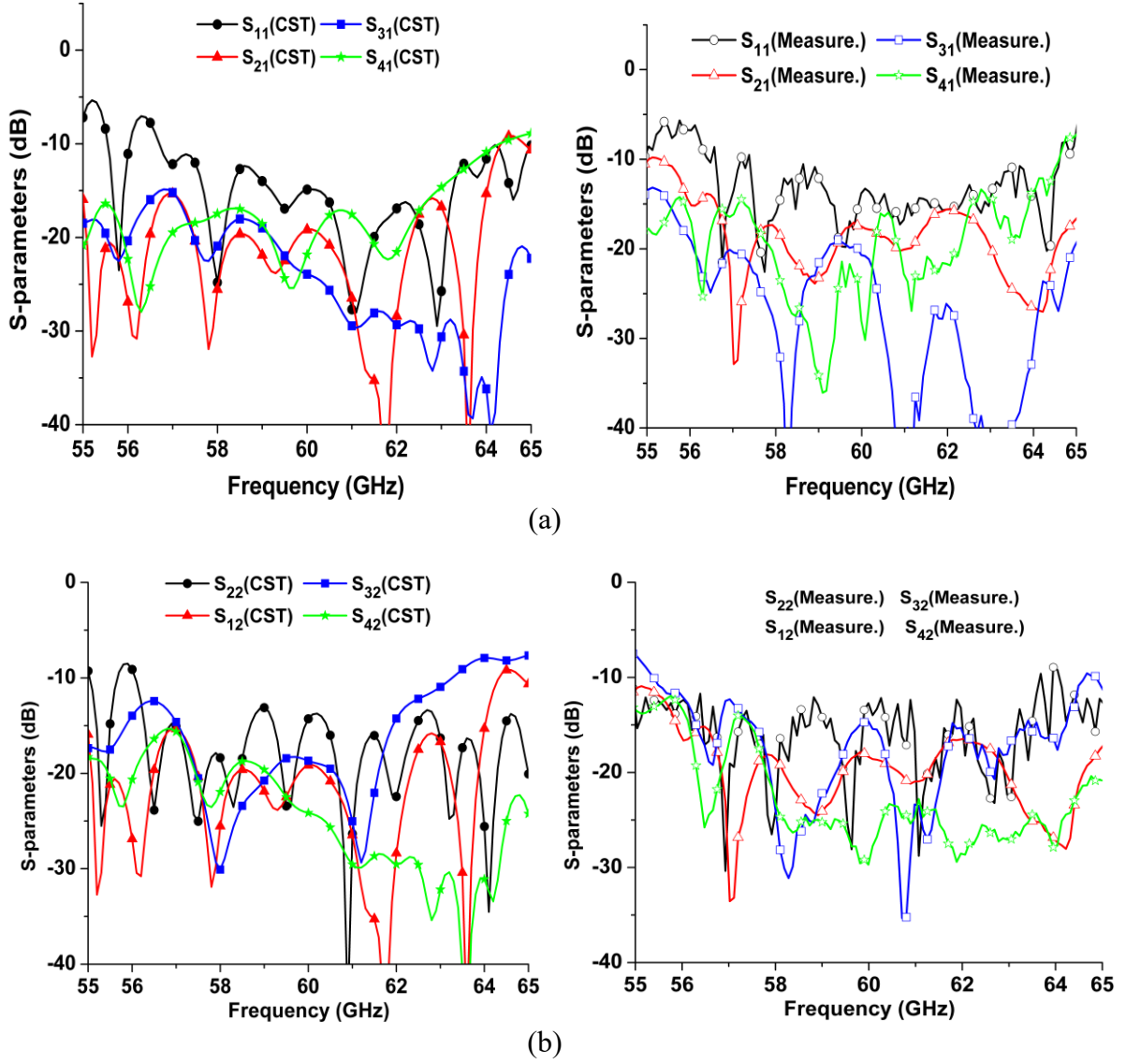


Figure 4.20: Measured and simulated S-parameters of the multi-beam slot array. (a) Port 1 excitation. (b) Port 2 excitation.



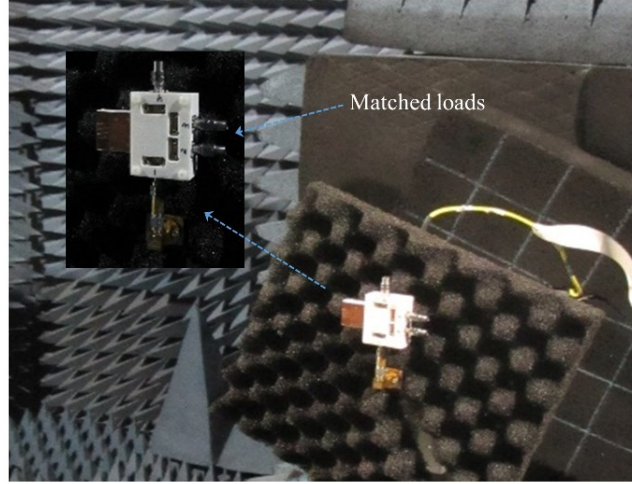


Figure 4.21: Photograph of the prototype in anechoic chamber for radiation patterns test.

pattern in an anechoic chamber, to verify the simulated results. Figure 4.20 (a) and (b) show the comparison between the simulated and measured results of the reflection and isolation losses when input port 1 or 2 is excited, respectively. For port 1 excitation, it can be seen that the return loss is better than 10 dB and the isolation between port 1 and other input ports is almost less than -15 dB over the frequency range from 57 to 64 GHz. Additionally, when port 2 is excited, the reflection coefficient is less than -12 dB within frequency range 57-63.5 GHz, while the isolation from other ports is almost below -15 dB in the range 58-62 GHz. Due to the structure symmetry, the measured and simulated results with port 3 or 4 excitation is similar to that of port 2 and 1, respectively. The slight difference between measured and simulated results may be caused by the dielectric loss, end launch connector mismatch, fabrication tolerance and/or the misalignment between SIW layers. For the radiation patterns measurements, the port under test is excited, whereas the other ports are connected to 50 Ohm matching loads through 1.8 mm end launch connectors as illustrated in Figure 4.21. Figure 4.22 (a), (b) and (c) show the simulated radiation patterns of all four input ports of the proposed multibeam slot array for 58.5, 60 and 61.5 GHz, respectively. It is observed that the main beam directions are almost  $+15^\circ$ ,  $-46^\circ$ ,  $+46^\circ$  and  $-15^\circ$ , when port 1, 2, 3 and 4 are excited, respectively. The simulated side lobe level (SLL) is around -12 dB when feeding at port 1 and 4 and around -9 dB for port 2 and 3, which is slightly higher than the theoretical value (-13 dB). This difference may be due to the mutual coupling between radiating elements, the ground

plane size of the Butler matrix and the impact of element array at larger tilted beam values, as it tends to

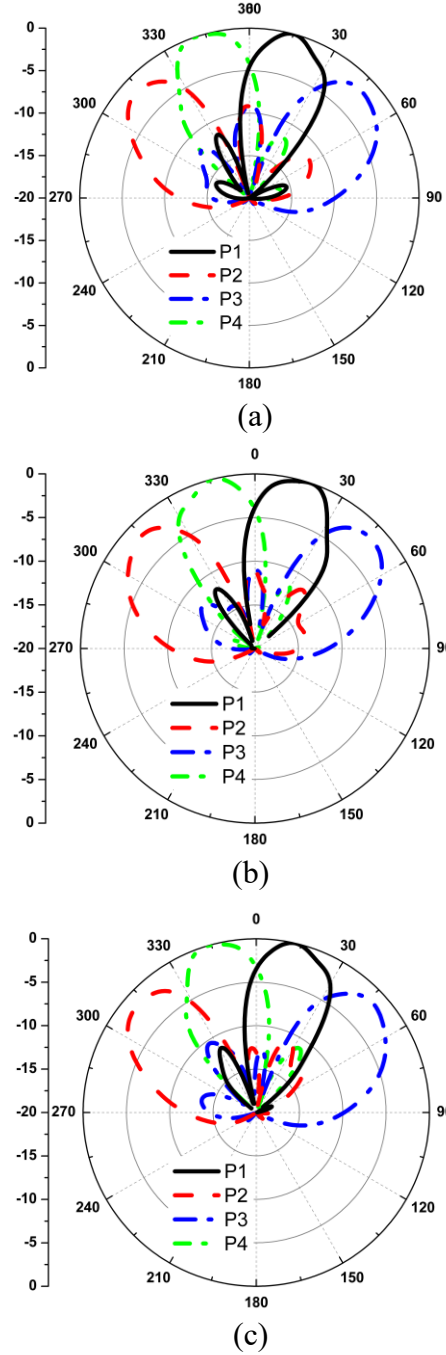


Figure 4.22: Simulated radiation pattern for all 4 input ports of the multibeam slot array. (a) 58.5 GHz. (b) 60 GHz. (c) 61.5 GHz.

degrade the SLL. The measured radiation pattern for all input ports (i.e., ports 1 to 4) at 60 GHz is shown in Figure 4.23. The main beams of the slot array are successfully steered in the directions

$+14^{\circ}$ ,  $-44^{\circ}$ ,  $+45^{\circ}$  and  $-14^{\circ}$ , when port 1, 2, 3 and 4 are excited, respectively. The measured half power beam width (HPBW) is  $32^{\circ}$ , when feeding at port 2 and 3 (i.e., beams in directions  $-44^{\circ}$  and  $+45^{\circ}$ ), thus the proposed multibeam slot array covered  $121^{\circ}$  in the azimuth direction. The measured SLL is still better than 8 dB of all ports, as they effected by the reflections from matched loads, cables and the measurement setup. Figure 4.24 shows the measured gain of the proposed multibeam slot array. At the center of the band, the array exhibits peak gains of 13.1, 11.5, 11.4, and 12.9 dBi, when port 1, 2, 3 or 4 is excited, respectively. It can be noticed that the gain is decreased at the edges of the band, which may be caused by the amplitude imbalance, and the mismatch at these frequencies.

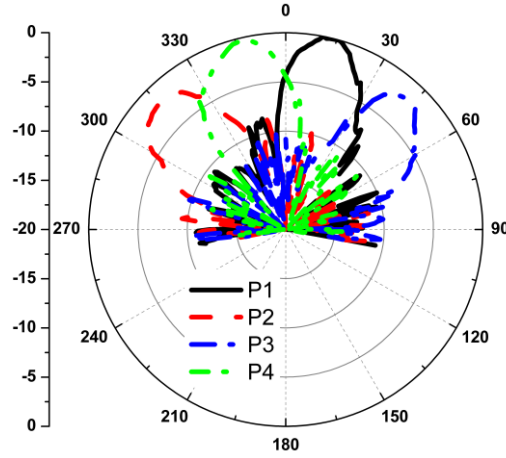


Figure 4.23: Measured radiation pattern of all 4 input ports for the multibeam slot array at 60 GHz.

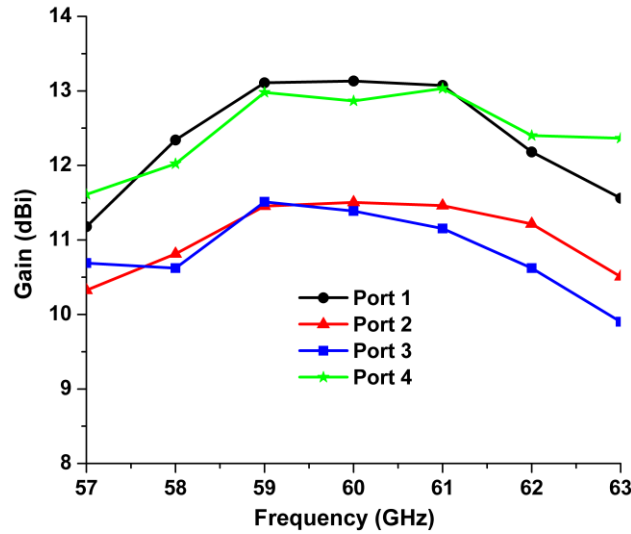


Figure 4.24: Measured gain for different input port excitation of the proposed multibeam slot array.

### 4.3 Multibeam End-Fire Fermi Tapered Slot Antenna Array

In this section, a wideband high gain multibeam end-fire antenna array is introduced to cover the unlicensed ISM band (57-64 GHz). The Butler matrix is utilized to archive the desired progressive phase shift between the radiating elements. A modified crossover coupler is designed to improve the matching, reduce the coupling between input ports and improve the phase balance of the output ports. Tapered slot antenna with a diamond-shaped slot and dielectric slap is adopted as a radiating element for the proposed antenna array. In order to fit the inter-element spacing, the tapered slot antennas are arranged in the H-plane direction, where an SIW-to-MS transition and  $90^\circ$  twisted microstrip line are utilized to implement this arrangement.

#### 4.3.1 Single Element Design and Characterization

Due to its wide bandwidth, high gain, symmetrical radiation pattern in principle planes, tapered slot antenna (TSA) is suitable for the radiating element of multibeam antenna arrays. The single element antenna geometry is illustrated in Figure 4.25. The antenna is designed on 0.254-mm-thick Rogers 6002 substrate, with dielectric permittivity of  $\epsilon_r = 2.2$  and  $\tan \delta = 0.0012$ . The design procedure is explained in detail through the work reported in section 3.1. The return loss is better than 20 dB over the band of interest, as depicted in Figure 4.26, while the realized gain is 12.4 dB at 60 GHz. However, the antenna gain could be easily increased by lengthening the antenna, but as the element will be used as a radiating element in the phased array configuration, its gain is restricted by the scan angle and the mechanical strength. Figure 4.27 shows the E- and H-plane radiation patterns of the single TSA antenna. Besides the symmetry of the radiation pattern, the antenna exhibits side lobe level less than -18 dB in both principal planes.

#### 4.3.2 Beamforming Network Design

The Butler matrix is adopted as a beamforming network in this design. It consists of hybrid junctions and phase shifters and computes the output signals in an identical manner to signals analyzed by Fast Fourier Transform (FFT) tree graph [144, 145]. It has  $2^n$  inputs and  $2^n$  outputs

and  $(N/2) \log_2 N$  hybrid junctions, where  $N=2^n$ . Therefore, an  $N$ -element array with  $N$  input ports produces  $N$  beam directions corresponding to input port excitations.

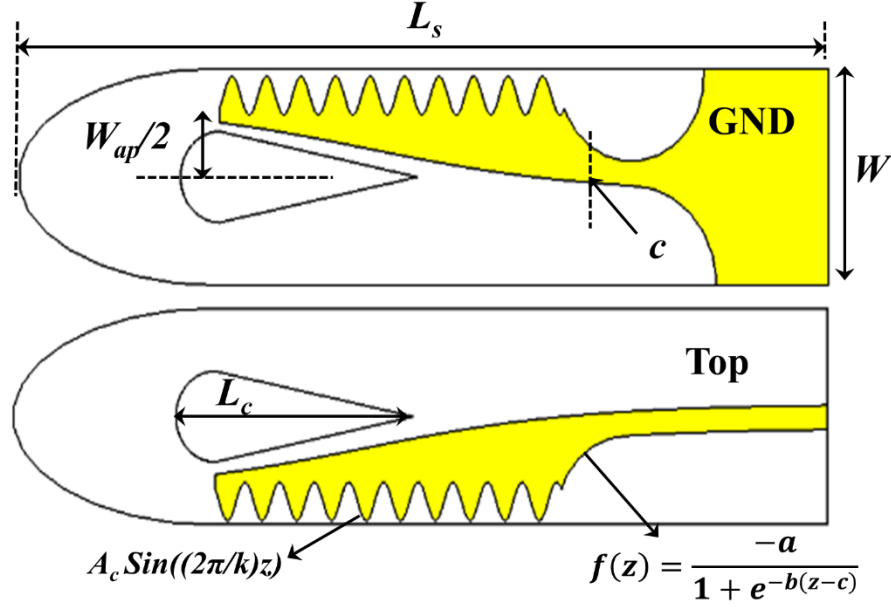


Figure 4.25: Top and ground view of TSA as seen from top ( $A_c=0.5$  mm,  $k =$ ,  $W_{ap}=2.8$  mm,  $c=4$ ,  $b = 0.3$ ,  $a= 2.3$ ).

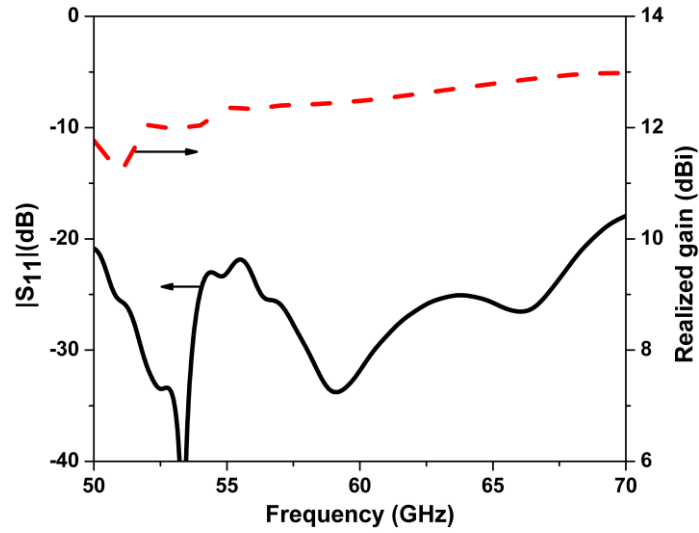


Figure 4.26: Simulated  $|S_{11}|$  and gain of the proposed TSA.

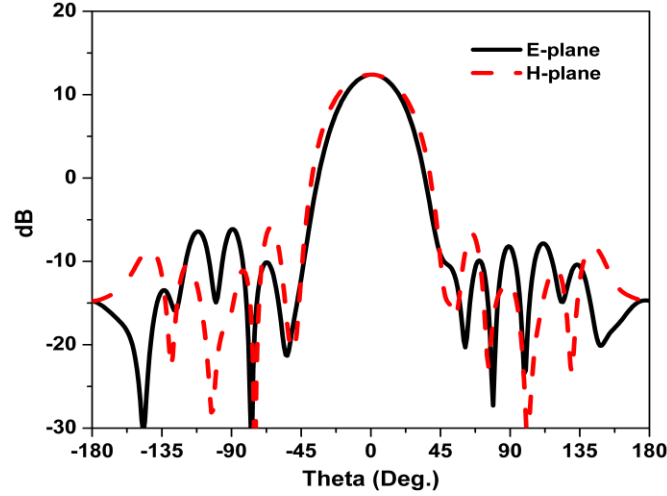


Figure 4.27: Simulated E- and H-plane radiation patterns of the single TSA at 60 GHz.

#### 4.3.2.1 90° Hybrid Coupler

The SIW hybrid coupler is designed by removing the common sidewall similar to the Riblet short coupler in [142]. The vertical walls are constructed using rows of metallic vias with a diameter of 0.3 mm and a longitudinal spacing of 0.54 mm. The geometry of the SIW 90° hybrid coupler is shown in Figure 4.28. The impedance matching at the input ports, power coupling ratio between output ports and output phase difference are mainly controlled by adjusting the length and width of the coupling region and the overall length of the coupler as well. The phase difference between the dominant and higher-order mode can be calculated using equation (4.10) or the following formula:

$$= 2\pi \left( \frac{L}{\lambda_{ge}} - \frac{L}{\lambda_{go}} \right) \quad (4.10)$$

where  $\lambda_{ge}$  is the even-mode wavelength,  $\lambda_{go}$  is odd-mode wavelength, and  $L$  is the length of the coupling region. Figure 4.29 shows the simulated S-parameters. As shown in Figure 4.29 (a), the return loss is better than 20 dB over the frequency range from 51 to 70 GHz (BW more than 31 %). The mutual coupling between port 1 and 4 is less than -20 dB over the band of interest. The magnitude difference between the output ports is less than 0.5 dB within the frequency range of 54-68.5 GHz, as depicted in Figure 4.29 (b). Also, the phase error of the output ports compared with the theoretical value 90° is smaller than 1° over the frequency band 50-70 GHz.

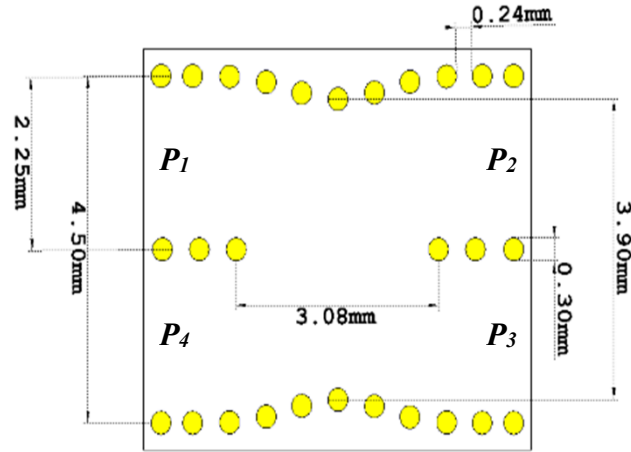


Figure 4.28: Layout of the SIW 3-dB coupler.

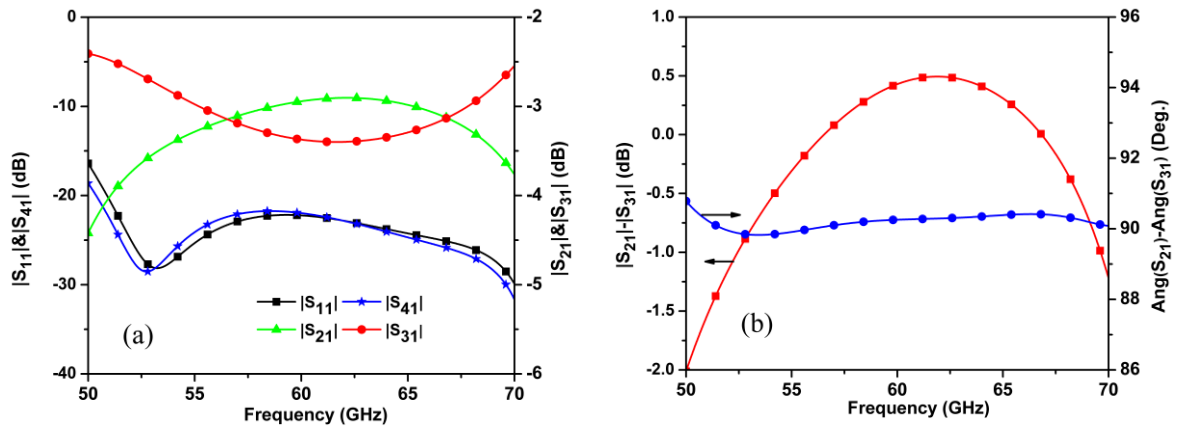


Figure 4.29: Performance of the SIW 3dB coupler. (a) S-parameters. (b) Differential phase and magnitude of port 2 and 3.

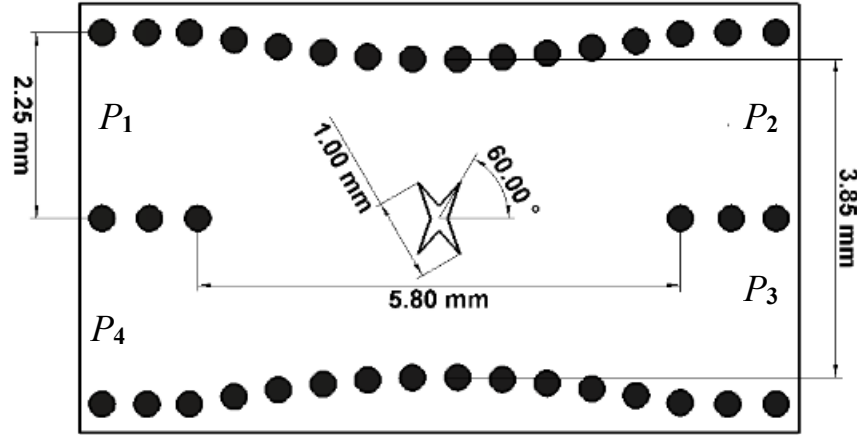


Figure 4.30: Topology of the modified SIW hybrid crossover with geometric dimensions.

#### 4.3.2.2 Modified Hybrid Crossover

Crossover is an essential component in the BFN, and its performance will be crucial to the output phase differences of the Butler matrix. Theoretically, the length and width of the aperture coupling region are calculated to allow the  $TE_{10}$  and  $TE_{20}$  mod to propagate with  $180^\circ$  phase difference and prevent the  $TE_{30}$  mode, in which the signal from port 1 is transferred to port 3 and no signal coupled to port 2 or port 4. Practically, a small portion of the input signal will leakage to port 2 and other portion will be reflected back to port 4. Therefore, in passive beamforming networks that utilize Butler matrix with cascaded crossovers, this portion of the unwanted signal will increase the phase and amplitude dispersion at the output ports and thereby the mismatch at the input ports of the Butler matrix as well. Therefore, well-designed crossover over a wide frequency range will improve the performance of the whole beamforming network. The proposed SIW crossover with the main design parameters is shown in Figure 4.30. In this design, two crossed rhombus-shaped slots rotated in opposite directions through the angle  $\theta$  are implemented to improve the characteristics of the crossover. The impact of the rotation angle  $\theta$  and length  $L$  of the rhombus-shaped slot on the s-parameters are explained throughout parametric studies, as shown in Figure 4.31. The impact of parameters  $L$  and  $\theta$  on the return loss is shown in Figure 4.31 (a) and (b), respectively. It can be noted that as the length  $L$  increases, the resonant frequency is shifted downward to a lower frequency, whereas there is no effect on the return loss in case of changing



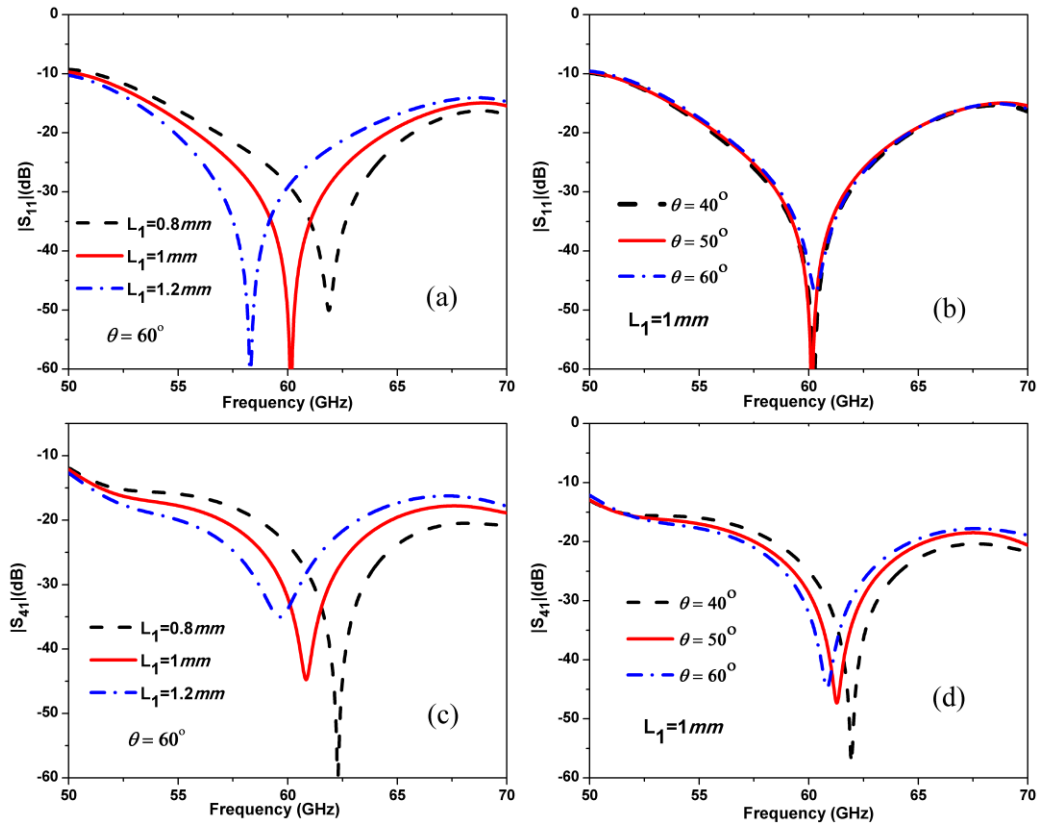


Figure 4.31: The impact of parameters  $L$  and  $\theta$  on the S-parameters of hybrid crossover.

the parameter  $\theta$ . Moreover, the effect of parameters  $L$  and  $\theta$  on the coupling between port 1 and port 4 is presented in Figure 4.31 (c) and (d), respectively. From Figure 4.31 (c), it is clear that as  $\theta$  increases the resonant frequency is shifted downward. Note that when one of the two parameters is changed, the other is fixed at its optimum value. Through the design procedure of the proposed SIW crossover, first, the resonant frequency of the return loss is shifted to the central operating frequency by adjusting the length  $L$  of the rhombus-shaped slots to its optimum value ( $L=1\text{mm}$ ). Secondly, the rotation angle is set to  $\theta = 60^\circ$  to minimize the coupling between port 1 and 4, in other words, to reduce the power that reflected to port 4. The S-parameters of the optimized design of the proposed crossover is illustrated in Figure 4.32. For the frequency band 55-65 GHz, the  $|S_{11}|$  and  $|S_{41}|$  is less than -18 dB, while the isolation of port 1 to 2 is less than -10 dB at 55 GHz and decrease to -25 dB at 65 GHz.

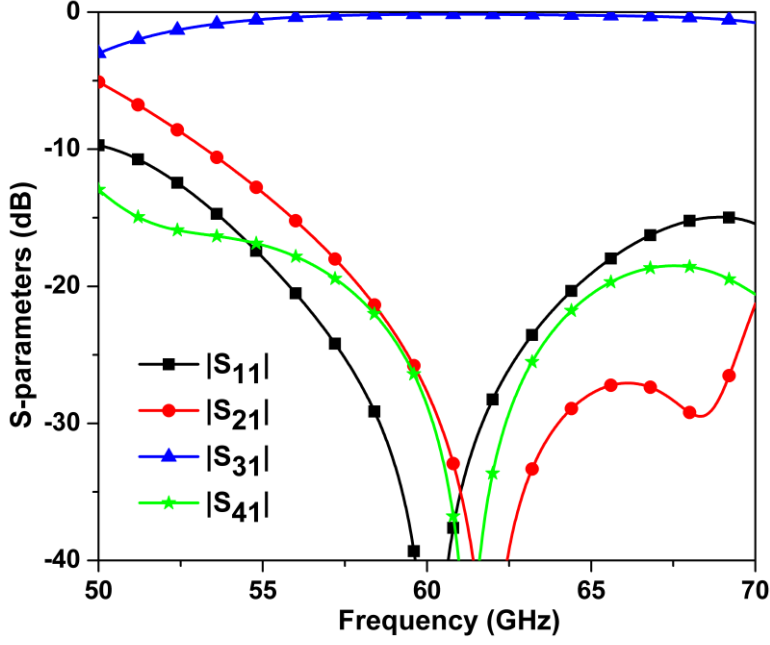


Figure 4.32: Simulated  $S$ -parameters of the proposed SIW hybrid crossover.

#### 4.3.2.3 Phase Shifters

At low frequencies where the electrical size of phase shifters is relatively small, a meandered microstrip delay lines is a common approach to achieve the required phase shifts [146-147, 126]. As the frequency increase, the microstrip lines becomes unpractical to design phase shifters, due to the high losses and the coupling between lines as well. SIW with the features of low loss and planar structure, are alternative solutions to design phase shifters at high frequencies [113]. Theoretically, the required phase shift can be effectively obtained by changing the length or the width of SIW. The phase difference ( $\Delta\phi$ ) between two delay lines with unequal length and equal width is given by equation (4.11), while in the case of equal length and unequal width is given by equation (4.12).

$$\Delta\phi = (l_1 - l_2)\beta \quad (4.11)$$

$$\Delta\phi = (\beta_1 - \beta_2)l \quad (4.12)$$

where  $L$  is the length of the line, and  $\beta$  is the propagation constant of the propagating mode and given by equation (4.5). Since the wider width produces higher propagation constant, which is inversely proportional to the phase velocity; thus, the width is inversely proportional to propagation constant as well. However, in many designs, the phase shifters are referenced to other components such as crossovers, which is the case in our design; thus, the phase shifter length is restricted by the crossover. Therefore, a curved SIW is necessary, but with sharp curved, the mismatch will increase. The trade-off between the required phase shifts ( $0^\circ$  or  $45^\circ$ ) and the excellent matching can be realized by changing both the length and width of SIW. Figure 4.33 depicts the reflection and transmission coefficients of  $0^\circ$  and  $45^\circ$  phase shifters. It can be seen that the reflection coefficient of  $0^\circ$  and  $45^\circ$  phase shifter is less than -20 and -15 dB, respectively, over the frequency range of 52.5-67.5 GHz. The beak to beak phase error of  $45^\circ$  phase shifter is better than  $7^\circ$  within the range from 54 to 64 GHz, whereas for the  $0^\circ$  phase shifter is better than  $2^\circ$  over the band 57- 66 GHz, as illustrated in Figure 4.34. The electrical field distribution of  $0^\circ$  and  $45^\circ$  phase shifter referenced with crossover, is shown in Figure 4.35 (a) and (b), respectively. It is clear that the phase shifters adequately compensate the phase delay introduced by the crossover.

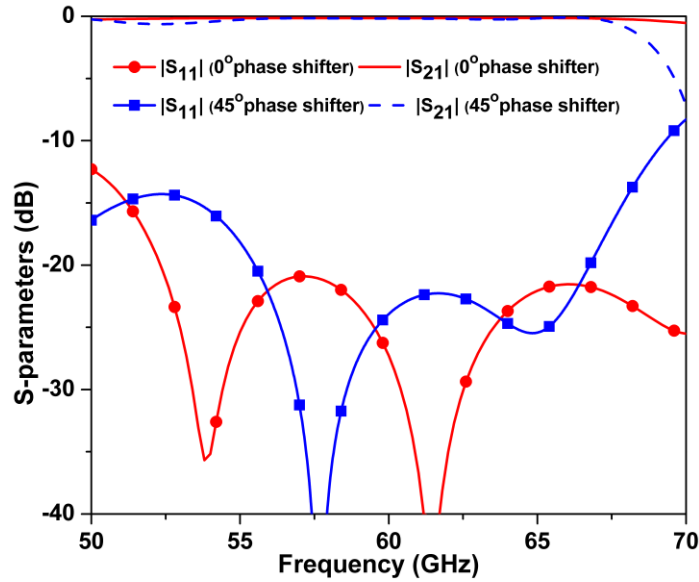


Figure 4.33 Simulated S-parameters of the SIW phase shifters.

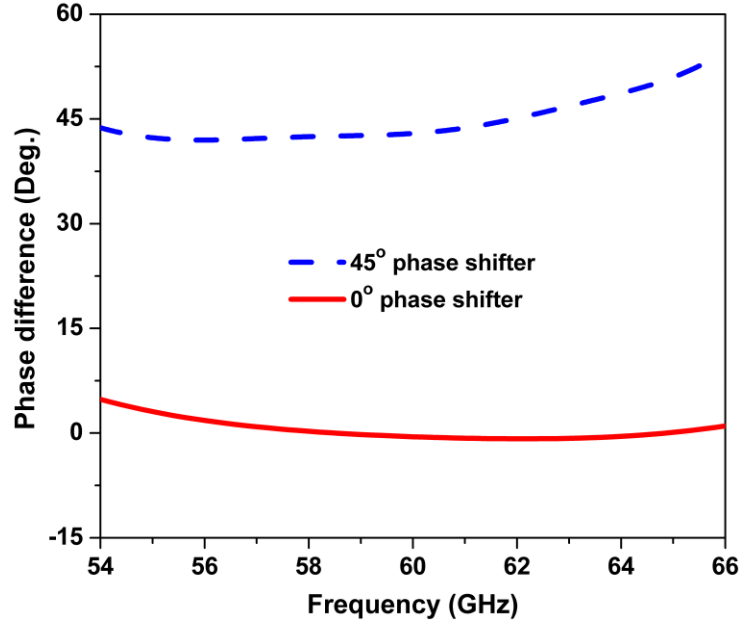


Figure 4.34: Simulated differential phases of the proposed SIW phase shifters.

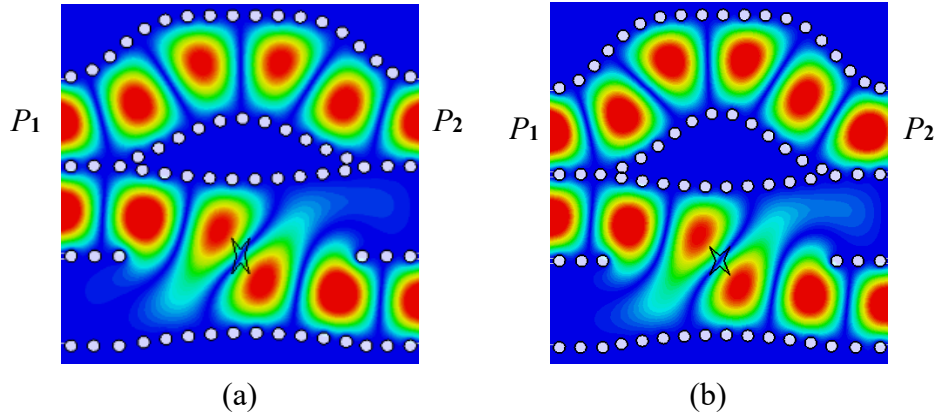


Figure 4.35: Electric field distribution of the SIW phase shifters referenced with modified crossover, (a)  $0^\circ$  and (b)  $45^\circ$  phase shifter.

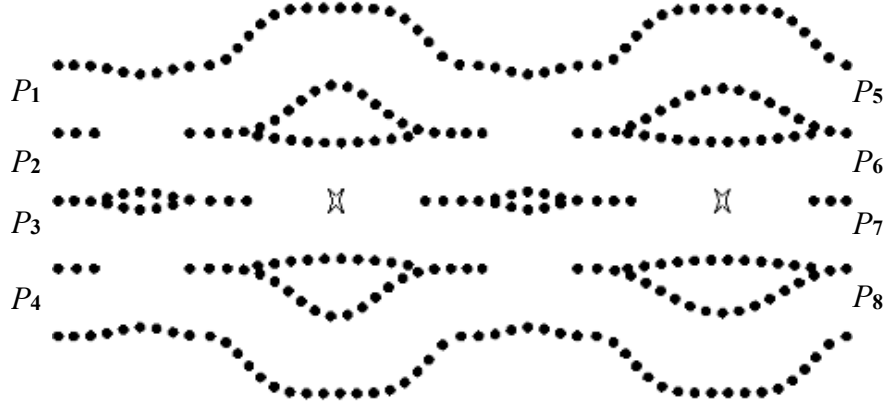


Figure 4.36: Geometry of the SIW Butler matrix.

#### 4.3.2.4 Butler Matrix

The optimized components in previous subsections are integrated together to implement the cascaded Butler matrix. The layout of SIW Butler matrix is shown in Figure 4.36. A final tune is performed to obtain the required progressive phase shift between output ports with equal amplitude. The simulated results were carried out using CST MWS simulator. Figure 4.37 (a) and (b) depict the simulated S-parameters magnitude of beam forming network with port 1 and port 2 excitation, respectively. For port 1 excitation, the transmission coefficient is  $6.7 \pm 1$  dB over the frequency band of 57 to 64 GHz, whereas the reflection and isolation coefficients are less than -14 dB from 56.5 to 66 GHz. For port 2 excitation, the transmission coefficient of all output ports is  $6.7 \pm 0.8$  dB within the frequency band of 57-64 GHz, and the return and isolation loss is better than 14 dB over the frequency range of interest. The electric field distribution of the proposed Butler matrix, shown in Figure 4.38 with port 1 and 2 excitations, with the uniform distribution and well isolation between different ports, evidence the design approach. Figure 4.39 represents the phase difference between output ports when one of the input ports is excited. Theoretically, when one of the input ports 1-4 is excited individually, the relative phase difference between adjacent output ports is  $-45^\circ$ ,  $135^\circ$ ,  $-135^\circ$  and  $45^\circ$ , respectively. For port 1 or 4, the simulated phase imbalance is  $\pm 7^\circ$ , while for port 2 or 3 the peak-to-peak phase error is  $12^\circ$  as compared to the ideal values over the frequency range from 57 to 64 GHz.

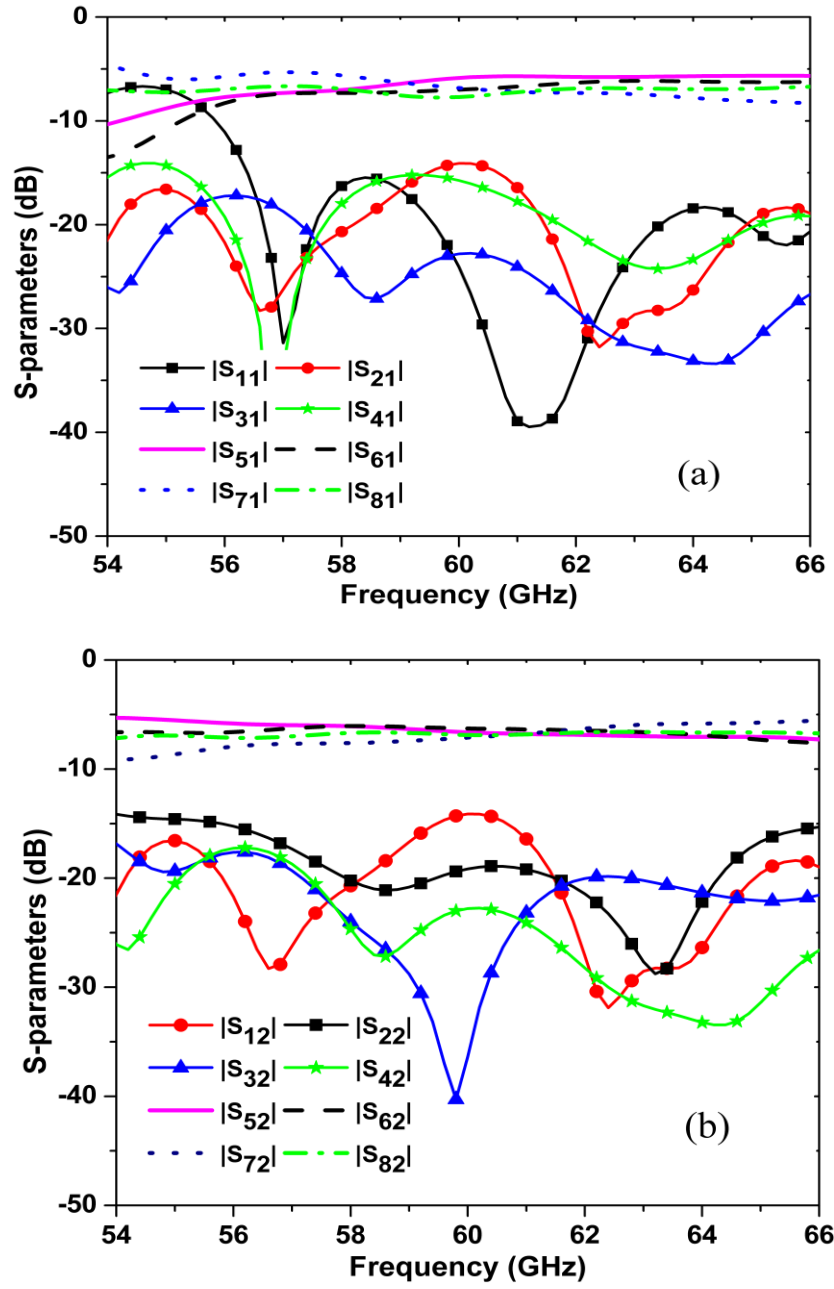


Figure 4.37: Simulated S-parameters of the SIW Butler matrix. (a) Port 1 excitation. (b) Port 2 excitation.

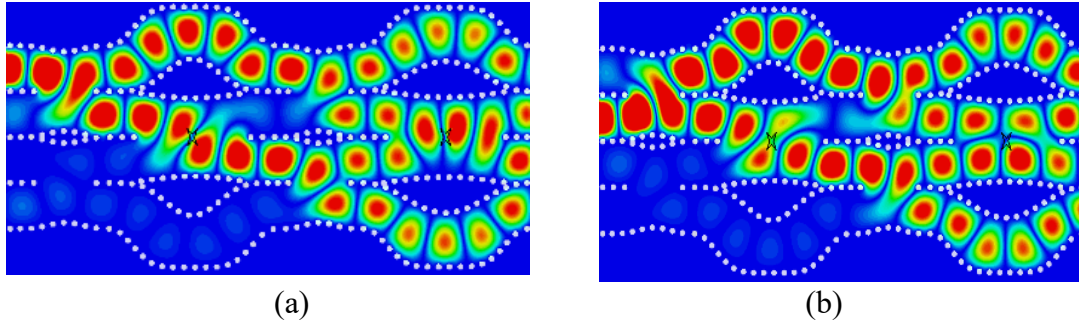


Figure 4.38: Electric field distribution of the proposed SIW Butler matrix. (a) Port 1 excitation. (b) Port 2 excitation.

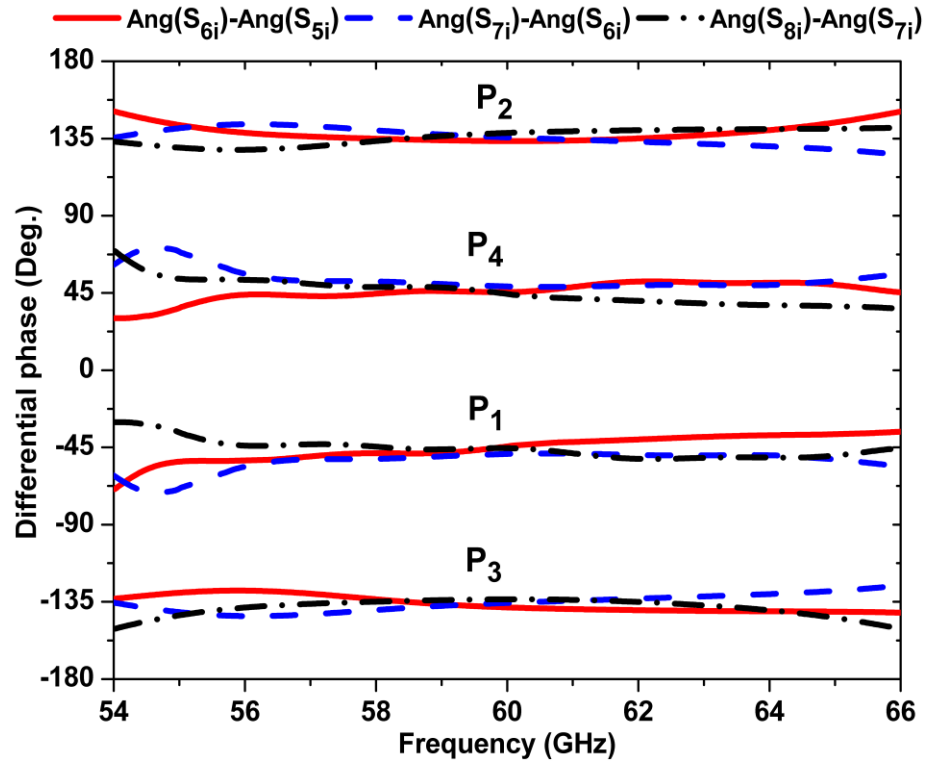


Figure 4.39: Output phase difference of Butler matrix. ( $P_i$ , port  $i$  excited, where  $i=1,2,3$  and  $4$ )

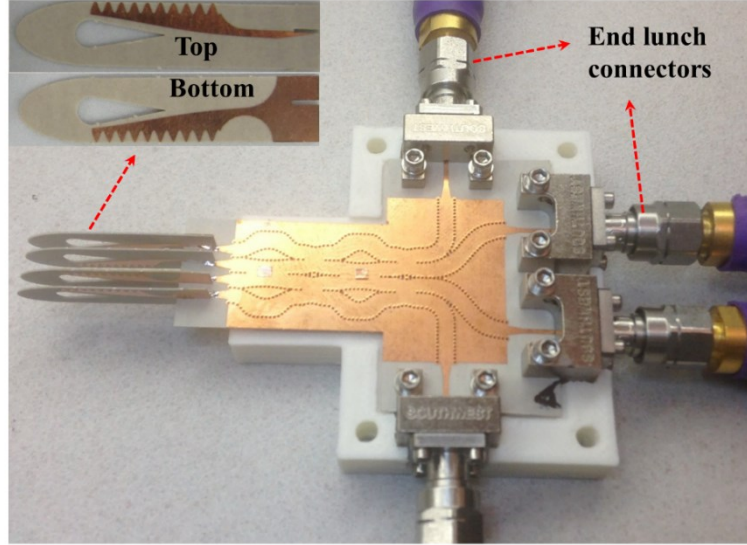


Figure 4.40: Photograph of the assembled prototype of the proposed multibeam end-fire FTSA array.

### 4.3.3 Fabrication and Measurements

As the width of the single element antenna is large compared to SIW width, it is quite difficult to arrange the radiating elements in E-plane direction, where the inter-element spacing is restricted by the SIW width. Therefore, to tackle this issue, the elements are arranged in a stacked H-plane configuration. Moreover, the stacked array is mirrored about the center line of the Butler matrix, which not only reduces the cross-polarization of the array, but also reduce the mutual coupling between radiating elements. Moreover, a wideband transition between the output ports of Butler matrix and the ports of radiating elements is designed and optimized to build up this configuration. The transition consists of SIW-to-MS transition and microstrip line  $90^\circ$  twist. In order to match the BFN with the radiating elements, the proposed microstrip  $90^\circ$  twist is configured by gradually changing the width of 50 ohm microstrip line of the antenna and the SIW-to-MS transition. An assembled prototype of the radiating elements and the Butler matrix with extended SIW ports is presented in Figure 4.40. As the size of the end launch connector is larger than the SIW width, the input ports of Butler matrix were extended curvedly in such a way that all ports can be connected simultaneously to perform the measurements. However, when one or two ports are connected to the measurement setup, the other ports were terminated with 50 ohm matched loads through 1.85 mm end launch connectors. The system performance in terms of S- parameters, were tested using Agilent N5227A vector network analyzer (VNA). Figure 4.41 shows the measured and simulated



reflection coefficients of the proposed multibeam array. It can be seen that the measured and simulated return loss of port 1 and 2 is better than -13 dB over the frequency range from 56 to 68 GHz. As depicted in Figure 4.42 (a), the measured and simulated isolation between port 1 and other ports 2-4 are less than -13 dB cross the frequency band 53-68 GHz. Also, the isolation between port 2 and other ports (1, 3 and 4) is less than -12.5 dB from 51 to 68 GHz as shown in Figure 4.42 (b). Note that, due the limitation of VNA used to measure  $S$ -parameters, the response is shown up to 67 GHz only. The measured and simulated results agree very well with each other.

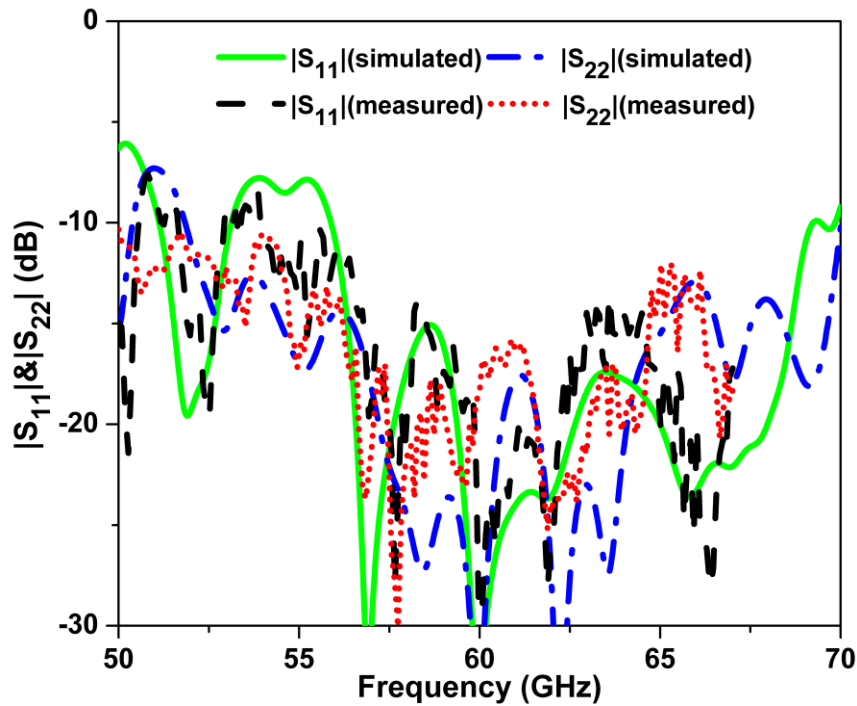


Figure 4.41: Measured and simulated reflection coefficients of the multibeam end-fire FTSA array for port 1 and 2 excitations.

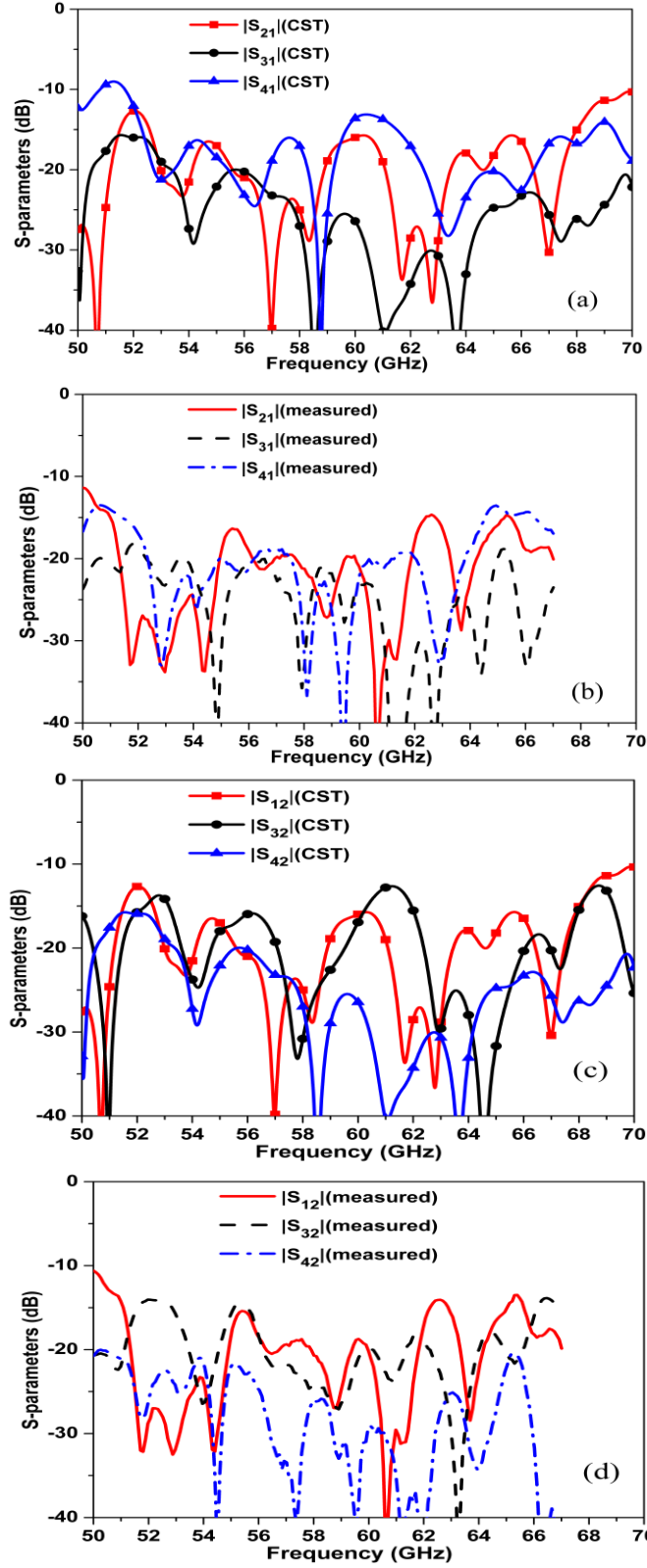


Figure 4.42: Measured and simulated isolation between input ports of the multibeam end-fire FTSA array for port 1 and 2 excitations.

Figure 4.43 illustrates the measured and simulated tilted beam patterns of the proposed multibeam array when only one of the input ports 1-4 is excited at each time while the others are terminated with 50 ohm matched loads. For measured and simulated results, It is clear that the directions of maximum radiation of tilted beams corresponding to input ports 1 and 4 are around  $\pm 14^\circ$ , whereas for ports 2 and 3 are around  $\pm 35^\circ$ . For ports 1 and 4, the side lobe level (SLL) is -12 dB and for ports 2 and 3 is -7 dB, which is higher than the theoretical value -13 dB, that mainly influenced by the relatively large size of the beam forming network. The measured -3 dB beamwidth of the tilted beams that generated by ports 1 and 4 is around  $21^\circ$ , whereas for those with port 2 and 3 is around  $27^\circ$ , with beam overlap level between inclined beams is almost -3 dB. Therefore, the four tilted beams are successfully coverage  $97^\circ$  in the azimuth direction, which is satisfactory for most 5G applications. The simulated and measured realized gain of the multibeam array fed by input ports 1 and 2 is shown in Figure 4.44. Due to the symmetry of the structure, the gain of port 3 and 4 should be similar. When port 1 is excited, the simulated and measured gain is fluctuated in the range of 15.5-16.6 dB and 14.3-15.6 dB, respectively, over the frequency band 56-65 GHz. For port 2 excitation, the simulated and measured gain falls within the range of 14-15 dB and 12.7-13.8 dB, respectively, cross the band 56-66 GHz. The discrepancy between measured and simulated gain is mainly due to the fabrication tolerance, connector mismatch, soldering effect and the loss tangent, which is given by the manufacturer at low frequency, does not reflect the precise value at 60 GHz.

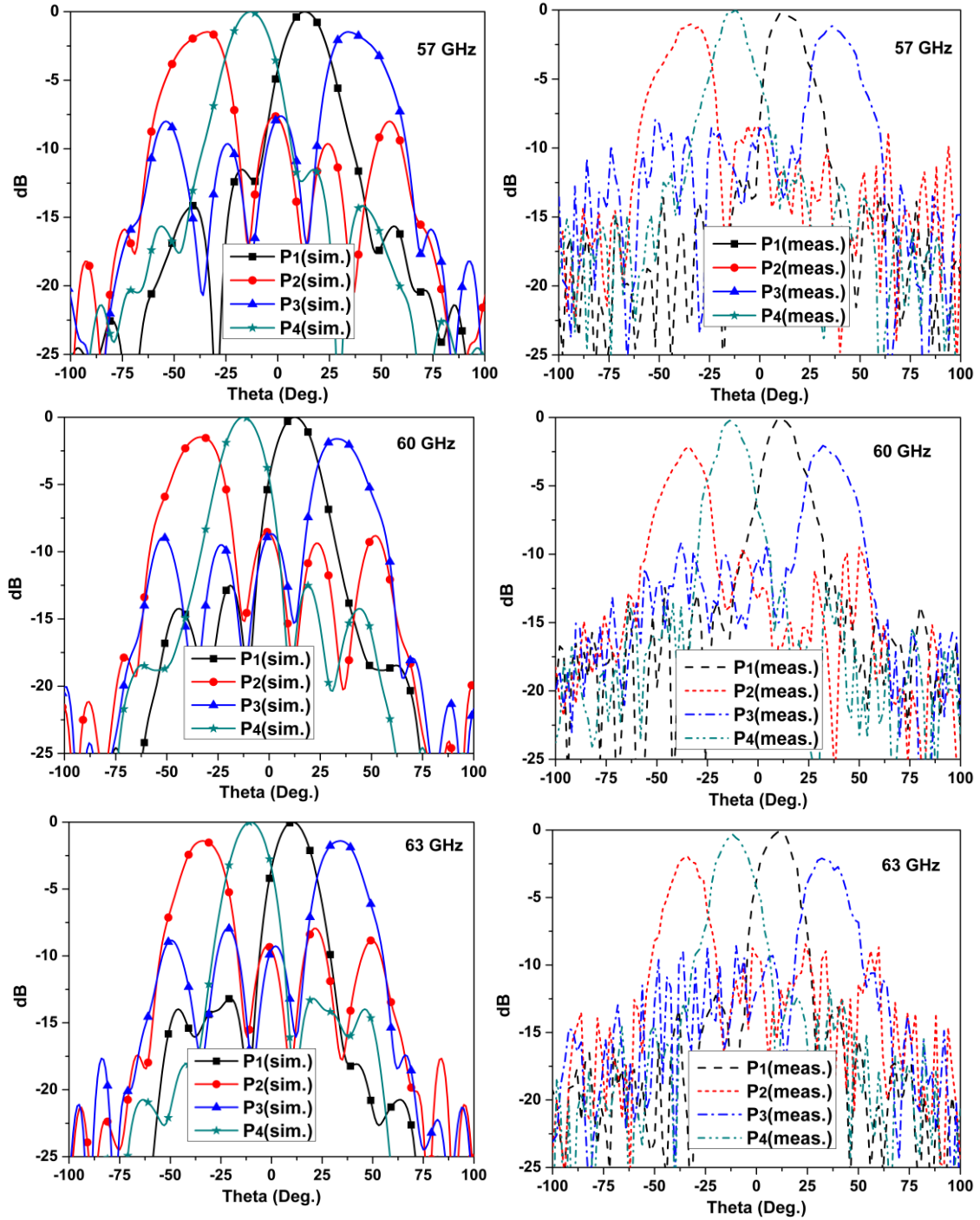


Figure 4.43 Measured and simulated radiation patterns of the proposed multibeam FTSA array.

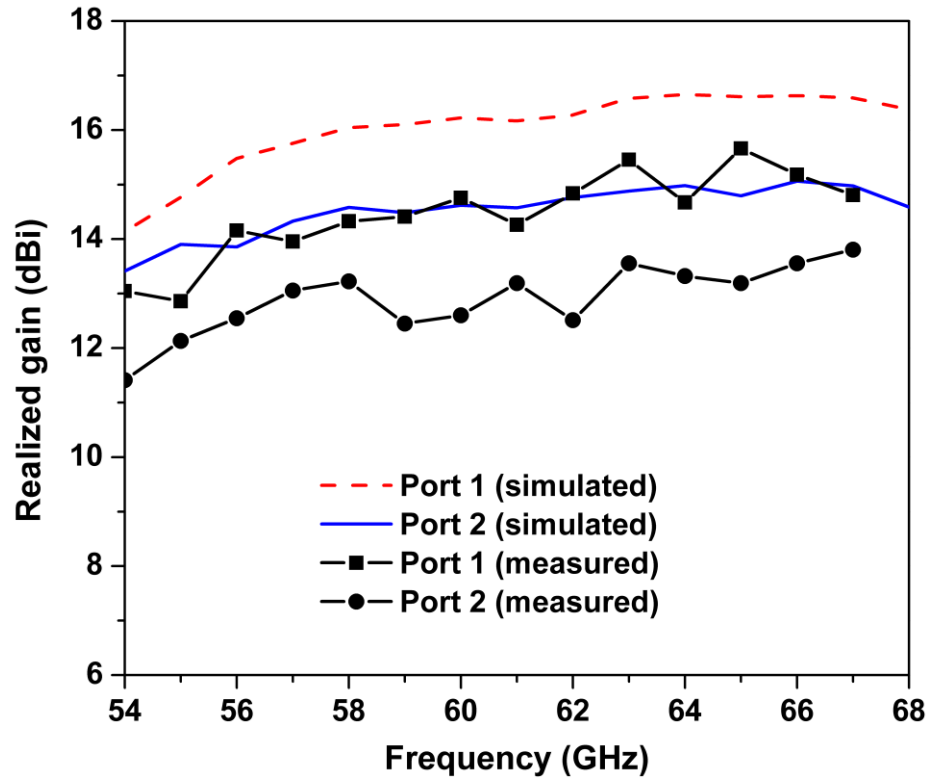


Figure 4.44: Measured and simulated gain of the FTSA array with port 1 and 2 excitation.

## **Chapter 5 Two-dimensional Scanning Multibeam Cavity-Backed Patch Antenna Array**

### **5.1 Introduction**

Recently, with the rapid development of smart wireless networks for 5G applications, two-dimensional (2-D) scanning phased array antenna with a passive beam-forming network (BFN) has been attracted much attention for high-speed data transfer, automotive radar systems and high-resolution imaging applications. The combination of the 1-D scanning based on phased-controlled BFN in azimuth plane and frequency-scanned leaky-wave source in the elevation plane to achieve 2-D beam-scanning capability [148] is not suitable for many applications that required a fixed beam over the operating band. In this chapter, we present a 2x2 multi-beam phased array employing a novel wideband linearly polarized (LP) cavity-backed patch antenna. A compact two-layered SIW-based BFN is utilized to feed the proposed 2-D scanning Array. This chapter is organized as follows. The geometry, principle of operation, and the simulated and measured performance of the novel LP antenna element are explained and investigated in section 5.2. The proposed beam-forming network and multibeam array design are introduced in section 5.3. The measurement and simulation results of the multi-beam array are discussed in section 5.4.

### **5.2 Single Element Design and Realization**

In addition to the BFN, the right selection of the single element is vital to the overall performance of the multibeam phased array. However, an antenna with symmetrical radiation pattern in both principal planes, low cross-polarization, low sidelobe levels, and stable gain over wide frequency range can be suitable for wideband 2-D scanning phased array antenna. A cavity-backed patch antenna can achieve all mentioned characteristics. Moreover, besides the compact profile and low-cost, cavity-backed antennas based on SIW technology are appropriate to arrange into an array and have the capability of suppressing the surface waves. Therefore, the SIW cavity-backed patch antenna has been adopted as a radiating element of the proposed multibeam array in this work.

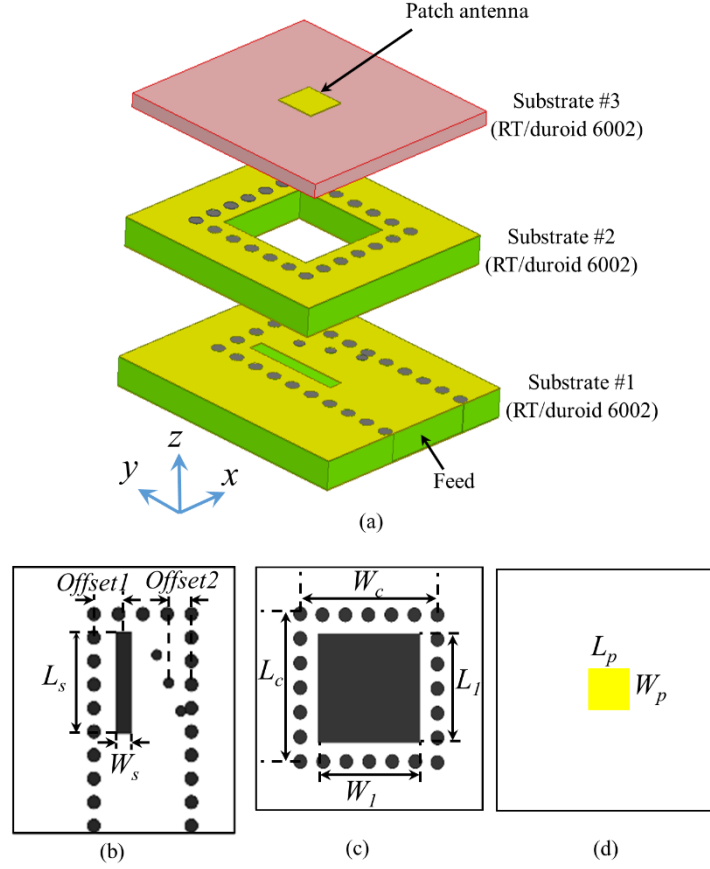


Figure 5.1: Geometry of the proposed cavity-backed patch antenna. (a) Exploded view. (b) Feed layer (substrate #1). (c) Cavity layer (substrate #2). (d) Antenna layer (substrate #3).

### 5.2.1 Geometry and Working Principle

The geometry of the proposed SIW cavity-backed patch antenna is depicted in Figure 5.1. The overall structure consists of three PCB layers. The bottom substrate represents the SIW feed layer (substrate #1); the intermediate substrate represents cavity layer (substrate #2), and the top substrate represents the patch antenna layer (substrate #3). The cavity walls and SIW feeding structure are formed by rows of plated via holes with via diameter of  $d=0.3$  mm and the spacing between adjacent via is  $p=0.54$  mm. To prevent the electromagnetic wave leakage and minimize the radiation loss, and to satisfy the two conditions  $p \leq 2d$  and  $d/\lambda_g < 0.2$ , where  $\lambda_g$  is the guided wavelength at the operating frequency. The width of the SIW feed ( $W_{siw}=2.25$  mm) is designed to prevent the higher-order mode from propagating into the SIW within the frequency range of interest. Detailed dimensions of the antenna are listed in Table 5.1. In this design, substrates 1 and

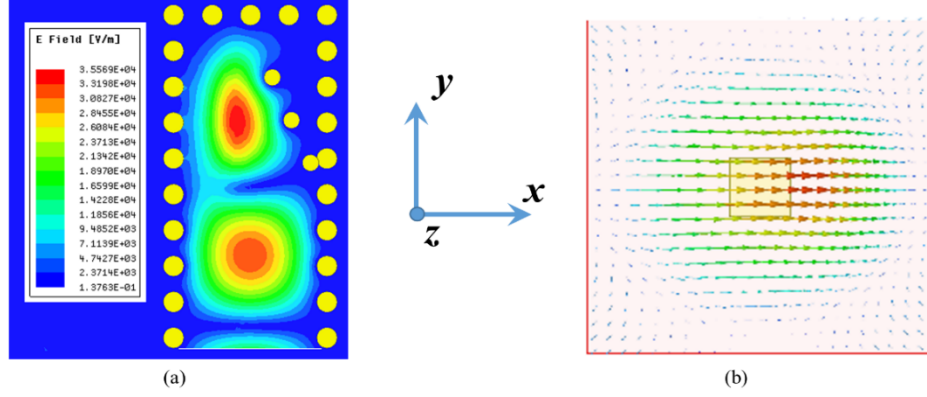


Figure 5.2: Electric field distribution at different layers of the proposed cavity-backed patch antenna: (a) E-field magnitude of the  $TE_{10}$  mode in SIW feed (b) radiating E-field above the patch at height of 1 mm.

Table 5.1: Dimensions of the proposed antenna.

Parameter	Value (mm)	Parameter	Value(mm)
$L_s$	2.25	$W_p$	0.9
$L_p$	0.9	$W_c$	3.1
$L_c$	3.1	$W_l$	2.3
$L_l$	2.3	<i>Offset1</i>	0.7
$W_s$	0.34	<i>Offset2</i>	0.52

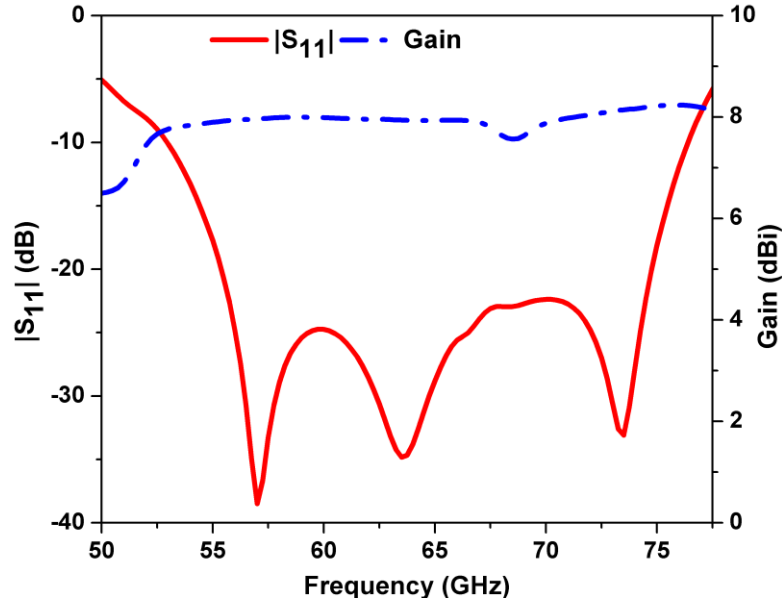


Figure 5.3: Simulated reflection coefficient and gain of the single cavity-backed patch antenna.



2 are 0.508 mm-thick Rogers RT/ Duroid 6002 laminate with a dielectric constant of 2.94, a loss tangent of  $\tan \delta = 0.0012$ , and copper cladding of  $18 \mu\text{m}$ . Substrate 3 is Rogers RT/ Duroid 5880 with a dielectric constant of 2.2 and loss tangent of 0.0009. To reduce the surface wave in the patch antenna layer, the thickness of substrate 3 should be relatively small (0.254 mm). A longitudinal offset slot with length  $L_s$  and width  $W_s$  is etched on the top ground plane of the SIW feed layer and placed at a distance of about 5 mm from the shorted-end wall, which effectively couples the energy from the feed layer to the SIW cavity. The square cavity is formed using plated vias in substrate 2. As the dielectric permittivity of the substrate increases, the cavity tends to confine the energy, thus increasing the quality factor and resulting in a narrow bandwidth and lower radiation efficiency. Therefore, filling the cavity with a lower permittivity substrate will further enhance the bandwidth and efficiency. To do so, part of the substrate filling of the SIW cavity is cut out, forming an air-filled cavity. The only amount of substrate that remains inside the cavity is for fabrication tolerance. A microstrip patch antenna is designed on the top of substrate 3, which has a lower permittivity and small thickness compared to substrates 1 and 2 in order to improve the matching and reduce the potential surface waves excited in the antenna layer. Moreover, three inductive matching vias with a radius of 0.12 mm and different offsets from the sidewall are embedded in the SIW feed, which acts as guidance to concentrate the electromagnetic energy underneath the coupled slot as shown in Figure 5.2 (a), thus leading to widened impedance bandwidth and further enhance the coupling between the feed and the cavity layer. As the dominant mode ( $\text{TE}_{10}$ ) in SIW generates an electric field at both sides of the slot with opposite phases, resulting in a transverse electric field across the slot. When the cavity is excited by the longitudinal slot placed at its center, the  $x$ -axis components of the E-field (transverse E-fields) along the two edges of the radiating slot are in phase, while the E-field components along the  $z$ -axis direction cancel out as they are out of phase. Besides working as a radiating element, the cavity acts as a reflector for the patch antenna as well. At the patch antenna level, the  $x$ -axis components of the E-field at the two edges of the patch are in phase, whereas the  $y$ - and  $z$ -components are out of phase. Consequently, the only radiating E-fields above the patch antenna will be the  $x$ -axis components as shown in Figure 5.2 (b), leading to a pure linear polarization (LP) antenna with low cross polarization. All simulated results are carried out using a 3-D full-wave electromagnetic solver, Ansoft HFSS.

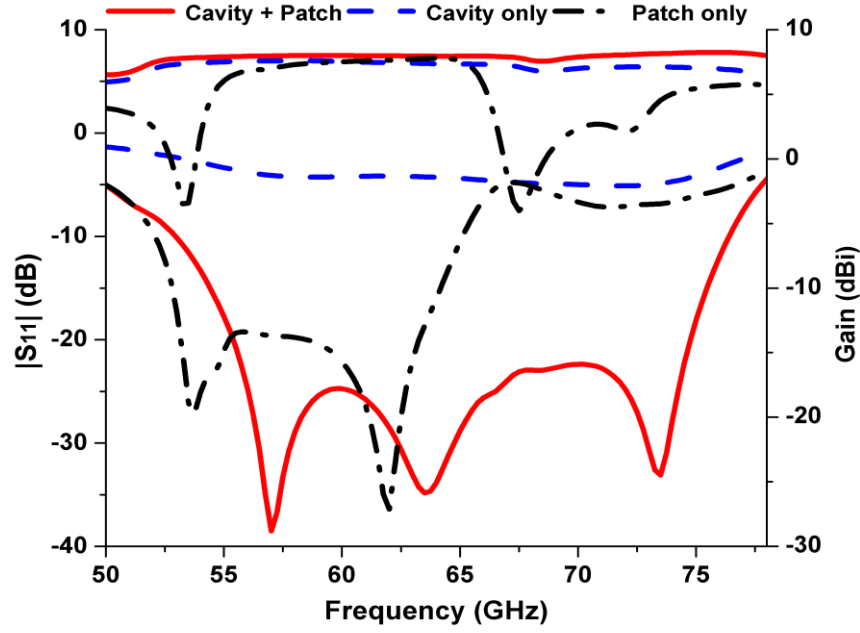


Figure 5.4: Comparison of the proposed antenna with cavity-only and patch-only antennas in terms of  $|S_{11}|$  and radiation gain.

### 5.2.2 Antenna Performance

The simulated reflection coefficient and realized gain versus frequency of the single element antenna are shown in Figure 5.3. The impedance bandwidth for  $|S_{11}| \leq -10$  dB is 36.2 %, ranging from 53 to 76.4 GHz, and it is below -22 dB from 55.5 to 74.5 GHz. The antenna exhibits a very flat gain of 8 dBi with a peak-to-peak variation less than 0.6 dB over the entire band of interest. The patch antenna size, coupling slot and the three matching vias are the key parameters to control the operating frequency and impedance matching. To further understand the radiation mechanism and options of different components of the proposed antenna, two other configurations, i.e., a cavity antenna without a patch and a patch antenna without backed cavity have been simulated. The design parameters, as shown in Figure 5.1 (b), are optimized for good impedance matching.

Comparisons between the proposed and two other structures regarding return loss and gain are depicted in Figure 5.4. It can be seen that the radiating patch has entirely affected the impedance matching, as deduced from the total mismatch of the cavity-only case. When the backed cavity is removed, i.e., patch-only case, the bandwidth becomes narrower and ranges from 52 to 65 GHz,

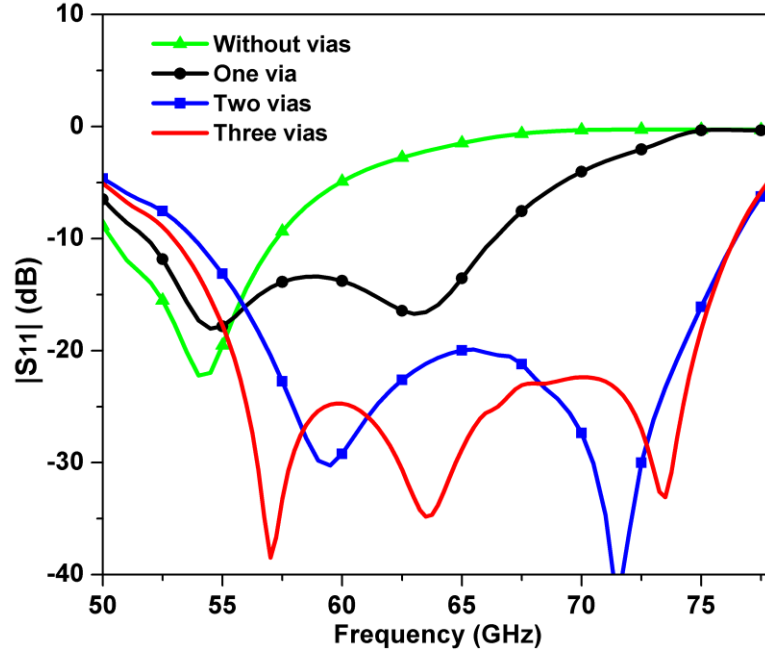


Figure 5.5: The effect of number of vias on the reflection coefficient.

similar to results reported in [66]. As compared to the proposed structure, the radiation gain of the cavity antenna is reduced by the average value of 0.4 dB in the frequency range of 53-65 GHz and by about 0.8 dB in range 65-76.5 GHz. As for the patch structure, the radiation gain is almost the same as that of the cavity within the range of 56-65 GHz and drops dramatically outside this range, even though the matching is better than that of the cavity antenna. The reason is that the cavity antenna suppresses the surface wave and directes most of the energy in the boresight direction. Moreover, the effect of the matching vias on the return loss has been investigated as depicted in Figure 5.5. It obvious that the case without vias has the narrowest bandwidth. Moreover, the matching and impedance bandwidth increases as the number of vias increases. Note that, in all cases in Figure 5.5, the vias and slot offsets (i.e. offset1 and offset2 as shown in Figure 5.1 (b)) are optimized for a good impedance match. The simulated E-plane ( $xoz$  plane) and H-plane ( $yo z$  plane) radiation patterns of the backed-cavity patch antenna are illustrated in Figure 5.6. The -3dB beam width is almost  $70^\circ$  for the E- and H-plane, except at 53 and 57 GHz, which increase to  $80^\circ$  and  $75^\circ$  in the H-plane, respectively. The front to back radiation value of about -20 dB, which is acceptable for most MMW applications and multibeam forming techniques. It is observed that the proposed antenna has an excellent symmetrical radiation pattern in all planes. The simulated

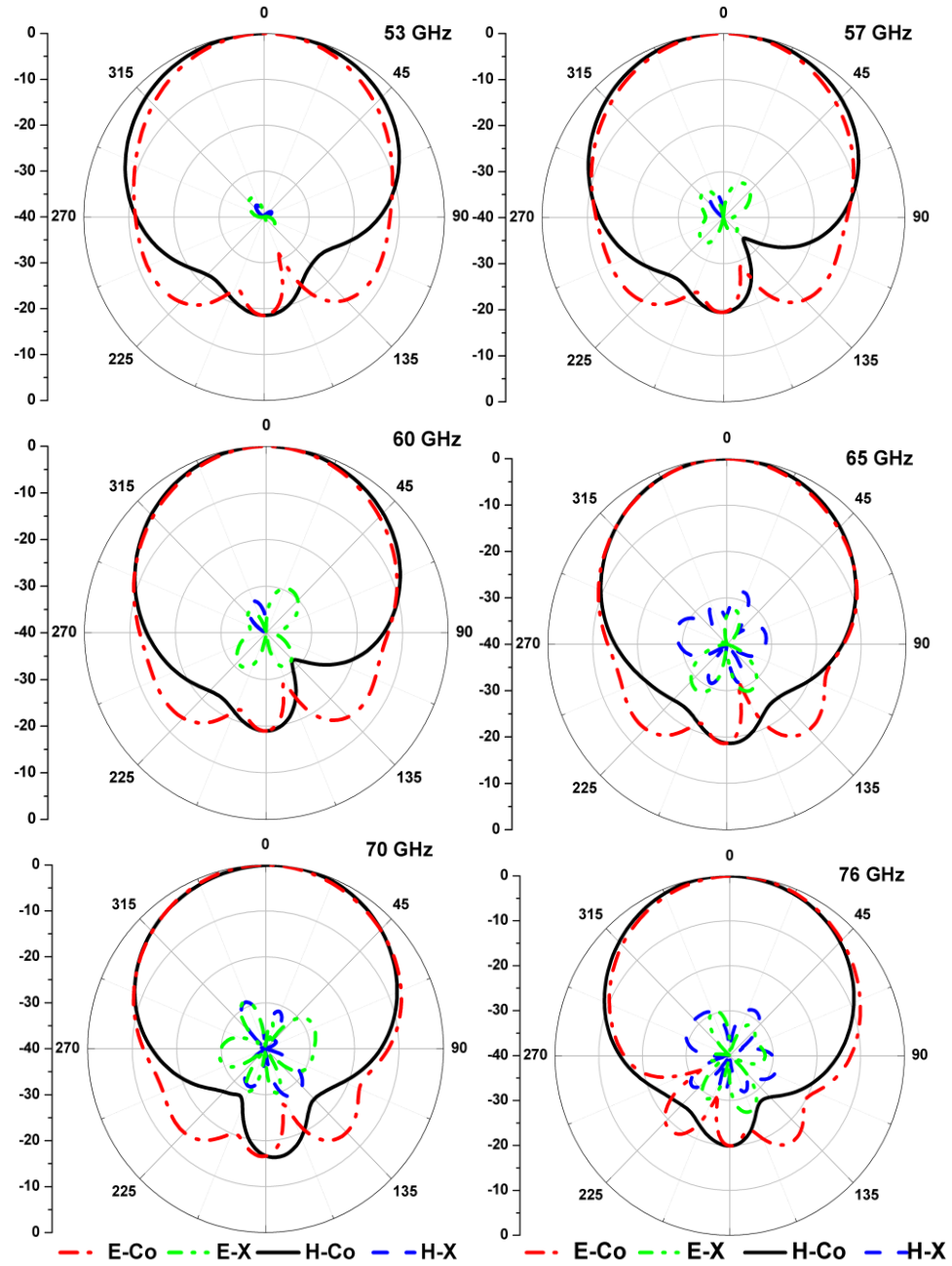


Figure 5.6: Simulated E- and H-plane radiation patterns of the proposed cavity-backed patch antenna at 53, 57, 60, 65, 70, and 76 GHz.

radiation efficiency of the proposed antenna is better than 96% with a maximum value of 98% at the band center as shown in Figure 5.7.

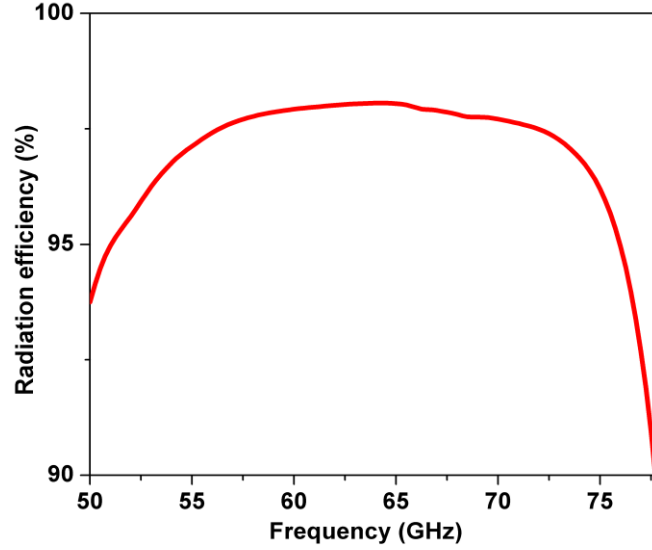


Figure 5.7: Simulated radiation efficiency of the proposed cavity-backed patch antenna.

The performance of the proposed antenna in this work and other published 60-GHz LP antennas are summarized in Table 5.2. It is clear that the proposed antenna has a wide 1-dB gain bandwidth, with only gain variation of less than 0.6 dBi over the entire band. Although the design in [66] has a simple structure and relatively wide bandwidth, the radiation pattern is unsymmetrical and has a high ripple in the E-plane. The 18-layer LTCC DRA in [149] shows a stable gain over a wide bandwidth. Such a large number of layers increases the complexity and cost. The series-fed E-shaped patch antenna in [67] exhibits relatively wide bandwidth and high gain, but the microstrip feed lines tend to radiate at high frequency; thus, they are not suitable for array designs. The low-cost cavity-backed dipoles in [79] demonstrate a wide bandwidth and high gain with relatively high cross-polarization. In [91], the cavity-backed antenna illustrates a wide bandwidth and low cross-polarization, but the metallic cavity utilized in the structure relatively increases the complexity and cost. However, except for the cross-polarization in [91], the proposed structure has the wider 1-dB gain bandwidth and lower cross-polarization compared to published work listed in Table 5.2.

Table 5.2: Comparison among proposed and reported 60-GHz LP antenna.

Ref.	Antenna type	X-pol. (dB)	FBW% (GHz)	1-dB Gain B.W.	Gain (dBi)
[66]	Rectangular patch	n. a.	22.1 % (56.3-70.3)	19 %	5.7-6.8*
[149]	DRA	n.a.	24.9 % (54.5-70)	24%	6.6-7.76
[67]	E-shaped patch	n.a.	22 % (51.5-64.1)	18 % *	7.4-9.2*
[79]	Cavity backed dipoles	-19	38.7 % (50-74 )	31.5%*	7.5-9.4
[91]	Cavity backed patch	-30	29.6% (49.6-66.8)	21%*	7-8.5
This work	Cavity backed patch	-28	36.2% (53-76.4)	36.2%	7.6-8.2

\* estimated graphically

### 5.2.3 Measurement of Single Element

To validate the proposed design, a prototype of the cavity-backed patch antenna with an SIW to standard WR-15 waveguide transition is fabricated as shown in Figure 5.8. Each layer is fabricated separately using low-cost standard PCB technology, and then assembled together by a few screws without any adhesive. Since the distance between assembly screws is small and the substrate layers are stacked perfectly, the effect of air gaps between layers is negligible. The simulated and measured return loss and radiation gain of the cavity-backed patch antenna are shown in Figure 5.9. The simulated reflection coefficient shows a fractional impedance bandwidth of 38 % (52.4-77GHz) for  $|S_{11}| \leq -10$  dB, which increases about 1.2 GHz compared to simulated results without WR15-to-SIW transition. The measured and simulated gain exhibits a stable response over the band of interest with a maximum value of 8.4 dBi. The measured results show perfect agreement with the simulations. Due to the limitations of the measurement setup, the tests above 67 GHz are not available. The measured results are carried out with an Agilent N5227A vector network analyzer (VNA), where the losses of the WR15-to-coaxial adapter are calibrated using a TRL calibration kit as depicted in Figure 5.10. The measured E- and H-plane radiation pattern of the proposed antenna is compared to the simulation results in Figure 5.11. It can be seen that the measured results of the co-polar pattern agree well with the simulations. The measured and simulated cross-polar pattern is better than -20 dB and -28 dB, respectively, over the entire band. The difference between the measured and simulated results of the cross-polar pattern may be attributed to the high level of the noise floor, the limited dynamic range of the measurement setup

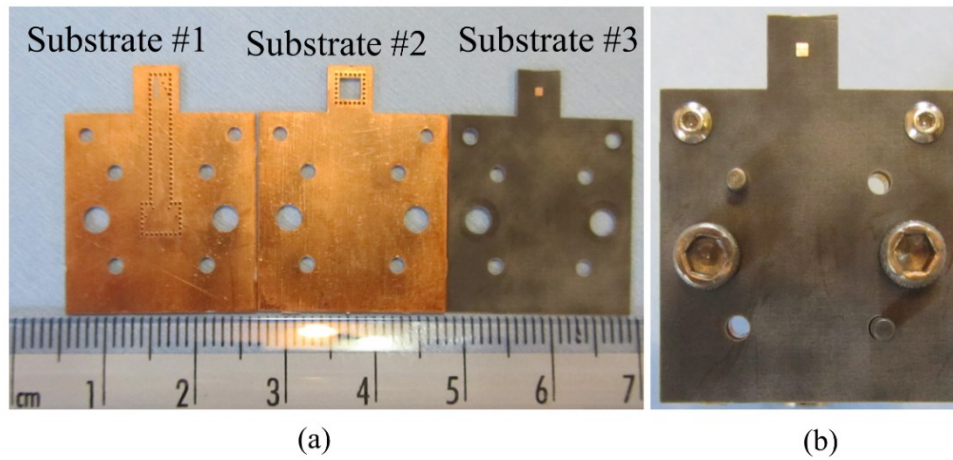


Figure 5.8: Fabricated prototype of the proposed cavity-backed patch antenna element. (a) Disassembled. (b) Assembled.

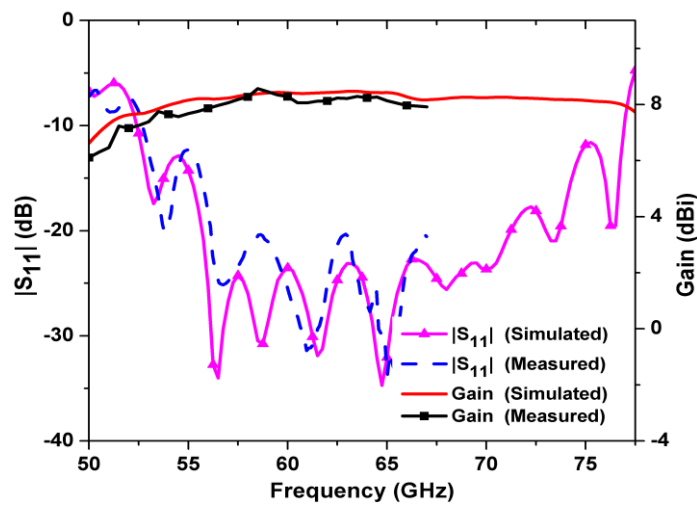


Figure 5.9: Simulated and measured  $|S_{11}|$  and radiation gain of cavity-backed patch antenna element.

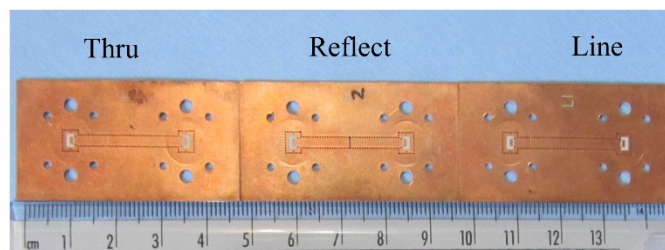


Figure 5.10: Photograph of TRL calibration kit used to de-embed the WR15 to coaxial and transition from measurements.

and unpredictable reflections from the cables. Note that the measured radiation pattern ranges from  $-120^\circ$  to  $+120^\circ$  due to the limited measurement setup.

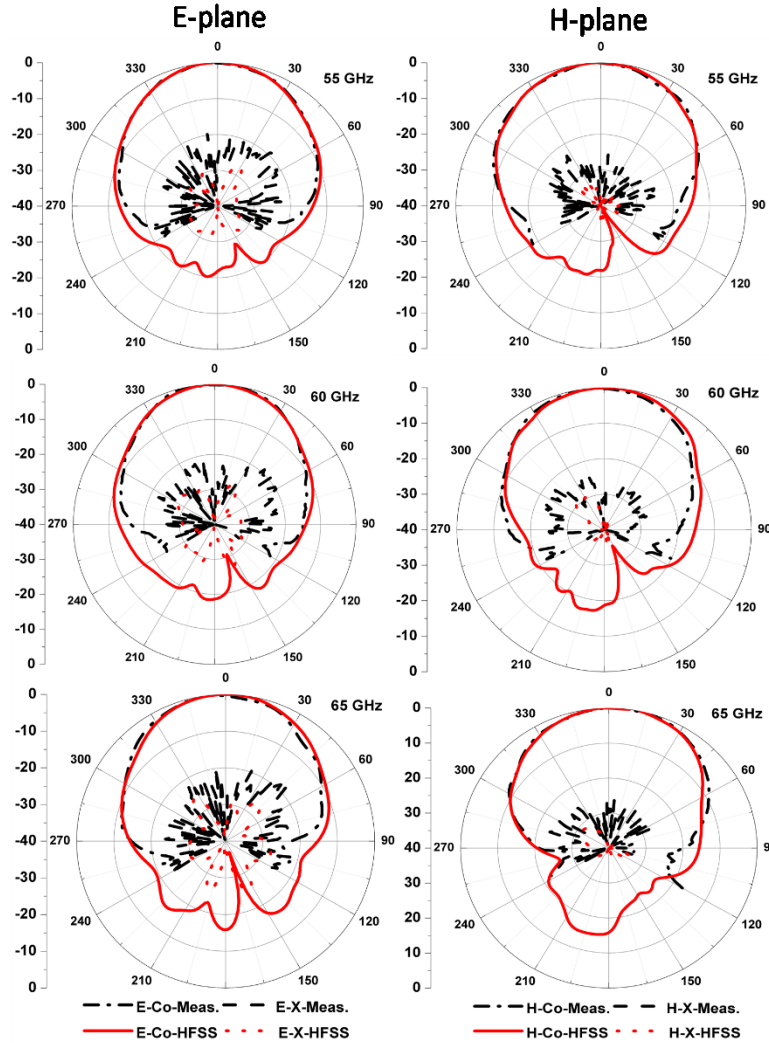


Figure 5.11: Comparison between measured and simulated radiation patterns for E- and H-plane of the cavity backed patch antenna element at 55, 60, 65 GHz.

### 5.3 2-D Multibeam Array

The cavity-backed patch antenna designed in the previous section is employed as a radiating element to construct a 2-D multibeam 2x2 antenna array. Moreover, the modified version of SIW-to-WR15 transition [150] with extended SIWs is utilized to excite the array. The array geometry and beam forming network are presented and discussed in the following subsections.



### 5.3.1 Antenna Array Structure

The perspective view of the whole geometry of the multibeam 2x2 antenna array is illustrated in Figure 5.12. The antenna array comprises four layers stacked on top of one another. Substrates 1 and 2 are employed to build up the proposed compact BFN. In order to measure the s-parameters and radiation performance of the antenna array, the SIW-to-WR15 transitions with extended SIWs are designed on layer 1, where the distance between transitions is chosen to fit the size of the WR15 waveguide loads. The two big holes and four small holes around each transition are used for the screws and dowels, respectively, which are applied to align and fix the WR15 waveguides. 2x2 SIW backed cavities are designed on substrate 3, whereas a 2x2 patch antenna array is printed on the top of layer 4, which has lower permittivity with a relatively small thickness in order to reduce the surface waves. The inter-element spacing in x and y directions (i.e.,  $d_x$  and  $d_y$ ) is 3.3 mm, corresponding to  $0.66 \lambda_0$  at 60 GHz. The signal is transferred between different layers through longitudinal coupling slots.

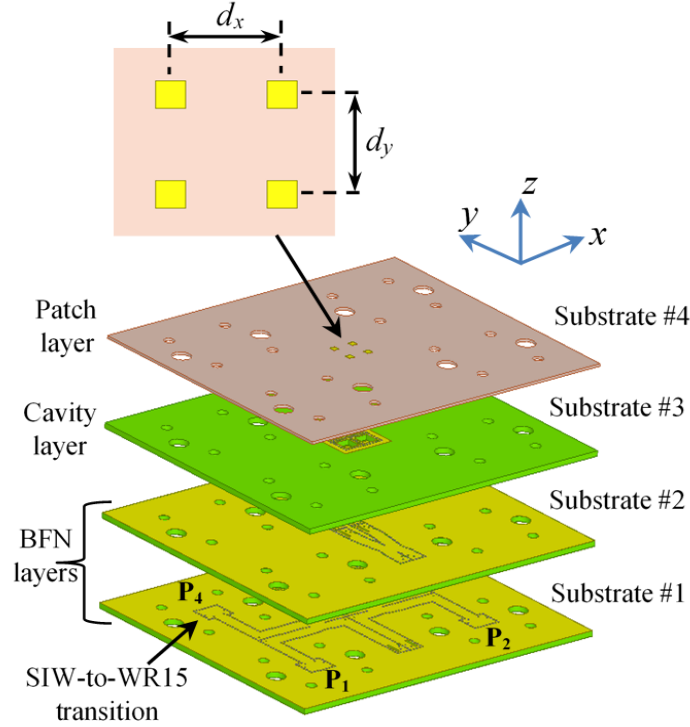


Figure 5.12: Exploded view of the proposed multibeam 2x2 cavity-backed patch antenna array. (Substrates #1 to #3 are 0.508-mm thick Rogers 6002 and substrate #4 is 0.254-mm thick Rogers 588 coupling slots.

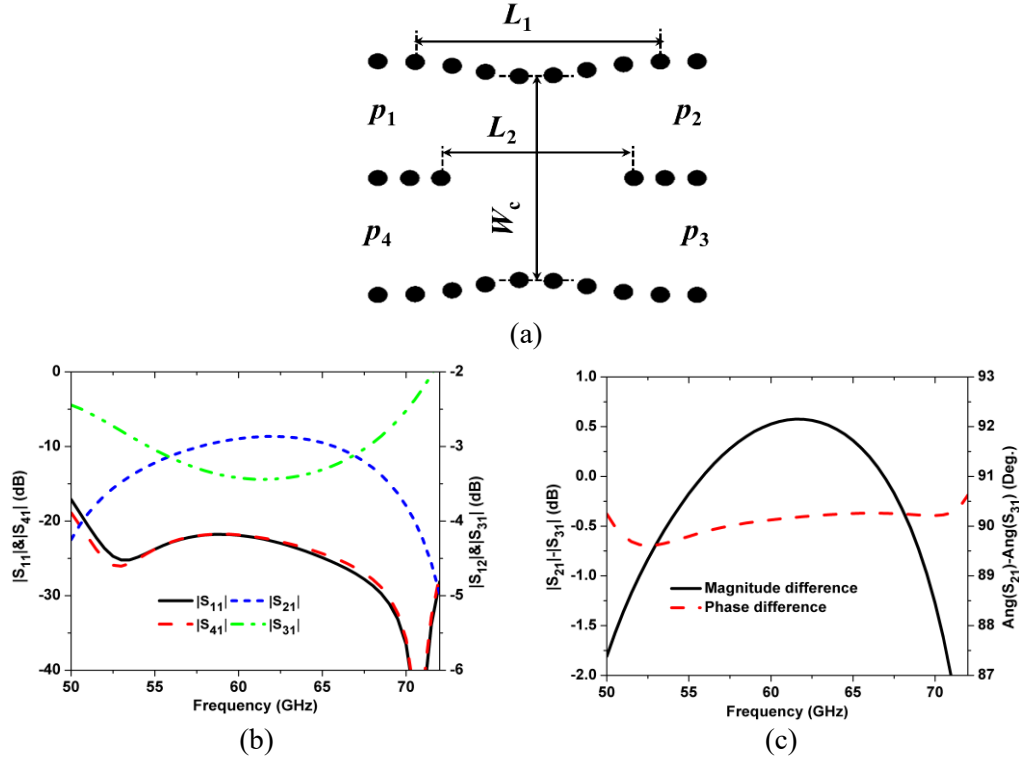


Figure 5.13: SIW 90° hybrid coupler. (a) Geometry ( $L_1 = 3.75$  mm,  $L_2 = 3.06$  mm and  $W_c = 3.9$  mm). (b) Simulated s-parameters. (c) Differential magnitude and phase of output ports.

### 5.3.2 Beamforming Network

A 3-dB 90° hybrid coupler is an essential of the BFN, and a well-designed coupler leads to an equal amplitude with a 90° phase difference of output ports. The topology of the SIW 3-dB hybrid coupler is shown in Figure 5.13 (a). The required power coupling ratio and differential phase of output ports can be achieved by adjusting the dimensions of the coupling region. In addition, the impedance matching of the input port (port1) and isolation is improved by controlling the length of the coupler. As shown in Figure 5.13 (b), the impedance bandwidth of the SIW coupler is larger than 34% for a return loss better than 20 dB. The isolation between ports 1 and 4 is better than 20 dB over the entire band of interest. The insertion loss is less than 0.25 dB within a frequency range from 53 to 69 GHz. Moreover, the differential magnitude is less than 0.6 dB in the frequency range 53-69 GHz as shown in Figure 5.13 (c). The differential phase of output ports is 90° with peak-to-peak error less than 0.80 over the whole band, which agrees with the ideal value. The proposed two-layered SIW BFN has four input ports P1-P4 on layer 1 and four output ports P5-P8 on layer

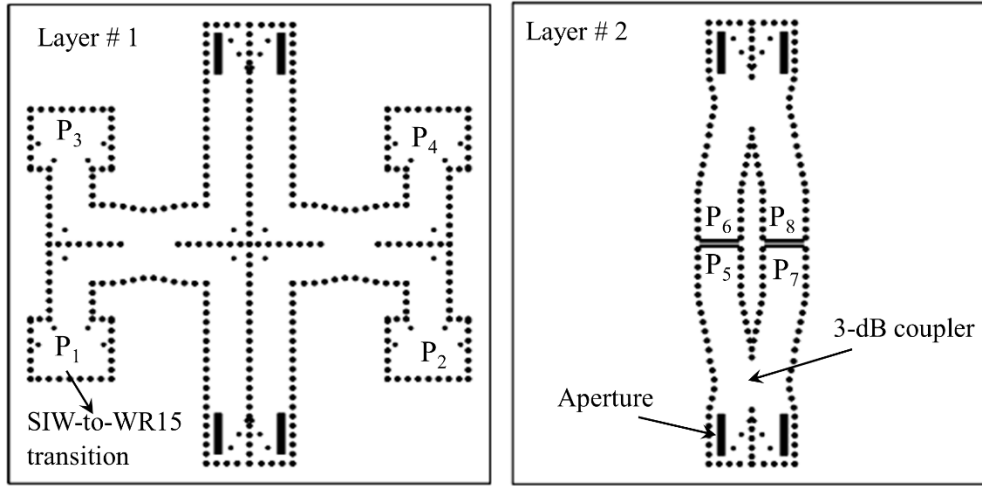


Figure 5.14: Geometry of the proposed SIW beam-forming network.

Table 5.3: Theoretical phase of the output ports of the proposed BFN

	Port5	Port6	Port7	Port8
Port1	$0^0$	$-90^0$	$-90^0$	$-180^0$
Port 2	$-90^0$	$-180^0$	$0^0$	$-90^0$
Port 3	$-90^0$	$0^0$	$-180^0$	$-90^0$
Port 4	$-180^0$	$-90^0$	$-90^0$	$-0^0$

2 as shown in Figure 5.14. The four input ports are connected to the two hybrid couplers through SIW-to-WR15 waveguide transitions, whereas the output ports are directly connected to the two hybrid couplers. The signal is coupled between couplers on the two layers using four  $180^0$  bends. For input ports P1-P4 excitation, the ideal phase values of output ports P5-P8 are listed in Table 5.3. Simulated s-parameters of the BFN with port 1 excitation are shown in Figure 5.15 (a). It can be seen that the  $|S_{11}|$  is less than -16 dB in the frequency range 51.5-70.5 GHz. Within a frequency range from 52 to 72 GHz, the isolation between input ports is  $<-37$  dB for  $|S_{21}|$ ,  $<-15$  dB for  $|S_{31}|$  and  $<-22$  dB for  $|S_{41}|$ . It is obvious that the isolation between ports 1 and 2 is high compared to other ports, which is reasonable as the signals reflected back from output ports 5 and 7 will be  $180^0$  out of phase with those of ports 6 and 8, thereby canceling each other at port 2. The magnitude of simulated transmission coefficients is  $6.7 \pm 0.6$  dB in the frequency range from 53 to 69.5 GHz with  $|S_{51}|$  decreases to -7.6 dB in the vicinity of 54.5 GHz.

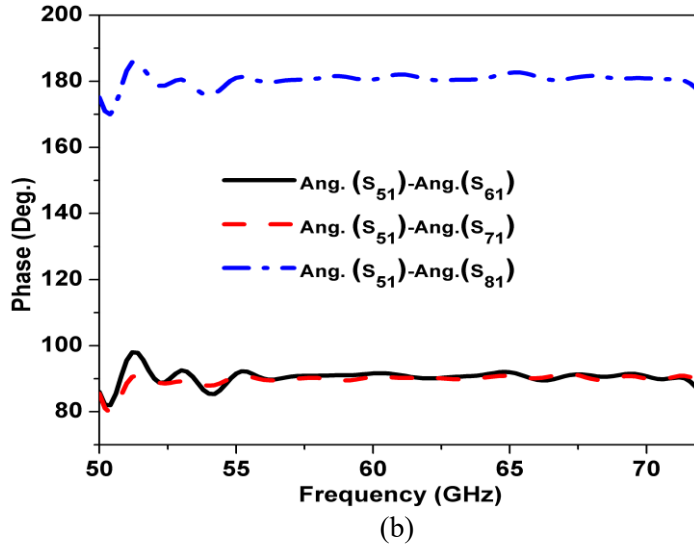
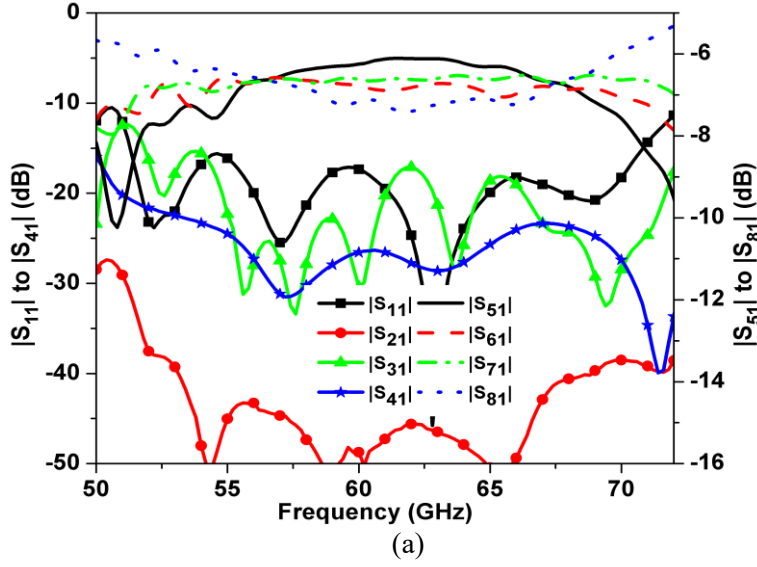


Figure 5.15: BFN performance with port 1 excitation. (a) S-parameters performance. (c) Phase differences between output ports.

Moreover, the average value of the insertion loss with port 1 excitation is below 1.3 dB over the band of interest ,as calculated from (5.1),

$$Il = -10 \log(|S_{51}|^2 + |S_{61}|^2 + |S_{71}|^2 + |S_{81}|^2) \quad (5.1)$$

Figure 5.15 (b) shows the phase differences between the output ports of the proposed BFN with port 1 excitation. Within the frequency range from 55 to 71GHz, the phase difference between output port 5 and output port 6 and 7 is  $90^\circ$  with a peak-to-peak phase error of less than  $2^\circ$ , while

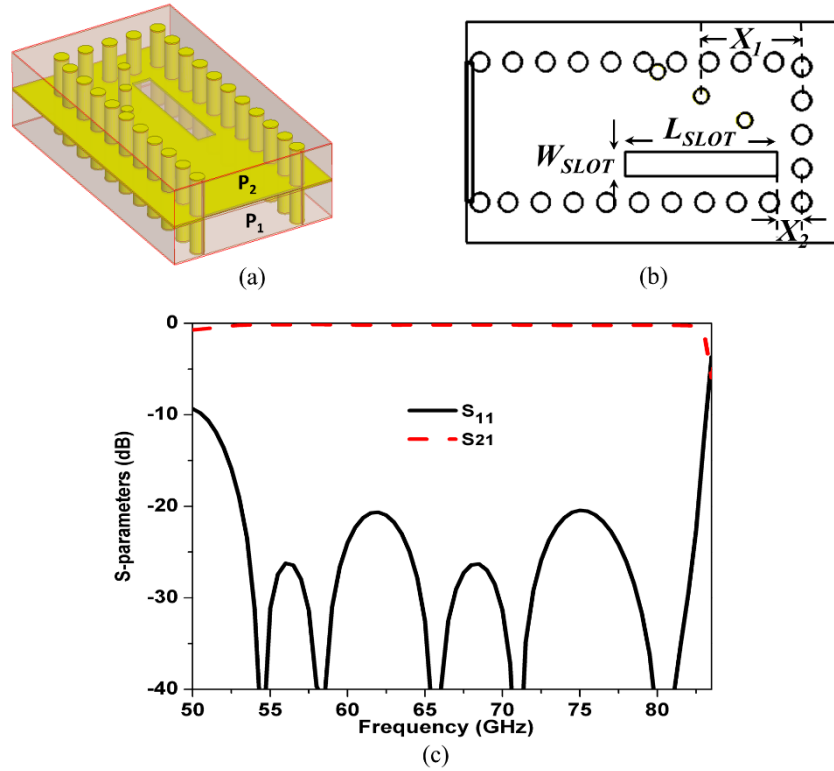


Figure 5.16: The proposed SIW E-plane 180° bend. (a) Perspective view. (b) Top view (where  $W_{slot} = 0.4$  mm,  $L_{slot} = 2.5$  mm,  $X_1 = 1.66$  mm and  $X_2 = 0.4$  mm) (c) Reflection and transmission coefficient.

the difference between ports 5 and 8 is 180° with a peak error less than 2.5°. The geometry, with the detailed dimensions of the proposed SIW E-plane 180° bend, is depicted in Figure 5.16 (a) and (b). The bend is formed by placing two short-ended SIWs on top of each other with the longitudinal slot etched onto the broad common wall. Three inductive posts with different offsets are employed to improve the impedance bandwidth of the 180° bend. The simulated impedance bandwidth is 48.7% for  $|S_{11}| < -10$  dB (50.5-83 GHz), as can be observed in Figure 5.16 (c). The main benefit of using an SIW aperture-coupled feed method is to excite the radiating elements over a wide band with complete isolation from the feed network. The proposed two-layered BFN has dimensions of  $5.1 \lambda_0 \times 4.2 \lambda_0$  ( $\lambda_0$  is the free space wavelength at 60 GHz), achieving a size reduction of 28 % compared to a conventional one-layered BFN ( $5 \lambda_0 \times 6 \lambda_0$ ), designed on the same substrate. Moreover, comparisons with other reported work are listed in Table 5.4. As can be seen from this table, the proposed BFN shows a size reduction of 59% and 39% compared to the conventional BFN in [151] and [152], respectively.

Table 5.4: Comparison between proposed BFN and other work

Ref.	Frequency	Substrate	BFN	Size ( $\lambda_o^2$ )*
[151]	30 GHz	Rog. 5880	SIW	7.3 x 7.2
[152]	60 GHz	Rog. 4003 C	SIW	6.4 x 5.5
This work	60 GHz	Rog. 6002	SIW	5.1 x 4.2

\*  $\lambda_o$  is the free space wavelength at the center frequency.

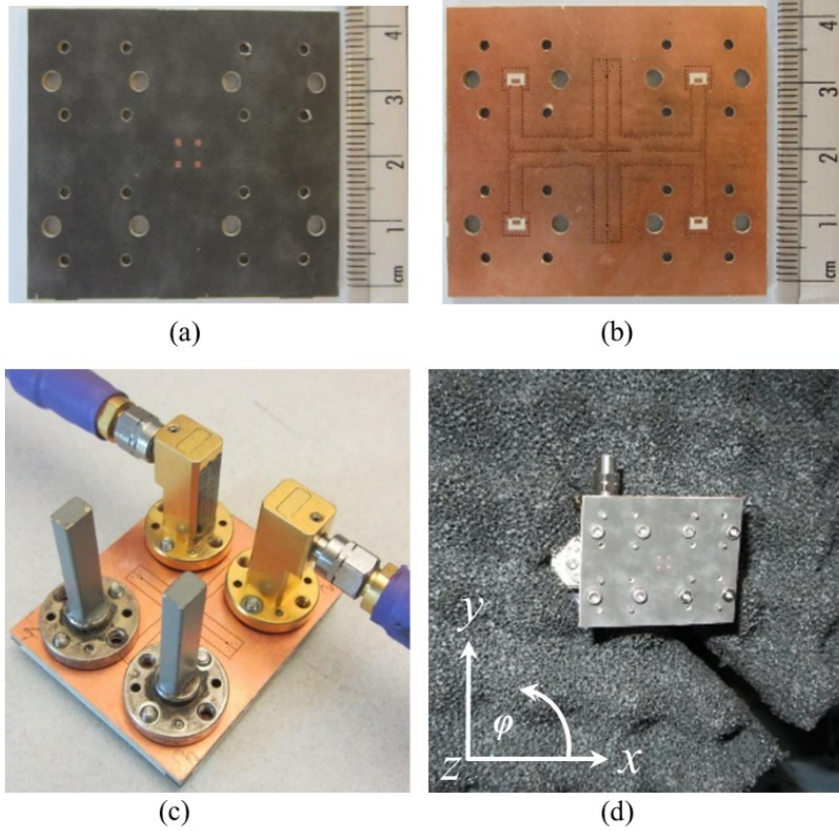


Figure 5.17: Fabricated prototype of the proposed multibeam cavity-backed patch array. (a) Top view (b) Bottom view. (c) Prototype connected to WR15 waveguides for s-parameters test. (d) Prototype inside the anechoic chamber for radiation pattern test.

## 5.4 Measurement Results and Discussion

A fabricated prototype of the proposed multibeam array is presented in Figure 5.17 (a) and (b). Figure 5.17 (c) and (d) show photographs of the fabricated prototype connected to WR15 waveguides for s-parameters and radiation pattern measurement, respectively. Each layer is fabricated using low-cost PCB technology, then all layers are assembled using an adhesive and pressure in order to avoid air gaps between the different layers.

For the s-parameters test, all ports are connected to WR15 waveguide loads except the ports under test as shown in Figure 5.17 (c). The measured and simulated return loss and isolation of input ports with port 1 excitation are shown in Figure 5.18. It can be observed that the impedance bandwidth is 34.5 % (51.5-73 GHz) for  $|S_{11}| < -10$  dB. The measured and simulated isolations between port 1 and input ports 3 and 4 are better than 15 dB over the frequency range 53.8 to 73 GHz. The isolation between port 1 and 2 is less than -20 dB within the band of interest. The broadband characteristics of the BFN and radiating element enable the proposed multibeam array to achieve a bandwidth better than 27 %. The scattering parameters are performed using an Agilent N5227A vector network analyzer. As can be seen from Figure 5.18, all measured and simulated results are in good agreement. Measured S-parameters of fabricated antenna array with ports 2, 3, and 4 excitations are shown in Figure 5.19. The measured reflection coefficients of ports 2, 3, and 4 are similar to each other and to that of port1. The measured isolation between input ports with port 2, 3, or 4 excitation is less than -15 dB in the frequency range 54-67 GHz as shown in Figure 5.19. However, the measured results of isolation between input ports when ports 1, 2, 3, and 4 excited one at a time are similar.

For a planar rectangular array, the theoretical beam pointing angles can be calculated using equation (5.2).

$$\phi_0 = \tan^{-1} \left( \frac{\phi_y d_x}{\phi_x d_y} \right); \theta_0 = \sin^{-1} \sqrt{\left( \frac{\phi_x}{\kappa d_x} \right)^2 + \left( \frac{\phi_y}{\kappa d_y} \right)^2} \quad (5.2)$$

where  $d_x$  and  $d_y$  are the inter-element spaces in the x- and y-directions, respectively, and  $\kappa$  is the propagation constant in free space. The main beam scan angles ( $\Phi_0$ ,  $\Theta_0$ ) according to the progressive phase difference  $\Phi_x$ ,  $\Phi_y$  in x- and y-directions for different input ports are listed in

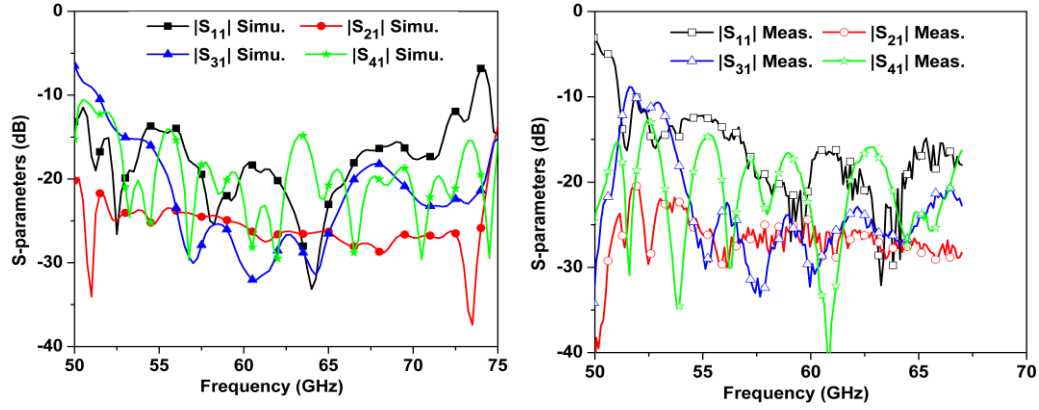


Figure 5.18: Measured and simulation s-parameters of the multibeam array with port 1 excitation.

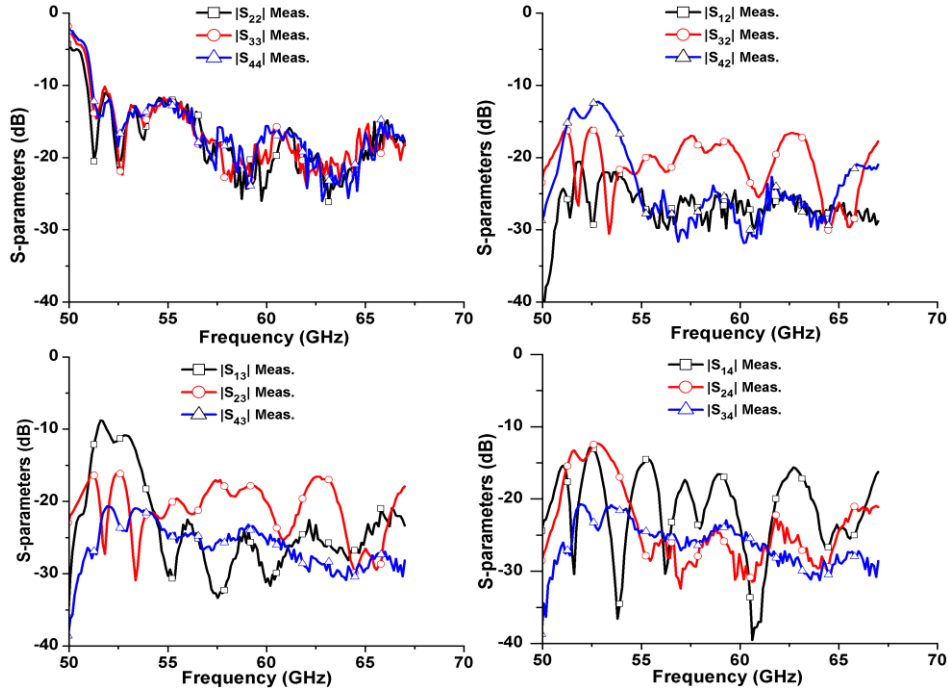


Figure 5.19: Measured S-parameters of fabricated antenna array with ports 2, 3, and 4 excitations.

Table 5.5. The proposed multibeam array features four tilted beams at  $33^\circ$  from a boresight direction with  $45^\circ$ ,  $135^\circ$ ,  $225^\circ$  and  $315^\circ$  in azimuth directions, i.e., one beam in each quadrant. Measured and simulated radiation patterns for  $xoz$ - and  $yo$ z-planes with port1 excitation for 55, 60, and 66 GHz are shown in Fig. 5.22. It can be seen that the main beam direction of the two planes is oriented close to  $20^\circ$ . As shown in Figure 5.20, the SLLs are higher than -9 dB in both perpendicular planes and normalized to the maximum radiations of  $xoz$ - and  $yo$ z-planes. One



reason for this relatively high level is that the SLLs are significantly affected by the ground plane size of the BFN.

Table 5.5: Theoretical phase difference along x- and y-axis and main directions of multibeam array.

Port	$\Phi_x$	$\Phi_y$	$\Phi_\theta$	$\Theta_0$
1	$+90^\circ$	$+90^\circ$	$+45^\circ$	$+33^\circ$
2	$-90^\circ$	$+90^\circ$	$-45^\circ$	$-33^\circ$
3	$+90^\circ$	$-90^\circ$	$-45^\circ$	$+33^\circ$
4	$-90^\circ$	$-90^\circ$	$+45^\circ$	$-33^\circ$

There is some difference between the measured and simulated results of the radiation pattern in terms of the sidelobe level and cross polarization, which is attribute to the measurement setup, including the reflections effect of waveguide adapters, loads, screws and cables near the antenna under test. The fabrication tolerance, the uncertainty of dielectric loss at 60 GHz, and a polarization mismatch during the radiation test could be another factor. As seen in Figure 5.20, the difference between measured and simulated cross-polarization and sidle lobe levels results occurred in the  $xoz$ -plane where the signal level is lower compared to the main beam, and maybe affected by the noise and reflections from the measurement setup. Moreover, since the matched loads and the feed adapters have cross section profiles in the  $xoz$ -plane unlike those of  $yo$ z-plane that may lead to different reflected signals in these two orthogonal planes, and thus may account for the difference between the measured and simulated results in the  $xoz$ -plane. Figure 5.21 illustrates the measured radiation patterns in the  $xoz$ - and  $yo$ z-palne for ports 2, 3, and 4 excitation at 60 GHz. The corresponding measured radiation patterns are similar to measured radiation patterns of port1. However, when the radiation patterns are normalized to the global maximum, the SLLs are less than -10 dB for  $xoz$ - and  $yo$ z-planes and less than -15 dB in  $45^\circ$  plane, over the whole band of interest, as shown in Figure 5.22. Note that the radiation patterns are measured from  $-120^\circ$  to  $+120^\circ$  due to the limitation of the anechoic chamber measurement setup. Generally speaking, the proposed multibeam array antenna has symmetrical radiation patterns in both orthogonal planes with stable radiation and good consisting between measured and HFSS results, over the entire band of interest.

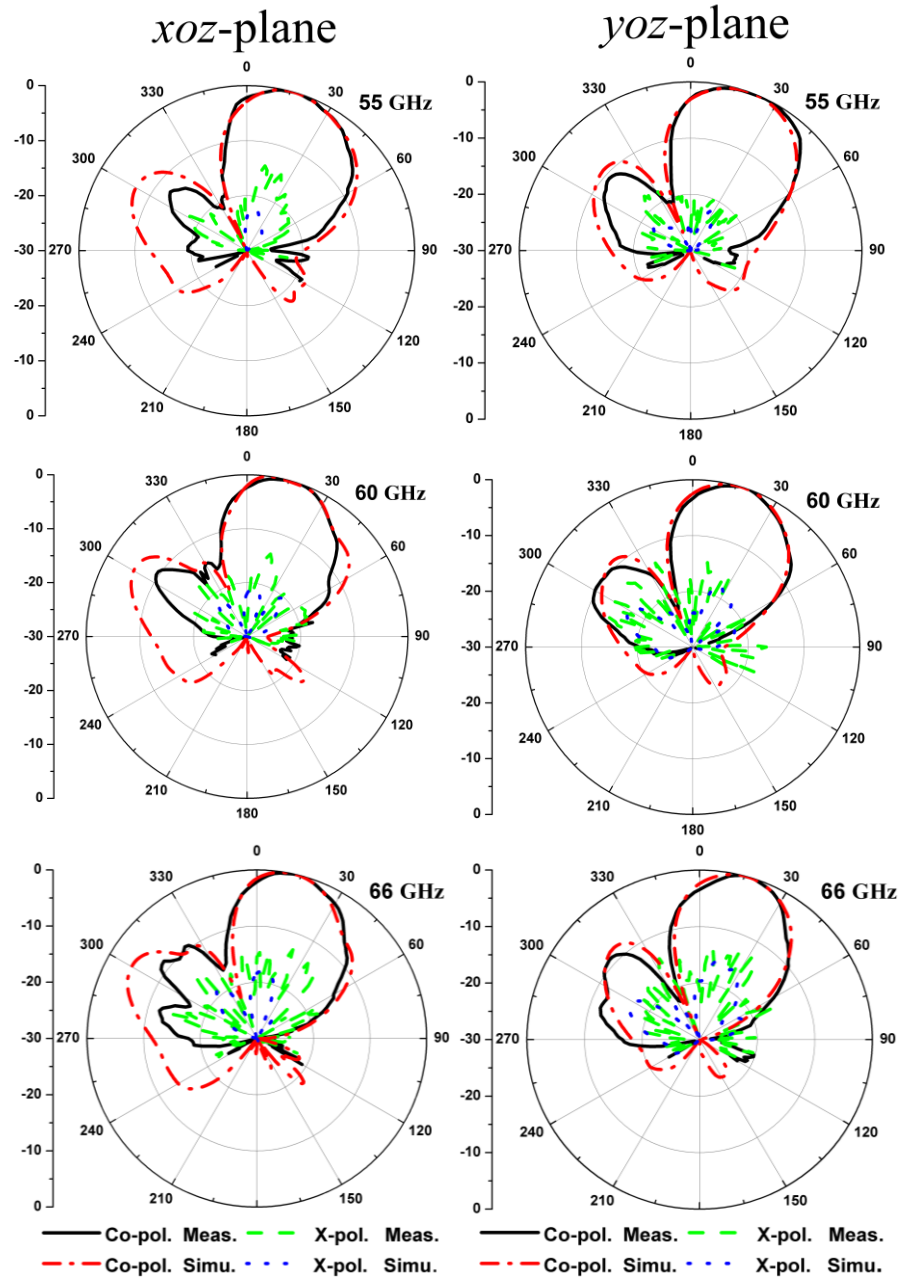


Figure 5.20: Measured and simulated radiation patterns of the proposed multibeam cavity-backed patch array at 55, 60 and 66 GHz.

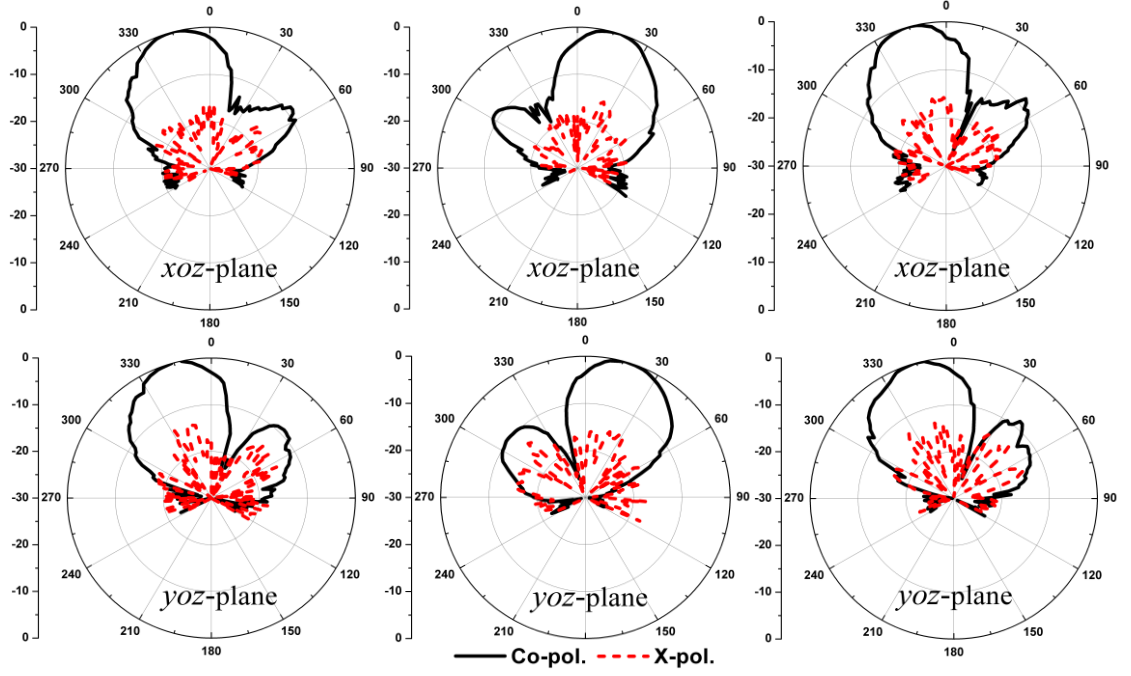


Figure 5.21: Measured radiation patterns of  $xoz$ - and  $yo$ z-plane for different port excitations at 60 GHz. (a) port 2 (b) port 3 and (c) port 4.

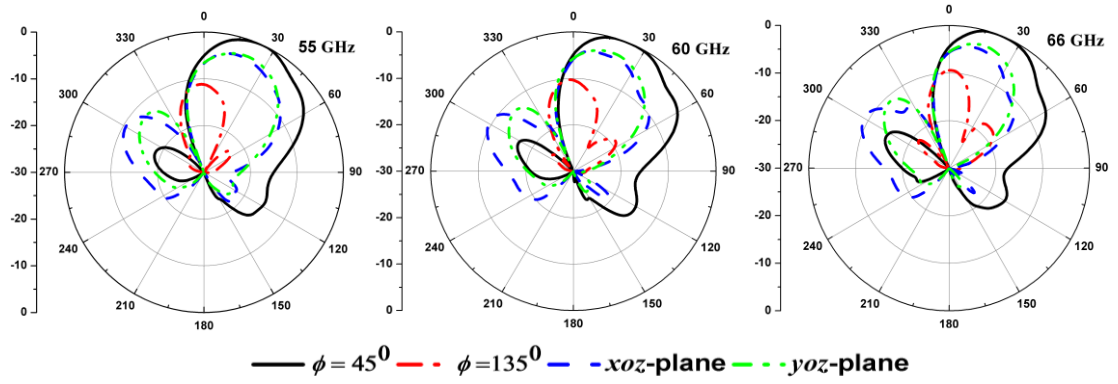


Figure 5.22: Simulated radiation pattern of the multibeam cavity-backed patch array at  $45^\circ$ ,  $135^\circ$  cut planes and principal planes ( $xoz$ - and  $yo$ z-plane) with port 1 excitation for 55, 60 and 66 GHz.

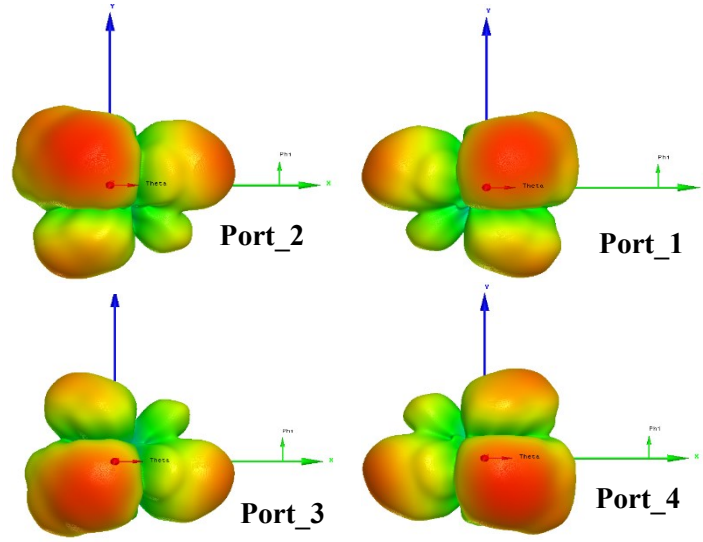


Figure 5.23: Simulated radiation patterns for all input ports of the proposed multibeam cavity-backed patch array.

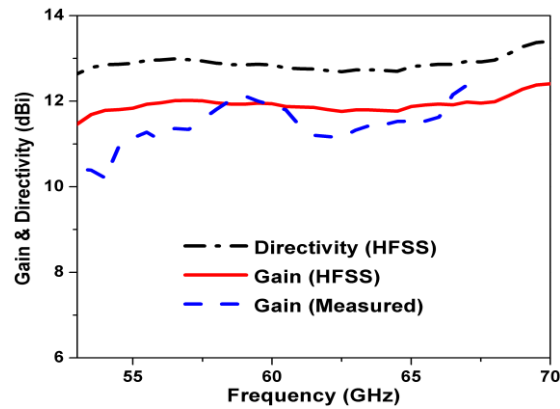


Figure 5.24: Gain and directivity of the proposed multibeam cavity-backed patch array.

The measured and simulated gain of the proposed array with port 1 excitation is shown in Figure 5.23, which is ranges from 11.1-12.4 dBi and 11.5-12.4, respectively, over the frequency band 55-70 GHz. The gain is measured by using a standard gain horn antenna as a reference. Due to the measurement set up limitations, gain is measured up to 67 GHz. Figure 5.23 shows the 3-D patterns of the proposed multibeam array for all input ports . As seen in Figure 5.24, the simulated directivity ranges from 12.7 to 13.4 dBi within a frequency band 55-70 GHz. The measured and simulated gain are in good agreement with a flat response over the band of interest. The measured efficiency ranges from 64 to 83% within the frequency range 55-66 GHz, which is calculated from the measured gain and simulated directivity.

## Chapter 6 Conclusion and Future Work

### 6.1 Conclusion

This thesis focusses on the development of several interesting antennas at 60 GHz to address several challenges at millimeter wave (MMW) bands. The high atmospheric absorption loss associated with MMW bands is the main challenge of wireless communication systems. Another challenge is the multipath fading channels issue that degrades the signal to noise ratio (S/N). Therefore, a wide bandwidth multiple-beam antenna array with stable radiation characteristics, including symmetrical radiation patterns, low cross-polarization, high efficiency and high-gain is a crucial component for high-speed short-range wireless connectivity at MMW bands. Tapered slot and cavity backing antennas are good candidates to achieve these requirements and to overcome some of the challenges associated with MMW wireless communications. The main activities of the thesis can be summarized as follows:

An antipodal Fermi tapered slot antenna (AFTSA) with sine-shaped corrugations is presented. To improve the antenna characteristics, in terms of impedance matching, radiation symmetry and gain, two modified antennas are constructed, optimized and tested. The proposed antenna provides a flat measured gain of 20 dB with a return loss better than 22 dB. Moreover, a broadband double-layer SIW-to-slotline transition is proposed to feed a planar linearly tapered slot antenna (PLTSA) covering the band 46-72 GHz. This new feeding technique overcomes the bandwidth limits of regular microstrip-to-slotline transitions and avoids the bond wires and air bridges. Therefore, the proposed antenna with this transition features superior performance, in terms of wide bandwidth, high gain, low cross-polarization, radiation symmetry and high efficiency. The antenna element shows a -10 dB impedance bandwidth of 44 % over the frequency range 46-72 GHz with a measured gain of 15.3 dB. Moreover, for maximum gain, a wide-band four-way SIW power divider with equal amplitude and zero phase delay is proposed to feed a 1x4 PLTSA array.

A novel wideband linearly polarized (LP) cavity-backed patch antenna is proposed for short-range 60 GHz wireless communications. The antenna element shows an overlapped 1-dB gain and impedance bandwidth of 43.4% from 56 to 87 GHz, a peak gain of 8.8 dBi, low cross-polarization, and a stable symmetrical radiation pattern over the entire band. Based on the proposed single-element, a wideband 1x8 array is presented, with a low side lobe level, whose beam-shape is

synthesized by amplitude tapering according to Taylor distribution. The array is fed by a broadband 8-way SIW power divider with unequal power dividing ratios and an equalized phase. The 1x8 array demonstrates a bandwidth of 37.6% from 54.7 to 80 GHz and a peak gain of 17.3 dBi. A 2x2 subarray employing a 4-way broad wall power divider is designed, exhibiting a bandwidth of 41.6% and a peak gain of 15.2 dBi. A 4x4 array with a bandwidth of 37.9% (54.9-80.6 GHz) and a peak gain of 20.8 dBi is presented. As a wideband transition with a good matching performance is crucial to feed the antenna arrays, a novel wideband right-angle transition between SIW and standard WR-15 rectangular waveguide has been implemented at V-band. The transition achieves a bandwidth of 48.6% for return loss better than 10 dB with a measured insertion loss of less than 0.5 dB.

To address the multipath fading challenges, two 1-D scanning multi-beam phased array designs based on SIW technology, at 60 GHz, have been presented. The first design is a compact multi-beam scanning slot antenna array with broadside radiation. The beamforming network (BFN) is implemented using a dual-layer 4x4 Butler matrix, where the  $45^\circ$  and  $0^\circ$  phase shifters are designed on a separate layer with different permittivity, resulting in a significant size reduction ( $25 \times 9.3 \times 0.508 \text{ mm}^3$ ). An extensive analysis of the principle of operation and the circuit-model of the proposed phase shifter have been discussed, showing less desperation characteristics compared to conventional phase shifters. The differential phase is  $\pm 45^\circ$  and  $\pm 135^\circ$ , corresponding to input ports (P1-4) with a maximum phase error of  $\pm 8^\circ$  over the frequency range 57-63 GHz. A 4x4 slot antenna array fed by the proposed matrix is fabricated, and the measured prototype results show an azimuthal coverage of  $121^\circ$ , with peak gains of 13.1, 11.5, 11.4, and 12.9 dBi, when port 1, 2, 3 and 4 are excited, respectively. The second design is a wideband high gain multi-beam tapered slot array with endfire radiation for 1-D scan applications. An SIW Butler matrix with a modified hybrid crossover is utilized as a beamformer network. The proposed crossover shows return loss better than 18 dB and good isolation between port 1 and ports 2 and 4, over the band of interest. The fabricated prototype exhibits a field of view of  $97^\circ$  in the azimuthal plane, with measured gain ranges from 12.7 to 15.6 dBi over the ISM band (56-66 GHz). The measured reflection and isolation coefficients of all input ports are less than -12.5 dB.

A novel multilayer SIW-fed LP cavity-backed patch antenna element with a flat gain and wide bandwidth has been developed. The antenna covers a bandwidth of 36.2 % (53-76.4 GHz) with a

flat gain ranging from 7.6 to 8.2 dBi. A prototype is fabricated and tested to validate the design approach, where the measured and simulated results are in good agreement. A compact two-layered beamforming network is designed with a size reduction of 28 % compared to a standard one-layered BFN without affecting its scattering parameters. The results show that the impedance bandwidth is 31.1 % (51.5-70.5 GHz) for  $|S_{11}| < -16$  dB with an average insertion loss of 1.3 dB. The proposed antenna element and BFN are employed to form a compact 2-D scanning multibeam array at 60 GHz. The proposed 2x2 multibeam array shows a bandwidth better than 27% with a radiation gain up to 12.4 dBi and simulated radiation efficiency of 80%.

## 6.2 Future Work

The following tasks summarize some recommendations for future work:

Extracting the s-parameters based on the equivalent circuit model of the SIW-to-air-filled WG transition and compare the results with full-wave simulation to further understand the matching mechanism and improve the impedance bandwidth and reduce the insertion loss of the transition.

Based on the low loss SIW full-corporate feed network that proposed to feed 4x4 cavity-backed patch array, an extended large-scale array consists of 8x8 or 16x16 element can be implemented for gain enhancement. Moreover, two-dimensional amplitude-tapering based on Taylor distribution can be used to achieve low SLLs, which could be a practical solution for false alarm issues in 77-GHz automotive radar systems.

Based on the proposed SIW cavity-backed rectangular patch and by using one-layer BFN and adding a transverse slot underneath the cavity, in addition to the existing longitudinal slot, a dual-polarized two-dimensional scanning switch-beam array can be implemented to mitigate the multipath fading interference.

## Bibliography

- [1] "IEEE Standard Letter Designations for Radar-Frequency Bands," IEEE Std 521-2002 (Revision of IEEE Std 521-1984), 2003.
- [2] Fact Sheet: Spectrum Frontiers Rules Identify, Open up Vast Amounts of New High-Band Spectrum for Next Generation (5G) Wireless Broadband. [Online]. <https://www.fcc.gov/document/rules-facilitate-next-generation-wireless-technologies>.
- [3] M. Marcus and B. Pattan, "Millimeter wave propagation; spectrum management implications," IEEE Microwave Magazine, vol. 6, no. 2, pp. 54-62, Jun. 2005.
- [4] FCC, "Code of Federal Regulation, Title 47 Telecommunication, Chapter 1, Part 15.255." Oct. 2004.
- [5] I. Mohamed, Z. Briqech, and A. Sebak. "Antipodal Fermi Tapered Slot Antenna For 60 GHz Band Applications," IEEE, Antennas and Wireless Propagation Letters, Vol.14, pp. 96 - 99, 2015.
- [6] I. Mohamed and A. R. Sebak, "High-Gain SIW-Based Antipodal Linearly Tapered Slot Antenna for 60-GHz Applications," IEEE Antennas and Propagation Society International Symposium (IEEE-APS/URSI), pp.217-218, July 2014.
- [7] M. Sun, C. Zhi Ning, and Q. Xianming, "Gain Enhancement of 60-GHz Antipodal Tapered Slot Antenna Using Zero-Index Meta-material," IEEE Transactions on Antennas and Propagation, vol.61, no.4, pp.1741, 1746, April 2013.
- [8] T. S. Rappaport, E. Ben-Dor, J. N. Murdock, and Y. Qiao, "38 GHz and 60 GHz Angle dependent Propagation for Cellular and peer-to-peer wireless communications," in Proc. IEEE Int. Conf. Commun., Jun. 2012, pp. 4568–4573.
- [9] P. Chen, W. Hong, Z. Kuai, and J. Xu, "A double layer substrate integrated waveguide Blass matrix for beamforming applications," IEEE Microw. Wireless Compon. Lett., vol. 19, no. 6, pp. 374–376, Jun. 2009.
- [10] T. Djerafi and N. J. G. Fonseca, "Planar Ku-band  $4 \times 4$  Nolen matrix in SIW technology," IEEE Trans. Microwave Theory Tech., vol. 58, no. 2, pp. 259–266, Feb. 2010.
- [11] K. Tekkouk, M. Ettorre and R. Sauleau, "SIW Rotman Lens Antenna with Ridged Delay Lines and Reduced Footprint," IEEE Trans. On Microw. Theory and Techn., April 2018.
- [12] C.-J. Chen and T.-H. Chu, "Design of a 60-GHz substrate integrated waveguide Butler matrix—A systematic approach," IEEE Trans. Microw. Theory Tech., vol. 58, no. 7, pp. 1724, 1733, Jul. 2010.
- [13] M. Bozzi, A. Georgiadis, and K. Wu, "Review of substrate-integrated waveguide circuits and antennas," IET Microw., Antennas Propag., vol. 5, no. 8, pp. 909–920, Jun. 2011.
- [14] M. S. Sorkherizi, A. Dadgarpour, and A. A. Kishk, "Planar high efficiency antenna array using new printed ridge gap waveguide technology," IEEE Trans. Antennas Propag., vol. 65, no. 7, pp. 3772–3776, Jul. 2017.
- [15] E. H. Mujammami, I. Afifi and A. B. Sebak, "Optimum Wideband High Gain Analog Beamforming Network for 5G Applications," *IEEE Access*, vol. 7, pp. 52226-52237, 2019.
- [16] A. Dadgarpour, M. S. Sorkherizi, T. A. Denidni, and A. A. Kishk, "Passive beam switching and dual-beam radiation slot antenna loaded with ENZ medium and excited



- through ridge gap waveguide at millimeter-waves,” IEEE Trans. Antennas Propag., vol. 65, no. 1, pp. 92–102, Jan. 2017.
- [17] Z. Briqech, A.-R. Sebak, and T. A. Denidni, “Wide-scan MSC-AFTSA array-fed grooved spherical lens antenna for millimeter-wave MIMO applications,” IEEE Trans. Antennas Propag., vol. 64, no. 7, pp. 2971–2980, Jul. 2016.
  - [18] W. Hong et al., “Multibeam antenna technologies for 5G wireless communications,” IEEE Trans. Antennas Propag., vol. 65, no. 12, pp. 6231–6249, Dec. 2017.
  - [19] J. Wells, Multi-Gigabit Microwave and Millimeter-Wave Wireless Communications. First Edition. Artech House, 2010.
  - [20] E. E. Altshuler and R. A. Marr, “A comparison of experimental and theoretical values of atmospheric absorption at the longer millimeter wavelengths,” IEEE Trans. Antennas Propag., vol. AP-36, no. 10, pp. 1471–1480, Oct. 1988.
  - [21] T. Manning, Microwave Radio Transmission Design Guide, Second Edition, Norwood, MA: Artech House, 2009.
  - [22] K. C. Huang, and D. J. Edwards, “Millimeter-Wave Antennas for Gigabit Wireless Communications,” John Wiley & Sons Ltd, 2008.
  - [23] F. Xu and K. Wu, “Guided-wave and leakage characteristics of substrate integrated waveguide,” IEEE Trans. Microw. Theory Techn., vol. 53, no. 1, pp. 66–73, Jan. 2005.
  - [24] Y. Cassivi, L. Perregrini, P. Arcioni, M. Bressan, K. Wu, and G. Conciauro, “Dispersion characteristics of substrate integrated rectangular waveguide,” IEEE Microwave Wireless Compon. Lett., vol. 12, pp. 333–335, Sep. 2002.
  - [25] A. K. Ozturk and R. Paknys, “Analysis of propagation between rows of conducting cylinders that model solid surfaces using the same surface area rule,” IEEE Trans. Antennas and Propag., on , vol. 60, no. 5, pp. 2602–2606, May 2012.
  - [26] G. F. Engen and C. A. Hoer, “Thru-reflect-line: An improved technique for calibrating the dual six-port automatic network analyzer,” IEEE Trans. Microw. Theory Techn., vol. MTT-27, no. 12, pp. 987–993, Apr. 1979.
  - [27] H. J. Eul and B. Schiek, ‘A generalized theory and new calibration procedures for network analyzer self-calibration’, IEEE Trans. Microw. Theory Tech., 39, (4), pp. 724–731, 1991.
  - [28] L.R. Lewis, M. Fassett and J. Hunt, “A Broadband Stripline Array Element,” 1974 IEEE AP-S International Symposium, Atlanta, GA June 1974, pp. 335–337.
  - [29] P. J. Gibson, “The Vivaldi aerial,” in Proc. 9th Eur. Microw. Conf., Brighton, U.K., p105, Jun. 1979.
  - [30] S. N. Parasad and S. Mahapatra, “A novel MIC slot-line antenna,” in Proc. 9th Eur. Microw. Conf., Brighton, U.K., Sep. 1979, pp. 120–124.
  - [31] K.S. Yngvesson, T.L. Korzeniowski, K Young-Sik, E.L. Kollberg, and J.F. Johansson, “The tapered slot antenna-A new integrated element for millimetre-wave applications,” IEEE Transactions on Microwave Theory and Techniques, vol.37, no.2, pp. 365–374, Feb. 1989.
  - [32] D. H. Schaubert, E.L. Kollberg, T. Korzeniowski, T. Thungren, J. Johansson, and K.S. Yngvesson, “Endfire tapered slot antennas on dielectric substrates,” IEEE Transaction on Antennas and Propagation, vol.33, no.12, pp.1392–1400, Dec. 1985.

- [33] Y. Dong, J. Choi, and T. Itoh, "Vivaldi antenna with pattern diversity for 0.7 to 2.7 GHz cellular band applications," *IEEE Antennas Wireless Propag. Lett.*, vol. 17, no. 2, pp. 247–250, Feb. 2018.
- [34] S. Sugawara, Y. Maita, K. Adahi, K. Mori, and K. Mizuno, "A mm-wave taper slot antenna with improved radiation pattern," *IEEE MTT-S International Microwave Symposium Digest. Vol.2*, pp. 959–962, June 1997.
- [35] Z. C. Hao, W. Hong, J. X. Chen, X. P. Chen, and K. Wu, "A novel feeding technique for antipodal linearly tapered slot antenna array," *IEEE MTT-S Int. Microw. Symp. Dig.*, CA, pp. 1641–1643, Jun. 2005.
- [36] D. Deslandes,, "Design equations for tapered microstrip-to Substrate Integrated Waveguidetransitions, " *Microwave Symposium Digest (MTT)*, 2010 *IEEE MTT-S International* , vol., no., pp.704,707, 23-28, May 2010.
- [37] Y. J. Cheng, W. Hong, and K. Wu, "Design of a monopulse antenna using a dual V-type linearly tapered slot antenna (DVL TSA)," *IEEE Trans. Antennas Propag.*, vol. 56, no. 9, pp. 2903–2906, Sep. 2008.
- [38] F. Taringou, D. Dousset, J. Bornemann, and K. Wu, "Broadband CPW feed for millimeter wave SIW-based antipodal linearly tapered slot antennas," *IEEE Trans. Antennas Propag.*, vol. 61, no. 4, pp. 1756–1762, Apr. 2013.
- [39] Y. Zhang, S. Shi, R. D. Martin, and D. W. Prather, "High-gain linearly tapered antipodal slot antenna on LCP substrate at E- and W-bands" *IEEE Antennas Wireless Propag. Lett.*, Vol. 15, pp.1357-1360, 2016.
- [40] J. Langley, P. Hall, and P. Newham, "Novel ultrawide-bandwidth Vivaldi antenna with low cross polarisation," *Electron. Lett.*, vol.29, no. 23, pp. 2004-2005, Nov. 1993.
- [41] Z. Briqech, A. Sebak, and T. A. Denidni, "60 GHz Fermi tapered slot antenna with sin-corrugation," in *Proc. IEEE APSURSI*, Jul. 2013, pp.160–161.
- [42] J. Bai, S. Shi, and Dennis W. Prather, "Modified compact antipodal Vivaldi antenna for 4-50 GHz UWB application," *IEEE Transactions on Microwave Theory and Techniques*, vol. 59, No. 4, pp. 1051–1057, 2011.
- [43] M. Moosazadeh and S. Kharkovsky, "A compact high-gain and front-to-back ratio elliptically tapered antipodal Vivaldi antenna with a trapezoid-shaped dielectric lens," *IEEE Antennas Wireless Propag. Lett.*, vol. 15, pp. 552–555, 2016.
- [44] Z. Wang, Y. Yin, J. Wu, and R. Lian, "A miniaturized CPW-fed antipodal Vivaldi antenna with enhanced radiation performance for wideband applications," *IEEE Antennas Wireless Propag. Lett.*, vol. 15, pp. 16–19, Dec. 2016.
- [45] D. Yang, S. Liu, and D. Geng, "A miniaturized ultra-wideband Vivaldi antenna with low cross-polarization," *IEEE Access*, vol. 5, pp. 23352– 23357, 2017.
- [46] J. Eichenberger, E. Yetisir and N. Ghalichechian, "High-Gain Antipodal Vivaldi Antenna With Pseudo element and Notched Tapered Slot Operating at (2.5 to 57) GHz," *IEEE Trans. Antennas Propag.*, vol. 67, no. 7, pp. 4357-4366, July 2019.
- [47] C. Jarufe et al., "Optimized corrugated tapered slot antenna for mmWave applications," *IEEE Trans. Antennas Propag.*, vol. 66, no. 3, pp. 1227–1235, Mar. 2018.

- [48] P. Liu, X. Zhu, Z. H. Jiang, Y. Zhang, H. Tang, and W. Hong, "A compact single-layer Q-band tapered slot antenna array with phase-shifting inductive windows for end-fire patterns," *IEEE Trans. Antennas Propag.*, vol. 67, no. 1, pp. 169–178, Jan. 2019.
- [49] J. T. Logan, R. W. Kindt, and M. N. Vouvakis, "Low cross-polarization Vivaldi arrays," *IEEE Trans. Antennas Propag.*, vol. 66, no. 4, pp. 1827–1837, Apr. 2018.
- [50] J. T. Logan, R. W. Kindt, and M. N. Vouvakis, "A 1.2-12 GHz sliced notch antenna array," *IEEE Trans. Antennas Propag.*, vol. 66, no. 4, pp. 1818–1826, Apr. 2018.
- [51] B. Youzkatli El-Khatib, T. Djerafi, and K. Wu, "Three-dimensional architecture of substrate integrated waveguide feeder for Fermi tapered slot antenna array applications," *IEEE Trans. Antennas Propag.*, vol. 60, no. 10, pp. 4610–4618, Oct. 2012.
- [52] E. G. Tianang, M. A. Elmansouri, and D. S. Filipovic, "Ultra-Wideband Lossless Cavity-Backed Vivaldi Antenna," *IEEE Trans. Antennas and Propag.*, vol. 66, no. 1, pp. 115–124, Jan. 2018.
- [53] R. Q. Lee and R. N. Simons, "Measured mutual coupling between linearly tapered slot antennas," *IEEE Trans. Antennas Propag.*, vol. 45, no. 8, pp. 1320–1322, Aug. 1997.
- [54] S. Gupta, Z. Briqech, A. R. Sebak, and T. A. Denidni, "Mutual-coupling reduction using metasurface corrugations for 28 GHz MIMO applications," *IEEE Antennas Wireless Propag. Lett.*, vol. 16, pp. 2763–2766, 2017.
- [55] M. Farahani, J. Pourahmadazar, M. Akbari, M. Nedil, A. R. Sebak, and T. A. Denidni, "Mutual coupling reduction in millimeter-wave MIMO antenna array using a metamaterial polarization-rotator wall," *IEEE Antennas Wireless Propag. Lett.*, vol. 16, pp. 2324–2327, Aug. 2017.
- [56] J. Li, G. Wen, and F. Xiao, "Broadband transition between rectangular waveguide and substrate integrated waveguide" *Electron. Lett.*, 46, pp. 223–224, 2010.
- [57] L. Xia, R. Xu, B. Yan, J. Li, Y. Guo, and J. Wang, "Broadband transition between air-filled waveguide and substrate integrated waveguide," *Electron. Lett.*, vol. 42, no. 24, pp. 1403–1405, Nov. 2006.
- [58] Y. Zhang, S. *et al.* "Broadband SIW-to-Waveguide Transition in Multilayer LCP Substrates at W-Band," *IEEE Microw. Wireless Compon. Lett.*, vol. 27, no. 3, pp. 224–226, March 2017.
- [59] Y. Li and K. M. Luk, "A broadband V-band rectangular waveguide to substrate integrated waveguide transition," *IEEE Microw. Wireless Compon. Lett.*, vol. 24, no. 9, pp. 590–592, Sep. 2014.
- [60] Y. Huang and K. L. Wu, "A broad-band LTCC integrated transition of laminated waveguide to the air-filled waveguide for millimeter-wave applications," *IEEE Trans. Microw. Theory Tech.*, vol. 51, no. 5, pp. 1613–1617, May 2003.
- [61] G. Zhang, H. Yi, S. Wang and M. Han, "Broadband right-angle transition from substrate integrated waveguide to rectangular waveguide," *Electr. Letters*, vol. 53, no. 7, pp. 473–475, March 2017.
- [62] Li, T., and Dou, W.B.: 'Broadband right-angle transition from substrate integrated waveguide to rectangular waveguide,' *Electron. Lett*, 50, pp. 1355–1356, 2014.

- [63] L. Li, X. P. Chen, R. Khazaka, and K. Wu, "A transition from substrate integrated waveguide (SIW) to rectangular waveguide," in Proc. Asia Pacific Microw. Conf., pp. 2605–2608, 2009.
- [64] H. Iizuka, K. Sakakibara and N. Kikuma, "Millimeter-Wave Transition From Waveguide to Two Microstrip Lines Using Rectangular Patch Element," *IEEE Trans. Microw. Theory Techn.*, vol. 55, no. 5, pp. 899-905, May 2007.
- [65] L. Wang, Y.-X. Guo, and W.-X. Sheng, "Wideband high-gain 60-GHz LTCC L-probe patch antenna array with a soft surface," *IEEE Trans. Antennas Propag.*, vol. 61, no. 4, pp. 1802–1809, Apr. 2013.
- [66] W. M. Abdel-Wahab, and S. Safavi-Naeini. "Wide-Bandwidth 60-GHz Aperture-Coupled Microstrip Patch Antennas (MPAs) Fed by Substrate Integrated Waveguide (SIW)," *IEEE Antennas Wireless Propag. Lett.* vol. 10, pp. 1003-1005, 2011.
- [67] T. H. Jang, H. Y. Kim, I. S. Song, C. J. Lee, J. H. Lee, and C. S. Park, "A wideband aperture efficient 60-GHz series-fed E-shaped patch antenna array with copolarized parasitic patches," *IEEE Trans. Antennas Propag.*, vol. 64, no. 12, pp. 5518–5521, Dec. 2016
- [68] N. C. Karmakar, "Investigations into a cavity-backed circular-patch antenna," *IEEE Trans. Antennas Propag.*, vol. 50, no. 12, pp. 1706– 1715, Dec. 2002.
- [69] M. M. Honari, R. Mirzavand, H. Saghlatoon, and P. Mousavi, "A dualband low-profile aperture antenna with substrate-integrated waveguide grooves," *IEEE Trans. Antennas Propag.*, vol. 64, no. 4, pp. 1561–1566, Apr. 2016.
- [70] K.-S. Chin et al., "Wideband LTCC 60-GHz antenna array with a dual-resonant slot and patch structure," *IEEE Trans. Antennas Propag.*, vol. 62, no. 1, pp. 174–182, Jan. 2014.
- [71] M. H. Awida and A. E. Fathy, "Substrate-integrated waveguide Ku-band cavity-backed 2x2 microstrip patch array antenna," *IEEE Antennas Wireless Propag. Lett.*, vol. 8, pp. 1054-1056, 2009.
- [72] T. Y. Yang et al., "Wideband millimeter-wave substrate integrated waveguide cavity-backed rectangular patch antenna," *IEEE Trans. Antennas Propag.*, Lett. vol. 13, pp. 205-208, 2014.
- [73] J. Zhu, C. Chu, L. Deng, C. Zhang, Y. Yang, and S. Li, "mm-Wave High Gain Cavity-Backed Aperture-Coupled Patch Antenna Array," *IEEE Access*, vol. 6, pp. 44050-44058, 2018.
- [74] G. Q. Luo, Z. F. Hu, L. X. Dong, and L. L. Sun, "Planar Slot Antenna Backed by Substrate Integrated Waveguide Cavity," *IEEE Antenna Wireless Propag. Lett.*, vol. 7, pp. 236–239, 2008.
- [75] W. Han, F. Yang, J. Ouyang and P. Yang, "Low-cost Wideband and High-Gain Slotted Cavity Antenna Using High-Order Modes For Millimeter-Wave Application," *IEEE Trans. Antennas Propag.*, vol. 63, no. 11, pp. 4624-4631, Nov. 2015.
- [76] K. Gong, Z. Chen, X. Qing, P. Chen, and W. Hong, "Substrate Integrated Waveguide Cavity-Backed Wide Slot Antenna for 60-GHz Bands," *IEEE Trans. Antennas Propag.*, vol. 60, no. 12, pp. 6023–6026, Dec. 2012.

- [77] Z. Chen, H. Liu, J. Yu, and X. Chen, "High gain, Broadband and Dual-polarized Substrate Integrated Waveguide Cavity-Backed Slot Antenna Array for 60 GHz Band," *IEEE Access*, vol. 6, pp. 31012-31022, 2018.
- [78] A. Beltayib, I. Afifi and A. Sebak, "4x4 -Element Cavity Slot Antenna Differentially-Fed by Odd Mode Ridge Gap Waveguide," *IEEE Access*, vol. 7, pp. 48185-48195, 2019.
- [79] Q. Zhu, K. B. Ng, C. H. Chan and K. M. Luk, "Substrate-Integrated-Waveguide-Fed Array Antenna Covering 57–71 GHz Band for 5G Applications," *IEEE Trans. Antennas Propag.*, vol. 65, no. 12, pp. 6298-6306, Dec. 2017.
- [80] X. Ruan, K. B. Ng, and C. H. Chan, "A differentially Fed Transmission-line Excited Magneto electric Dipole Antenna Array for 5G applications," *IEEE Trans. Antennas Propag.*, vol. 66, no. 10, pp. 5224-5230, Oct. 2018.
- [81] D. Zarifi, A. Farahbakhsh, A. U. Zaman, and P.-S. Kildal, "Design and fabrication of a high-gain 60-GHz corrugated slot antenna array with ridge gap waveguide distribution layer," *IEEE Trans. Antennas Propag.*, vol. 64, no. 7, pp. 2905-2913, Jul. 2016.
- [82] J. Liu, A. Vosoogh, A. U. Zaman, and J. Yang, "A slot array antenna with single-layered corporate-feed based on ridge gap waveguide in the 60 GHz band," *IEEE Trans. Antennas Propag.*, vol. 67, no. 3, pp. 1650-1658, Mar. 2019.
- [83] J. F. Xu, Z. N. Chen, X. M. Qing, and W. Hong, "Bandwidth enhancement for a 60 GHz substrate integrated waveguide fed cavity array antenna on LTCC," *IEEE Trans. Antennas Propag.*, vol. 59, no. 3, pp. 826-832, Mar. 2011.
- [84] K. Fan, Z. C. Hao and Q. Yuan, "A Low-Profile Wideband Substrate Integrated Waveguide Cavity-Backed E-Shaped Patch Antenna for the Q-LINKPAN Applications," *IEEE Trans. Antennas Propag.*, vol. 65, no. 11, pp. 5667-5676, Nov. 2017.
- [85] X.-P. Chen, K. Wu, L. Han, and F. He, "Low-cost, high gain planar antenna array for 60-GHz band applications," *IEEE Trans. Antennas Propag.*, vol. 58, pp. 2126-2129, Jun. 2010.
- [86] S. Liao, P. Chen, P. Wu, K. M. Shum, and Q. Xue, "Substrate integrated waveguide-based 60- resonant slotted waveguide arrays with wide impedance bandwidth and high gain," *IEEE Trans. Antennas Propag.*, vol. 63, no. 7, pp. 2922-2931, Jul. 2015.
- [87] X. Li, J. Xiao, Z. Qi, and H. Zhu, "Broadband and high-gain SIW-fed antenna array for 5G applications," *IEEE Access*, vol. 6, pp. 56282-56289, 2018.
- [88] C. Mao, M. Khalily, P. Xiao, T. W. C. Brown, S. Gao, "Planar Sub Millimeter-Wave Array Antenna with Enhanced Gain and Reduced Sidelobes for 5G Broadcast Applications", *IEEE Trans. Antennas Propag.*, Vol. 67, pp. 160-168, Jan. 2019.
- [89] Y. J. Cheng, Y. X. Guo, and Z. Q. Liu, "W-Band large-scale high-gain planar integrated antenna array," *IEEE Trans. Antennas Propag.*, vol. 62, no. 6, pp. 3370-3373, Jun. 2014.
- [90] M. Li, K. M. Luk, "Low-cost wideband microstrip antenna array for 60- GHz applications," *IEEE Trans. Antennas Propag.*, vol. 62, no. 6, pp. 3012-3018, June 2014.
- [91] Y. J. Li and K. M. Luk, "Low-cost high-gain and broadband substrate integrated waveguide fed patch antenna array for 60 GHz band," *IEEE Trans. Antennas Propag.*, vol. 62, no. 11, pp. 5531-5538, Nov. 2014.

- [92] Y. Li and K.-M. Luk, "60-GHz substrate integrated waveguide fed cavity-backed aperture-coupled microstrip patch antenna arrays," *IEEE Trans. Antennas Propag.*, vol. 63, no. 3, pp. 1075–1085, Mar. 2015.
- [93] L. Qin, Y. Lu, Q. You, Y. Wang, J. Huang, and G. Peter, "Millimeter wave slotted waveguide array with unequal beam-widths and low sidelobe levels for vehicle radars and communications," *IEEE Trans. Veh. Technol.*, vol. 67, no. 11, pp. 10574-10582, Aug. 2018.
- [94] S.-J. Park, D.-H. Shin, and S.-O. Park, "Low side-lobe substrate integrated-waveguide antenna array using broadband unequal feeding network for millimeter-wave handset device," *IEEE Trans. Antennas Propag.*, vol. 64, no. 3, pp. 923-932, Mar. 2016.
- [95] K. C. Huang, and Z. C. Wang, *Millimeter Wave Communication Systems*, 133-162, John Wiley & Sons, 2011.
- [96] A. F. Molisch, *Wireless Communications*, Wiley-IEEE Press, 2005.
- [97] L. C. Godara, "Application of antenna arrays to mobile communications. II. Beamforming and direction-of-arrival considerations," *IEEE Proceedings*, vol.85, no.8, pp.1195-1245, Aug 1997.
- [98] J. Butler and R. Lowe, "Beamforming Matrix Simplifies Design of Electronically Scanned Antennas," *Electronic Design*, Apr. 1961.
- [99] J. P. Shelton and K. S. Kelleher, "Multiple beams from linear arrays," *IEEE Trans. Antennas Propag.*, vol. 9, no. 2, pp. 154–161, 1961.
- [100] H. N. Chu and T. G. Ma, "An Extended 4x4 Butler Matrix With Enhanced Beam Controllability and Widened Spatial Coverage," *IEEE Trans. Microw. Theory Tech.*, vol. 66, no. 3, pp. 1301-1311, March 2018.
- [101] K. Ding and A. A. Kishk, "2-D Butler matrix and phase-shifter group," *IEEE Trans. Microw. Theory Techn.*, vol. 66, no. 12, pp. 1-9, Dec. 2018.
- [102] K. Ding and A. A. Kishk, "Extension of Butler Matrix Number of Beams Based on Reconfigurable Couplers," *IEEE Trans. Antennas Propag.*, vol. 67, no. 6, pp. 3789-3796, June 2019.
- [103] K. Xiang, F. Chen, Q. Chu and M. J. Lancaster, "A Broadband 3×4 Butler Matrix and its Application in Multibeam Antenna Arrays," *IEEE Trans. Antennas Propag.*, August 2019.
- [104] C. H. Tseng, C. J. Chen, and T. H. Chu, "A low-cost 60-GHz switched beam patch antenna array with Butler matrix network," *IEEE Antennas Wireless Propag. Lett.*, vol. 7, pp. 432–435, 2008.
- [105] W.F. Moulder, W. Khalil, and J.L. Volakis, "60-GHz Two-Dimensionally Scanning Array Employing Wideband Planar Switched Beam Network," *IEEE Antennas and Wireless Propagation Letters*, vol.9, pp. 818-821, 2010.
- [106] R. Movahedinia, A.-R. Sebak, M. R. Chaharmir, M. R. Nikkhah, and A. A. Kishk, "X-band circularly polarized electronically steerable parasitic array radiator of DRA," *IEEE Trans. Antennas Propag.*, vol. 66, no. 2, pp. 721–728, Feb. 2018.
- [107] S. A. Babale, S. K. A. Rahim, O. A. Barro, M. Himdi, and M. Khalily, "Single layered 4x4 butler matrix without phase-shifters and crossovers," *IEEE Access*, vol. 6, pp. 77 289 -77 298, 2018.

- [108] M. Mantash and T. A. Denidni, "CP Antenna Array With Switching-Beam Capability Using Electromagnetic Periodic Structures for 5G Applications," *IEEE Access*, vol. 7, pp. 26192-26199, 2019.
- [109] A. Doghri, T. Djerafi, A. Ghiotto, K. Wu, "Substrate integrated waveguide directional couplers for compact 3-D integrated circuits", *IEEE Transactions on Microwave Theory and Techniques*, vol. 63, no. 1, pp. 209-221, Jan. 2015.
- [110] F. Parment, A. Ghiotto, T. P. Vuong, J. M. Duchamp and K. Wu, "Double Dielectric Slab-Loaded Air-Filled SIW Phase Shifters for High-Performance Millimeter-Wave Integration," *IEEE Transactions on Microwave Theory and Techniques*, vol. 64, no. 9, pp. 2833-2842, Sept. 2016.
- [111] X. Cheng, Y. Yao, T. Tomura, J. Hirokawa, T. Yu, J. Yu, and X. Chen, "Millimeter-wave frequency beam scanning array with a phase shifter based on substrate-integrated-waveguide," *IEEE Access*, vol. 6, pp. 47408–47414, 2018.
- [112] T. Djerafi and K. Wu, "60 GHz substrate integrated waveguide crossover structure," in *Proc. Eur. Microw. Conf.*, Rome, Italy, 2009, pp. 1014–1017.
- [113] Y. J. Cheng, W. Hong, and K. Wu, "Broadband self-compensating phase shifter combining delay line and equal-length unequal-width phaser," *IEEE Trans. Microw. Theory Techn.*, vol. 58, no. 1, pp. 203–210, Jan. 2010.
- [114] Y. F. Wu, Y. J. Cheng, and Z. X. Huang, "Ka-band near-field-focused 2-D steering antenna array with a focused rotman lens," *IEEE Trans. Antennas Propag.*, vol. 66, no. 10, pp. 5204–5213, Oct. 2018.
- [115] Y. J. Cheng et al., "Substrate integrated waveguide (SIW) rotman lens and its Ka-band multibeam array antenna applications," *IEEE Trans. Antennas Propag.*, vol. 56, no. 8, pp. 2504–2513, Aug. 2008.
- [116] H. Ren, H. Zhang, Y. Jin, Y. Gu and B. Arigong, "A Novel 2-D 3x 3 Nolen Matrix for 2-D Beamforming Applications," *IEEE Trans. Microw. Theory Techn.*, June 2019.
- [117] L.H. Zhong, Y.L. Ban, J.W. Lian, Q.-L. Yang, J. Guo, and Z.-F. Yu, "Miniaturized SIW multibeam antenna array fed by dual-layer  $8 \times 8$  Butler matrix," *IEEE Antennas Wireless Propag. Lett.*, vol. 16, pp. 3018–3021, 2017.
- [118] Y. Li and K. M. Luk, "A Multibeam End-Fire Magnetolectric Dipole Antenna Array for Millimeter-Wave Applications," *IEEE Trans. Antennas Propag.*, vol. 64, no. 7, pp. 2894-2904, July 2016.
- [119] J. Wang, Y. Li, L. Ge, J. Wang and K. M. Luk, "A 60 GHz Horizontally Polarized Magnetolectric Dipole Antenna Array With 2-D Multibeam Endfire Radiation," *IEEE Trans. Antennas Propag.*, vol. 65, no. 11, pp. 5837-5845, Nov. 2017.
- [120] J. Zhu, B. Peng, and S. Li, "Cavity-backed high gain switch beam antenna array for 60 GHz applications", *IET Microw. Antennas Propag.*, 11, (12), pp. 1776–1781, 2017.
- [121] X. Cheng et al. "A compact multi-beam end-fire circularly polarized septum antenna array for millimeter-wave applications," *IEEE Access*, vol. 6, pp. 62784–62792, 2018.
- [122] T. Djerafi and K. Wu, "A Low-Cost Wideband 77-GHz Planar Butler Matrix in SIW Technology," *IEEE Trans. Antennas Propag.*, vol. 60, no. 10, pp. 4949-4954, Oct. 2012.
- [123] J. W. Lian, Y. L. Ban, Q. L. Yang, B. Fu, Z. F. Yu and L. K. Sun, "Planar Millimeter-Wave 2-D Beam-Scanning Multibeam Array Antenna Fed by Compact SIW Beam-

- Forming Network," IEEE Trans. Antennas Propag., vol. 66, no. 3, pp. 1299-1310, March 2018.
- [124] J. Lian, Y. Ban, J. Zhu, J. Guo and Z. Chen, "Planar 2-D Scanning SIW Multibeam Array With Low Sidelobe Level for Millimeter-Wave Applications," IEEE Trans. Antennas Propag., vol. 67, no. 7, pp. 4570-4578, July 2019.
  - [125] M. M. M. Ali and A.-R. Sebak, "2-D scanning magnetoelectric dipole antenna array fed by RGW butler matrix," IEEE Trans. Antennas Propag., vol. 66, no. 11, pp. 6313–6321, Nov. 2018.
  - [126] C.W. Wang, T.G. Ma, and C.F. Yang, "A new planar artificail transmission line and its application to a miniaturized Bulter matrix", IEEE Trans. on Microwave Theory and Tech., VOL. 55, NO. 12, pp. 2792–2801, Dec. 2007.
  - [127] M. Bona, L. Manholm, J. P. Starski, and B. Svensson, "Low-loss compact Butler matrix for a microstrip antenna," IEEE Trans. Microw. Theory Tech., vol. 50, no. 9, pp. 2069–2075, Sep. 2002.
  - [128] A. B. Guntupalli, T. Djerafi, and K. Wu, "Two-dimensional scanning antenna array driven by integrated waveguide phase shifter," IEEE Trans. Antennas Propag., vol. 62, no. 3, pp. 1117-1124, Mar. 2014.
  - [129] W. Yang, Y. Yang, W. Che, C. Fan and Q. Xue, "94-GHz Compact 2-D Multibeam LTCC Antenna Based on Multifolded SIW Beam-Forming Network," IEEE Trans. Antennas Propag., vol. 65, no. 8, pp. 4328-4333, Aug. 2017.
  - [130] M. Nedil, T. A. Denidni, and L. Talbi, "Novel Butler matrix using CPW multilayer technology," IEEE Trans. Microw. Theory Tech., vol. 54, no. 1, pp. 499–507, Jan. 2006.
  - [131] A. A. M. Ali, N. J. G. Fonseca, F. Coccetti, and H. Aubert, "Design and implementation of two-layer compact wideband Butler matrices in SIW technology for ku-band applications," IEEE Trans. Antennas Propag., vol. 59, no. 2, pp. 503-512, Feb. 2011.
  - [132] P. Chen et al., "A multibeam antenna based on substrate integrated waveguide technology for MIMO wireless communications," IEEE Trans. Antennas Propag., vol. 57, no. 6, pp. 1813–1821, Jun. 2009.
  - [133] Q. L. Yang, Y. L. Ban, K. Kang, C. Y. D. Sim, and G. Wu, "SIW multibeam array for 5G mobile devices," IEEE Access, vol. 4, pp. 2788–2796, Jun. 2016.
  - [134] Q.-L. Yang, Y.-L. Ban, J.-W. Lian, Z.-F. Yu, and B. Wu, "SIW Butler matrix with modified hybrid coupler for slot antenna array," IEEE Access, vol. 4, pp. 9561–9569, 2016.
  - [135] C. E. Shannon, A Mathematical Theory of Communication, vol. 27, pp. 379–423, 623–656, 1948.
  - [136] D. M. Pozar, and B. Kaufman, "Comparison of three methods for the measurement of printed antenna efficiency," IEEE Transactions on Antennas and Propagation, vol. 36, no. 1, pp. 136-139, Jan. 1988.
  - [137] C. A. Balanis, Antenna Theory-Analysis and design. Hoboken, NJ, USA: Wiley, 2016.
  - [138] L. Yan, W. Hong, G. Hua, J. Chen, and K. Wu, "Simulation and experiment on SIW slot array antennas," IEEE Microw. Wireless Compon. Lett., vol. 14, no. 9, pp. 446-448, Sep. 2004.
  - [139] J. D. Kraus, Antennas, McGraw-Hill, New York, pp. 26-27, 1988.



- [140] W. L. Stutzman and G. A. Thiele, *Antenna Theory and Design*, 3rd ed. Hoboken, NJ, USA: Wiley, 2012.
- [141] R. S. Elliott, "An improved design procedure for small arrays of shunt slots," *IEEE Trans. Antennas Propag.*, vol. AP-31, pp. 48–53, Jan. 1983.
- [142] H. J. Riblet, "The short-slot hybrid junction," *Proceedings of the IRE*, vol. 40, no. 2, pp. 180–184, 1952.
- [143] I. A. Eshrah, A. A. Kishk, A. B. Yakovlev, W. G. Glisson, and C. E. Smith, "Analysis of waveguide slot-based structures using wideband equivalent-circuit model," *IEEE Trans. Microw. Theory Tech.*, vol. 52, no. 12, pp. 2691–2696, Dec. 2004.
- [144] W. H. Nester, "The fast Fourier transform and the Butler matrix," *IEEE Trans. Antenna Propag.*, vol. 16, no. 3, p. 360, May 1968.
- [145] J. P. Shelton, "Fast Fourier transforms and Butler matrices," *Proc. IEEE*, vol. 56, no. 3, p. 350, Mar. 1968.
- [146] H. Ren, B. Arigong, M. Zhou, J. Ding, and H. Zhang, "A novel design of  $4 \times 4$  Butler matrix with relatively flexible phase differences," *IEEE Antennas Wireless Propag. Lett.*, vol. 15, pp. 1277–1280, 2016.
- [147] K. Wincza and S. Gruszczynski, "Broadband integrated  $8 \times 8$  Butler matrix utilizing quadrature couplers and Schiffman phase shifters for multibeam antennas with broadside beam," *IEEE Trans. Microw. Theory Techn.*, vol. 64, no. 8, pp. 2596–2604, Aug. 2016.
- [148] A. B. Guntupalli, K. Wu, "Multi-dimensional scanning multi-beam array antenna fed by integrated waveguide Butler matrix," *IEEE MTT-S Int. Micro. Symp.*, June 2012, pp. 1–3.
- [149] Y.-X. Guo and H. Chu, "60-GHz LTCC dielectric resonator antenna array," in *Proc. IEEE APS*, Orlando, FL, USA, Jul. 2013, pp. 1874–1875.
- [150] I. Mohamed and A. Sebak, "Broadband Transition of Substrate-Integrated Waveguide-to-Air-Filled Rectangular Waveguide," *IEEE Microw. Wireless Compon. Lett.* vol. 28, no. 11, pp. 966–968, Nov. 2018.
- [151] Y. J. Cheng, W. Hong and K. Wu, "Millimeter-Wave Multibeam Antenna Based on Eight-Port Hybrid," *IEEE Microw. Wireless Compon. Lett.*, vol. 19, no. 4, pp. 212–214, April 2009.
- [152] Y. Li and K. M. Luk, "60-GHz Dual-Polarized Two-Dimensional Switch-Beam Wideband Antenna Array of Aperture-Coupled Magneto-Electric Dipoles," *IEEE Trans. Antenna Propag.*, vol. 64, no. 2, pp. 554–563, Feb. 2016.

## List of Publications

### *Journal Papers*

- [J1] I. Mohamed and A. Sebak, "60 GHz 2-D Scanning Multibeam Cavity-Backed Patch Array Fed by Compact SIW Beamforming Network for 5G Applications," *IEEE Transactions on Antennas and Propagation*, vol. 67, no. 4, pp. 2320-2331, April 2019.
- [J2] I. Mohamed and A. Sebak, "Broadband Transition of Substrate-Integrated Waveguide-to-Air-Filled Rectangular Waveguide," *IEEE Microwave and Wireless Components Letters*, vol. 28, no. 11, pp. 966-968, Nov. 2018.
- [J3] I. Mohamed, Z. Briqech and A. Sebak, "Antipodal Fermi Tapered Slot Antenna for 60-GHz Band Applications," *IEEE Antennas and Wireless Propagation Letters*, vol. 14, pp. 96-99, 2015.
- [J4] I. Mohamed, and A. R. Sebak. "High-gain series-fed aperture-coupled microstrip antenna array." *Microwave and Optical Technology Letters*, Vol. 57, no.1, pp. 91-94, 2015.
- [J5] I. Mohamed, and A. R. Sebak. "A Broadband Double-Layered SIW-Based Planar Linearly Tapered Slot Antenna with Low Cross-Polarization for 5G Applications" *IET Microw. Antennas Propag.*, 2019, submitted.
- [J6] I. Mohamed, and A. R. Sebak. "Miniaturized SIW-Based Multi-Beam Slot Antenna Array Fed by Dual-Layered 4x4 Butler Matrix, *IEEE Trans. Antennas Propag.*, 2019, submitted.
- [J7] I. Mohamed, and A. R. Sebak. "A Wideband Multibeam End-Fire Fermi Tapered Slot Antenna Array with SIW Butler Matrix for 60 GHz Wireless Communications". *IEEE Access*, 2019, submitted.
- [J8] I. Mohamed, and A. R. Sebak "A Compact Wideband SIW-Fed Cavity-Backed Patch Antenna Array for 5G Applications" *IEEE Trans. Antennas Propag.*, 2019, submitted.

### *Conference Papers*

- [C1] I. Mohamed and A. Sebak, "A 60 GHz SIW-based Vivaldi antenna with improved radiation patterns," *2016 IEEE International Symposium on Antennas and Propagation (APSURSI)*, Fajardo, 2016, pp. 805-806.
- [C2] I. Mohamed and A. Sebak, "Linearly tapered slot antenna array with SIW feed network for 60 GHz applications," *2016 17th International Symposium on Antenna Technology and Applied Electromagnetics (ANTEM)*, Montreal, QC, 2016, pp. 1-2.
- [C3] I. Mohamed and A. Sebak, "A 50-70 GHz SIW-Based Linearly Tapered Slot Antenna with Low Cross Polarization," *2015 IEEE International Conference on Ubiquitous Wireless Broadband (ICUWB)*, Montreal, QC, 2015, pp. 1-4.
- [C4] I. Mohamed and A. Sebak, "Aperture-coupled 2x2 microstrip antenna array for 60 GHz applications," *2015 IEEE International Symposium on Antennas and Propagation & USNC/URSI National Radio Science Meeting*, Vancouver, BC, 2015, pp. 1900-1901.

- [C5] I. Mohamed and A. Sebak, "Dielectric loaded antipodal linearly tapered slot antenna for 60 GHz applications," *Global Symposium on Millimeter-Waves (GSMM)*, Montreal, QC, 2015, pp. 1-2.
- [C6] I. Mohamed and A. Sebak, "High-gain SIW-based antipodal linearly tapered slot antenna for 60-GHz applications," *2014 IEEE Antennas and Propagation Society International Symposium (APSURSI)*, Memphis, TN, 2014, pp. 217-218.
- [C7] I. Mohamed, Z. Briqech and A. Sebak, "High-gain dielectric-loaded antipodal Fermi tapered slot antenna for MM-wave applications," *2014 16th International Symposium on Antenna Technology and Applied Electromag. (ANTEM)*, Victoria, BC, 2014, pp. 1-2.